Probing Magnetism in Magneto-electric Multiferroics using Circularly Polarized X-rays

Federica Fabrizi

A Thesis presented for the degree of

Doctor of Philosophy

I, Federica Fabrizi, confirm that the work presented in this thesis is my own. Wherever information has been derived from other sources, this has been indicated in the thesis.

Abstract

Multiferroic materials (in which electric and magnetic order coexist) that also display magneto-electric coupling have recently raised considerable interest as candidate compounds for advanced applications in electronics and data storage. In particular, the magneto-electric coupling is relevant in those materials such as $TbMnO_3$ and $Ni_3V_2O_8$ in which the onset of a cycloidal magnetic order drives the formation of a ferroelectric state. A key feature in these compounds is the possibility to control the population of magnetic domains (defined by the handedness of the cycloids) by an in situ electric field.

The combination of magnetic non-resonant diffraction by circularly polarised X-rays with the full linear polarimetry of the scattered beam opens the way to a new class of experiments, in which the magnetic order of complex magnetic materials under applied electric and magnetic fields is probed. This technique brings a strong experimental sensitivity to the imbalance in the domain populations, since the handedness of the circular polarisation naturally couples to the sense of rotation of the magnetic moments, leading to an accurate description of the domain state and to the refinement of the magnetic structure.

The results shed more light on the complex magnetic structure of $TbMnO_3$, a challenging test case due to its two magnetic sublattices on the Mn and Tb sites, by identifying components of the ordering on the Tb sublattice and phase shifts that earlier neutron diffraction experiments could not resolve. In the case of $Ni_3V_2O_8$, the method not only facilitated the refinement of the magnetic structure, but also allowed real space images of the magnetic cycloidal domains to be obtained. Their evolution is followed as they are controlled via magneto-electric coupling by the applied electric field and cycled through a hysteresis loop, thus collecting valuable information on domain formation, inhomogeneities and domain wall movement.

Acknowledgements

The first person I would like to thank is my supervisor Des McMorrow, for his guidance and help through all of my thesis. I also wish to thank Christian Ruegg for supervising this work. I am indebted to Luigi Paolasini who superintended my experimental work at the European Synchrotron Radiation Facility with constant assistance throughout these years, and to the Facility for supporting my research project at the ID20 beamline.

A special mention must go to Helen Walker with whom I enjoyed a very good collaboration, which has been essential for this thesis. Many thanks to the ID20 team and collaborators who worked with me during my staying at the beamline, in particular Valerio Scagnoli, Claudio Mazzoli, Javier Herrero-Martin, Javier Fernandez-Rodriguez. I also wish to thank Tom Forrest, Tom Fennell and all the UCL students and staff with whom I shared experimental time. I enjoyed helpful discussions with Paolo Ghigna and Sergio Di Matteo. I would like to show all my gratitude to Andrea Fondacaro and all the technical staff who offered great support during the experiments. I am especially grateful to Francois de Bergevin for many lengthy discussions which enourmously helped my study, especially regarding the interpretation of the experimental results.

As for the study on $Ni_3V_2O_8$ I am indebted to Michel Kenzelmann both for growing the samples and for his help and advice in the experiments. My thanks also go to the crystal growers who provided the $TbMnO_3$ samples, Prabhakaran Dharmalingam and Andrew Boothroyd at the University of Oxford.

Finally I wish to express my gratitude to my parents and family for their unconditional support during these years.

Contents

List of Figures

Chapter 1

Spin-driven Multiferroic Materials

Interest in magneto-electric multiferroics has flourished in recent years due to the discovery of new classes of materials in which the coupling between the ferroic order − magnetism and ferroelectricity − has been shown to be established by novel mechanisms. An important driver for this research on the applied side is the hope that it will provide new materials to be used in data storage and processing devices. Amongst the various classes of materials that are being investigated, arguably the most promising and intriguing is the one where the onset of non-collinear magnetic order leads to the formation of a ferroelectric state. Typically, cycloidal magnetic structures (in which the spins rotate in a plane containing the propagation vector of the structure) break the inversion symmetry of the system, thus allowing the appearance of an electric polarisation along a specific direction. In this scenario, a fundamentally important issue is to obtain an accurate and complete microscopic description of the magnetic order, and to understand how that magnetic order and the associated domains evolve as a function of applied electric and magnetic fields.

The renaissance of interest in multiferroics was sparked in 2004 when Kimura and co-workers [1] discovered that $TbMnO_3$, which up until that point had been thought of as a fairly conventional transition metal oxide, exhibits a large magneto-electric coupling of the magnetic and ferroelectric order parameters. In $TbMnO_3$ it was shown that the phase transition to a cycloidal Mn^{3+} spin arrangement at T = 27 K is concomitant with the onset of electric polarisation [1, 2]. Moreover, it was demonstrated that the electric (magnetic) polarisation can be controlled by application of a magnetic (electric) field. Many other materials were subsequently shown to exhibit similar phenomenology, including other $RMnO_3$, and RMn_2O_5 compounds (as reviewed in Nature Materials [3], Nature [4], and many others [5] - [9]). One particular material that has been the focus of recent studies is $Ni_3V_2O_8$. Its structure is characterized by a buckled kagomé staircase, resulting in two inequivalent Ni sites; below 6.3 K, the Ni^{2+} S=1 spins are reported to be arranged in a cycloid [10].

One of the key outstanding experimental challenges in this field is to develop methods that allow the imaging of the magneto-electric domains, and in particular to control and understand the population of magnetic domains (defined by the handedness of the cycloids) by means of an in situ electric field. In this thesis a new experimental method is introduced based on the use of the non-resonant magnetic diffraction of circularly polarised X-rays combined with full linear polarimetry of the scattered beam. It is shown how this technique is capable of providing unique information on

the magnetic state of complex magnetic materials. In particular, when applied to magneto-electric multiferroics such as $TbMnO_3$ and $Ni_3V_2O_8$ the technique provides high experimental sensitivity to the imbalance in the magnetic domain populations of cycloidal structures, since the handedness of the circular polarisation naturally couples to the sense of rotation of the magnetic moments. This sensitivity in turn allows an accurate description of the domain state and to the refinement of the magnetic ordering. The experiments were performed at the ID20 beamline in the European Synchrotron Radiation Facility. A quarter-wave phase plate operating at X-ray frequencies has been used to tune the polarisation of the synchrotron light into a left or right-handed circular state, while a set of polarisation analyser crystals has been employed in the detection of the magnetically diffracted X-rays. A new sample stick was developed that allowed the simultaneous application of electric fields and magnetic fields up to 10 T using a cryomagnet.

The results obtained with this technique provide important new information on the complex magnetic structure of multiferroic $TbMnO_3$, a challenging test case due to its two magnetic sublattices on the Mn and Tb sites. The method led to the identication of components of the ordering on the Tb sublattice and phase shifts that earlier neutron diffraction experiments could not resolve [2]. The effect of an applied magnetic field on $TbMnO_3$ has also been investigated, allowing the identification of the induced magnetostrictive atomic displacements, which, in turn, provide insight into the multiferroic mechanism leading to the spontaneous electric polarisation in zero field. In the case of $Ni_3V_2O_8$, polarisation analysis not only facilitated the refinement of the magnetic structure, but also has allowed real space images of the magnetic cycloidal domains to be obtained. Their evolution is followed as they are controlled via magneto-electric coupling by the applied electric field and cycled through a hysteresis loop, thus collecting valuable information on domain formation, inhomogeneities and domain wall movement.This work led to two papers published in Physical Review Letters [11] and Physical Review B [12]; a third paper authored by Walker and co-workers is to be published (cf. Chapter 6).

1.1 Magneto-electric multiferroics

1.1.1 Definitions

A generic *ferroic* material is a compound that develops a certain form of spontaneous order below a characteristic temperature, described by an appropriate crystal tensor such as, for example, an electric polarisation ($\mathbf{P}$), a magnetic polarisation ($\mathbf{M}$), or an elastic strain. Depending on the physical nature of this order parameter, the material is correspondingly classified as a ferroelectric, ferromagnetic or ferroelastic compound. The order parameter can assume equivalent but distiguishable values (domains), which can be favoured by applying an appropriate external field; for instance, in a ferroelectric material, it is possible to reverse the sign of the polarisation $\mathbf{P}$ upon application of an external electric field. Following these definitions, a compound is defined as a *multiferroic* when two or more of the primary ferroic properties are united in the same phase.

Among multiferroic compounds, the most interesting candidates for applications are those in which a coupling exists between the ferroic properties. From a practical viewpoint, this would be appealing to switch the magnetisation (or electric polarisation) of magnetic (ferroelectric) memories

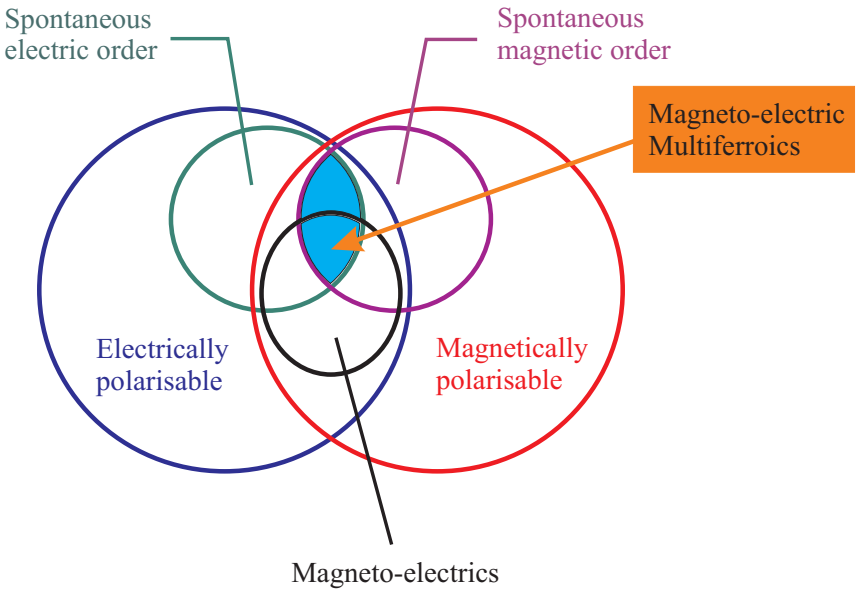

Figure 1.1: Classification of electric and magnetic properties of materials (see text). The intersection between ferroelectric materials (green set), ferro/antiferromagnetic materials (purple set) and magneto-electric materials (black set) is the class of compounds known as magneto-electric multiferroics.

under the application of an electrical (magnetic) field. In its most general definition, the magneto-electric effect denominates the coupling between electric and magnetic fields in solids. Given a certain material upon which external fields are applied, its free energy can be expanded in terms of the fields as

$$F(\mathbf{E},\mathbf{H}) = F_0 - P_i^S E_i - M_i^S H_i - \frac{1}{2}\epsilon_0\epsilon_{ij}E_iE_j$$
$$- \frac{1}{2}\mu_0\mu_{ij}H_iH_j - \alpha_{ij}E_iH_j - \frac{1}{2}\beta_{ijk}E_iH_jH_k - \frac{1}{2}\gamma_{ijk}H_iE_jE_k - ...$$

and its differentiation leads to the expressions for the electric polarisation

$$P_i(\mathbf{E},\mathbf{H}) = -\frac{\partial F}{\partial E_i} =$$
$$= P_i^S + \epsilon_0\epsilon_{ij}E_j + \alpha_{ij}H_j + \frac{1}{2}\beta_{ijk}H_jH_k + \gamma_{ijk}H_iE_j - ...$$

and the magnetisation

$$M_i(\mathbf{E},\mathbf{H}) = -\frac{\partial F}{\partial H_i} =$$
$$= M_i^S + \mu_0\mu_{ij}H_j + \alpha_{ij}E_i + \beta_{ijk}E_iH_j + \frac{1}{2}\gamma_{ijk}E_jE_k - ...$$

where the coefficients $\mathbf{P}^S$ and $\mathbf{M}^S$ denote the spontaneous polarisation and magnetisation, while tensors ϵ and μ are the electric and magnetic susceptibilities. The tensor α corresponds to the induction of electric polarisation by magnetic field or the induction of magnetisation by electric field, via linear magneto-electric effect. This is supplemented by higher-order magneto-eletric effects like those parametrised by the tensors β and γ.

The relation between multiferroic materials and the magneto-electric effect is summarised in the diagram depicted in Fig. 1.1. In the bigger set on the left are grouped together all materials that can be electrically polarised with the application of an external electric field; in the inset there

are the ones where the electric polarisation is spontaneous, namely, the electric ferroic materials. On the right, the same is done for magnetic materials (the magnetically polarisable ones and the ferro/antiferromagnetic ones); the intersection between the magnetic and the ferroelectric materials defines the class of multiferroics (highlighted in pale blue). The materials that show a magneto-electric effect are the ones in the black circle set. The intersection between magneto-electric and multiferroic materials is the kind of compound which this work is devoted to. It should be noted that a slightly broader definition has been employed in this case to include antiferromagnetic systems in the group; in such materials, the interaction between electric and magnetic properties is not defined by the simple linear magneto-electric effect, but shows more complex and exhotic behaviours, as will be detailed in the following of this chapter.

1.1.2 The search for magneto-electric multiferroics

The search for magneto-electric multiferroics has been reviewed recently in a series of papers: [3] - [9]. The attempts to combine in one system both magnetic and ferroelectric (FE) properties started in the 1960s, predominantly by two groups in the then Soviet Union: the group of Smolenskii [14], and Venevtsev [15]. Even though multiferroics presented an extremely interesting class of systems and problems, for some time this field of research progressed slowly, and was not well known. The issues encountered were essentially of two kinds. One is what are called the microscopic conditions, which determine the possibility to combine in one system both magnetic and ferroelectric properties. This turned out to be a quite nontrivial question, and usually in conventional systems these two phenomena tend to exclude one another. The second group of problems concerns, given the multiferroic system, what is the coupling between different degrees of freedom (How strong is it? What are its symmetry properties? etc.). These questions usually require detailed group symmetry analysis of a given particular system.

The conceptually simplest situation is met within materials that contain separate structural units which can give rise to strong dielectric response and eventually ferroelectricity, and which simultaneously contain, somewhere else, magnetic ions. Such are for example many borates, containing BO_3 groups, e.g. $GdFe_3(BO_3)_4$. These materials display interesting properties, especially optical ones [16], but one should not in general expect very strong coupling between magnetic and electric degrees of freedom here.

Transition metal perovskites (ABO_3) were considered among the most promising multiferroic materials. There are many magnetic materials with diverse properties among them; also most of the classical ferroelectrics, such as $BaTiO_3$ or $(PbZr)TiO_3$ (PZT), belong to this class. It is therefore not surprising that the first attempts to create multiferroic materials were mostly concentrated on this class of compounds. However, it soon became clear that the situation was far from simple. There exist hundreds of magnetic perovskites; a collection is presented in the tables compiled by Goodenough and Longo [17]. Another extensive volume in the same series lists hundreds of ferroelectric perovskites [18]. But the inspection of these tables showed that there was practically no overlap between these two lists of materials; magnetism and FE in perovskites seem to exclude one another. Apparently, the only exceptions in the stoichiometric (not mixed) perovskites were $BiFeO_3$ [19] and $BiMnO_3$ [20].

The reason for this mutual exclusion was investigated by empirical observation. In conventional

FE perovskites containing transition metal (TM) ions, such ions have the formal configuration d^0, i.e. they have an empty d-shell, and this seemed to be a necessary condition for FE in this class of materials: all known FE perovskites contained TM ions with empty d-shells (Ti^{4+}, Ta^{5+}, W^{6+}, etc.). Conversely, as soon as there is at least one or more d-electrons on the d-shell, such systems may be magnetic, but it was thought that they could never be FE. This question was extensively elaborated by Hill [21]. In conventional FE perovskites, the positively charged TM ions like to form molecules with the neighbouring negative oxygen ions; this collective shift of cations and anions inside a periodic crystal induces bulk electric polarisation. The mechanism of the covalent bonding in such molecules is the virtual hopping of electrons from the filled oxygen shell to the empty d-shell of the TM ion. Magnetism, on the contrary, requires TM ions with partially filled d-shells, as the spins of electrons occupying completely filled shells add to zero and do not participate in magnetic ordering. The exchange interaction between uncompensated spins of different ions gives rise to long-range magnetic ordering. The difference in filling of the d-shells required for ferroelectricity and magnetism appeared to make these two ordered states mutually exclusive.

Still, there were a few apparent exceptions in the perovskite family mentioned above: some compounds, such as $BiMnO_3$ or $BiFeO_3$, with magnetic Mn^{3+} and Fe^{3+} ions, are ferroelectric. It turned out that the main instability leading to FE in these systems is not due to TM ions, as e.g. in $BaTiO_3$, but is rather driven by the A-ions, in this case Bi [22]. Since the ferroelectric and magnetic orders in these materials are associated with different ions, the coupling between them is rather weak.

There exists yet another class of compounds, which are often cited as violating the d-emptiness rule: hexagonal manganites $RMnO_3$ (R = Y or small rare earths). Sometimes they are called hexagonal perovskites, although in fact it is a misnomer, as despite apparently similar formula ABO_3, these systems can have very different crystal and electronic structures. It was found that the FE in these materials has a completely different nature; however, as the mechanisms of magnetic and FE ordering are independent even in these systems, one should not expect a very strong coupling of magnetic and FE degrees of freedom, although certain coupling is definitely present and leads to quite interesting effects [23, 7].

1.1.3 Spin-driven multiferroics

An upsurge of interest in multiferroics started around 2001. This was connected with two main factors. First, the techniques, especially those of preparing and studying thin films of oxides, to which most of multiferroics belong, were developed enormously, also opening a possibility to use these systems, e.g., for ferroelectric memory [24]. Second, several new multiferroic systems were discovered with rather spectacular properties, in particular, very strong coupling between ferroelectric and magnetic degrees of freedom. They are characterised by the generation of ferroelectricity by magnetic ordering. In the proper ferroelectrics, structural instability towards the polar state, associated with the electronic pairing, is the main driving force of the transition. If, on the other hand, polarisation is only a part of a more complex lattice distortion or if it appears as an accidental by-product of some other ordering, as it is in this case, the ferroelectricity is called improper. This is what happens in the recently discovered multiferroic materials $RMnO_3$ (with perovskite structure; R = Tb, Gd) [1],

in RMn_2O_5 (R = different rare earths, such as Tb, Y etc.) [25], in $Ni_3V_2O_8$ [26], and in hexaferrite [27]. In all these systems, FE appears simultaneously to the magnetically ordered state of a specific phase: the phase with the cycloidal ordering in $TbMnO_3$ [2], and in similar phases in other such systems. As the FE in these systems appears only in certain magnetically ordered states, it turns out that the coupling between magnetic and electric subsystems in them is especially strong, and one can expect giant effects. Indeed spectacular effects were observed in these systems by application of magnetic field: change of the direction of polarisation in $TbMnO_3$ [1], switching from positive to negative polarisation in $TbMn_2O_5$ [25], etc.

As for the detailed mechanism of generation of FE by magnetic ordering in these systems, it seems that in most of them FE appears in magnetic phases with non-collinear magnetic structures. Let's consider $TbMnO_3$ as a canonical example. The crystal structure at room temperature is the orthorhombically distorted perovskite sketched in Fig. 5.5 in Chapter 5 (space group *Pbnm*): the crystal symmetry does have an inversion center, and the system is non-polar. At lower temperatures, the system shows successive magnetic phase transitions. Figure 1.2 shows temperature profiles of magnetisation $\mathbf{M}$ at a magnetic field of 0.5 T, specific heat divided by temperature, and electric polarisation along the $\mathbf{c}$ axis for a single crystal of $TbMnO_3$. According to neutron diffraction studies [28, 29], the Mn moments undergo an antiferromagnetic transition at $T_N \approx 41$ K; this ordering corresponds to the anomaly in magnetisation and specific heat. Below T_N the Mn moments are collinear and aligned along the $\mathbf{b}$ axis, and show sinusoidal order with a propagation wave vector $(0, \tau, 1)$ [28]. The second anomaly is observed in magnetisation and specific heat at $T_C \approx 28$ K; FE order with spontaneous polarisation along the $\mathbf{c}$ axis also develops at ≈ 28 K, as shown in Fig. 1.2. The proposed magnetic model below T_C is an elliptically modulated cycloidal structure [2], i.e. a non-collinear magnetic structure with components along the $\mathbf{b}$ and $\mathbf{c}$ axes (see Fig. 1.2 - (c); a more systematic classification for spin density wave structures will be given below). At the lowest temperature, the magnitude of electric polarisation is approximately 6-8 $\times 10^{-4}$ C m^{-2} (which is rather small as compared with that of conventional perovskite ferroelectrics, e.g., $\approx 2.6 \times 10^{-2}$ C m^{-2} at 296 K in $BaTiO_3$). In conclusion, when the magnetic structure is collinear the system is paraelectric, whereas in the FE phase the magnetic structure is an elliptically modulated cycloid. This simultaneous appearance of the cycloidal structure and the FE phase transition is important in understanding the origin of ferroelectricity in $TbMnO_3$ and in similar materials. Qualitatively it can be understood that the very notion of cycloidal order implies that the inversion symmetry is actually already broken: there may either be a left-moving or a right-moving cycloid. This in itself shows that the system is already close to becoming FE.

Mostovoy [30] obtained from a phenomenological approach a simple expression for electric polarisation induced by incommensurate spin density wave (SDW) states. These states are largely insensitive to the details of crystal structure and can be described by a continuum field theory of the Ginzburg-Landau type. The form of the coupling of the electric polarisation $\mathbf{P}$ to the magnetisation $\mathbf{M}$ can be found using general symmetry arguments [31, 32]. The invariance upon the time reversal ($t \to -t$) which transforms $\mathbf{P} \to \mathbf{P}$ and $\mathbf{M} \to -\mathbf{M}$, requires the lowest-order coupling to be quadratic in $\mathbf{M}$. The symmetry with respect to the spatial inversion ($\mathbf{x} \to -\mathbf{x}$), upon which $\mathbf{P} \to -\mathbf{P}$ and $\mathbf{M} \to \mathbf{M}$, is respected when the coupling of a uniform polarisation to an inhomogeneous magneti-

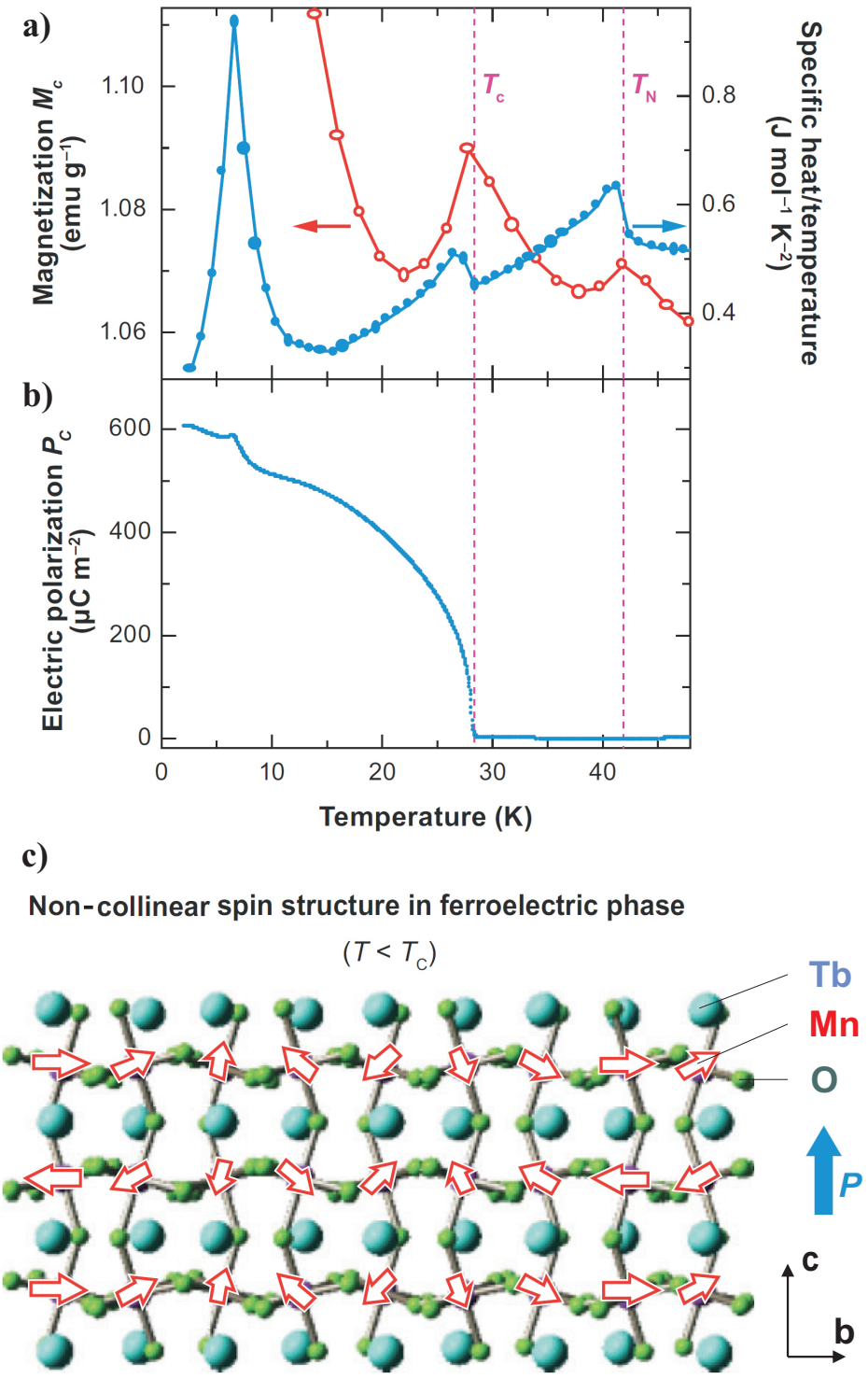

Figure 1.2: Temperature profiles of magnetic susceptibility (a), specific heat divided by temperature, and electric polarisation (b) along the c axis in $TbMnO_3$, from Kimura [6]. Below T_C, the system enters the FE phase; the schematic drawing (c) of the proposed magnetic structure shows a cycloidal ordering in the $(\mathbf{b}, \mathbf{c})$ plane, propagating along the $\mathbf{b}$ axis.

sation is linear in $\mathbf{P}$ and contains one gradient of $\mathbf{M}$. This is where frustration comes into play: its role is to induce spatial variations of magnetisation. Complex and periodically modulated magnetic structures in insulators result from competing exchange interactions [33] and are often found in so-called geometrically frustrated materials, such as the ferroelectric kagomé magnet $Ni_3V_2O_8$ [26].

This mechanism outlined by Mostovoy does not require a special kind of crystal lattice. In the simplest case of cubic symmetry the coupling term has the form

$$\Phi_{em}(\mathbf{P},\mathbf{M}) = \gamma\mathbf{P}\cdot[\mathbf{M}(\nabla\cdot\mathbf{M}) - (\mathbf{M}\cdot\nabla)\mathbf{M} + ...] \tag{1.1}$$

and the omitted terms do not contribute to the uniform polarisation. Assuming that in the absence of magnetism the system shows no instability towards ferroelectricity, the electric part of the thermodinamic potential is completed by the term $\Phi_e = P^2/2\chi_e$, where χ_e is the dielectric susceptibility in absence of magnetism, and the equilibrium found from the variation of $\Phi_e + \Phi_{em}$ with respect to $\mathbf{P}$ gives:

$$\mathbf{P} = \gamma\chi_e[(\mathbf{M}\cdot\nabla)\mathbf{M} - \mathbf{M}(\nabla\cdot\mathbf{M})]. \tag{1.2}$$

Consider now a SDW state characterised by the wave vector $\mathbf{q}$ and the magnetsation function

$$\mathbf{M}(\mathbf{x}) = M_1\hat{\mathbf{e}}_1\cos(\mathbf{q}\cdot\mathbf{x}) + M_2\hat{\mathbf{e}}_2\sin(\mathbf{q}\cdot\mathbf{x}) + M_3\hat{\mathbf{e}}_3 \tag{1.3}$$

where $\mathbf{x}$ is a generic position in space, and the unit vectors $\hat{\mathbf{e}}_i$, i=1,2,3 form an orthogonal basis. If only M_1 or M_2 is different from zero, the expression describes a sinusoidal wave (Fig. 1.3), while for $M_1, M_2 \neq 0$ it describes a spiral ($\mathbf{q} \parallel \hat{\mathbf{e}}_3$) or cycloid ($\mathbf{q} \perp \hat{\mathbf{e}}_3$), and the spin rotation axis is $\hat{\mathbf{e}}_3$ (if also $M_3 \neq 0$, the spiral is conical). Using Eq. 1.2, it is found that the average polarisation is transverse both to $\hat{\mathbf{e}}_3$ and $\mathbf{q}$, and is independent of M_3:

$$\bar{\mathbf{P}} = \frac{1}{V}\int d^3x\mathbf{P} = \gamma\chi_e M_1 M_2[\hat{\mathbf{e}}_3\times\mathbf{q}]. \tag{1.4}$$

This equation also holds for orthorombic crystals, provided that $\hat{\mathbf{e}}_3$ and $\mathbf{q}$ are parallel to crystal axes. No average polarisation is induced by a sinusoidal SDW, as the inversion symmetry at the sites where the magnetisation reaches maximum or minimum remains unbroken. Following this model, a spiral magnetic structure alone is also not sufficient: FE can appear only if the spin rotation axis $\hat{\mathbf{e}}_3$ does not coincide with the wave vector $\mathbf{q}$, and the polarisation $\mathbf{P}$ is proportional to their vector product. The sign of the polarisation depends on the handedness of the cycloid, as shown in Fig. 1.4. The propagation vector defined by Eq. 1.3 changes its direction depending on the sense of rotation of the magnetic moments in the ($\hat{\mathbf{e}}_1$,$\hat{\mathbf{e}}_2$) plane; therefore, the resulting vector product $\hat{\mathbf{e}}_3\times\mathbf{q}$ and $\mathbf{P}$ change their sign as well. This effect can be better emphasized by using the alternative formulation for the electric polarisation derived from Eq. 1.4

$$\mathbf{P} \propto \hat{\mathbf{e}}_{ij}\times(\mathbf{M}_i\times\mathbf{M}_j) \tag{1.5}$$

where $\hat{\mathbf{e}}_{ij}$ is the unit vector connecting the atomic site i to the site j, and $\mathbf{M}_i$ and $\mathbf{M}_j$ are the magnetic moments localised on the two sites (see Fig. 1.4). The two magnetic domains allowed by a cycloidal stucture are thus related to the two opposite directions of the electric polarisation $\mathbf{P}$.

Turning back to the specific case of $TbMnO_3$, this explains why the transition at T $\approx$ 40 K to the sinusoidal SDW state [1, 2] does not give rise to ferroelectricity, and polarisation is only induced below the transition at T $\approx$ 30 K, at which the sinusoidal SDW is replaced by a cycloid with the propagation vector $\mathbf{q} \parallel \mathbf{b}$ and the spin rotation axis $\hat{\mathbf{e}}_3 \parallel \mathbf{a}$, thus corresponding to the situation $\mathbf{q} \perp \hat{\mathbf{e}}_3$. Since the Mn spins rotate in the $(\mathbf{b},\mathbf{c})$ plane, Eq. 1.4 gives $\mathbf{P} \parallel \mathbf{c}$, in agreement with experiment. Similarly, the polarisation is absent in the high-temperature incommensurate phase of

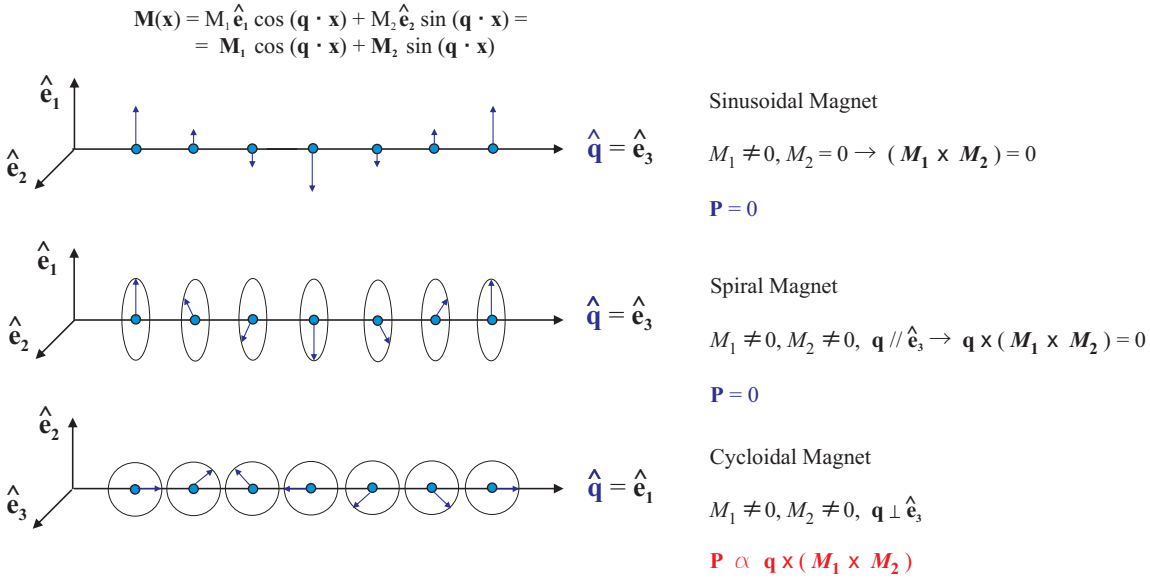

Figure 1.3: Overview of the possible magnetic orderings defined by Eq. 1.3. No transverse component M_3 has been supposed for the sake of simplicity; the corresponding magnetisation function is reported on the top of the figure. A collinear, sinusoidal spin density wave and a spiral wave do not meet the condition for ferroelectricity expressed by Eq. 1.4 and 1.5. In the spiral wave, the propagation vector of the magnetic modulation $\mathbf{q}$ and the axis of the rotation $\hat{\mathbf{e}}_3$ are parallel. Conversely, in a cycloidal density wave, the two are perpendicular and an electric polarisation is expected to emerge.

$Ni_3V_2O_8$, which is the sinusoidal SDW state [26]. The cycloid with $\mathbf{q} \parallel \mathbf{a}$ and the rotation axis $\hat{\mathbf{e}}_3 \parallel \mathbf{c}$, observed in the low-temperature incommensurate phase, induces $\mathbf{P}$ along the $\mathbf{b}$ axis. By inspecting the phase diagram of ferroelectric SDW magnets, using the values of the induced polarisation and magnetic transition temperatures (5-40 K) for these materials, it is found that the energy gain due to the induced polarisation is small compared to the magnetic energy gain. Therefore, the temperature and magnetic field dependence of the polarisation merely reflect the changes in magnetic ordering.

This phenomenological approach, based on symmetry considerations, is complementary to the recent discussions of microscopic mechanisms of FE in magnets. A plausible microscopic mechanism inducing FE in magnetic non-collinear systems was discussed in references [34] and [35], involving the antisymmetric Dzyaloshinskii-Moriya (DM) interaction. The so-called "direct" DM interaction is an anisotropic superexchange coupling between two spins $\mathbf{S}_i$ and $\mathbf{S}_j$ located on a lattice bond ij with no inversion centre (see Fig. 1.5, top part). The exchange between spins of transition metal ions is usually mediated by ligands, for example oxygen ions: the lack of an inversion centre between $\mathbf{S}_i$ and $\mathbf{S}_j$ may be due to a small shift of the oxygen atom from the centrosymmetric position. The DM interaction is described by the term $H_{DM} = \mathbf{D}_{ij} \cdot \mathbf{S}_i \times \mathbf{S}_j$, where $\mathbf{D}_{ij}$ is the Dzyaloshinskii vector discussed below [32, 36], and typically favours non-collinear spin ordering by inducing a small canting of the magnetic moments that would otherwise be parallel or antiparallel. This interaction arises from a relativistic correction to the usual superexchange and its strength is proportional to the spin-orbit coupling constant λ. The Dzyaloshinskii vector $\mathbf{D}_{ij}$ is proportional to $\mathbf{x} \times \hat{\mathbf{e}}_{ij}$, where $\hat{\mathbf{e}}_{ij}$ is the unit vector along the line connecting the magnetic ions i and j, and $\mathbf{x}$ is the shift of the oxygen ion from this line (see Fig. 1.5). Thus, the energy of the DM interaction increases with $\mathbf{x}$, describing

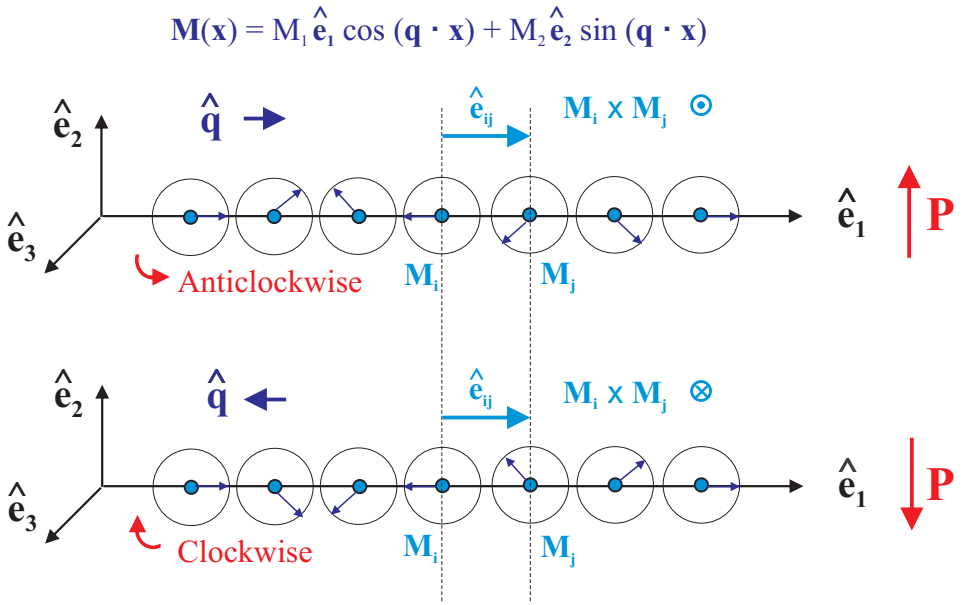

Figure 1.4: In a cycloidal magnetic density wave, the handedness of the rotation of the magnetic moments (clockwise or anticlockwise) determines the sign of the electric polarisation $\mathbf{P}$. Following Eq. 1.4 and the definition of the magnetisation function in Eq. 1.3, it can be seen that the vector product $\hat{\mathbf{e}}_3 \times \mathbf{q}$ reverses its sign as the handedness is reversed. Alternatively, from Eq. 1.5, the expression $\hat{\mathbf{e}}_{ij} \times (\mathbf{M}_i \times \mathbf{M}_j)$ can be evaluated to deduce the effect of the change of handedness on the sign of $\mathbf{P}$.

the degree of inversion symmetry breaking at the oxygen site. Conversely, the ferroelectricity induced by cycloidal magnetic ordering is the "inverse" effect, that is, lattice relaxation and breaking of the inversion symmetry in a magnetically ordered non-collinear state, such as a cycloidal one. Because in the cycloidal state the vector product $\mathbf{S}_i \times \mathbf{S}_j$ has the same sign for all pairs of neighbouring spins, the DM interaction pushes negative oxygen ions in one direction perpendicular to the spin chain formed by positive magnetic ions, thus inducing electric polarisation perpendicular to the chain [35] (see Fig. 1.5). The microscopic mechanism can also be explained in terms of the spin current, $\mathbf{j}_{ij} \propto \mathbf{S}_i \times \mathbf{S}_j$, describing the precession of the spin $\mathbf{S}_i$ in the exchange field created by the spin $\mathbf{S}_j$. The induced electric dipole is then given by $\mathbf{P}_{ij} \propto \hat{\mathbf{e}}_{ij}\mathbf{j}_{ij}$ [34].

Although the model described by Eq. 1.4 works for many multiferroics (and in particular $TbMnO_3$ and $Ni_3V_2O_8$ discussed in this work, as detailed in Fig. 1.6), the general expression for magnetically induced polarisation is more complicated. In particular, when the spin rotation axis $\hat{\mathbf{e}}_3$ is not oriented along a crystal axis, the orientation of $\mathbf{P}$ depends on the strengths of the magneto-electric couplings along different crystallographic directions (such a situation occurs in $MnWO_4$ [37, 38]). Furthermore, when the crystal unit cell contains more than one magnetic ion, the SDW state cannot be described by a single magnetisation vector, as was assumed in Eq. 1.1. With additional magnetic vectors, one can construct other third-order terms that can induce electric polarisation. Correspondingly, from the microscopic point of view, it should be noted that the inverse DM interaction is not the unique mechanism to induce FE polarisation [39]. For a general symmetry analysis of the conditions for the development of a macroscopic electrical polarisation as a secondary order parameter to a magnetic ordering transition, see ref. [40].

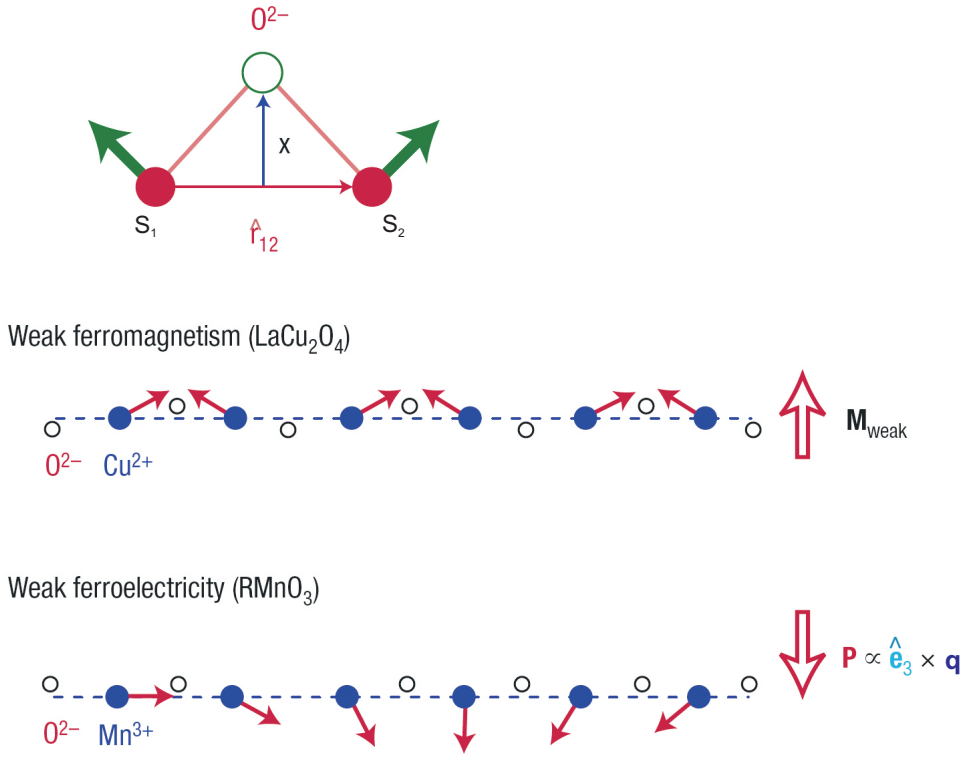

Figure 1.5: Effect of DM interaction $H_{DM} = \mathbf{D}_{ij} \cdot (\mathbf{S}_i \times \mathbf{S}_j)$, adapted from [3]. The Dzyaloshinskii vector $\mathbf{D}_{12}$ is proportional to spin-orbit coupling constant λ, and depends on the position of the oxygen ion (open circle) between two magnetic transition metal ions (filled circles): $\mathbf{D}_{12} \propto \lambda \mathbf{x} \times \hat{\mathbf{e}}_{12}$. A weak ferromagnetic component in antiferromagnets (for example, $LaCu_2O_4$ layers) results from the alternating Dzyaloshinskii vector between adjacent pairs of transition metal atoms. The inverse effect consists in inducing a (weak) ferroelectricity in a magnetic spiral state, as negative oxygen ions are pushed in one direction transverse to the spin chain formed by positive transition metal ions.

In summary, magnetic frustration naturally gives rise to multiferroic behaviour. Competing magnetic interactions in frustrated magnets often result in magnetic structures that lack the inversion symmetry of a high-temperature crystal lattice. The ionic relaxation in such magnetic states, driven by lowering of the magnetic energy of the Heisenberg and Dzyaloshinskii-Moriya exchange interactions, induces polar lattice distortions. These magnetic ferroelectrics can produce unprecedented cross-coupling effects, such as the high tuneability of the magnetically induced electric polarisation and dielectric constant by applied magnetic fields, which has given a new impulse to the search for other multiferroic materials and raised hopes for their practical applications.

This thesis is organised as follows. In Chapter 2, the theoretical description of X-ray magnetic scattering is given. In particular, the general non-resonant magnetic scattering cross-section is detailed for the case of incommensurate non-collinear magnetic structures, thus highlighting the role of circularly polarised incident light in discriminating the handedness of the magnetic cycloidal domains. In Chapter 3, the experimental technique is reviewed in its technical details. Beside the classical features characteristic of non-resonant magnetic X-ray scattering measurements from synchrotron light, the approach used in the present work involves the control of the incident polarisation, the linear polarimetry on the diffracted beam, and the application of in situ electric and magnetic fields.

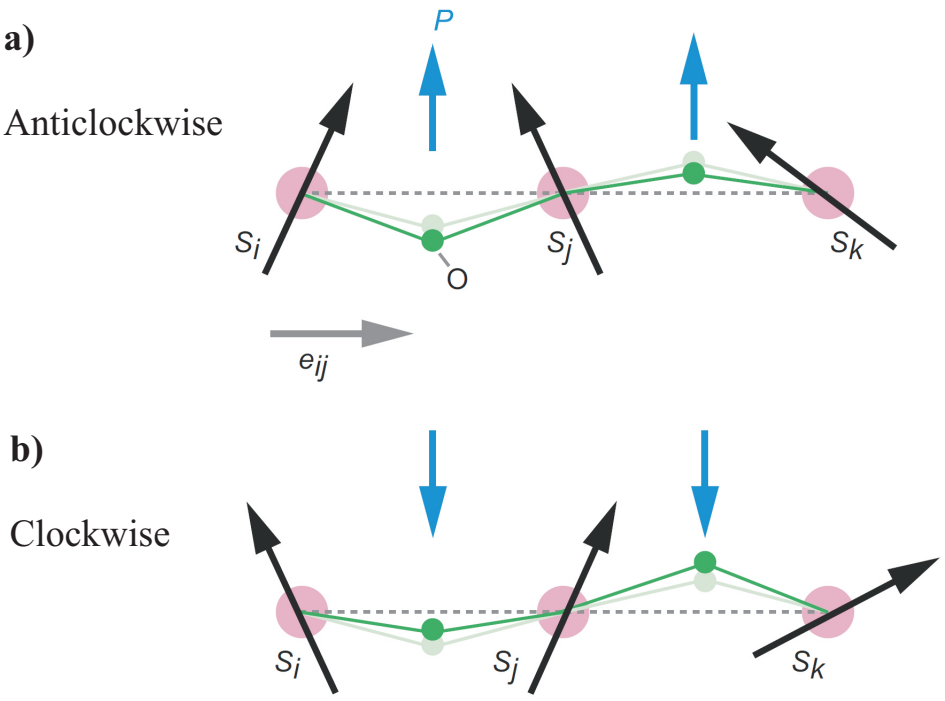

Figure 1.6: Schematic drawings from [6] of the change of local electric polarisation in $TbMnO_3$ induced by spin canting in (a) anticlockwise and (b) clockwise cycloid. The difference between dark green and light green dots represents the shift of oxygen ions due to the spin canting between the neighboring two magnetic moments. The blue arrows denote the resultant change of the local electric polarisation **P**.

In Chapter 4, the results obtained on $Ni_3V_2O_8$ are presented. New information on the magnetic structure was obtained, integrating and correcting the picture emerging from previously published neutron data [10]. It is furthermore demonstrated that the technique enables the imaging of multiferroic domains through polarisation enhanced topography, an approach used to image the domains as the sample is cycled by an electric field through a hysteresis loop, revealing the gradual switching of domains in accord with direct polarisation measurements previously reported [13]. The data and analysis reported in this Chapter have been published in Physical Review B [12]. In Chapter 5, the results obtained on $TbMnO_3$ in zero magnetic field are presented. The data allowed the discovery of components of the ordering on the Tb sublattice and phase shifts that earlier neutron diffraction experiments could not resolve. This work has been published in Physical Review Letters [11] and represents the first study of circularly polarised X-ray magnetic scattering combined with the application of in situ electric field to determine the absolute sense of rotation of non-collinear moments. In Chapter 6, the results obtained on $TbMnO_3$ in applied magnetic field are presented. The investigation has revealed the possibility of finding magnetic and Thomson displacive amplitudes interfering at the same reflections. The data analysis is still ongoing, however the preliminary results suggest that magnetostrictive displacements can be held responsible for the insurgence of the Thomson contribution, thus offering valuable insight into the different atomic modes involved and their order of magnitude. This work is being prepared for publication.

Chapter 2

X-ray Magnetic Scattering

Although traditional diffraction techniques exploit neutrons to study magnetism in condensed matter, X-ray scattering has been proved to constitute a notable and complementary experimental method. In the interaction with matter the X-rays are mostly scattered by the charge distribution, however, a weaker contribution to the scattering process is given by the magnetic properties of the sample, leading to the inclusion of additional terms in the cross-section. The possibility of exploiting this interaction between field and matter to study magnetic densities was first suggested by the theoretical work of Platzman and Tzoar [41] in 1970, and experimentally performed by de Bergevin and Brunel [42, 43]. A full treatment of X-ray magnetic scattering is reported by Blume in [44]. The intensity arising from purely magnetic diffraction (the so called non-resonant contribution) is estimated to be 10^6-10^9 smaller than the intensity of classical Thomson charge scattering, since it arises from small relativistic effects. Nonetheless, the exploitation of third generation synchrotron radiation sources, provided with beamlines specifically designed to perform magnetic scattering experiments, now allows us to undertake this kind of measurement by means of a high flux beam, tunable energy and an excellent degree of polarisation.

The first part of this chapter (2.1) is devoted to review the basic concepts of the experimental technique: 1) the derivation of the non-resonant X-ray magnetic scattering amplitude (NRXMS) from the physics of the interaction between electromagnetic radiation and matter, and the discussion of its properties (2.1.1 to 2.1.3); 2) the construction of the global diffraction intensity in the case of an ordered magnetic density, be its period commensurate or incommensurate with respect to the crystallographic lattice (2.1.4); 3) the basic setup of a standard magnetic diffraction experiment (2.1.5).

The second part of this chapter (2.2) focuses on the peculiar aspects of the magnetic diffraction experiments undertaken in the present work, i.e. the exploitation of the dependence of the scattering length found in (2.1.3) on the polarisation of the incident and the diffracted beam. A full account of this polarisation dependence was given by Blume and Gibbs in [45], and by Hill and McMorrow in [46]. This section presents a comparison between classical experimental methods based on azimuthal scans (2.2.1) and the polarisation-based method known as Stokes scan (2.2.2); it then provides some formal beackground to deal with the characterisation of polarised light in terms of the Jones and the Stokes representations (2.2.3).

The third and final part of this chapter (2.3) contains some observations on the application of this technique to the specific case of cycloidally ordered magnetic densities, thus providing a general frame for the subsequent chapters dealing with measurements on $Ni_3V_2O_8$ and $TbMnO_3$. The derivation of the magnetic diffraction intensity for such a class of magnetic materials is shown, as well as the use of circularly polarised incident radiation in order to discriminate between magnetic cycloidal domains.

2.1 X-ray Magnetic Scattering

The aim of this section is to introduce the general theoretical framework describing the interaction between elecromagnetic radiation and a system of charges (electrons), following Blume's development reported in [44]. The scattering cross-section will be derived with particular attention to its magnetic contribution. The calculations are derived by a perturbative model, and take into account the effects of electron binding. In subsection 2.1.4, this discussion will be focused to the case of diffraction from an ordered distribution of magnetic density.

2.1.1 The interaction Hamiltonian

A radiation field can be characterised by its vector potential $\mathbf{A}(\mathbf{r})$, expanded as a linear combination of the photon creation (c) and annihilation (c^+) operators:

$$\mathbf{A}(\mathbf{r}) = \sum_{\mathbf{q},\ \rho} \left(\frac{2\pi\hbar c^2}{V\omega_q} \right)^{1/2} \ [\ \epsilon_\rho(\mathbf{q}) c_\rho(\mathbf{q}) e^{i\mathbf{q}\cdot\mathbf{r}} + \epsilon^\star_\rho(\mathbf{q}) c^+_\rho(\mathbf{q}) e^{-i\mathbf{q}\cdot\mathbf{r}}\ ] \tag{2.1}$$

where V is a quantization volume, the index $\rho = 1, 2$ labels two independent polarisation states for each wavevector $\mathbf{q}$, and $\epsilon_\rho(\mathbf{q})$ are the corresponding unit polarisation vectors. Let's assume that the unperturbed radiation is monochromatic, so to consider only one wave vector $\mathbf{q} = \mathbf{k}$, in its two possible states of polarisation. The system of charges, in quite a general view, is constituted of several particles interacting with each other via a scalar potential $V(r_{ij}) = V(|\mathbf{r}_i - \mathbf{r}_j|)$. Let's now consider the possibility of interaction between field and charges. The total system can be described by the Hamiltonian:

$$\begin{aligned} H \ = \ & \sum_j \frac{1}{2m} (\mathbf{p}_j - \frac{e}{c}\mathbf{A}(\mathbf{r}_j))^2 \ + \ \sum_{ij} V(\mathbf{r}_{ij}) \ - \ \frac{e\hbar}{2mc} \sum_j \mathbf{s}_j \cdot (\nabla \times \mathbf{A}(\mathbf{r}_j)) \\ & - \frac{e\hbar}{2(mc)^2} \sum_j \mathbf{s}_j \cdot [\mathbf{E}(\mathbf{r}_j) \times (\mathbf{p}_j - \frac{e}{c}\mathbf{A}(\mathbf{r}_j))] \ + \ \sum_{\rho=1,2} \hbar\omega_k (c^+_\rho(\mathbf{k}) c_\rho(\mathbf{k}) + \frac{1}{2}) \end{aligned} \tag{2.2}$$

where $\mathbf{E}(\mathbf{r})$ and $\mathbf{B}(\mathbf{r})$ are the electric and magnetic fields, $\mathbf{s}_j$ and $\mathbf{p}_j$ are the spin and momentum operators of the jth electron located at $\mathbf{r}_j$. The five terms describe respectively: the kinetic energy of electrons in an electromagnetic field; the Coulomb potential energy of the electrons; the Zeeman energy (interaction between the electron spin and a magnetic field); the spin-orbit interaction; the energy of the electromagnetic field.

In order to separate the contributions related to the unperturbed radiation and the unperturbed system of charges from the interaction terms, it is convenient to rewrite the spin-orbit term, by distinguishing between the electric radiation field and the electric field created by the charges. The

latter can be expressed via a scalar Coulomb potential ϕ_j. The Hamiltonian can now be written:

$$H = H_{rad} + H_{mat} + H' \tag{2.3}$$

with

$$H_{rad} \;=\; \sum_{\rho=1,2} \hbar\omega_k (c_\rho^+(\mathbf{k}) c_\rho(\mathbf{k}) + \frac{1}{2});$$

$$H_{mat} \;=\; \sum_j \frac{1}{2m} \mathbf{p}_j{}^2 \;+\; \sum_{ij} \mathbf{V}(r_{ij}) \;+\; \frac{e\hbar}{2(mc)^2} \sum_j \mathbf{s}_j \cdot (\nabla\phi_j \times \mathbf{p}_j);$$

$$H' \;=\; \frac{e^2}{2mc^2} \sum_j \mathbf{A}^2(\mathbf{r}_j) \;-\; \frac{e}{mc} \sum_j \mathbf{A}(\mathbf{r}_j) \cdot \mathbf{p}_j \;-\; \frac{e\hbar}{mc} \sum_j \mathbf{s}_j \cdot (\nabla \times \mathbf{A}(\mathbf{r}_j))$$

$$- \frac{e\hbar}{2(mc)^2} \frac{e^2}{c^2} \sum_j \mathbf{s}_j \cdot (\dot{\mathbf{A}}(\mathbf{r}_j) \times \mathbf{A}(\mathbf{r}_j)) \;=\; H'_1 + H'_2 + H'_3 + H'_4.$$

2.1.2 The differential scattering cross-section

For all cases in which the interaction potential is small, if compared with the unperturbed energies of the isolated systems (radiation and charges), the time-dependent perturbation theory can be applied to the Schroedinger's equation. The transition probability/unit time induced by H' in the unperturbed system is given by Fermi's golden rule (to the second order):

$$W \;=\; \frac{2\pi}{\hbar} \left| < f|H'|i > + \sum_n \frac{< f|H'|n >< n|H'|i >}{E_i - E_n} \right|^2 \delta(E_i - E_f)$$

where initial state $|i>$ and final state $|f>$ are eigenstates including the two non-interacting systems. Let's assume that the solid initially lies in a given quantum state $|a>$, which is an eigenstate of H_{mat} with energy E_a, while the incoming photon is characterized by wave vector $\mathbf{k}$ and polarisation ρ. After the interaction, the expression above considers the probability of a transition to a final state $|b>$ of the solid, with outcoming photon $\mathbf{k}'$, ρ':

$$|i>= |a\ ;\ \mathbf{k}\ \rho>, \quad |f>= |b\ ;\ \mathbf{k}'\ \rho'>;$$

$$E_i = E_a + \hbar\omega_k, \quad E_f = E_b + \hbar\omega_{k'}.$$

If only scattering phenomena are considered, only those terms of the Hamiltonian which include both annihilation and creation of a photon will be retained. The vector potential $\mathbf{A}$ is linear in operators c and c^+, so that this kind of event occurs for even powers of $\mathbf{A}$. By considering only quadratic terms, elastic scattering occurs in first perturbation order for terms quadratic in $\mathbf{A}$ (H'_1 and H'_4), and in second perturbation order for linear terms (H'_2 and H'_3):

$$W \;=\; \frac{2\pi}{\hbar} \left| < b\ ;\ \mathbf{k}'\ \rho'|\ H'_1 + H'_4\ |a\ ;\ \mathbf{k}\ \rho> \right.$$

$$\left. + \sum_n \frac{< b\ ;\ \mathbf{k}'\ \rho'|\ H'_2 + H'_3\ |n >< n|\ H'_2 + H'_3\ |a\ ;\ \mathbf{k}\ \rho>}{E_a + \hbar\omega_k - E_n} \right|^2. \tag{2.4}$$

The cross-section is obtained from the transition probability by multiplying W by the density of final states and dividing by the incident flux:

$$\frac{d^2\sigma}{d\Omega\ dE} \;=\; W\rho(E_f)/I_0,$$

$$\rho(E_f) \;=\; \frac{V}{(2\pi)^3}\frac{\omega^2}{\hbar c^3}, \qquad I_0 \;=\; c/V$$

where V is a quantisation volume that drops out of any physical expression.

Finally, let's substitute the explicit form in the H' terms, and let the operators act on the radiation states, to obtain the differential scattering cross-section. Assuming $\omega_k \approx \omega_{k'}$, this gives:

$$\frac{d^2\sigma}{d\Omega\; dE} \;=\; \left(\frac{e^2}{mc^2}\right)^2 \;\left|\left\langle b\left|\sum_j e^{i\mathbf{K}\cdot\mathbf{r_j}}\right|a\right\rangle\; \epsilon\cdot\epsilon'\right.$$

$$-\; i\frac{\hbar\omega}{mc^2}\left\langle b\left|\sum_j e^{i\mathbf{K}\cdot\mathbf{r_j}}\;\mathbf{s}_j\right|a\right\rangle\; \epsilon\times\epsilon'$$

$$+\;\frac{1}{m}\sum_c\;\left(\frac{\langle b\,|\;O^+(\mathbf{k}')\;|\,c\rangle\;\;\langle c\,|\;O(\mathbf{k})\;|\,a\rangle}{E_a-E_c+\hbar\omega_k-i\Gamma_c/2}\;\;+\right.$$

$$\left.+\;\;\frac{\langle b\,|\;O(\mathbf{k})\;|\,c\rangle\;\;\langle c\,|\;O^+(\mathbf{k}')\;|\,a\rangle}{E_a-E_c-\hbar\omega_k}\;\right)\Bigg|^2\;\delta(E_a-E_b+\hbar\omega_k-\hbar\omega_{k'}) \tag{2.5}$$

where, for simplicity, a shorthand notation for the polarisation unit vectors has been introduced:

$$\epsilon \;=\; \hat{\epsilon}_\rho\;(\mathbf{k}), \qquad \epsilon' \;=\; \hat{\epsilon}^*_{\rho'}\;(\mathbf{k}').$$

To get a more compact expression, the scattering vector $\mathbf{K}$ has been defined as

$$\mathbf{K} \;=\; \mathbf{k}-\mathbf{k}' \tag{2.6}$$

and the operator $O(\mathbf{k})$ as

$$O(\mathbf{k}) \;=\; \sum_j\; e^{i\mathbf{k}\cdot\mathbf{r}_j}\;\;[\;\epsilon\cdot\mathbf{p}_j - i\hbar(\mathbf{k}\times\epsilon)\cdot\mathbf{s}_j\;], \tag{2.7}$$

so that, in Eq. 2.5, the operator O^+ has the following explicit form:

$$O^+(\mathbf{k}') \;=\; \sum_j\; e^{-i\mathbf{k}'\cdot\mathbf{r}_j}\;\;[\;\epsilon'\cdot\mathbf{p}_j + i\hbar(\mathbf{k}'\times\epsilon')\cdot\mathbf{s}_j\;].$$

By considering the second-order perturbation term, one can appreciate the dependence of the scattering event not only on the initial and final state of the system, but also on other excited states ($|c>$ states). Also, including the second-order perturbation term leads to the appearance of the energy $\hbar\omega_k$ in the denominators of the last two terms, in Eq. 2.5. In particular, for any addend in the summation over c, the first denominator can become very small, when $\hbar\omega_k \sim E_c - E_a$. The $i\Gamma_c/2$ correction has been introduced to take into account the level width when the energy approaches to this critical value. By algebric manipulation of Eq. 2.5, and by applying the closure relation on the $|c>$ states, the final expression is found:

$$\frac{d^2\sigma}{d\Omega\; dE} \;=\; \left(\frac{e^2}{mc^2}\right)^2 \;\left|\left\langle b\left|\sum_j e^{i\mathbf{K}\cdot\mathbf{r_j}}\right|a\right\rangle\; \epsilon\cdot\epsilon'\right.$$

$$-\; i\frac{\hbar\omega}{mc^2}\left\langle b\left|\sum_j e^{i\mathbf{K}\cdot\mathbf{r_j}}\;\left[\;\frac{i\mathbf{K}\times\mathbf{p}_j}{\hbar k^2}\cdot\mathbf{A}\;+\;\mathbf{s}_j\cdot\mathbf{B}\;\right]\right|a\right\rangle$$

$$+\;\frac{1}{m}\sum_c\;\frac{E_a-E_c}{\hbar\omega_k}\;\left(-\;\frac{\langle b\,|\;O^+(\mathbf{k}')\;|\,c\rangle\;\;\langle c\,|\;O(\mathbf{k})\;|\,a\rangle}{E_a-E_c+\hbar\omega_k-i\Gamma_c/2}\right.$$

$$+ \quad \frac{\langle b \mid O(\mathbf{k}) \mid c\rangle \ \langle c \mid O^{+}(\mathbf{k}') \mid a\rangle}{E_a - E_c - \hbar\omega_k}\Bigg) \Bigg|^{2} \tag{2.8}$$

where

$$\mathbf{A} = \epsilon' \times \epsilon \tag{2.9}$$

$$\mathbf{B} = \epsilon' \times \epsilon + (\hat{\mathbf{k}}' \times \epsilon')(\hat{\mathbf{k}}' \cdot \epsilon) - (\hat{\mathbf{k}} \times \epsilon)(\hat{\mathbf{k}} \cdot \epsilon') - (\hat{\mathbf{k}}' \times \epsilon') \times (\hat{\mathbf{k}} \times \epsilon). \tag{2.10}$$

In the case of elastic scattering ($|a>=|b>$) the contributions become:

1) The usual Thomson contribution depending on the Fourier transform of the electron density

$$f_0 \ = \ \left\langle a \left| \sum_j e^{i\mathbf{K}\cdot\mathbf{r_j}} \right| a \right\rangle \ \epsilon \cdot \epsilon' \tag{2.11}$$

2) The non-resonant contribution, which will be described in detail in the next subsection

$$f_{nr} \ = \ - \, i \frac{\hbar\omega}{mc^2} \left\langle a \left| \sum_j e^{i\mathbf{K}\cdot\mathbf{r_j}} \ \left[\ \frac{i\mathbf{K} \times \mathbf{p}_j}{\hbar k^2} \cdot \mathbf{A} \ + \ \mathbf{s}_j \cdot \mathbf{B} \ \right] \right| a \right\rangle$$

3) The anomalous or resonant contribution

$$f_{an} \ = \ f'_{an} \ + \ i f''_{an} \ =$$

$$\frac{1}{m} \sum_c \ \frac{E_a - E_c}{\hbar\omega_k} \ \left(- \ \frac{\langle a \mid O^{+}(\mathbf{k}') \mid c\rangle \ \langle c \mid O(\mathbf{k}) \mid a\rangle}{E_a - E_c + \hbar\omega_k - i\Gamma_c/2} \ + \ \frac{\langle a \mid O(\mathbf{k}) \mid c\rangle \ \langle c \mid O^{+}(\mathbf{k}') \mid a\rangle}{E_a - E_c - \hbar\omega_k} \right).$$

Namely, it can be written:

$$\frac{d^2\sigma}{d\Omega \ dE} \ = \ \left(\frac{e^2}{mc^2} \right)^2 \ \mid f_0 \ + \ f_{nr} \ + \ f_{an} \mid^2 .$$

2.1.3 Non-resonant magnetic scattering

When dealing with ordered structures (crystals), the scattered signal is diffracted in discrete directions of space (Bragg's law). If the symmetry of the magnetic structure is different from the crystallographic one, the magnetic and Thomson contributions are separated in different reflections. A further discrimination between non resonant and resonant contribution can be obtained by tuning the radiation energy away from any atomic edge of the system, thus making it possible to neglect the resonant term. Although the non-resonant contribution is much weaker than the Thomson one, it provides a direct coupling with the magnetic structure, and is not mixed with additional terms as it may be the case for the resonant contribution. Moreover, the spin and orbital part are separated (in contrast, for example, with neutron diffraction). Since the magnetic diffraction experiments performed on $TbMnO_3$ and $Ni_3V_2O_8$ have been carried out in the non resonant regime, the cross-section evaluated above for this term will now be examined in more detail. To simplify its expression, it can be demonstrated that

$$\left\langle a \left| \sum_j e^{i\mathbf{K}\cdot\mathbf{r_j}} \ \frac{i\mathbf{K} \times \mathbf{p}_j}{\hbar k^2} \cdot \mathbf{A} \right| a \right\rangle \ =$$

$$= \ - \left(\frac{K^2}{k^2} \right) \ \left\langle a \left| \sum_j e^{i\mathbf{K}\cdot\mathbf{r}_j} \ \frac{-i\mathbf{K} \times \mathbf{p}_j}{\hbar k^2} \right| a \right\rangle \cdot \mathbf{A} \ = \ - \left(\frac{K^2}{2k^2} \right) \ \hat{\mathbf{K}} \times [\mathbf{L}(\mathbf{K}) \times \hat{\mathbf{K}}] \cdot \mathbf{A} \ =$$

$$= \ \frac{1}{2} \ \mathbf{L}(\mathbf{K}) \cdot \mathbf{A}''$$

where

$$\mathbf{A}'' = -\left(\frac{K^2}{2k^2}\right)\mathbf{A} - [-\left(\frac{K^2}{2k^2}\right)\mathbf{A}\cdot\hat{\mathbf{K}}]\,\hat{\mathbf{K}} =$$

$$= 2(1-\hat{\mathbf{k}}\cdot\hat{\mathbf{k}}')(\hat{\epsilon}'\times\hat{\epsilon}) - (\hat{\mathbf{k}}\times\hat{\epsilon})(\hat{\mathbf{k}}\cdot\hat{\epsilon}') + (\hat{\mathbf{k}}'\times\epsilon')(\hat{\mathbf{k}}'\cdot\epsilon), \tag{2.12}$$

and the quantity $\mathbf{L}(\mathbf{K})$ results from the application of an operator related to the orbital angular momentum $\mathbf{l}_j$

$$\mathbf{L}(\mathbf{K}) = \frac{1}{2}\left\langle a\left|\sum_j [f(\mathbf{K}\cdot\mathbf{r}_j)\mathbf{l}_j + \mathbf{l}_j f(\mathbf{K}\cdot\mathbf{r}_j)]\right|a\right\rangle$$

by the function

$$f(x) = 2\sum_{n=0}^{\infty}\frac{(ix)^n}{(n+2)n!} = \frac{2}{(ix)^2}\int_0^{ix} ye^y dy.$$

Let's define as $\mathbf{S}(\mathbf{K})$ the spin density Fourier transform of the charge distribution:

$$\mathbf{S}(\mathbf{K}) = \left\langle a\left|\sum_j e^{i\mathbf{K}\cdot\mathbf{r}_j}\mathbf{s}_j\right|a\right\rangle.$$

At this point, the following expression has been obtained:

$$f_{nr} = i\frac{\hbar\omega}{mc^2}\left[\frac{1}{2}\mathbf{L}(\mathbf{K})\cdot\mathbf{A}'' + \mathbf{S}(\mathbf{K})\cdot\mathbf{B}\right]. \tag{2.13}$$

In section 2.2 the state of the polarisation of the incident and of the diffracted beam and their role in the scattering process is examined in detail. For the moment, it is convenient to stress that the expression for the non resonant amplitude can be simplified by assuming an explicit polarisation basis $\hat{\epsilon}_1$ ($\rho = 1$) and $\hat{\epsilon}_2$ ($\rho = 2$). Once the basis has been selected, the amplitude can be expressed by a 2×2 matrix, constructed from the values assumed in the four possible channels of polarisation:

$$(\epsilon', \epsilon) = \begin{bmatrix} (\hat{\epsilon}'_1, \hat{\epsilon}_1) & (\hat{\epsilon}'_1, \hat{\epsilon}_2) \\ (\hat{\epsilon}'_2, \hat{\epsilon}_1) & (\hat{\epsilon}'_2, \hat{\epsilon}_2) \end{bmatrix}. \tag{2.14}$$

The most suitable choice is a linear polarisation basis, constituted by:

$\hat{\epsilon}_1 = \hat{\epsilon}_\sigma$ orthogonal to the scattering plane;

$\hat{\epsilon}_2 = \hat{\epsilon}_\pi$ lying into the scattering plane.

The scattering amplitude can therefore be expressed in the form of a so-called Jones matrix:

$$f_{nr} = i\frac{\hbar\omega}{mc^2}\cdot$$

$$\begin{bmatrix} \mathbf{S}(\mathbf{K})\cdot(\hat{\mathbf{k}}\times\hat{\mathbf{k}}') & -\frac{K^2}{2k^2}[(\frac{1}{2}\mathbf{L}(\mathbf{K}) + \mathbf{S}(\mathbf{K}))\cdot\hat{\mathbf{k}}' + \frac{1}{2}\mathbf{L}(\mathbf{K})\cdot\hat{\mathbf{k}}] \\ \frac{K^2}{2k^2}[(\frac{1}{2}\mathbf{L}(\mathbf{K}) + \mathbf{S}(\mathbf{K}))\cdot\hat{\mathbf{k}} + \frac{1}{2}\mathbf{L}(\mathbf{K})\cdot\hat{\mathbf{k}}'] & (\frac{K^2}{2k^2}\mathbf{L}(\mathbf{K}) + \mathbf{S}(\mathbf{K}))\cdot(\hat{\mathbf{k}}\times\hat{\mathbf{k}}') \end{bmatrix}.$$

The significance of the different polarisation channels can be highlighted by the introduction of a reference frame Σ centered on the sample. The orientation of the axes is determined by the incident and the diffracted beams (see Fig. 2.1):

$$\Sigma = \begin{cases} \hat{\mathbf{u}}_1 = (\hat{\mathbf{k}} + \hat{\mathbf{k}}')/2\cos\theta \\ \hat{\mathbf{u}}_2 = (\hat{\mathbf{k}}\times\hat{\mathbf{k}}')/\sin 2\theta \\ \hat{\mathbf{u}}_3 = (\hat{\mathbf{k}} - \hat{\mathbf{k}}')/2\sin\theta \end{cases} \tag{2.15}$$

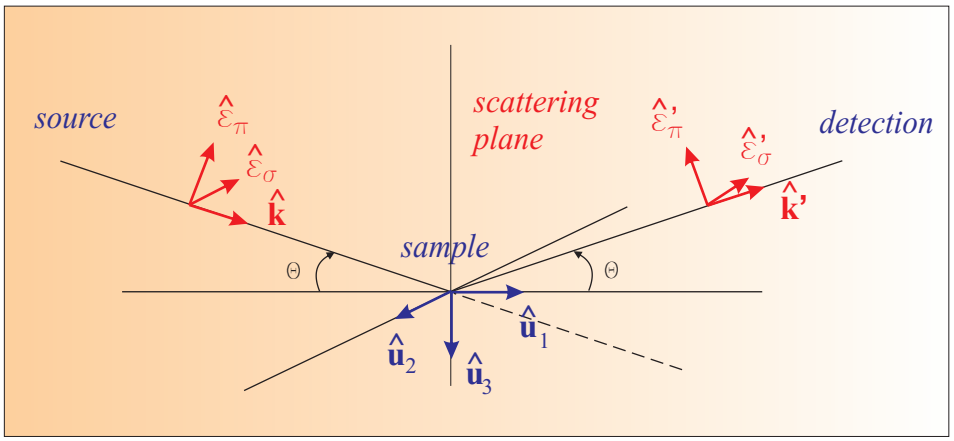

Figure 2.1: Definition of the reference frame.

The direction $\hat{\mathbf{u}}_3$ coincides with the direction of $\mathbf{K}$, while $\hat{\mathbf{u}}_1$ lies into the scattering plane, and $\hat{\mathbf{u}}_2$ is orthogonal to that plane. The angle 2θ is the Bragg angle between the two wave vectors $\hat{\mathbf{k}}$ and $\hat{\mathbf{k}}'$. Within this frame,

$$f_{nr} = i\frac{\hbar\omega}{mc^2} \cdot \begin{bmatrix} (\sin 2\theta)S_2 & -2(\sin^2\theta)[(\cos\theta)(L_1+S_1) - (\sin\theta)S_3] \\ 2(\sin^2\theta)[(\cos\theta)(L_1+S_1) - (\sin\theta)S_3] & (\sin 2\theta)[2(\sin^2\theta)L_2 + S_2] \end{bmatrix} . \tag{2.16}$$

It is now apparent that the diagonal matrix elements (the polarisation is conserved) involve the magnetisation density oriented perpendicularly to the scattering plane, while the off-diagonal matrix elements (the polarisation is turned) involve the magnetisation density oriented within the scattering plane. The possibility to select and measure specific polarisation channels is a powerful tool for the refinement of complex magnetic structures. A more detailed review of this aspect will be done in the next sections (2.2 and 2.3), with particular attention to the observation of cycloidal magnetic structures by means of circularly polarised light.

2.1.4 Magnetic diffraction from ordered structures

The results found so far can be now applied to the specific case of ordered magnetic structures, to derive the corresponding magnetic diffraction intensity. While in the case of a commensurate magnetic structure this derivation is straightforward and closely mirroring the canonical Laue condition for charge diffraction, it will be worth to present in more detail the case of an incommensurate magnetic structure. In the latter, the ratio between the period of the magnetic modulation and the period of the crystallographic cell is an irrational number, thus preventing the existence of a super-cell which is also a magnetic unit cell.

Commensurate magnetic order

Starting with the case of a commensurate magnetic structure, a magnetic unit cell can be identified, be it coincident with the crystallographic cell or composed by a finite number of crystallographic

units. The expression found up to now for the magnetic scattering cross-section from an isolated system of charges can be directly extended to a periodic arrangement of magnetic atoms, each characterised by a spin moment $\mathbf{S}_j$ and an orbital moment $\mathbf{L}_j$. A general summation over the contributions from all the magnetic atoms in the sample gives:

$$f_{nr} \;=\; i\frac{\hbar\omega}{mc^2}\;\Sigma_j\; e^{i\mathbf{K}\cdot\mathbf{r}_j}\left[\frac{1}{2}\mathbf{L}_j(\mathbf{K})\cdot\mathbf{A}''\;+\;\mathbf{S}_j(\mathbf{K})\cdot\mathbf{B}\right]\;=\;\Sigma_j\; e^{i\mathbf{K}\cdot\mathbf{r}_j}f_{nr_j}. \tag{2.17}$$

Since a magnetic unit cell is defined, it is possible to derive from this expression the Laue condition for magnetic diffraction, as usually done in the case of charge scattering (Bragg's law). Based on the magnetic cell periodicity, it can be assumed

$$\mathbf{r}_j \;=\; \mathbf{R}_n \;+\; \mathbf{d}_s \tag{2.18}$$

where $\mathbf{R}_n$ identifies the position of the n^{th} unit cell to which the j^{th} atom belongs, and $\mathbf{d}_s$ identifies the position of the atom within the cell. By spanning the scattering vector $\mathbf{K}$ on the basis defined by the reciprocal lattice

$$\mathbf{a}^* = 2\pi\frac{\mathbf{b}\times\mathbf{c}}{\mathbf{a}\cdot(\mathbf{b}\times\mathbf{c})}\;,\quad \mathbf{b}^* = 2\pi\frac{\mathbf{c}\times\mathbf{a}}{\mathbf{a}\cdot(\mathbf{b}\times\mathbf{c})}\;,\quad \mathbf{c}^* = 2\pi\frac{\mathbf{a}\times\mathbf{b}}{\mathbf{a}\cdot(\mathbf{b}\times\mathbf{c})} \tag{2.19}$$

it is found that diffraction occurs for discrete values of the scattering vector $\mathbf{K} = h\mathbf{a}^* + k\mathbf{b}^* + l\mathbf{c}^*$, where h, k, l are integer numbers, and the scattering amplitude is proportional to the summation within the cell

$$f_{nr} \;=\; \Sigma_s\; e^{i\mathbf{K}\cdot\mathbf{d}_s}f_{nr_s}. \tag{2.20}$$

It should be noted at this point that following the conventions employed in crystallography, the reflection labeled by indexes (h k l) is associated to a scattering vector $\mathbf{K} = \mathbf{k}' - \mathbf{k}$, while the literature of magnetic scattering employs the definition $\mathbf{K} = \mathbf{k} - \mathbf{k}'$ which has been used up to now; since this might ingenerate some ambiguity about absolute signs in the next chapters, in particular with respect to the handedness of the magnetic cycloidal domains, the convention employed for $\mathbf{K}$ will be always specified.

Incommensurate magnetic order

In the case of an incommensurate magnetic order, the crystallographic periodicity and the magnetic one are irrational lengths, so that it is no longer possible to identify a magnetic unit cell which captures both periodicities, and to reduce the atomic scattering amplitudes f_{nr_j} to a finite set of values f_{nr_s}. However, since the magnetic order is still periodic, it is possible to expand this modulation into a Fourier series characterised by one or more frequency parameters. In this example, it will be assumed that only the first harmonic of the modulation carries significant weight, thus considering the simplest case of an arrangement of sinusoidally modulated magnetic moments.

For the sake of demonstration, let's consider an ideal simple structure. Let's suppose that only two magnetic atoms per crystallographic cell are present, carrying a pure spin moment $\mathbf{S}_j$ (j running as usual over all the magnetic atoms in the crystal), and ferromagnetically coupled within the cell, as per Fig. 2.2. The magnetic structure is collinear (say oriented along the crystallographic axis $\mathbf{a}$), and the incommensurate modulation for all the atoms is associated to a sinusoidal function varying along $\mathbf{a}$:

$$\mathbf{S}_j \;=\; S\;\cos(\mathbf{q}\cdot\mathbf{r}_j)\;\hat{\mathbf{a}}. \tag{2.21}$$

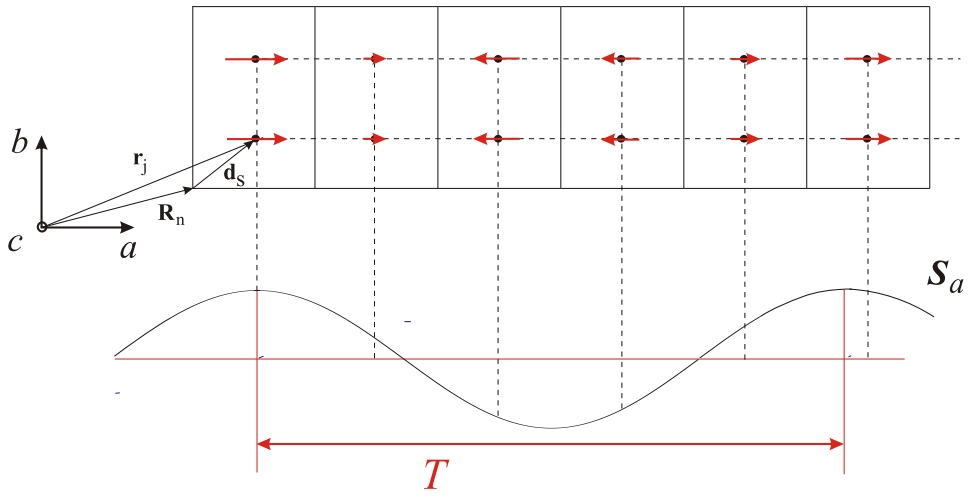

Figure 2.2: Example of collinear incommensurate magnetic structure. The spin moments are oriented along **a** and sinusoidally modulated, T being the period. Two atoms ferromagnetically coupled are depicted for each crystallographic cell.

In this expression $\hat{\mathbf{a}}$ is the unitary vector identifying the crystallographic direction **a**; $S = S(\mathbf{K})$ is the amplitude of the magnetic modulation; $\mathbf{r}_j$ is a vector identifying the position of the j^{th} atom in the crystal; $\mathbf{q} = 2\pi/T\ \hat{\mathbf{a}}$ contains the frequency and the direction of the modulation (T being the period). By developing the Fourier series of the modulation, in this simple case it can be written:

$$\mathbf{S}_j \ = \ \frac{1}{2} S \ [e^{i\mathbf{q}\cdot\mathbf{r}_j} + e^{-i\mathbf{q}\cdot\mathbf{r}_j}]\hat{\mathbf{a}}. \tag{2.22}$$

Starting again from Eq. 2.13, the scattering amplitude from the sum over the whole crystal is:

$$f_{nr} \ = \ i\frac{\hbar\omega}{mc^2} \ \Sigma_j \ e^{i\mathbf{K}\cdot\mathbf{r}_j} \ \mathbf{S}_j(\mathbf{K}) \cdot \mathbf{B} \ =$$

$$= \ (\frac{1}{2} \ i\frac{\hbar\omega}{mc^2}) \ \Sigma_j \ e^{i\mathbf{K}\cdot\mathbf{r}_j} \ [e^{i\mathbf{q}\cdot\mathbf{r}_j} + e^{-i\mathbf{q}\cdot\mathbf{r}_j}] \ (S \ \hat{\mathbf{a}} \cdot \mathbf{B}) \tag{2.23}$$

and $\mathbf{r}_j$ can be decomposed as before in $\mathbf{R}_n$ and $\mathbf{d}_s$, leading to

$$f_{nr} \ = \ (\frac{1}{2} \ i\frac{\hbar\omega}{mc^2}) \ \left\{ \left(\Sigma_n e^{i(\mathbf{K}+\mathbf{q})\cdot\mathbf{R}_n}\right) \left(\Sigma_s e^{i(\mathbf{K}+\mathbf{q})\cdot\mathbf{d}_s}\right) + \right.$$

$$\left. + \left(\Sigma_n e^{i(\mathbf{K}-\mathbf{q})\cdot\mathbf{R}_n}\right) \left(\Sigma_s e^{i(\mathbf{K}-\mathbf{q})\cdot\mathbf{d}_s}\right) \right\} (S \ \hat{\mathbf{a}} \cdot \mathbf{B}) \, . \tag{2.24}$$

Once again the sums over the various crystallographic cells (n) provide the condition to get a nonzero total contribution. Note that now **K** is replaced by $\mathbf{K} \pm \mathbf{q}$, thus giving rise to the two twin reflections

$$\begin{aligned} \Sigma_n e^{i(\mathbf{K}+\mathbf{q})\cdot\mathbf{R}_n} \ &\rightarrow \ \mathbf{K} = (h-\tau)\mathbf{a}^* + k\mathbf{b}^* + l\mathbf{c}^* \\ \Sigma_n e^{i(\mathbf{K}-\mathbf{q})\cdot\mathbf{R}_n} \ &\rightarrow \ \mathbf{K} = (h+\tau)\mathbf{a}^* + k\mathbf{b}^* + l\mathbf{c}^* \end{aligned} \tag{2.25}$$

characterised by the diffraction amplitudes

$$f_{nr} \ = \ \left(\ \frac{1}{2} \ i\frac{\hbar\omega}{mc^2} \ \right) \ \cdot \left\{ \begin{array}{l} \Sigma_s e^{i(\mathbf{K}+\mathbf{q})\cdot\mathbf{d}_s} \ (S \ \hat{\mathbf{a}} \cdot \mathbf{B}) \ \big|_{\mathbf{K}=(h-\tau)\mathbf{a}^*+k\mathbf{b}^*+l\mathbf{c}^*} \\ \\ \Sigma_s e^{i(\mathbf{K}-\mathbf{q})\cdot\mathbf{d}_s} \ (S \ \hat{\mathbf{a}} \cdot \mathbf{B}) \ \big|_{\mathbf{K}=(h+\tau)\mathbf{a}^*+k\mathbf{b}^*+l\mathbf{c}^*} \end{array} \right. \tag{2.26}$$

The parameter τ is defined as $\tau = \Delta\Phi/2\pi = a/T$, $\Delta\Phi$ being the phase shift of the magnetic modulation upon passing from one crystallographic cell to the next one, and a being the cell parameter. The conditions found on $\mathbf{K}$ can be inserted within the sum over s in the expressions above. The vector products $(\mathbf{K} \pm \mathbf{q}) \cdot \mathbf{d}_s$ are simplified by taking into account the relationships between direct and reciprocal lattice: $\mathbf{a} \cdot \mathbf{a}^* = 2\pi$, $\mathbf{a} \cdot \mathbf{b}^* = \mathbf{a} \cdot \mathbf{c}^* = 0$, etc.; if $\mathbf{d}_s$ describes the positions of the two atoms (s = 1,2) within the crystallographic cell, and their coordinates are written as

$$\mathbf{d}_s = x_s\mathbf{a} + y_s\mathbf{b} + z_s\mathbf{c} \qquad (s = 1, 2)$$

then the expressions 2.26 become

$$f_{nr} \;=\; \left(\frac{1}{2}\, i\frac{\hbar\omega}{mc^2} \right) \cdot \begin{cases} \Sigma_s e^{i2\pi(hx_s+ky_s+lz_s)} \left(S\ \hat{\mathbf{a}} \cdot \mathbf{B}\right) \big|_{\mathbf{K}=(h-\tau)\mathbf{a}^*+k\mathbf{b}^*+l\mathbf{c}^*} \\ \\ \Sigma_s e^{i2\pi(hx_s+ky_s+lz_s)} \left(S\ \hat{\mathbf{a}} \cdot \mathbf{B}\right) \big|_{\mathbf{K}=(h+\tau)\mathbf{a}^*+k\mathbf{b}^*+l\mathbf{c}^*} \end{cases} \tag{2.27}$$

Some general considerations can be done at this point. The magnetic reflections, in the general case of an incommensurate modulation of period $T = a/\tau$, arise as the scattering vector $\mathbf{K}$ is shifted from the position of a charge reflection by an amount of $\pm\tau$ along the direction of the magnetic modulation. It is important to note that in the example considered above the magnetic amplitudes calculated for the two twin reflections at $\pm\tau$ turn out to be the same (Eq. 2.27). This is a consequence of the magnetic moments being collinear. In section 2.3, it will be treated the particular case of interest for the present work, namely, the investigation of a non-collinear magnetic order by means of X-ray diffraction. It will be seen that the magnetic structure factors in twin reflections are not coincident anymore, and that this difference is conserved in the magnetic intensity when the polarisation of the incident beam is circular.

2.1.5 Experimental setup

The typical setup of a magnetic diffraction experiment implementing the physical principles described so far is schematically depicted in Fig. 2.3. The technical details about the generation of X-rays by synchrotron source, the experimental devices and their operation will be presented in the next chapter. The incident beam emerging from the synchrotron is processed by the optics stage and aimed towards the sample. The sample itself is mounted on a six-circle diffractometer, to satisfy the diffraction conditions stated in Eq. 2.25 in 2.1.4. It is equipped with temperature control and the possibility to apply in situ electric and magnetic fields. The detection stage is provided with a polarisation analysis setup, able to filter the component of the diffracted beam linearly oriented along an arbitrary direction. The polarisation of the incoming beam is manipulated by means of a phase plate setup, employed to tune the beam into a circularly polarised state. Given the importance that the polarimetry techniques carry within the present work, the description of the polarisation analysis setup and of the phase plate will be extensively covered in the next chapter (3.1.5 and 3.1.6).

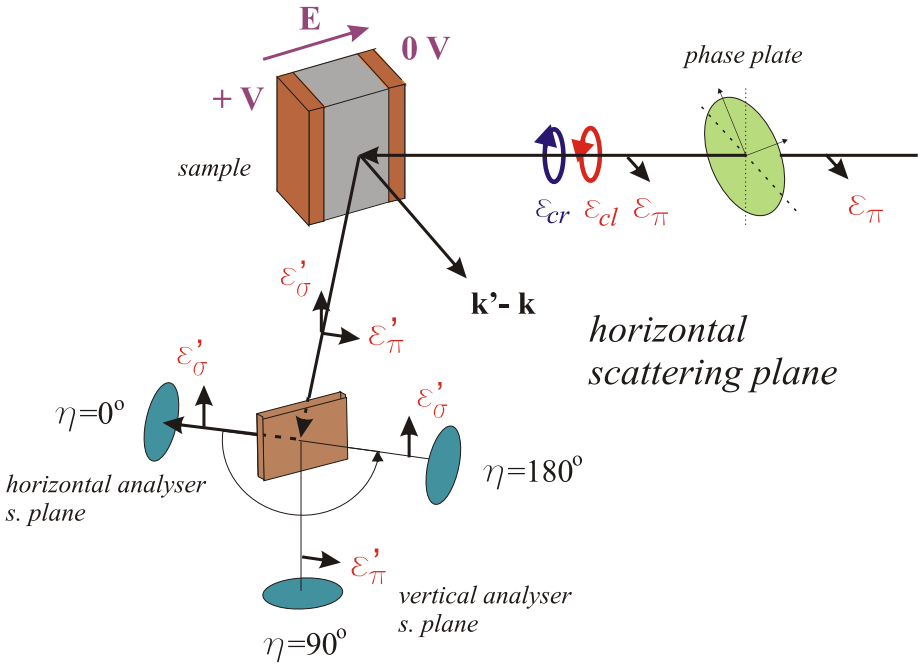

Figure 2.3: Sketch of the experimental setup for magnetic diffraction. The polarisation of the incident beam, upon being transmitted through the phase plate, may lie in a linear, circular left or circular right state. An in situ electric field can be applied on the sample. The diffracted beam is filtered by an analyser; the direction of the polarisation to be transmitted is selected by rotating the angle η (see 3.1 for details).

2.2 Polarimetry and control of the incident polarisation

2.2.1 The azimuthal scan

Since the NRXM Scattering is sensitive to the direction of the magnetic moments, a common experimental method consists in scanning over one geometric parameter from Eq. 2.13 and measuring the variation induced on the diffracted intensity. Once a suitable energy and the indexes of a diffraction peak have been chosen, the direction of the diffracted beam is fixed, as well as two out of the three angles that identify the orientation of the crystal with respect to the beams. A traditional technique consists in varying the one remaining geometric degree of freedom, the azimuthal angle (ψ) defining the rotation of the sample about the scattering vector, and collecting the dependence of the intensity $I(\psi)$. This method has been for long the most used in NRXM Scattering experiments, and provided valuable results. However, this technique is not exempted from several drawbacks. Firstly, it requires us to constantly change the incident angle between the beam and the surface of the sample, so that the absorption effects exert an influence on the diffracted intensity that varies correspondingly. It is possible to correct the measured values to take these effects into account, both via the theoretical estimation of the absorption coefficient as a function of the incident and diffracted angles between beam and surface, and via experimental measurement of the azimuthal dependence of a charge peak whose Miller indexes are close to the magnetic peak of interest. Nevertheless, the introduction of this further stage in the data acquisition and analysis can lower the accuracy of the measurement. Morevover, an azimuthal scan poses some constraints on the in situ sample environment. As the

sample must be free to rotate about the scattering vector, the application of external magnetic and electric fields become technically challenging.

2.2.2 The Stokes scan

An alternative solution is found in recognising that, beside the geometric degrees of freedom mentioned so far, Eq. 2.13 provides an additional degree of choice if it is possible to freely change the polarisation vectors ϵ and ϵ' that concur to build up the vectors $\mathbf{A}''$ and $\mathbf{B}$. The importance of the polarisation dependence in X-ray magnetic scattering has been recognised from the beginning, leading to calculate the general expressions for the differential cross-section and the final polarisation, assuming an arbitrary incident polarisation [45].

Regarding the selection of the diffracted polarisation ϵ', the linear polarisation analyser setup introduced in 2.3 is an established part of a classical magnetic diffraction experiment. Its purpose is to measure the projection of ϵ' along any arbitrary direction. By repeated measurements along a set of possible directions in the polarisation plane, one obtains a full description of the linear component of the polarisation of the diffracted beam. With the experimental setup shown in Fig. 2.3, this is done by performing a complete rotation of the analyser with respect to the beam (wavevector $\mathbf{k}'$). The technical details will be covered in the next chapter (3.1.5). For the purposes of the present chapter, it is sufficient to note that, when η is the angle used to define the rotation of the analyser, by collecting the dependence of the intensity as a function of η one performs a so-called Stokes scan. This dependence takes the form

$$I(\eta) = I_0 \left(1 + P_1 \cos 2\eta + P_2 \sin 2\eta\right)$$

where the two polarisation factors P_1 and P_2 are sufficient to describe the total degree of linear polarisation. In order to understand the significance of P_1 and P_2, a full review of the characterisation of polarised light is given in the next subsection (2.2.3). This technique has the advantage, if compared to the azimuthal method, of requiring no movement of the sample with respect to the beam. The measurements are more accurate, no correction for absorption is needed, and the setup of specific sample environments is allowed, such as the application of electric/magnetic fields.

As for the incident polarisation ϵ, the radiation emerging from a synchrotron source is highly polarised in the horizontal plane ($> 99\%$). This state can be manipulated by means of a phase plate device designed for X-ray frequencies, as described in 3.1.6. While the control of the incident polarisation is in any case a useful tool for collecting information (e.g. by linear incident polarisation scans [47]), in the specific case of cycloidal magnetic structures it assumes a particular relevance. When the incoming polarisation is tuned to be circular, it finds its handedness naturally coupled with the handedness of the magnetic moments. It has been seen that two magnetic domains are possible, characterised by opposite handedness of the rotating moments with respect to the same propagation direction. Circularly polarised light is expected to scatter with different intensity on the two domains; a difference that can be reversed by reversing the handedness of the circular polarisation. Conversely, when the two domains are present in equal distribution, these differences are averaged out and the diffracted beam has similar intensity for the two circular polarisation states. It is clear that this is a powerful tool to reveal whether an imbalance of magnetic domains has been achieved in the crystal

by means of an electric field annealing (cf. section 2.3).

2.2.3 Polarised light

The aim of this subsection is to provide some mathematical tools to describe the different states of polarisation for an electromagnetic field traveling in space: completely polarised light; partially polarised light; natural light. As the most general basis function for electromagnetic radiation, consider a plane wave. From a classical point of view, the general solution of the Maxwell's equations, if the plane wave propagates along the direction $\hat{\mathbf{z}}$, is:

$$\begin{aligned} \mathbf{E}(z,t) &= \mathbf{E}_x(z,t) + \mathbf{E}_y(z,t) \\ &= E_{0x}\ \cos(kz - \omega t + \phi_x)\ \hat{\mathbf{x}}\ +\ E_{0y}\ \cos(kz - \omega t + \phi_y)\ \hat{\mathbf{y}} \end{aligned} \tag{2.28}$$

where $\phi = \phi_y - \phi_x$ is the relative phase difference between the projections of $\mathbf{E}$ along $\hat{\mathbf{x}}$ and $\hat{\mathbf{y}}$. The resultant vector can thus belong to one of the following polarisation states:
a) if $\phi = 2n\pi$, the two projections are in-phase or out-of-phase, and $\mathbf{E}$ is linearly polarised, in the direction spanned by the vector $E_{0x}\ \hat{\mathbf{x}}\ \pm\ E_{0y}\ \hat{\mathbf{y}}$: $\mathbf{E}\ =\ [\ E_{0x}\ \hat{\mathbf{x}}\ \pm\ E_{0y}\ \hat{\mathbf{y}}\ ]\ \cos(kz - \omega t)$.
b) if both the projections have equal amplitudes ($E_{0x} = E_{0y} = E_0$) and $\phi = \pm\pi/2$, then $\mathbf{E}$ is right or left circularly polarised: $\mathbf{E}\ =\ E_0\ [\ \cos(kz - \omega t)\ \hat{\mathbf{x}}\ \pm\ \sin(kz - \omega t)\ \hat{\mathbf{y}}\ ]$.
c) otherwise, the plane wave belongs to the most general case of elliptical polarisation.

While a single plane wave is completely polarised (it lies in a well defined polarisation state), this is not always the case for a generic radiation, i.e., a superposition of several plane waves. An *ordinary* light source consists of a very large number of atomic emitters, randomly orientated. They can be envisioned as oscillating with different phases at some dominant frequency ν. Each excited atom radiates a *polarised* wavetrain; the frequency bandwidth is inversely proportional to the coherence time of the pulse. During an interval shorter than the average coherence time, the waves give rise to a coherent superposition, namely, to a wave having one defined polarisation state. However, as new wavetrains are constantly emitted, the overall polarisation changes in time. If the coherence time is long (in comparison with the detection time), the succession of the different states can form a resultant wave having some dominant polarisation character. It is said to be *partially polarised*. Conversely, if any polarisation state is short-lived, these changes take place at so rapid a rate as to render any single polarisation state indiscernible. This wave is referred to as *natural light* or unpolarised light. A useful way to describe this partially polarised radiation is to envision it as the result of the superposition of specific amounts of natural and polarised light. In the particular case of a synchrotron source, the radiation is expected to be almost completely linearly polarised, with a small amount (less than 1%) of unpolarised contribution.

The Jones description

The Jones formulation for the polarisation leads to a direct procedure for predicting the effects of a complex system of polarising elements on the ultimate state of a wave. Its principal drawback is that it is applicable only to polarised waves. If this condition is satisfied, the most natural way to represent the beam is by means of the electric vector itself. The general expression for $\mathbf{E}$ (Eq.

2.28) is the linear combination of two orthonormal basis functions. They can be chosen as two linear states of unitary amplitude, with coincident phases, directed along $\hat{\mathbf{x}}$ ('horizontal' direction) and $\hat{\mathbf{y}}$ ('vertical'): $\mathbf{E}_h = \cos(kz - \omega t)\ \hat{\mathbf{x}}$; $\mathbf{E}_v = \cos(kz - \omega t)\ \hat{\mathbf{y}}$. As the radiation is monochromatic, the information about the frequency can be dropped, and the description can be given in the more compact form of phasors: $\mathbf{E}_h = \hat{\mathbf{x}}$; $\mathbf{E}_v = \hat{\mathbf{y}}$. With this basis, a generic $\mathbf{E}$ field can be written as a vector in a two-dimensional space of functions:

$$\mathbf{E} = \begin{bmatrix} E_{0x} \\ E_{0y}\ e^{i\phi} \end{bmatrix}$$

where the wave along $\hat{\mathbf{x}}$ has been selected as the reference for the relative phase ($\phi_x = 0$). For instance, the circular right-handed state and the left-handed one become, respectively:

$$\mathbf{E}_{cr} = \frac{1}{\sqrt{2}} \begin{bmatrix} 1 \\ -i \end{bmatrix}, \qquad \mathbf{E}_{cl} = \frac{1}{\sqrt{2}} \begin{bmatrix} 1 \\ i \end{bmatrix}.$$

Consider an incident beam ($\mathbf{E}_i$) passing through a generic polarising element (phase plate, analyser, sample...), and emerging as a final vector ($\mathbf{E}_f$).Once two arbitrary polarisation bases have been fixed for the incident and the outcoming beam, the device is described by a 2×2 matrix (Jones matrix) $\mathcal{A}$: $\mathbf{E}_f = \mathcal{A}\mathbf{E}_i$.

The Poincaré-Stokes description

Beside defining the polarisation by means of the components of the electric field, it is advantageous to dispose of an alternative description in terms of more convenient observables, such as the intensities. Moreover, the Poincaré-Stokes formulation is able to describe not only a completely polarised beam, but a generic (polarised, partially polarised, natural) beam. A general discussion of these techniques has been given by Fano [48]; their application to neutron scattering and to the transmission of X-rays through matter has been elaborated by Blume and Kistner [49, 50]. The first application of the Poincaré-Stokes representation to X-ray magnetic scattering is found in the work of de Bergevin and Brunel [43], and a systematic elaboration on the subject is contained in the work elaborated by Blume [45].

From an operational point of view, consider disposing of a set of the following polarisation filters: a linear horizontal polariser; a linear 45° polariser; a circular right polariser. By positioning each of these filters, alone, in the path of the beam, the transmitted intensities (say I_1, I_2, I_3) can be measured to quantify the amount of the various polarisation states. The Stokes parameters P_1, P_2, P_3 are intended to express the intensity fractions of the total beam belonging to these states. They are defined as

$$P_1 = (2I_1 - I_0)/I_0$$

$$P_2 = (2I_2 - I_0)/I_0$$

$$P_3 = (2I_3 - I_0)/I_0$$

where the denominators represent a normalization by the intensity of the incident beam I_0.

To relate these parameters to the definitions formulated by Jones, it is necessary to consider the case of completely polarised light. It can be demonstrated that:

$$P_1 = \frac{E_{0x}^2 - E_{0y}^2}{E_{0x}^2 + E_{0y}^2}, \tag{2.29}$$

$$P_2 = \frac{2\ E_{0x}E_{0y}\ \cos\phi}{E_{0x}^2 + E_{0y}^2}, \tag{2.30}$$

$$P_3 = \frac{2\ E_{0x}E_{0y}\ \sin\phi}{E_{0x}^2 + E_{0y}^2}. \tag{2.31}$$

The state of a polarised beam is entirely described by the three real quantities P_1, P_2, P_3, just as in the Jones formulation it is characterised by E_{0x}, E_{0y}, ϕ.

To extend these definitions to the case of a partially polarised beam and a natural beam, consider that they are composed by different polarisation states which follow each other in time. In the form of a Jones vector

$$\mathbf{E} = \begin{bmatrix} E_{0x}(t)\ e^{i\phi_x(t)} \\ E_{0y}(t)\ e^{i\phi_y(t)} \end{bmatrix}$$

where, even for natural light, the quantities E_{0x}, E_{0y}, ϕ_x and ϕ_y are functions of time which change quite slowly in comparison to the wave oscillation in $(kz - \omega t)$. For example, if the mean frequency is 10^{15} Hz and the coherence time is $10^{-9}s$, the wave will pass through 10^6 cycles during this time. The intensity in an interval of time shorter than the coherence time would be

$$I = |\mathbf{E}_x|^2 + |\mathbf{E}_y|^2 = E_{0x}^2 + E_{0y}^2$$

and would be constant within the interval, as E_{0x} and E_{0y} are. In contrast, the intensity which would actually be measured by a detector is the average of the previous equation, over a comparatively long time interval (longer than the coherence time), i.e.,

$$I = <|\mathbf{E}_x|^2> + <|\mathbf{E}_y|^2> = <E_{0x}^2(t)> + <E_{0y}^2(t)>\ .$$

Therefore, the measured Stokes parameters are related to the electric field by the same expression introduced for I_1, I_2 and I_3 in the case of polarised beam, but averaged in time. By definition, a beam of natural light is composed of a succession of monochromatic waves varying rapidly (with short coherence time) and randomly. So, all the Stokes parameters tend to average to zero. Conversely, for a partially polarised beam some prevailing polarisation state can be recognized by the detecting instruments. In these cases:

- The P_1 parameter reflects a tendency for the polarisation to resemble either a horizontally linear polarised state (whereupon $P_1 > 0$) or a vertically linear one ($P_1 < 0$). If $P_1 = 0$, the beam displays no preferential orientation with respect to these axes (elliptical with axes oriented at $\pm 45°$, circular, or unpolarised).
- Similarly, P_2 implies a tendency for the beam to resemble a linear state oriented in the direction of $+45°$,$-45°$, or neither.
- Similarly, P_3 implies a tendency for the beam toward right-handedness, left-handedness, or neither.

A fourth parameter P_4 may be defined to quantify the unpolarised fraction of the beam:

$$P_4^2 = 1 - (P_1^2 + P_2^2 + P_3^2) \tag{2.32}$$

so that the overall polarisation state is characterized by a unitary vector of components [P_1, P_2, P_3, P_4] (see Fig. 3.4). A reduced vector $[P_1, P_2, P_3]$ is employed to describe the polarised fraction of the beam (the vector being unitary when the beam is completely polarised); and similarly, the two-dimensional vector $[P_1, P_2]$ of modulus $P' = \sqrt{P_1^2 + P_2^2}$ describes the linearly polarised fraction of the beam.

The Stokes parameters are most often combined into a 4-dimensional vector, known as the Mueller or Stokes vector, spanning the space of polarisation states of a generic beam and keeping track of its intensity I:

$$\mathbf{S} = \begin{bmatrix} S_0 \\ S_1 \\ S_2 \\ S_3 \end{bmatrix} = \begin{bmatrix} I \\ I\ P_1 \\ I\ P_2 \\ I\ P_3 \end{bmatrix}$$

A linear device is then characterised by a 4×4 square matrix (Mueller matrix), converting the incident beam $\mathbf{S}_i$ to $\mathbf{S}_f = \mathcal{M}\ \mathbf{S}_i$.

2.3 Investigation of cycloidal magnetic structures

The kind of polarisation analysis described thus far proves particularly useful in the case of cycloidal magnetic densities. The essential features of NRXM Scattering from a cycloidal magnetic order can be highlighted in the simplest case in which the atoms within the crystallographic cell are ferromagnetically coupled, as was supposed in the case of collinear incommensurate magnetic order in 2.1.4. The most general case will be treated immediately afterwards.

2.3.1 Non-resonant magnetic scattering from a cycloidal structure

Say that the atoms carry a pure spin moment, that the cycloid lies in the crystallographic plane $(\mathbf{a}, \mathbf{b})$, and that the direction of the magnetic propagation is $\mathbf{a}$. The magnitude of the spin moment may be different for the components oriented along $\mathbf{a}$ and $\mathbf{b}$, thus giving rise to an elliptically shaped cycloid characterized by two main axes S_a and S_b, as in Fig. 2.4. The incommensurate modulation in all the atoms (indexed by j) is associated to a sinusoidal function

$$\mathbf{S}_j = S_a\ \cos(\mathbf{q} \cdot \mathbf{r}_j)\ \hat{\mathbf{a}}\ +\ S_b\ \cos(\mathbf{q} \cdot \mathbf{r}_j + \pi/2)\ \hat{\mathbf{b}} \tag{2.33}$$

where the components along $\mathbf{a}$ and $\mathbf{b}$ are out-of-phase by $\pm\pi/2$, thus indicating a cycloid whose main axes coincide with the crystallographic ones. The sign of the phase shift $\pm\pi/2$ determines the handedness of the cycloid. In Eq. 2.33, the component along $\mathbf{b}$ is advanced by $+\pi/2$ over the component along $\mathbf{a}$, and thus the sense of rotation is clockwise, when looking at the $(\mathbf{a}, \mathbf{b})$ plane from $+\mathbf{c}$ and moving along $+\mathbf{a}$. This cycloidal domain will be referred to as Domain 1 in this section. The opposite handedness of the cycloid is described by a phase shift of $-\pi/2$ and will be called Domain 2 (Fig. 2.5).

The derivation of the diffraction amplitude can proceed as in the case previously considered of a generic incommensurate modulation (2.1.4 can be consulted as a reference; the details of the

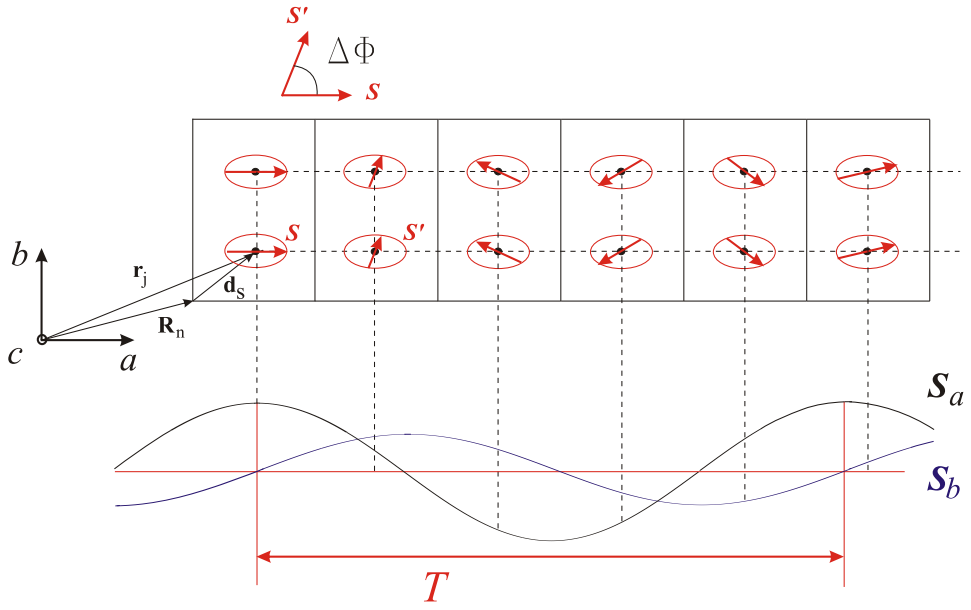

Figure 2.4: Example of cycloidal incommensurate magnetic structure. The spin moments are oriented along **a** and **b** and sinusoidally modulated. The two components are out-of-phase by $\pi/2$, and the overall moment rotates by $\Delta\Phi = 2\pi\tau$ from one crystallographic cell to the next. Two atoms ferromagnetically coupled are depicted for each crystallographic cell.

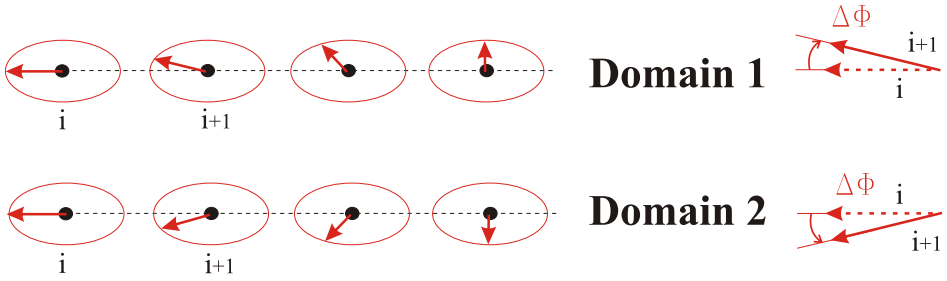

Figure 2.5: Definition of the two cycloidal magnetic domains.

calculation already covered there are not repeated in the present discussion). The Fourier series of the modulation becomes:

$$\begin{aligned}\mathbf{S}_j &= \frac{1}{2} S_a \left[e^{i\mathbf{q}\cdot\mathbf{r}_j} + e^{-i\mathbf{q}\cdot\mathbf{r}_j} \right] \hat{\mathbf{a}} \\ &+ \frac{1}{2} S_b \left[e^{i\mathbf{q}\cdot\mathbf{r}_j}\, e^{i\pi/2} + e^{-i\mathbf{q}\cdot\mathbf{r}_j}\, e^{-i\pi/2} \right] \hat{\mathbf{b}} = \\ &= \frac{1}{2} e^{i\mathbf{q}\cdot\mathbf{r}_j} \left[S_a\, \hat{\mathbf{a}} + S_b\, e^{i\pi/2}\, \hat{\mathbf{b}} \right] \\ &+ \frac{1}{2} e^{-i\mathbf{q}\cdot\mathbf{r}_j} \left[S_a\, \hat{\mathbf{a}} + S_b\, e^{-i\pi/2}\, \hat{\mathbf{b}} \right], \end{aligned} \tag{2.34}$$

and in shorthand notation

$$\mathbf{S}_j = \frac{1}{2} e^{i\mathbf{q}\cdot\mathbf{r}_j}\, \mathbf{M} + \frac{1}{2} e^{-i\mathbf{q}\cdot\mathbf{r}_j}\, \mathbf{M}^* \tag{2.35}$$

where the vector $\mathbf{M}$ and its complex conjugate $\mathbf{M}^*$ are defined as:

$$\begin{aligned} \mathbf{M} &= S_a\,\hat{\mathbf{a}} + S_b\,e^{i\pi/2}\,\hat{\mathbf{b}} = S_a\hat{\mathbf{a}} + i\,S_b\,\hat{\mathbf{b}} \\ \mathbf{M}^* &= S_a\,\hat{\mathbf{a}} + S_b\,e^{-i\pi/2}\,\hat{\mathbf{b}} = S_a\hat{\mathbf{a}} - i\,S_b\,\hat{\mathbf{b}}. \end{aligned} \tag{2.36}$$

The expression for $\mathbf{S}_j$ is then substituted into the general expression of the diffraction amplitude 2.13:

$$\begin{aligned} f_{nr} &= i\frac{\hbar\omega}{mc^2}\,\Sigma_j\,e^{i\mathbf{K}\cdot\mathbf{r}_j}\,\mathbf{S}_j(\mathbf{K})\cdot\mathbf{B} = \\ &= \left(\frac{1}{2}\,i\frac{\hbar\omega}{mc^2}\right)\,\Sigma_j\,[\,e^{i\mathbf{q}\cdot\mathbf{r}_j}\,\mathbf{M} + e^{-i\mathbf{q}\cdot\mathbf{r}_j}\,\mathbf{M}^*\,]\cdot\mathbf{B}. \end{aligned} \tag{2.37}$$

The position vector $\mathbf{r}_j$ is decomposed in the sum of the cell position vector $\mathbf{R}_n$ and the intra-cell position vector $\mathbf{d}_s$, leading to

$$\begin{aligned} f_{nr} = \left(\frac{1}{2}\,i\frac{\hbar\omega}{mc^2}\right) \Big\{ &\left(\Sigma_n e^{i(\mathbf{K}+\mathbf{q})\cdot\mathbf{R}_n}\right)\left(\Sigma_s e^{i(\mathbf{K}+\mathbf{q})\cdot\mathbf{d}_s}\right)\,\mathbf{M} + \\ &+\left(\Sigma_n e^{i(\mathbf{K}-\mathbf{q})\cdot\mathbf{R}_n}\right)\left(\Sigma_s e^{i(\mathbf{K}-\mathbf{q})\cdot\mathbf{d}_s}\right)\,\mathbf{M}^*\Big\}\cdot\mathbf{B} \end{aligned} \tag{2.38}$$

and the sum over the different cells (index n) defines the diffraction condition as in 2.1.4. The two twin reflections at $\pm\tau$ turn out to be associated to the amplitudes:

$$f_{nr} = \left(\frac{1}{2}\,i\frac{\hbar\omega}{mc^2}\right)\cdot\begin{cases} \Sigma_s e^{i2\pi(hx_s+ky_s+lz_s)}\,(\mathbf{M}\cdot\mathbf{B})\,\big|_{\mathbf{K}=(h-\tau)\mathbf{a}^*+k\mathbf{b}^*+l\mathbf{c}^*} \\ \\ \Sigma_s e^{i2\pi(hx_s+ky_s+lz_s)}\,(\mathbf{M}^*\cdot\mathbf{B})\,\big|_{\mathbf{K}=(h+\tau)\mathbf{a}^*+k\mathbf{b}^*+l\mathbf{c}^*} \end{cases} \tag{2.39}$$

2.3.2 Determination of domains via circular incident polarisation

The substantial difference that emerges here in comparison with the collinear case is that the amplitudes of the reflections $(h-\tau,k,l)$ and $(h+\tau,k,l)$ are no longer the same, but are proportional to the scalar products $\mathbf{M}\cdot\mathbf{B}$ and $\mathbf{M}^*\cdot\mathbf{B}$ respectively. Whether this imbalance between the two reflections is conserved in the diffraction intensity depends on the vector $\mathbf{B}$. Its expression was found in Eq. 2.10 to be linear in ϵ and ϵ'. If the incident (diffracted) beam is linearly polarised, then the vectorial components of ϵ (ϵ') are in phase with each other and can be expressed by real quantities (short of a common phase factor that does not bring physical relevance). Therefore the resulting vector $\mathbf{B}$ is also real. The consequence is that the two scattering amplitudes for $(h-\tau,k,l)$ and $(h+\tau,k,l)$ turn out to be the complex conjugate of each other: $\mathbf{M}^*\cdot\mathbf{B} = (\mathbf{M}\cdot\mathbf{B})^*$. The corresponding intensities ($|f_{nr}|^2$) are not discernible:

$$|\mathbf{M}^*\cdot\mathbf{B}|^2 = |\mathbf{M}\cdot\mathbf{B}|^2 \;\rightarrow\; I|_{\mathbf{K}=(h-\tau)\mathbf{a}^*+k\mathbf{b}^*+l\mathbf{c}^*} = I|_{\mathbf{K}=(h+\tau)\mathbf{a}^*+k\mathbf{b}^*+l\mathbf{c}^*}\,.$$

The situation is different when the components of the polarisation vectors are out of phase with each other. In the case of, say, circular left polarisation, the two components of ϵ along σ and π are out-of-phase by $+\pi/2$, giving rise to a vector $\mathbf{B}$ which is complex. Since this is geometrically coupled to $\mathbf{M}$ via the scalar product, it turns out that not only the amplitudes of the reflections at $(h-\tau,k,l)$ and $(h+\tau,k,l)$ are different, but also that they are no longer the complex conjugate of each other: $\mathbf{M}^*\cdot\mathbf{B} \neq (\mathbf{M}\cdot\mathbf{B})^*$ and consequently $I|_{\mathbf{K}=(h-\tau)\mathbf{a}^*+k\mathbf{b}^*+l\mathbf{c}^*} \neq I|_{\mathbf{K}=(h+\tau)\mathbf{a}^*+k\mathbf{b}^*+l\mathbf{c}^*}$. An analogous result holds in the case of circular right polarisation, where the two components of ϵ along σ and π are out-of-phase by $-\pi/2$, and give rise to a vector $\mathbf{B}^*$ which is the complex

conjugate to the one found for circular left polarisation. The combination via scalar product of the three independent components of the complex vectors $\mathbf{M}(\mathbf{K})$ and $\mathbf{B}$ makes it impossible to extract a common phase factor such that $\mathbf{M}(\mathbf{K}) \cdot \mathbf{B} = [\mathbf{M}(-\mathbf{K}) \cdot \mathbf{B}]^*$. This result shows an imbalance in the diffraction intensities for the twin reflections at $(h \pm \tau, k, l)$, that can be reversed by switching the circular polarisation from circular left to circular right, and that would not be visible by performing the measurement with a linearly polarised beam:

DOMAIN 1	circ. left	circ. right
refl. $+\tau$	$\lvert\mathbf{M} \cdot \mathbf{B}\rvert^2 = I_1$	$\lvert\mathbf{M} \cdot \mathbf{B}^*\rvert^2 = I_2$
refl. $-\tau$	$\lvert\mathbf{M}^* \cdot \mathbf{B}\rvert^2 = I_2$	$\lvert\mathbf{M}^* \cdot \mathbf{B}^*\rvert^2 = I_1$

This imbalance between I_1 and I_2 is of particular importance as we switch to the case of Domain 2, previously defined as

$$\mathbf{S}_j = \; S_a \; \cos(\mathbf{q} \cdot \mathbf{r}_j) \; \hat{\mathbf{a}} \; + \; S_b \; \cos(\mathbf{q} \cdot \mathbf{r}_j - \pi/2) \; \hat{\mathbf{b}} \tag{2.40}$$

since $\mathbf{M}$ and $\mathbf{M}^*$ are swapped, resulting in the symmetric situation:

DOMAIN 2	circ. left	circ. right
refl. $+\tau$	$\lvert\mathbf{M}^* \cdot \mathbf{B}\rvert^2 = I_2$	$\lvert\mathbf{M}^* \cdot \mathbf{B}^*\rvert^2 = I_1$
refl. $-\tau$	$\lvert\mathbf{M} \cdot \mathbf{B}\rvert^2 = I_1$	$\lvert\mathbf{M} \cdot \mathbf{B}^*\rvert^2 = I_2$

Therefore the discrimination between the two domains is possible when the incident light is circularly polarised: the diffracted intensity becomes sensitive to the absolute sense of rotation of the cycloid [51]. The three parameters that can be extracted from a Stokes scan (I_0, P_1, P_2) are all sensitive to the domain state; however, in practical cases, the specific magnetc structure factor and the scattering geometry can bring more sensitivity to one or the other of the parameters, which then offers a reliable indication of the domain state (see for example Fig. 3.4).

If the volume of the sample contributing to the diffraction is composed of a fraction V ordered as Domain 1, and a fraction $1 - V$ ordered as Domain 2, the resulting intensity is constructed from the incoherent sum of the two contributions:

$$I_{tot} \;=\; V\; I_0^I\; [\; 1 \;+\; P_1^I \cos(2\eta) \;+\; P_2^I \sin(2\eta)\;] \;+$$

$$+\; (1-V)\; I_0^{II}\; [\; 1 \;+\; P_1^{II} \cos(2\eta) \;+\; P_2^{II} \sin(2\eta)\;] \;=$$

$$=\; I_0^{tot}\; [\; 1 \;+ P_1^{tot} \cos(2\eta) \;+\; P_2^{tot} \cos(2\eta)\;]$$

where

$$I_0^{tot} \;=\; V\; I_0^I \;+\; (1-V)\; I_0^{II},$$

$$P_1^{tot} \;=\; F\; P_1^I \;+\; (1-F)\; P_1^{II},$$

$$P_2^{tot} \;=\; F\; P_2^I \;+\; (1-F)\; P_2^{II},$$

$$F \;=\; \frac{V I_0^I}{V I_0^I \;+\; (1-V)\; I_0^{II}} \;\in\; [0,1].$$

The variation of I_0^{tot}, P_1^{tot}, P_2^{tot} can be calculated as function of V, and compared with the measured values to extract the domain population within the crystal.

2.3.3 Determination of phase shifts in complex cycloidal structures

Finally, in the general case in which the different atoms within the cell are not interacting ferromagnetically, their magnetic coupling can be expressed by one relative phase shift relating the modulation of one component at one fixed position in space. For instance in Fig. 2.6, the component $\mathbf{S}_a$ between the atoms within the cell labeled by $s = 1, 2$ is out-of-phase by $\Delta\phi = \pi/2$ at the same coordinate in space along the direction $\mathbf{a}$. The difference in the magnetic modulation of the two crystallographic sites

$$\mathbf{S}_j = \; S_a \;\cos(\mathbf{q}\cdot\mathbf{r}_j)\; \hat{\mathbf{a}} \;+\; S_b \;\cos(\mathbf{q}\cdot\mathbf{r}_j + \pi/2)\; \hat{\mathbf{b}} \qquad s = 1 \tag{2.41}$$

$$\mathbf{S}_j = \; S_a \;\cos(\mathbf{q}\cdot\mathbf{r}_j + \Delta\phi)\; \hat{\mathbf{a}} \;+\; S_b \;\cos(\mathbf{q}\cdot\mathbf{r}_j + \pi/2 + \Delta\phi)\; \hat{\mathbf{b}} \qquad s = 2 \tag{2.42}$$

is obviously retained in the final scattering intensity, thus making it possible to etract an unknown phase $\Delta\phi$ from the fit of the experimental data. When dealing with opposite cycloidal domains in magneto-electric compounds, the appropriate phase shifts corresponding to the two domains are found by inversion of the whole magnetic structure. An application of these techniques is found in the chapters dealing with the refinement of the magnetic structure of $Ni_3V_2O_8$ (Chapter 4) and $TbMnO_3$ (Chapter 5).

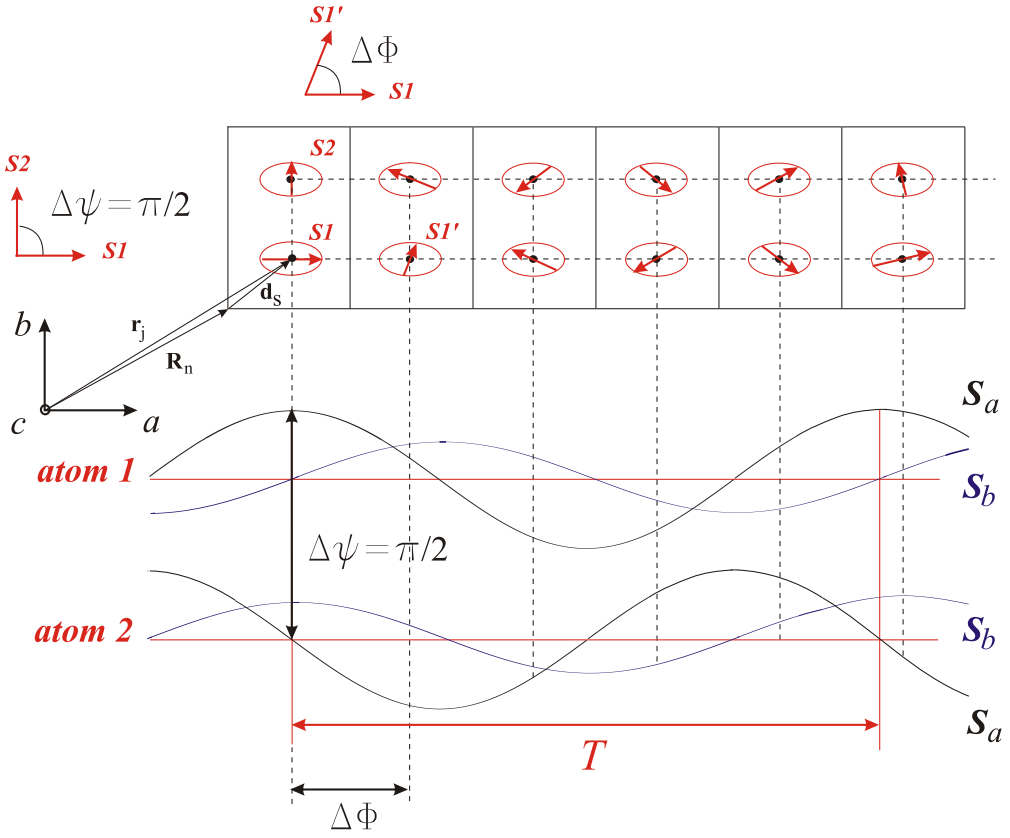

Figure 2.6: An example of cycloidal incommensurate magnetic structure, different from the one depicted in Fig. 2.4. The spin moments are oriented along **a** and **b** and sinusoidally modulated. The two components in each atom are out-of-phase by $\pi/2$. Two atoms are depicted for each crystallographic cell: the phase shift between the two atoms in the same component is $\Delta\psi = \pi/2$, as opposed to the simple ferromagnetic coupling of Fig. 2.4, in order to highlight the dependence of the scattering amplitude on the relative phases of the magnetic modulations (see text).

Chapter 3

Experimental Methods

This chapter covers the technical aspects of the experimental setup, with the aim of describing the elements previously introduced (see 2.1.5 and in particular Fig. 2.3) from a more detailed and operational point of view. Particular attention will be given to: 1) a description of the analyser crystal employed to perform complete linear polarisation analysis (Stokes scan) on the diffracted beam (3.1.5); 2) a description of the phase plate device employed to control the polarisation of the incident beam (3.1.6); 3) an exposition of the geometrical transformations needed to represent the polarisation of the incident and diffracted beam in a frame coherent with the experimental setup (3.1.7). Finally, the last part of the chapter (3.2) presents a simulation program elaborated in the course of this work, which calculates the expected Stokes dependence of the diffracted intensity for a given magnetic structure, depending on the reflection, the experimental geometry, the energy and the polarisation of the incident beam.

3.1 Technical details

3.1.1 Synchrotron source

In the course of the 20th century, X-rays have become established as an important probe for the investigation of the microscopic properties of matter. For this purpose, the quality of the beam produced by a synchrotron source is notable for the number of photons emitted per second, the focusing, the brilliance (photon density in the image spot per solid angle), the purity of the polarisation, and the spectral dependence of all previous features. The ESRF is the first synchrotron of the third generation (especially designed for the use of undulators as the source of X-rays). The electrons used to produce radiation are accelerated to an energy of 6 GeV, before being injected into the storage ring. The ID20 beamline at the ESRF [52] has been designed to meet the requirements of X-ray magnetic scattering experiments: a high photon flux ($\sim 10^{13}$ ph/sec at the sample position for photon energies in the range 6 - 10 keV); a wide energy range (3 - 40 keV) with a good energy resolution (1 eV at 8 keV); a well defined linear polarisation state of the photons ($> 99\%$ in the energy range of interest 6 - 10 keV). It is an ultra high vacuum (UHV) beamline, receiving radiation from three linear undulators, with period 35 mm (upstream), 35 mm (midstream) and 32 mm (downstream). The lower energy limit can be estimated around 3.5 keV; the upper limit around 20-25 keV. The

flux available at the sample position ranges from 10^{13} photons/sec at 4 keV up to 10^{14} photons/sec at 10 keV.

3.1.2 Optics and monitoring system

The general layout of the ID20 optics hutch represented in Fig. 3.1 consists of a double crystal Si(111) monochromator embedded between two vertically focusing mirrors, in a vertical scattering geometry. The ultra high vacuum section runs from the front end to the Be window in the experimental hutch, managing pressures in the 10^{-9}-10^{-10} mbar range.

The two mirrors are designed for high-order harmonic rejection and to provide longitudinal focusing over the energy range 3.5-25 keV. Both are made from 1m-long silicon slabs and contain two different reflecting surfaces: pure silicon and a 600 Å thick rhodium coating to be used above 12 keV. The two mirrors are positioned, respectively, before and after the monochromator; they are oriented in such a way to keep the trajectory of the beam horizontally undeflected and, when combined together, to keep it also vertically conserved.

The monochromator is made by a double-crystal Si(111) cooled by liquid nitrogen. The second crystal is mounted on a bender for tunable sagittal focusing. The energy is chosen by selecting the incidence angle between the radiation and the Si single crystal, thus assuring that only the portion of the polycromatic beam characterized by the appropriate frequency is diffracted. Two surfaces are necessary to keep the propagation direction of the beam conserved.

The attenuators are designed to control the intensity of the incident beam. They are foils of pure Al, Cu and Pb, several of which can be appropriately combined to achieve the required attenuation factor, depending on the energy of the radiation.

The monitoring system consists of several thin Kapton foils, located after each set of alignment slits, which scatter a small fraction of the beam towards a lateral detector. The values collected by the monitors can be used for normalisation of the intensities measured by the detector, by taking into account that the monitoring system is only sensitive to the horizontally polarised portion of the beam.

3.1.3 Diffractometer and sample space

The Huber six-circle diffractometer (3.2-c) is configured for horizontal or quasi-horizontal scattering geometries, and is designed to carry heavy load such as the cryostat or the cryomagnet. It is built from materials that are not affected by magnetic fields.

When the application of magnetic field is not needed, the cryogenic equipment employed for low temperatures is the Orange cryostat shown in Fig. 3.2-a, which can reach the lowest temperature of 1.55 K with a cooling power of about 20 mW by forcing the He evaporation with a pumping stage on the tail. It can be mounted only in horizontal geometry, as it cannot be inclined more than $\pm 5°$. The Be windows limit the inclination of an oblique scattering plane to an angle of $\sim \pm 7°$ for the detector arm.

The Oxford superconducting magnet shown in Fig. 3.2-b realises a vertical field of up to 10 T with a very wide accessible angle in the horizontal plane. The homogeneity of the field in the sample

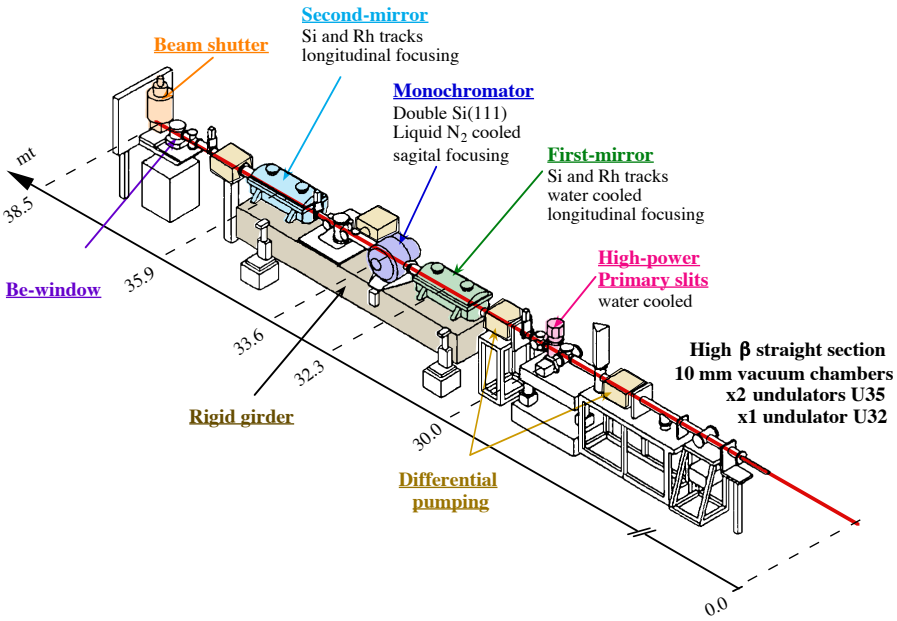

Figure 3.1: Sketch of the Optics section at ID20 [52].

zone extends over $\sim$ 1 cm^3. The opening angle in the vertical direction is $\sim \pm 5°$. The magnet cold bore has an internal diameter of 50 mm at the sample space, allowing very large sample sticks to be accommodated. The magnet is equipped with Variable Temperature Insert (VTI) standard Oxford cryostat, capable of a 2-300 K temperature range at the sample position. The cooling power is obtained by spilling part of the liquid He from the main magnet reservoir and evaporating it in the exchanger zone (solid Cu block) under forced low pressure atmosphere.

The sample space is realised as a separated chamber filled with exchange gas and in thermal contact via conduction with the exchanger. A pressure gauge permanently controls the sample space to avoid air contamination.

The electric field stick (Fig. 3.2-d) has been entirely designed at ID20. It is composed by a-magnetic materials and can be vertically inserted within the sample space of the Orange cryostat and the cryomagnet. The sample is glued between two copper electrodes by conducting silver paint. The electrodes are connected to an external power supply which can apply an electric voltage up to 3 kV. This configuration allows to obtain a rather homogeneous in-situ electric field. The application of voltage $>$ 1 kV may require the removal of the exchange gas in the sample space in order to prevent discharges.

3.1.4 Detector

The detection device (located after the polarisation analysis setup) is a Silicon Avalanche Photo-Diode (APD), ESRF design. The detection chain is constituted by a single module (ACE) both providing the detecting head (APD) with power supply and treating the preamplified detected signal (discrimination and counting stages). In case of high magnetic field measurement, the APD is currently the unique available detector on ID20.

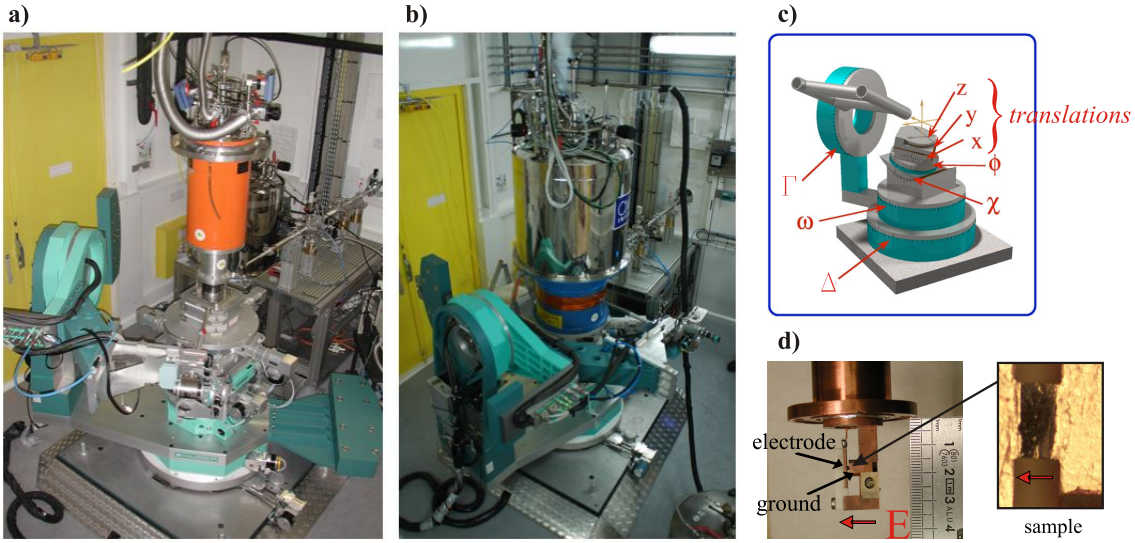

Figure 3.2: Experimental setup: the sample is inserted in the Orange cryostat (a) or the 10 T magnet (b); both can be placed on top of the six-circle diffractometer (c). The sample is mounted between two copper electrodes (d) by means of a stick that can be inserted within the sample space of the cryostat.

3.1.5 Polarisation analyser

The polarisation analyser (PA) setup consists of a single crystal inserted a small two-circle diffractometer mounted on the detector arm, as sketched in Fig. 3.3. This section is fully under vacuum to avoid air absorption along the diffracted light path. The crystal intercepts the diffracted beam and is set to satisfy the Bragg condition for elastic diffraction. This prevents sample fluorescence and other spurious signals coming from the sample environment to enter the detection chain, located at the PA exit, and increases the 2θ angular resolution. However, the main purpose of the analyser setup is to act as a polarisation filter. Only the portion of the beam linearly polarised along a given direction is allowed to pass. The filtering is realised by choosing a suitable crystal that fulfills the diffraction condition for $\theta \approx 45°$ at the current energy. This fact limits the use of any crystal to a narrow energy band, so that a complete collection of crystals is necessary to suitably cover a wide energy range. High quality single crystals with a high reflectivity and narrow rocking curve are needed, to enhance as much as possible the resolution by limiting the angular acceptance. The Jones matrix in such a case, in the reference system associated to the scattering plane of the analyser, is the canonical matrix from Thomson diffraction with $\theta = 45°$:

$$\mathcal{A}_{det} = \mathcal{A}_0 \begin{bmatrix} 1 & 0 \\ 0 & 0 \end{bmatrix},$$

and the corresponding Mueller matrix is:

$$\mathcal{M}_{det} = \mathcal{A}_0^2/2 \begin{bmatrix} 1 & 1 & 0 & 0 \\ 1 & 1 & 0 & 0 \\ 0 & 0 & 0 & 0 \\ 0 & 0 & 0 & 0 \end{bmatrix}. \tag{3.1}$$

These matrices have to be reformulated in relation to the scattering plane of the sample. The analyser setup is mechanically enabled to rotate about an axis coincident with the diffracted beam

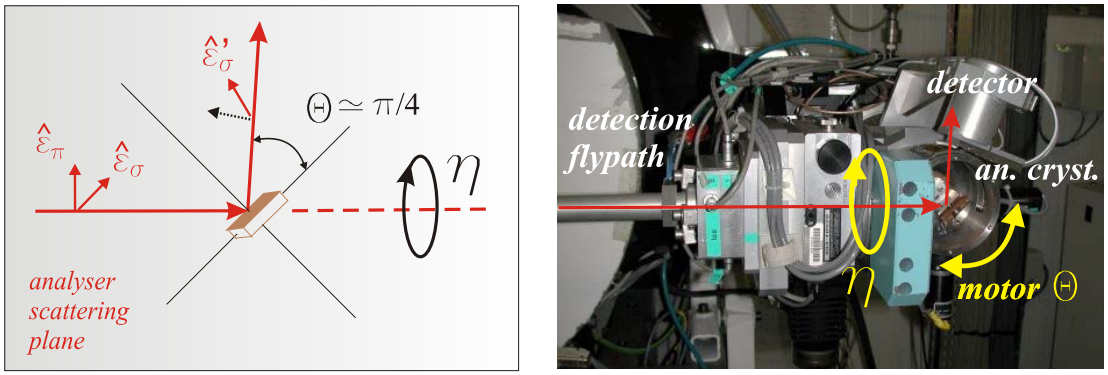

Figure 3.3: Polarisation Analyser. The scattering plane of the analyser is determined by the position of the motor η. The motor θ controls the scattering angle, which at the energy of interest must be close to 45°.

($\mathbf{k}'$); η is the angle associated to this rotation. The zero of the angle η corresponds to the configuration in which the scattering plane of the sample and the one of the analyser coincide. Note that this definition is not always matched in the experimental procedure when the sample scattering plane is oblique: for the sake of simplicity, in those cases the zero of the η motor is associated to a horizontal plane, and some corrections must be taken into account in the data analysis. This aspect will be covered in 3.1.7; in this subsection it is supposed that the ideal definition is being correctly employed.

The Mueller matrix assiciated to the scattering plane of the sample is:

$$\mathcal{M}'_{det} = \mathcal{A}_0^2/2 \begin{bmatrix} 1 & 1 & 0 & 0 \\ 1 & 1 & 0 & 0 \\ 0 & 0 & 0 & 0 \\ 0 & 0 & 0 & 0 \end{bmatrix} \begin{bmatrix} 1 & 0 & 0 & 0 \\ 0 & \cos 2\eta & \sin 2\eta & 0 \\ 0 & -\sin 2\eta & \cos 2\eta & 0 \\ 0 & 0 & 0 & 1 \end{bmatrix} =$$

$$= \mathcal{A}_0^2/2 \begin{bmatrix} 1 & \cos 2\eta & \sin 2\eta & 0 \\ 1 & \cos 2\eta & \sin 2\eta & 0 \\ 0 & 0 & 0 & 0 \\ 0 & 0 & 0 & 0 \end{bmatrix}.$$

A generic beam

$$\mathbf{S} = \begin{bmatrix} S_0 \\ S_1 \\ S_2 \\ S_3 \end{bmatrix} = \begin{bmatrix} I \\ I\ P_1 \\ I\ P_2 \\ I\ P_3 \end{bmatrix}$$

upon being filtered by the analyser set at a certain angle η, gives rise to the measured intensity

$$I_{meas} = \mathcal{A}_0^2 \frac{I}{2} [\ 1 + P_1 \cos 2\eta + P_2 \sin 2\eta\ ]. \tag{3.2}$$

In principle, it would be possible to determine P_1 and P_2 from two pairs of measurements at $\eta = 0°$, $\eta = 90°$ and $\eta = 45°$, $\eta = -45°$, where only one of the two parameters contributes to the measured intensity:

$$P_1 \;=\; \frac{I_{meas}(0°) - I_{meas}(90°)}{I_{meas}(0°) + I_{meas}(90°)}, \tag{3.3}$$

$$P_2 \;=\; \frac{I_{meas}(45°) - I_{meas}(-45°)}{I_{meas}(45°) + I_{meas}(-45°)}. \tag{3.4}$$

However, a more accurate method consists in extracting the integrated intensities from a series of rocking curves of the analyser crystal at 6 - 10 different positions of the angle η, ranging from 0 to 2π, and in fitting them with the equation above (Stokes scan). The Stokes dependence obtained from different degrees of polarisation of the beam is shown and explained in Fig. 3.4 - (c).

An equivalent expression for the Stokes scan highlighting the degree of total linear polarisation P' is

$$I_{meas} \;=\; \mathcal{A}_0^2 \, \frac{I}{2} \; [\; 1 \;+\; P' \cos 2(\eta - \eta_0) \;] \tag{3.5}$$

where η_0 identifies the direction of the strongest linear contribution (the main axis in the case of an elliptical beam). Note that the degree of circular polarisation, P_3, and the degree of unpolarised beam, P_4, are not distinguishable in this analysis, and only their sum can be extracted.

3.1.6 Phase plate

The phase plate device

The optical elements employed to change the polarisation of an electromagnetic wave are known as retarders. They are also referred to as phase plates, since this is the most common implementation of such a device. A retarder identifies, in the plane perpendicular to the propagation of the beam, two orthogonal axes (say $\hat{\mathbf{a}}$ and $\hat{\mathbf{b}}$). They can be distinguished by an anisotropic configuration with respect to the beam, or by an intrinsic anisotropy in the material of the device itself. In any case, the incoming beam can be projected onto the basis defined by two linear polarised states along $\hat{\mathbf{a}}$ and $\hat{\mathbf{b}}$. One of the two states is somehow caused to have its phase lag behind that of the other by a predetermined amount; thus, upon emerging from the retarder, the relative phase of the two components is different than it was initially. This changes the total polarisation of the beam.

Since the polarisation of the beam emerging from the synchrotron source is $> 99\%$ pure and its conversion to a circular state does not introduce a significant degree of depolarisation (see below), the Jones description will be employed. Consider ($\hat{\mathbf{a}}$,$\hat{\mathbf{b}}$) to be the characteristic axes of the phase plate. In the general case, a transmission-type phase plate is described by the Jones matrix

$$\mathcal{A}_{pp} \;=\; \begin{bmatrix} t_a & 0 \\ 0 & t_b e^{i\Delta\alpha} \end{bmatrix}. \tag{3.6}$$

The real parameters t_a, t_b represent the absolute transmissions, and the polarisation of the transmitted beam is changed by the relative phase shift $\Delta\alpha$ between the two components. In many practical cases dichroism does not occur, so that it can be assumed $t_a \sim t_b = t$.

Let ($\hat{\mathbf{x}}$,$\hat{\mathbf{y}}$) be a convenient frame in which the polarisation of the incident beam is described. In the case of a synchrotron source, $\hat{\mathbf{x}}$ is the horizontal direction, and $\hat{\mathbf{y}}$ the vertical one. In the general case the axes ($\hat{\mathbf{x}}$,$\hat{\mathbf{y}}$) are rotated, with respect to ($\hat{\mathbf{a}}$,$\hat{\mathbf{b}}$), by a certain angle χ. The beam emerging

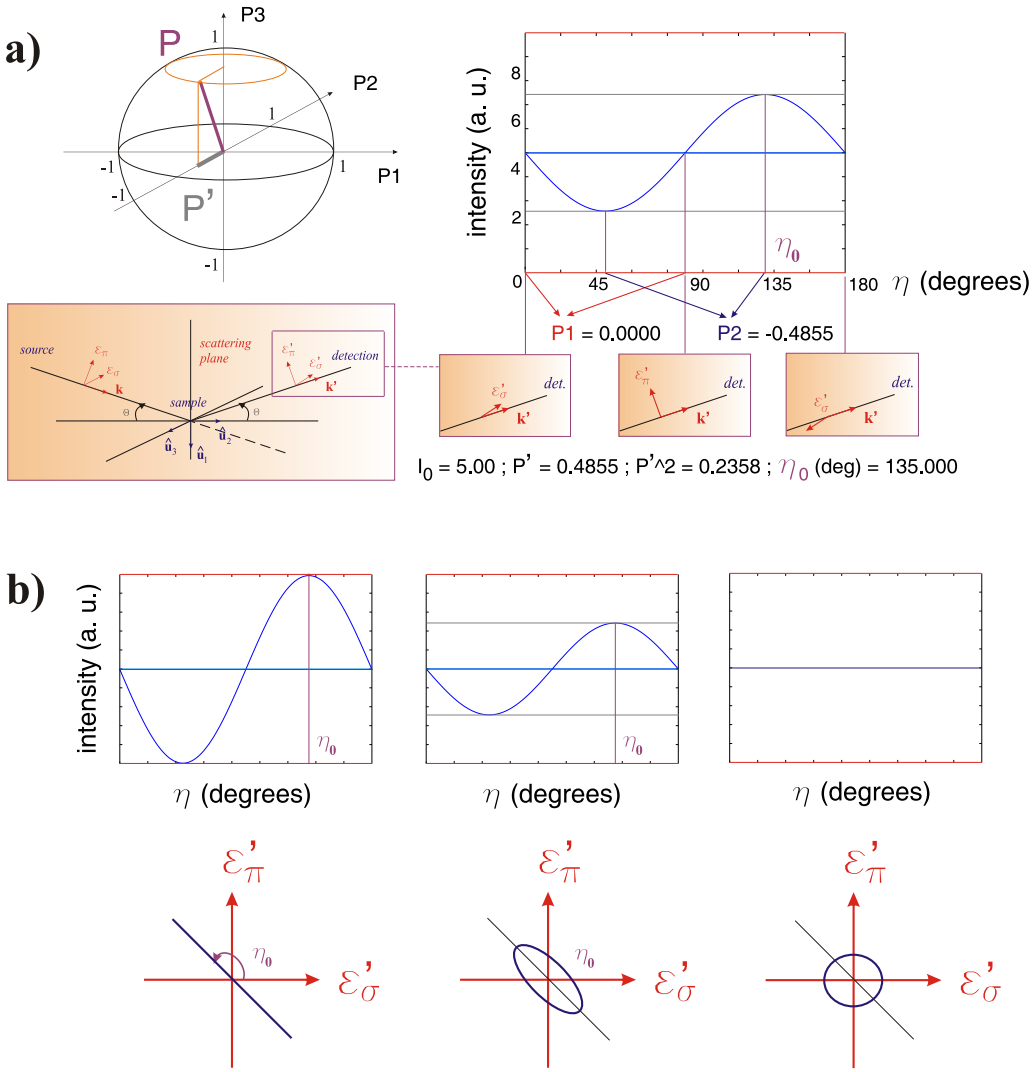

Figure 3.4: (a) Example of a Stokes scan for an elliptically polarised beam. In the parameters' space, the vector $\mathbf{P} = [P_1, P_2, P_3]$ represents the polarised fraction, while $\mathbf{P'} = [P_1, P_2]$ represents the linearly polarised fraction. The Stokes scan allows the extrapolation of both P_1 and P_2. The angle η_0 defines the direction of main axis of the ellipse. (b) Examples of Stokes scans for a linearly, elliptically, circularly polarised beam. In the last case, no preferential direction (η_0) is found.

from the source in the ($\hat{\mathbf{x}}$,$\hat{\mathbf{y}}$) frame is

$$\mathbf{E}_i \;=\; E_0 \begin{bmatrix} 1 \\ 0 \end{bmatrix}$$

and, in the phase plate frame ($\hat{\mathbf{a}}$,$\hat{\mathbf{b}}$),

$$\mathbf{E}_i \;=\; \begin{bmatrix} \cos\chi & -\sin\chi \\ \sin\chi & \cos\chi \end{bmatrix} E_0 \begin{bmatrix} 1 \\ 0 \end{bmatrix} \;=\; E_0 \begin{bmatrix} \cos\chi \\ \sin\chi \end{bmatrix}.$$

In the case of a quarter wave plate, designed in such a way that the relative phase shift is $\Delta\alpha = \pm\pi/2$, the transfer matrix in the frame ($\hat{\mathbf{a}}$,$\hat{\mathbf{b}}$) is (cf. Eq. 3.6):

$$\mathcal{A}_{pp}\;(\Delta\alpha = \pm\pi/2) \;=\; t \begin{bmatrix} 1 & 0 \\ 0 & \pm i \end{bmatrix}. \tag{3.7}$$

When the plate is oriented at $\chi = 45°$, the incident beam is expressed in the frame $(\hat{\mathbf{a}},\hat{\mathbf{b}})$ as

$$\mathbf{E}_i \;=\; \frac{1}{\sqrt{2}}\, E_0 \begin{bmatrix} 1 \\ 1 \end{bmatrix}$$

and is split by the plate in two equal projections, delayed each other by $\pm\pi/2$, so that the transmitted beam is circularly left/right polarised:

$$\mathbf{E}_f \;=\; \mathcal{A}_{pp}\,(\Delta\alpha = \pm\pi/2)\;\mathbf{E}_i \;=\; \frac{1}{\sqrt{2}}\, E_0 \begin{bmatrix} 1 \\ \pm i \end{bmatrix}.$$

Implementation of a phase plate device for X-rays

This subsection deals with a practical realization of the retarder device described so far, operating at X-ray frequencies. The dynamical theory of X-ray diffraction covers the complete analysis of multiple-scattering in perfect crystals, predicting its polarisation effects near the Bragg condition. These phenomena are well understood theoretically and have been observed experimentally; nevertheless, until recently, there were few or no practical applications, as they are observed only in near-perfect crystals and under stringent conditions of beam divergence and monochromaticy. The X-ray phase plate is in fact one application of this theory ([53] - [59]). At third generation synchrotron sources, this transmission-type phase plate offers many advantages over other methods for changing the polarisation of the light. Since it does not alter the beam direction, an X-ray phase plate can be designed as a compact optics module, easily inserted into and removed from the beam path of the beamline. The requirements of linear incident polarisation and very high collimation are perfectly matched by the undulator sources commonly employed at these institutions.

An X-ray phase plate consists of a perfect crystal cut to form a thin foil, introduced in the path of the beam and oriented in such a way that one reflection condition is almost satisfied, unless for a small shift from the exact direction required for the Bragg angle θ_B. In such a situation, the device scatters a small fraction of the beam away from its trajectory (as the peak's condition is not perfectly fulfilled), and also modifies the polarisation of the transmitting beam. Two specific crystallographic directions can be identified within the crystal giving rise to a relative phase shift $\Delta\alpha$ for the beam passing through the device:

$$\Delta\alpha \;=\; -\frac{\pi}{2}\left[\frac{r_e^2\; F_h\; F_{\bar{h}}\; \lambda^3\; \sin 2\theta_B}{\pi^2\; V^2\; \Delta\theta_B}\right] d \tag{3.8}$$

where F_h is the structure factor, r_e the classical electron radius, V the unit cell volume, λ the X-ray wave length, θ_B the Bragg angle, and d the thickness of the crystal. $\Delta\theta_B$ represents the misalignment relative to the Bragg condition. Any desired $\Delta\alpha$ can be obtained by modulating the orientation of the crystal ($\Delta\theta_B$). It is desirable to employ thin crystals, and to select a crystal with a large structure factor per unit volume (F_h/V), small mosaicity, and low X-ray absorption. High quality diamond crystals perfectly fulfill all these requirements.

Alignment of the phase plate and characterisation of the beam

At ID20, the experimental setup for the polarisation control of the incident beam is mounted in a vacuum chamber, equipped with a double phase plate diffractometer. The use of two phase plates

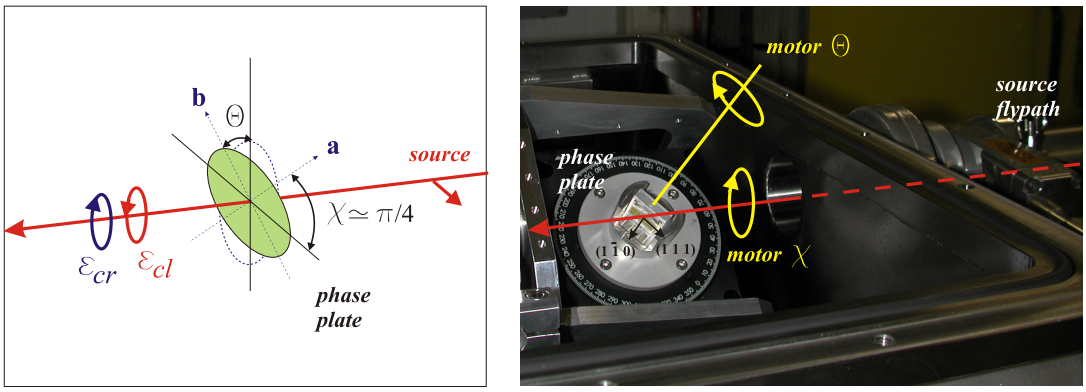

Figure 3.5: Phase plate setup. The in-vacuum chamber contains a two-circle diffractometer, equipped with motors χ (set to be $\approx 45°$) and θ (scattering angle around the (1 1 1)-type reflections).

enables us to correct some of the aberration effects due to the divergence of the beam and its energy spread. When a linear rotated polarisation is needed, the polarisation rate is remarkably higher in comparison to a system with only a single retarder [60, 61]. However, when the plate is being employed as a lambda-quarter retarder in order to obtain a circularly polarised light, the introduction of an unpolarised contribution is minimised and one retarder is sufficient to obtain a degree of circular polarisation typically $> 98\%$. The depolarisation effects caused by the imperfect collimation and the achromaticity are further reduced by increasing the thickness of the phase plate. Various plates of different thicknesses are available at ID20, the appropriate choice for each energy being made to ensure good performances without excessive absorption of the beam. The measurements on $TbMnO_3$ and $Ni_3V_2O_8$ have been carried out at non resonant energy E $\approx$ 7.45 keV, where one single plate 1.2 mm thick was able to reach the degree of circular polarisation stated above.

The diamond plates have polished (1 1 0) faces. They are aligned in the sample holder so that the (1 1 1)-type reflections are easily attainable, these being the ones that give the best results in terms of producing a relevant phase shift $\Delta\alpha$ as per Eq. 3.8, since they possess the biggest value for the structure factor F_h (cf. Eq. 3.8). The chamber is equipped with a small two-circle diffractometer that controls the alignment of the plate axes (**a**,**b**) with respect to the beam (motor χ), and the diffraction angle (motor θ) of the (1 1 1)-type reflections. The alignment procedure must be undertaken quite carefully, as misalignments from the ideal position, coupled with the small changes of the beam direction that may occur in the time span of a few hours, can cause significant degradation of the performances.

The motors χ and θ are optimised in the two positions necessary to obtain circular right and circular left polaristions. The effectiveness of the plate is monitored by placing the detection flypath straight in line with the incident beam and setting the analyser to allow the horizontally polarised component to be detected. This operation can be done at any moment during the experiment, since the six-circle diffractometer is equipped with translation motors that allow the sample to be moved out of the way. When the χ motor is set at 45°, and the θ motor is scanned around the Bragg value of the reflection (1 1 1), the measured intensity exhibits the dependence shown in Fig. 3.6. The horizontal polarisation of the beam is untouched for values of θ sufficiently far from the

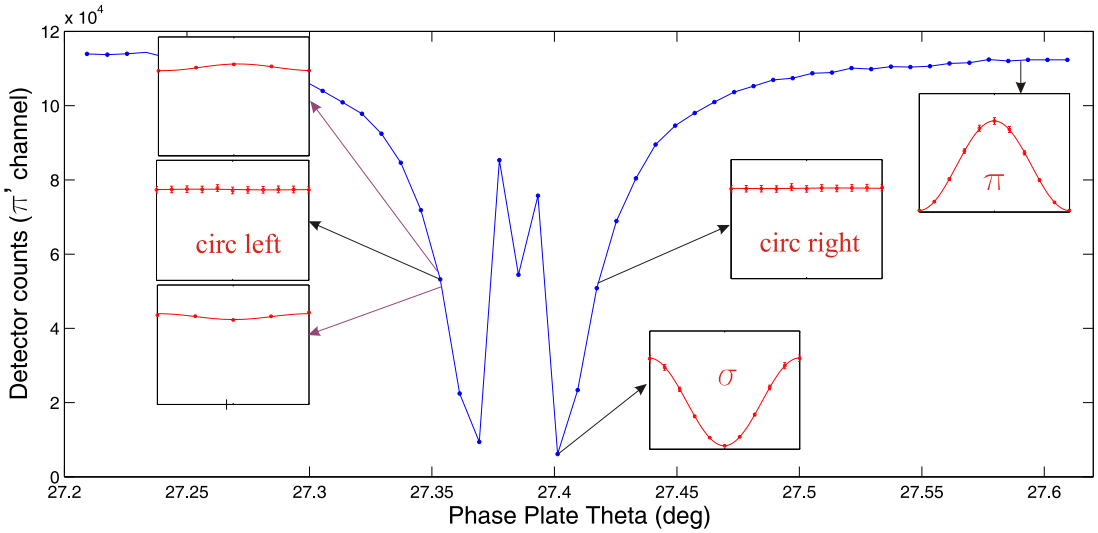

Figure 3.6: Phase plate alignment. The blue curve is collected as the angle θ of the phase plate varies around the diffraction position of the (1 1 1) reflection. The detection setup is configured to select the horizontally polarised fraction of the transmitted beam. The red curves represent the Stokes scans obtained by rotating the detection setup by 180° at various fixed values of θ. The positions of θ which generate vertically polarised light and circular light are highlighted (note the effects of a small misalignment with respect to the correct position).

reflection ($\approx 0.2°$), as the retarder-induced phase shift $\Delta\alpha$ tends to zero; upon approaching θ_B, a vertically polarised component appears and the beam becomes more and more elliptical, passing through a state of circular polarisation when $\Delta\alpha = \pi/2$ and reaching a purely linear vertical state when $\Delta\alpha = \pi$. Furhter progressing towards θ_B produces a mixed polarisation state thet cannot be reliably detected. This behaviour is mirrored symmetrically as θ_B is approached from bigger values of θ or from smaller ones, but the sign of $\Delta\alpha$ is opposite (cf. Eq. 3.8), and thus the handedness of the induced ellpitical polarisation is reversed.

The optimisation of the motor χ around the 45° position is done only once at the beginning of the experiment. This is best achieved by positioning the plate in the σ position (minimum of the curve) and performing there a Stokes scan to make sure that no emerging P_2 is obtained. If this is not the case, the motor χ must be corrected by the amount $\Delta\chi = -\arctan(P_2/P_1)/4$. Once this condition is met, χ is left unchanged for the whole experiment and no P_2 should arise in the emerging beam for any value of θ.

The alignment of θ must be checked several times during the experimental session. After placing the plate in the theoretical position, any misalignments result in a value of P_1 different from zero (see Fig. 3.6), which can be corrected by small deplacements of θ. Typically, this kind of check is done before and after any Stokes scan performed on a magnetic reflection of the sample.

3.1.7 Geometrical corrections

So far the polarisation of the incident and diffracted beam has been described alternatively in an external reference frame (horizontal and vertical directions) or in a frame adapted to the scattering

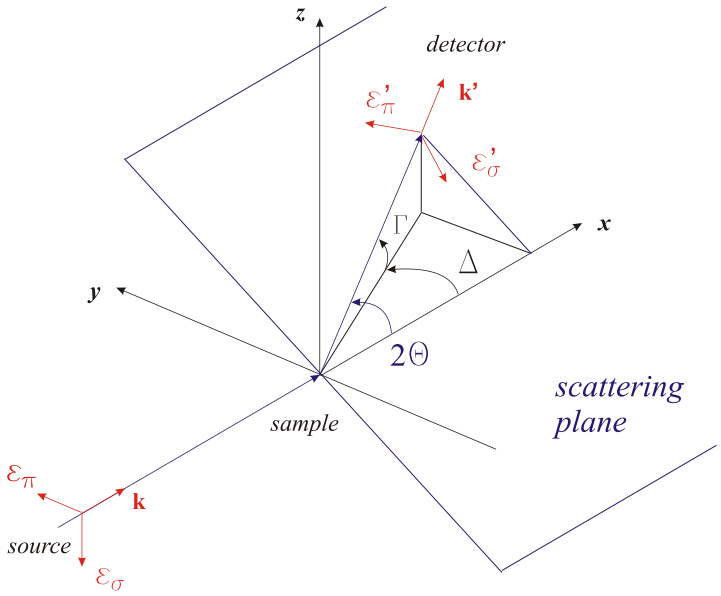

Figure 3.7: Oblique scattering plane. The directions identified as σ,π and σ',π' by the zeroes of the motors in the experimental setup (depicted in red) are only accurate in the case of a perfectly horizontal plane.

plane of the sample (σ/σ' and π/π'). The former is clearly useful to describe the polarisation in terms of the position of the analyser setup and of the phase plate setup, while the latter is used to determine the polarisation dependence of the magnetic diffraction from the sample. When the scattering plane is perfectly horizontal, the matching between the frames is trivial, σ/σ' being coincident with the vertical direction and π/π' with the horizontal one. This is in fact the convention adopted in setting the zero positions for the motors of the analyser and the phase plate. However, when the scattering plane is oblique, the directions defined by the motors and depicted in Fig. 3.7 may be off by several degrees, and the following corrections must be made in analysing the data.

In the figure, the external laboratory frame ($\hat{\mathbf{x}}$,$\hat{\mathbf{y}}$,$\hat{\mathbf{z}}$) provides a definition of the horizontal and vertical direction. The scattering plane is spanned by the vectors ($\mathbf{k}$,$\mathbf{k}'$); $\mathbf{k}$ being fixed with respect to the external frame, the inclination of the plane is ultimately determined by the motors Δ and Γ of the detection arm, set to satisfy the Bragg condition:

$$\cos 2\theta = \cos\Delta\cos\Gamma.$$

As for the polarisation of the incident beam (Fig. 3.8), the angle ξ between the frame defined by the motors and the corrected frame is given by

$$\tan\xi = \frac{\sin\Gamma}{\cos\Gamma\sin\Delta} \qquad \xi \in [-\pi/2, \pi/2].$$

For the polarisation of the diffracted beam (Fig. 3.9), the correction angle is found to be

$$\tan\zeta = \frac{\sin\Gamma\cos\Delta}{\sin\Delta} \qquad \zeta \in [-\pi, \pi].$$

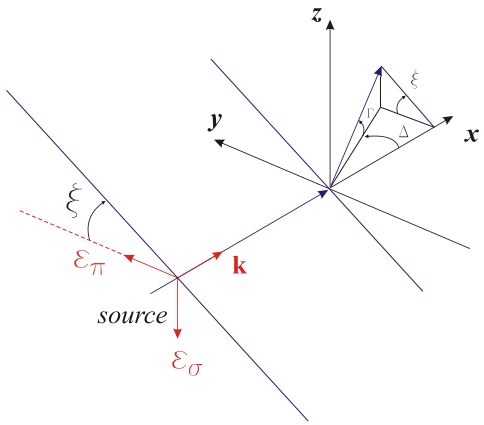

Figure 3.8: Geometrical correction in the polarisation of the incident beam. The angle ξ represents the shift between the directions defined by the motors (in red) and the ones defined by the scattering plane.

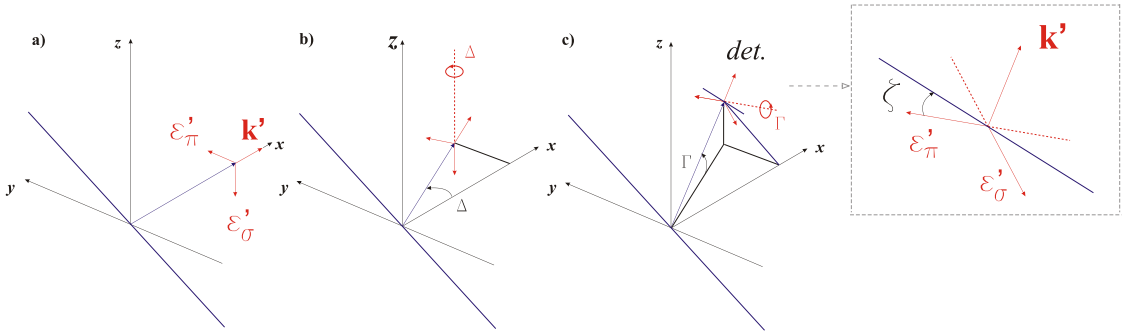

Figure 3.9: Geometrical correction in the polarisation of the scattered beam. The position of the detection system is defined by two successive rotations of the motor Δ (a)-(b) and Γ (c). The directions defined by the motors of the polarisation analyser (in red) turn out to be shifted by ζ from the directions defined by the scattering plane (c).

3.2 Numerical calculations

In the course of this work it became apparent that there was a need for a simulation program able to calculate the expected intensity of the Stokes scans for an arbitrary magnetic structure, polarisation of the incident beam and geometrical configuration, in order to fit the data and obtain real time indications during the experimental sessions. This application was elaborated by making use of the Matlab software package.

The program accepts as input: the details of the magnetic structure (the spin and orbital moment per atom, given as the magnitude and phase of the magnetic modulation, for each component along the crystallographic axes); the energy of the light; the indexes of the magnetic reflection; the incident polarisation state; the supposed domain population in the volume of the crystal illuminated by the beam. It returns the expected $I(\eta)$, taking into account the exact scattering geometry of the six-circle setup, including the azimuthal configuration (rotation of the sample about the scattering vector) and the deviation from a perfectly horizontal scattering plane.

This calculation is carried out in three stages. First, the magnetic structure factor is constructed on the basis of the magnetic moment associated with each atom in the cell. Secondly, the scattering

amplitude is found by projecting both the magnetic vectors and the polarisation vectors in the same reference frame $\{\hat{\mathbf{u}}_1, \hat{\mathbf{u}}_2, \hat{\mathbf{u}}_3\}$. A separate calculation is done at this point, taking into account the configuration of the motors of the diffractometer, to extract the azimuthal angle and the corrections due to the orientation of the scattering plane with respect to the incident and scattered beams. Finally, the intensity $I(\eta)$ and the Stokes parameters are given as output, either in resonant or non resonant regime, depending on the energy of the radiation. The evolution of the Stokes parameters as a function of the domain population is also calculated. The matching of the reference frames done by the program is sketched in Fig. 3.10.

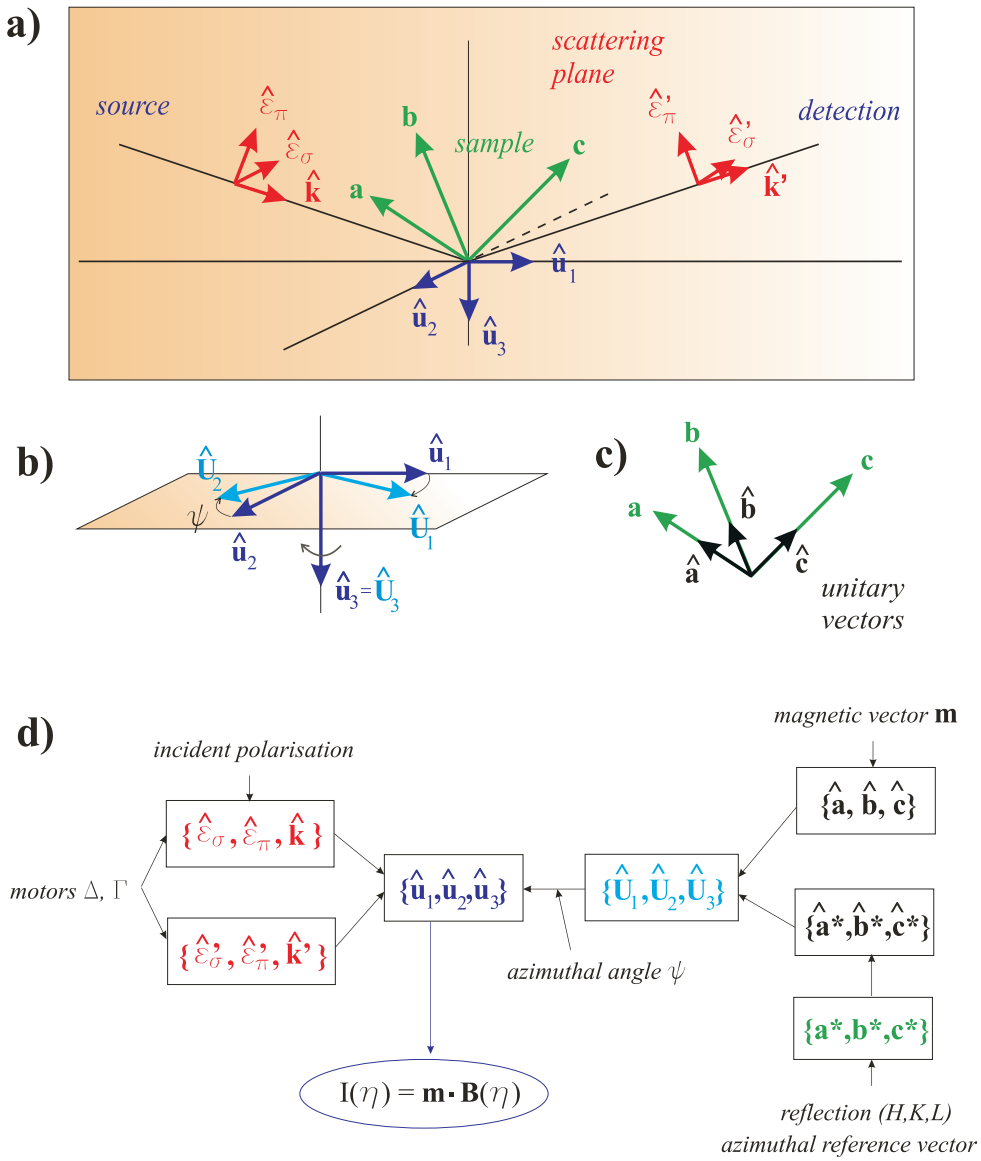

Figure 3.10: Matching of the reference frames performed by the Matlab program described in the text. (a) The frames associated to the incident and diffracted beam $\{\hat{\epsilon_\sigma}, \hat{\epsilon_\pi}, \hat{\mathbf{k}}\}$ and $\{\hat{\epsilon'_\sigma}, \hat{\epsilon'_\pi}, \hat{\mathbf{k}'}\}$, to the scattering geometry $\{\hat{\mathbf{u}}_1, \hat{\mathbf{u}}_2, \hat{\mathbf{u}}_3\}$, and to the crystallographic axes $\{\mathbf{a},\mathbf{b},\mathbf{c}\}$. (b) The azimuthal angle ψ is used to define the rotation of the frame with respect to the reference of choice. (c) An orthonormalised version of the crystallographic frame $\{\hat{\mathbf{a}},\hat{\mathbf{b}},\hat{\mathbf{c}}\}$ is employed for the description of the magnetic modulation. (d) The input values as accepted by the program in the various frames and their transformation (the magnetic moments indicated as $\mathbf{m}$ are given in their spin $\mathbf{S}$ and orbital $\mathbf{L}$ contribution). All the vectors are converted into the $\{\hat{\mathbf{u}}_1, \hat{\mathbf{u}}_2, \hat{\mathbf{u}}_3\}$ frame, where the magnetic scattering intensity $I(\eta)$ is calculated.

Chapter 4

Imaging of Multiferroic Domains in $Ni_3V_2O_8$

The magnetic structure of $Ni_3V_2O_8$ has been investigated using non-resonant X-ray magnetic scattering. Incident circularly polarised X-rays combined with full polarisation analysis of the diffracted beam have been shown to yield high sensitivity to the components of the cycloidal magnetic order, including their relative phases. New information on the magnetic structure was obtained, where it is found that the magnetic moments on the "cross-tie" sites are negligible relative to those on the "spine" sites. This implies that the onset of ferroelectricity is associated mainly with spine site magnetic order. It is furthermore demonstrated that the technique enables the imaging of multiferroic domains through polarisation enhanced topography. This approach was used to image the domains as the sample is cycled by an electric field through its hysteresis loop, revealing the gradual switching of domains without nucleation.

4.1 Refinement of the Magnetic Structure

4.1.1 Phase diagram of multiferroic $Ni_3V_2O_8$

$Ni_3V_2O_8$ is a magnetic insulator with a structure of *Cmca* orthorhombic symmetry (space group No. 64 in the International Tables for Crystallography [62]), characterised by planes of Ni^{2+} $S = 1$ spins arranged on a buckled kagomé staircase, resulting in two inequivalent Ni sites: cross-tie and spine type, as shown in Fig. 4.1 [63, 10]. While the ideal kagomé lattice is the canonical example of a frustrated system, the deviation from this geometry in $Ni_3V_2O_8$ leads to additional interactions relieving the frustration and producing the rich magnetic phase diagram reported in Fig. 4.2 [64, 26, 10]. At $T_{HL} = 6.3$ K a mainly longitudinal incommensurate phase arises, denoted as the high temperature incommensurate (HTI) phase; the spins on the spine sites are nearly oriented along the **a** axis and sinusoidally modulated along the same direction with a wavevector (δ 0 0), $\delta \approx 0.27$, while no significant ordering is observed on the cross-tie sites. Between $T_{LC} = 4$ K and T_{HL}, in the low temperature incommensurate (LTI) phase, the spins on both site types have been reported to be arranged in a cycloid in the $(\mathbf{a}, \mathbf{b})$ plane with similar propagation vector δ, breaking spatial

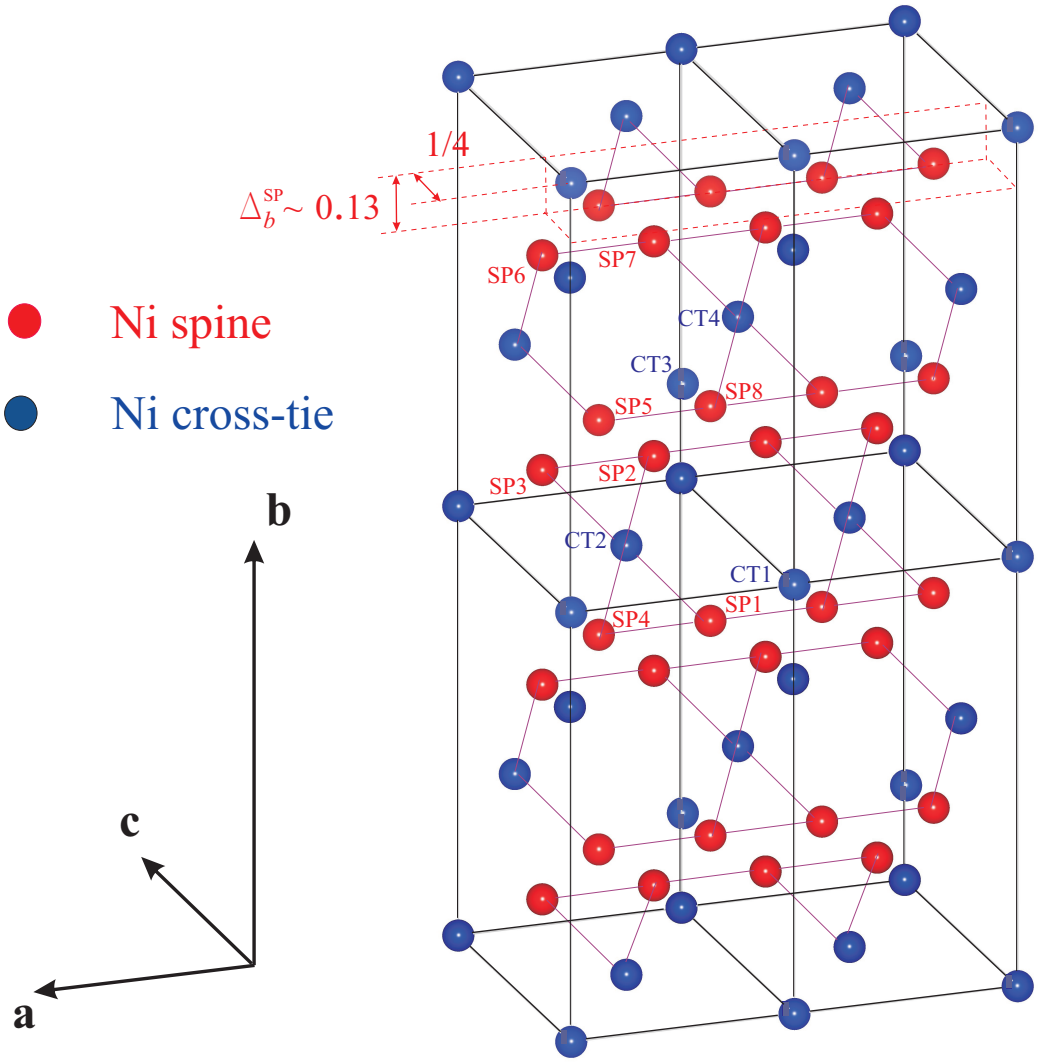

Figure 4.1: Positions in the unit cell for the two inequivalent crystallographic sites (spine and cross-tie) of the nickel ions. Black lines indicate the *Cmca* unit cell, while purple lines connect atoms belonging to the same layer of the buckled staircase structure. The atomic sites are labeled according to the coordinates given in 4.1.3.

inversion symmetry. It is in this phase that a spontaneous electric polarisation develops parallel to the **b** axis [26]. The magnetic structure in the LTI phase as derived from the neutron diffraction studies [10, 13] will be shown in detail in 4.1.3. It should be noted that in these studies it was not possible to uniquely determine the phase relationship between the two sites. Recent polarised neutron diffraction measurements performed in an applied electric field have demonstrated that the handedness of the cycloidal order can be switched by reversing the direction of the field, although no information on the spatial distribution of domains was obtained [13].

The complex phase diagram is explained in the work by Kenzelmann et al. [10] by a simplified model Hamiltonian. The average Ni-Ni distance (at 15 K) within the layers is $d_1 = 2.94\mathring{A}$, while

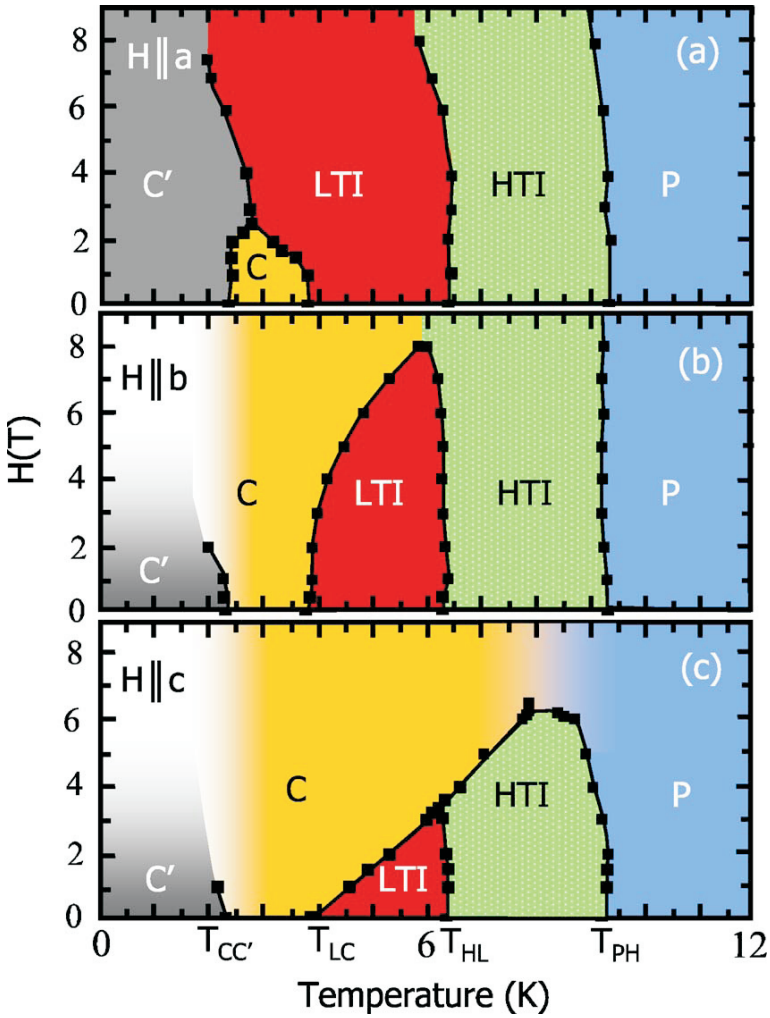

Figure 4.2: H-T phase diagram of $Ni_3V_2O_8$ with H applied along each of the three crystallographic axes [10]. The phases are labeled as follows: P is the paramagnetic magnetically disordered phase; HTI the high-temperature incommensurate phase; LTI the low-temperature incommensurate phase. Two additional phases are present at lower temperature: C (high-temperature canted antiferromagnetic phase), and C' (low-temperature canted antiferromagnetic phase). In the HTI phase the long-range order is mostly on the spine sites with their spins parallel to **a**, while in the LTI phase the spine and cross-tie spins are reported to rotate within the $(\mathbf{a}, \mathbf{b})$ plane. This magnetic ordering generates ferroelectricity, as spontaneous electric polarisation along the **b** axis emerges in the LTI phase [26].

the interlayer distance is $d_2 = 5.69\mathring{A}$. Based on the relatively large interlayer to intralayer ratio, d_2/d_1=1.9, a strong two-dimensional magnetic character may be expected, with the magnetism dominated by intralayer Ni-Ni exchange interactions. Since the Kagome planes in $Ni_3V_2O_8$ are buckled, the symmetry of the superexchange interactions mediated by O ions shows that there are inequivalent paths between neighbouring Ni ions within one Kagome plane. In particular, there is a superexchange path between Ni spine sites along the crystallographic direction **a** (indicated in Fig. 4.3 as J_1 for nearest neighbours and J_2 for next-nearest-neighbours), and a different one between neighbouring spine and cross-tie sites. The Hamiltonian proposed in [10] involves competing nearest-neighbour (NN) and next-nearest-neighbour (NNN) superexchange interactions between spine sites, combined with single ion anisotropy. By means of this model, and considering only the spine sites

for the moment, one can qualitatively understand the onset of a collinear incommensurate magnetic order (HTI phase) as a result of competing NN and NNN nearly-isotropic and antiferromagnetic interactions along the spine chains (**a**), combined with antiferromagnetic coupling along different chains both in the **b** and **c** directions, and with single ion anisotropy (the **a** axis being the easy direction, so that the energy is minimised when the magnetisation lies along it). The argument outlined in the cited work shows that, as the temperature is lowered, the Landau expansion of the free energy at first will have the spins aligned only along the easy axis. As the temperature further decreases, terms of higher order in the expansion of the free energy in the Fourier components of the spins come into play, and they progressively enforce the constraint of fixed spin length, rather than the modulation of spin magnitude present in a collinear sinusoidal structure when moving along the incommensurate propagation direction. This constraint is perfectly satisfied only at zero temperature. To comply with this requirement, and yet still satisfy the incommensurability enforced by the competition between J_1 and J_2, the system develops long-range transverse sinusoidal order, which triggers the transition into a new phase (LTI phase). In this case, the spins rotate along the propagation direction while mantaining an almost fixed magnitude from one ion to the next. In [10], additional terms of anisotropic interaction are then introduced to account for the details of the magnetic structure and, most notably, the apparently large values of the cross-tie spins in the LTI phase. The cross-tie sites have very different local symmetry from the spine sites. Although $Ni_3V_2O_8$ has several magnetic phases, a common feature of all of them is that the couple of spins on the spine sites SP1 and SP2 (cf. Fig. 4.1) have equal but opposite moments, as do the ones in the couple SP3 and SP4; the situation is shown in Fig. 4.3. Thus, within a model of isotropic interactions, the cross-tie spins are subject to zero mean field, i.e., they are frustrated. The apparent large values extracted from neutron diffraction in the LTI phase have been proposed to be due to anisotropic spin interactions between spine and cross-tie sites, both of the Dzyaloshinskii-Moriya type as well as pseudodipolar (i.e. having the same form as dipolar interactions but much larger strength, since arising from a type of superexchange [10]).

4.1.2 Experimental setup and preliminary measurements

The experimental setup consisted of the standard configuration with the Orange cryostat described in 3.1.3. The energy of the beam has been tuned to 7.45 keV, considerably below the nickel K-edge to avoid interference with the resonant signal. The 1.2 mm thick single crystal phase plate has been selected, and a high quality single crystal Au (2 2 2) with mosaic spread of $\approx 0.22°$ has been used as a linear polarisation analyser. The configuration is sketched in Fig. 4.4.

The single crystal of $Ni_3V_2O_8$ belongs to the same batch used by Kenzelmann et al. in [10]; it was grown from a BaO-V_2O_5 flux [64], and cut at the ID20 laboratories in the shape of a plaquette, whose dimensions are 600 μm (along the **b** axis) x 900 μm (**c**). The **a**-face has been polished to be used as the specular face for XRNM Scattering, while the thin thickness along **b** is intended to ease the application of the electric field. Particular attention has been devoted to obtain two parallel **b**-faces. These have then been glued to the electrodes of the electric field stick (described in 3.1.3) by means of conductive silver paint.

A preliminary investigation of the crystal quality has been performed by collecting charge reflec-

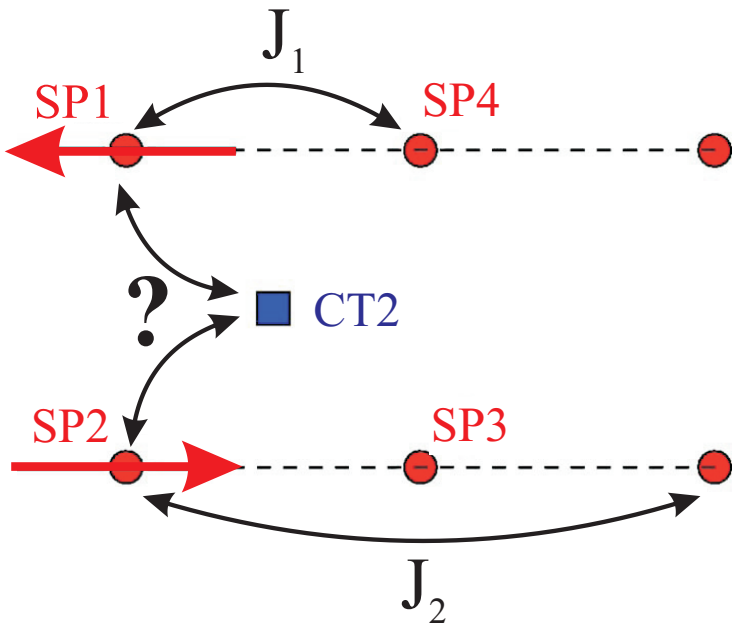

Figure 4.3: Model of isotropic exchange interactions developed by Kenzelmann and co-workers in [10], indicating the frustration of the cross-tie sites. The sketch represents a projection onto the (**a**,**c**) plane of the crystallographic sites indicated in Fig. 4.1; the atomic coordinates are reported in 4.1.3. Here J_1 and J_2 represent nearest-neighbour (NN) and next-nearest-neighbour (NNN) superexchange interactions between spine sites. Since a common feature of all magnetic phases is that sites SP1 and SP2 have opposite spins, the mean field at the cross-tie site (CT2) is zero. Sites SP3 and SP4 also have opposite spins which are not shown because their values relative to SP1 and SP2 are different for different magnetic phases.

tions at T = 4.4 K. The charge diffraction peaks typically present an angular width in the Bragg angle θ of $\approx 0.01°$ (Fig. 4.5). The insertion of the analyser crystal in the detection chain was followed by two alignment scans performed over the rocking angle of the analyser in the two polarisation channels σ' and π', over the direct beam. The ratio between the π' contribution correctly identified by the analyser and the leaked σ' contribution (cross-talk of the analyser) is less than 0.3% (Fig. 4.6). After cooling down to 2.2 K, the magnetic reflection $(5-\delta, 1, 0)$ is aligned (Fig. 4.7). The angular width in the rocking curve of the sample is $\approx 0.01°$, suggesting long-range magnetic order.

However, by comparison of the temperature dependence with the data published in [10], it became apparent that strong beam heating effects were altering the temperature on the sample surface with respect to the values collected by the sensors, and preventing the sample from entering the LTI and the lower temperature commensurate (C) phase (cf. the phase diagram in Fig. 4.2). In particular, the LTI phase is characterised by a narrow temperature range between 4 and 6.3 K, thus requiring a precise and stable control of the cryogenic system. A first approach to this issue had been taken by employing samples whose specular face had been covered with a thin layer of Al, but test measurements demonstrated that the effectiveness of this method was dubious. Instead, it was chosen to reduce the intensity of the incident beam and carefully collect a temperature dependence on magnetic reflection $(5-\delta, 1, 0)$, to make sure the sample was being brought into the correct phase (see Fig. 4.8). At the energy of 7.45 keV, given an incident photon flux of $\approx 10^{13}$ ph/sec and in

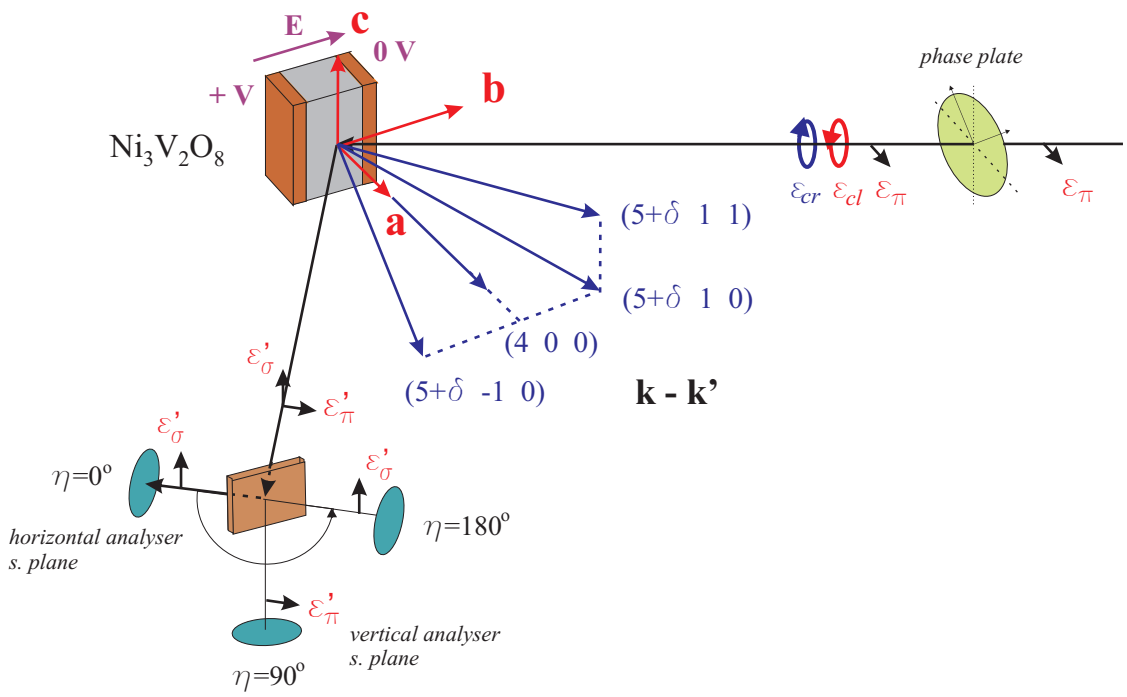

Figure 4.4: Schematic of the experimental setup, including the orientation of the sample with respect to the scattering plane and the applied electric field.

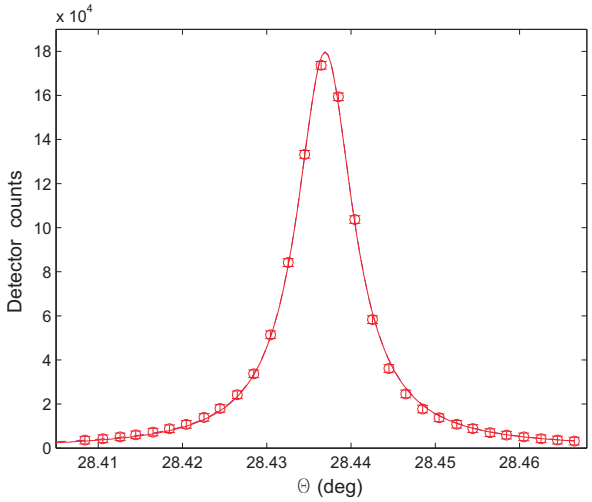

Figure 4.5: Profile of the charge reflection (4 0 0) measured at 4.4 K with no discrimination of the polarisation of the diffracted beam.

spite of the use of ^{4}He exchange gas in the sample space, it was found that the minimum attenuation required for the incident beam was a factor of 5. Figure 4.8 shows the temperature dependence of the reflection $(5-\delta, 1, 0)$ obtained from scans measured in the rotated $\pi - \sigma'$ channel along the reciprocal space $\mathbf{a}^*$ direction. The sharp change seen in the intensity of the scattering at T = 3.2 K, obtained by numerical integration, indicates the transition between the LTC and LTI phases, whilst the discontinuity seen in the evolution of the propagation wave-vector at T = 6.3 K occurs at the transition between the high (HTI) and low temperature incommensurate phases [10]. Hence the LTI

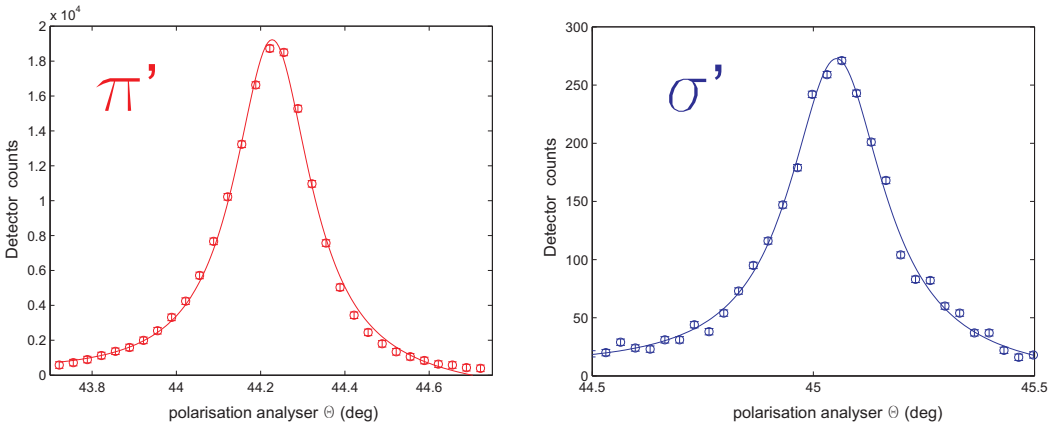

Figure 4.6: Rocking curves of the polarisation analyser in the two polarisation channels $\pi - \pi'$ and $\pi - \sigma'$ (leaked contribution). In the $\pi - \sigma'$ scan the intensity of the incident neam has been enhanced by a factor of ≈ 50 with respect to the $\pi - \pi'$ scan, in order to obtain a reasonable count rate.

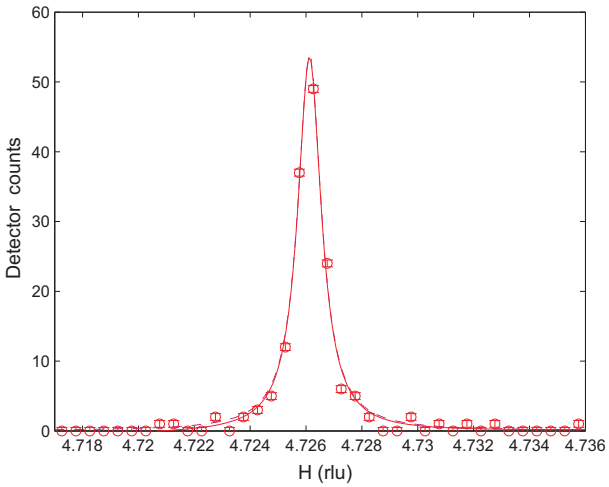

Figure 4.7: Profile of magnetic reflection $(5-\delta, 1, 0)$ along the crystallographic direction $\mathbf{a}^*$, in the polarisation channel $\pi - \sigma'$ (counting time: 30 seconds/point).

phase of interest was clearly defined, and measurements were performed at an optimised temperature. Specific care has been taken during the course of the experiments to avoid thermal instabilities and abrupt changes in the cryogenic system, especially during technical operations such as liquid N_2 and He refill in the Orange cryostat, and the temperature has been constantly monitored.

4.1.3 Proposed magnetic structure in the LTI Phase

The first experimental report on the magnetic structure of $Ni_3V_2O_8$ has been performed by Kenzelmann and co-workers [10] by means of neutron diffraction, and it constituted the starting point for the refinement achieved in the present work. According to it in the LTI phase the magnetic structure consists of elliptical cycloids in the $(\mathbf{a}, \mathbf{b})$ plane, combination of irreducible representations Γ_1 and Γ_4, propagating along the $\mathbf{a}$ direction with propagation vector $\delta \approx 0.27$. The magnitude of

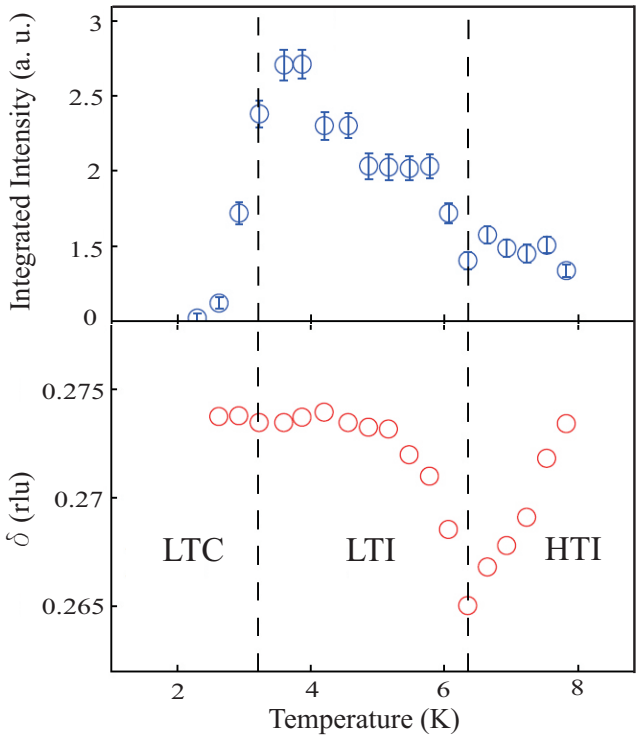

Figure 4.8: Temperature dependence of the scattering intensity (upper) and wave-vector position (lower panel) of the magnetic satellite $(5-\delta,1,0)$, measured in the $\pi-\sigma'$ channel through scans along the reciprocal space $\mathbf{a}^*$ direction, as in Fig. 4.7. The intensity data have been obtained by numerical integration of the detected signal normalised by the intensity of the incident beam; the wave-vector positions have been extracted from fits to a Gaussian function. The dotted lines define the boundaries of the low temperature incommensurate (LTI) phase.

the components of the magnetic moments measured at T = 5 K was reported to be for spine sites

$$\begin{aligned} \mathbf{m}_{\Gamma 4}^{SP} &= [1.6(1), 0.03(10), 0.01(7)]\mu_B \\ \mathbf{m}_{\Gamma 1}^{SP} &= [0.0(5), 1.3(1), 0.1(1)]\mu_B \end{aligned} \tag{4.1}$$

and for cross-tie sites

$$\begin{aligned} \mathbf{m}_{\Gamma 4}^{CT} &= [0, 1.4(1), 0.04(9)]\mu_B \\ \mathbf{m}_{\Gamma 1}^{CT} &= [2.2(1), 0, 0]\mu_B \end{aligned} \tag{4.2}$$

where components forbidden by symmetry are indicated by the absence of error bars. The quality of the fit is given by $R_p = \Sigma_i^n |I_o^i - I_c^i| / \Sigma_i^n I_0^i = 0.19$, where I_o^i and I_c^i are the n observed and calculated intensities, respectively, and by $\chi^2 = \Sigma_i^n w_i (|F_o^i| - |F_c^i|)^2/(n-m) = 7$, where F_o^i and F_c^i are the observed and calculated scattering amplitudes, $w_i = 1/\sigma_i^2$, σ_i is the error bar of the observed intensity I_o^i, and finally m is the number of fitted variables. While the only representation required to describe the HTI phase is Γ_4, for the LTI phase neutron diffraction data alone, on its own, did not unambiguously identify whether the additional representation is Γ_1 or Γ_2. However, the symmetry analysis of the spontaneous polarisation (cf. section 1.1.3) indicates that the correct choice is Γ_1. The experiment was not sensitive to the phase between eigenvectors of Γ_1 and Γ_4, however, the fixed spin length constraint favored by the quartic terms in the Landau expansion requires a relative phase of $\pi/2$ (cycloid).

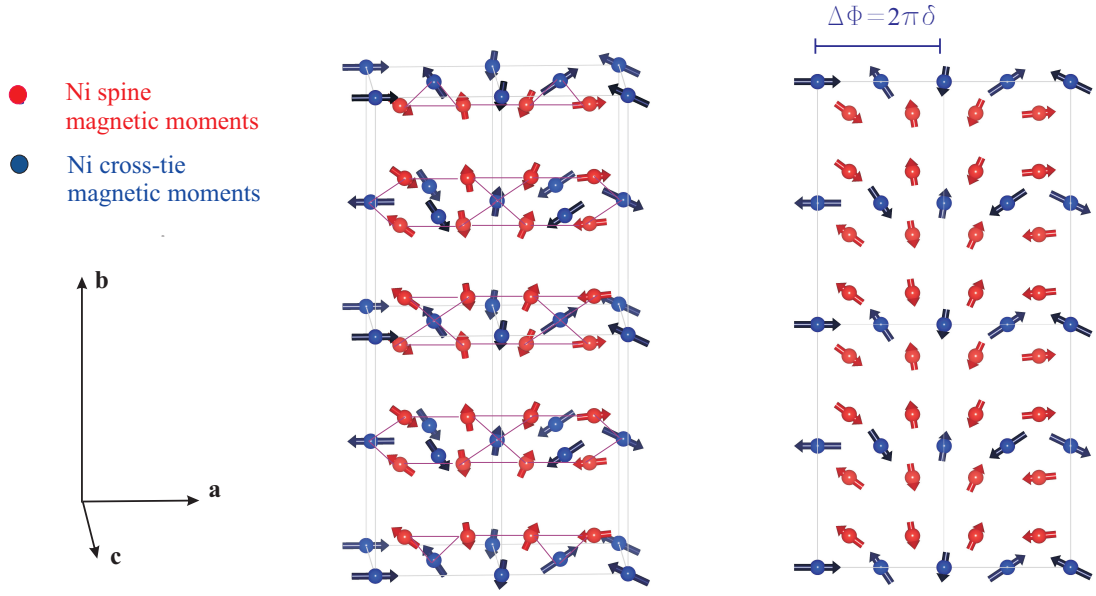

Figure 4.9: Sketch of the magnetic structure proposed in [10] (unit cell delimited by gray lines). The left figure shows the magnetic symmetry relations for all the atoms within the cell; the right figure depicts the projection onto the $(\mathbf{a}, \mathbf{b})$ plane. Since the phase relation between the modulations in the spine and cross-tie sites is not defined within this model, it has been arbitrarily established to be 0 in the present figure.

The magnetic components of different ions belonging to the same type are all related by symmetry. The only unknown parameter is the phase relationship between the spine and cross-tie magnetic modulation (defined as in 2.3.3). In the present work, it is defined as Domain 1 the domain in which the cycloids rotate clockwise along $+\mathbf{a}$ from one cell to the next, while looking at the $(\mathbf{a}, \mathbf{b})$ plane from the $+\mathbf{c}$ direction. In Domain 2, the cycloids rotate anticlockwise. The magnetic structure within the cell is depicted in Fig. 4.9. The calculations use these total magnetic moments as spin moments only on the Ni ions, having assumed that the orbital moment is negligible as compared to the strong polarisation effects induced by the spin component (note that in NiO the Ni orbital moment was estimated to be $0.32 \pm 0.05\ \mu_B$ [65]).

The character table for the irreducible representations is

	1	2_x	m_{xz}	m_{xy}
Γ_1	1	1	1	1
Γ_2	1	1	−1	−1
Γ_3	1	−1	1	−1
Γ_4	1	−1	−1	1

To describe the magnetic moments on the spine and cross-tie sites belonging to the two representa-

tions Γ_1 and Γ_4, the atomic positions within the unit cell are labeled as

$Ni\ SPINE$	$(1/4, -\Delta_b^{SP}, 1/4)$	$SP1$
	$(1/4, \Delta_b^{SP}, 3/4)$	$SP2$
	$(3/4, \Delta_b^{SP}, 3/4)$	$SP3$
	$(3/4, -\Delta_b^{SP}, 1/4)$	$SP4$
	$(3/4, 1/2 - \Delta_b^{SP}, 1/4)$	$SP5$
	$(3/4, 1/2 + \Delta_b^{SP}, 3/4)$	$SP6$
	$(1/4, 1/2 + \Delta_b^{SP}, 3/4)$	$SP7$
	$(1/4, 1/2 - \Delta_b^{SP}, 1/4)$	$SP8$

where $\Delta_b^{SP} = 0.13$ is the coordinate along the **b** axis of the Wyckoff position occupied by spine ions (cf. Fig. 4.1), and

$Ni\ CROSS-TIE$	$(0, 0, 0)$	$CT1$
	$(1/2, 0, 1/2)$	$CT2$
	$(1/2, 1/2, 0)$	$CT3$
	$(0, 1/2, 1/2)$	$CT4$

so that by applying the symmetry operations of the cell to the magnetic moments within each representation, it is found:

magnetic moment		Γ_1	Γ_4
$\mathbf{m}^{SP}$	$SP1, SP5$	m_a	m_a
		m_b	m_b
		m_c	m_c
	$SP2, SP6$	m_a	$-m_a$
		$-m_b$	m_b
		$-m_c$	m_c
	$SP3, SP7$	$-m_a$	m_a
		m_b	$-m_b$
		$-m_c$	m_c
	$SP4, SP8$	$-m_a$	$-m_a$
		$-m_b$	$-m_b$
		m_c	m_c
$\mathbf{m}^{CT}$	$CT1, CT3$	m_a	0
		0	m_b
		0	m_c
	$CT2, CT4$	$-m_a$	0
		0	$-m_b$
		0	m_c

The general expression for the X-ray non resonant magnetic amplitude has been given in Eq. 2.39, as a function of the Fourier components of the magnetic modulation M_s in the s atoms of the crystallographic unit cell, and their fractional coordinates within the cell (x_s, y_s, z_s). In the present case, the magnetic structure factor is calculated for a reflection $\mathbf{k} - \mathbf{k}' = (h + \alpha\delta,\, k,\, l)$, where $\alpha = \pm 1$ selects the sign of the incommensurate satellite next to the Bragg peak (h, k, l). The parameter $\gamma = \pm 1$ is employed to distinguish between Domain 1 ($\gamma = +1$) and Domain 2 ($\gamma = -1$). The scattering amplitude then becomes

$$f_{nr} \;=\; \left(\, \frac{1}{2}\; i\frac{\hbar\omega}{mc^2} \,\right) \;\cdot \sum_s e^{i2\pi(hx_s+ky_s+lz_s)}\,(\mathbf{M}_s \cdot \mathbf{B}) \tag{4.3}$$

where the vector $\mathbf{B}$ contains the dependence on the polarisations of the incident and scattered light, as per Eq. 2.10, and

$$\sum_s e^{i2\pi(hx_s+ky_s+lz_s)}\;\mathbf{M}_s =$$

$$\begin{aligned}
&e^{i2\pi[h(1/4)+k(-\Delta_b^{SP})+l(1/4)]} \;\cdot\; \tfrac{1}{2}[m_a^{SP}\hat{\mathbf{a}} + m_b^{SP}e^{-i\alpha\gamma\pi/2}\hat{\mathbf{b}}]+ && SP1\\
&e^{i2\pi[h(1/4)+k(\Delta_b^{SP})+l(3/4)]} \;\cdot\; \tfrac{1}{2}[-m_a^{SP}\hat{\mathbf{a}} - m_b^{SP}e^{-i\alpha\gamma\pi/2}\hat{\mathbf{b}}]+ && SP2\\
&e^{i2\pi[h(3/4)+k(\Delta_b^{SP})+l(3/4)]} \;\cdot\; \tfrac{1}{2}[m_a^{SP}\hat{\mathbf{a}} + m_b^{SP}e^{-i\alpha\gamma\pi/2}\hat{\mathbf{b}}]+ && SP3\\
&e^{i2\pi[h(3/4)+k(-\Delta_b^{SP})+l(1/4)]} \;\cdot\; \tfrac{1}{2}[-m_a^{SP}\hat{\mathbf{a}} - m_b^{SP}e^{-i\alpha\gamma\pi/2}\hat{\mathbf{b}}]+ && SP4\\
&e^{i2\pi[h(3/4)+k(1/2-\Delta_b^{SP})+l(1/4)]} \;\cdot\; \tfrac{1}{2}[m_a^{SP}\hat{\mathbf{a}} + m_b^{SP}e^{-i\alpha\gamma\pi/2}\hat{\mathbf{b}}]+ && SP5\\
&e^{i2\pi[h(3/4)+k(1/2+\Delta_b^{SP})+l(3/4)]} \;\cdot\; \tfrac{1}{2}[-m_a^{SP}\hat{\mathbf{a}} - m_b^{SP}e^{-i\alpha\gamma\pi/2}\hat{\mathbf{b}}]+ && SP6\\
&e^{i2\pi[h(1/4)+k(1/2+\Delta_b^{SP})+l(3/4)]} \;\cdot\; \tfrac{1}{2}[m_a^{SP}\hat{\mathbf{a}} + m_b^{SP}e^{-i\alpha\gamma\pi/2}\hat{\mathbf{b}}]+ && SP7\\
&e^{i2\pi[h(1/4)+k(1/2-\Delta_b^{SP})+l(1/4)]} \;\cdot\; \tfrac{1}{2}[-m_a^{SP}\hat{\mathbf{a}} - m_b^{SP}e^{-i\alpha\gamma\pi/2}\hat{\mathbf{b}}]+ && SP8\\
&e^{i2\pi[h(0)+k(0)+l(0)]} \;\cdot\; \tfrac{1}{2}[m_a^{CT}e^{i\alpha\gamma\phi_{SC}}\hat{\mathbf{a}} + m_b^{CT}e^{-i\alpha\gamma(\pi/2+\phi_{SC})}\hat{\mathbf{b}}]+ && CT1\\
&e^{i2\pi[h(1/2)+k(0)+l(1/2)]} \;\cdot\; \tfrac{1}{2}[-m_a^{CT}e^{i\alpha\gamma\phi_{SC}}\hat{\mathbf{a}} - m_b^{CT}e^{-i\alpha\gamma(\pi/2+\phi_{SC})}\hat{\mathbf{b}}]+ && CT2\\
&e^{i2\pi[h(1/2)+k(1/2)+l(0)]} \;\cdot\; \tfrac{1}{2}[m_a^{CT}e^{i\alpha\gamma\phi_{SC}}\hat{\mathbf{a}} + m_b^{CT}e^{-i\alpha\gamma(\pi/2+\phi_{SC})}\hat{\mathbf{b}}]+ && CT3\\
&e^{i2\pi[h(0)+k(1/2)+l(1/2)]} \;\cdot\; \tfrac{1}{2}[-m_a^{CT}e^{i\alpha\gamma\phi_{SC}}\hat{\mathbf{a}} - m_b^{CT}e^{-i\alpha\gamma(\pi/2+\phi_{SC})}\hat{\mathbf{b}}] = && CT4
\end{aligned}$$

$$= \;[m_a^{SP}\hat{\mathbf{a}} - i\alpha\gamma m_b^{SP}\hat{\mathbf{b}}]\cdot[1-(-1)^k]\cdot[2Re(i^{h+l}e^{-i2\pi k\Delta_b^{SP}}) + 2Re(-i^{-h+l}e^{-i2\pi k\Delta_b^{SP}})]+$$

$$+[m_a^{CT}\hat{\mathbf{a}} - i\alpha\gamma m_b^{CT}\hat{\mathbf{b}}]\cdot e^{i\alpha\gamma\phi_{SC}}\cdot[1-(-1)^{h+l}+(-1)^{h+k}-(-1)^{k+l}]$$

where ϕ_{SC} is the phase shift in the magnetic modulation ($\mathbf{a}$ component) between the cross-tie site C1 and the spine site SP1. It is defined as the phase shift at the same coordinates in space, following subsection 2.3.3, and the transformation by inversion symmetry between domains is made explicit by considering one phase parameter ϕ_{SC}, whose sign is determined by γ.

A particular feature of $Ni_3V_2O_8$ is that by taking advantage of the structure factor one may selectively probe the spine and cross-tie moments independently or in combination. By calculating the NRXMS amplitudes (cf. section 2.3), it is found that the scattering reflections can be classified into three different types. In the first type ($h = odd, k = odd, l = odd$), only the spine magnetic atoms are expected to contribute to the amplitude, while the contributions of the cross-tie atoms cancel each other. In the second type ($h = even, k = even, l = odd$), it is the contribution from cross-tie atoms that is singled out. In the third type ($h = odd, k = odd, l = even$), both contributions are present, but are summed with a sign that depends on the actual values of h, k, l. The scattering

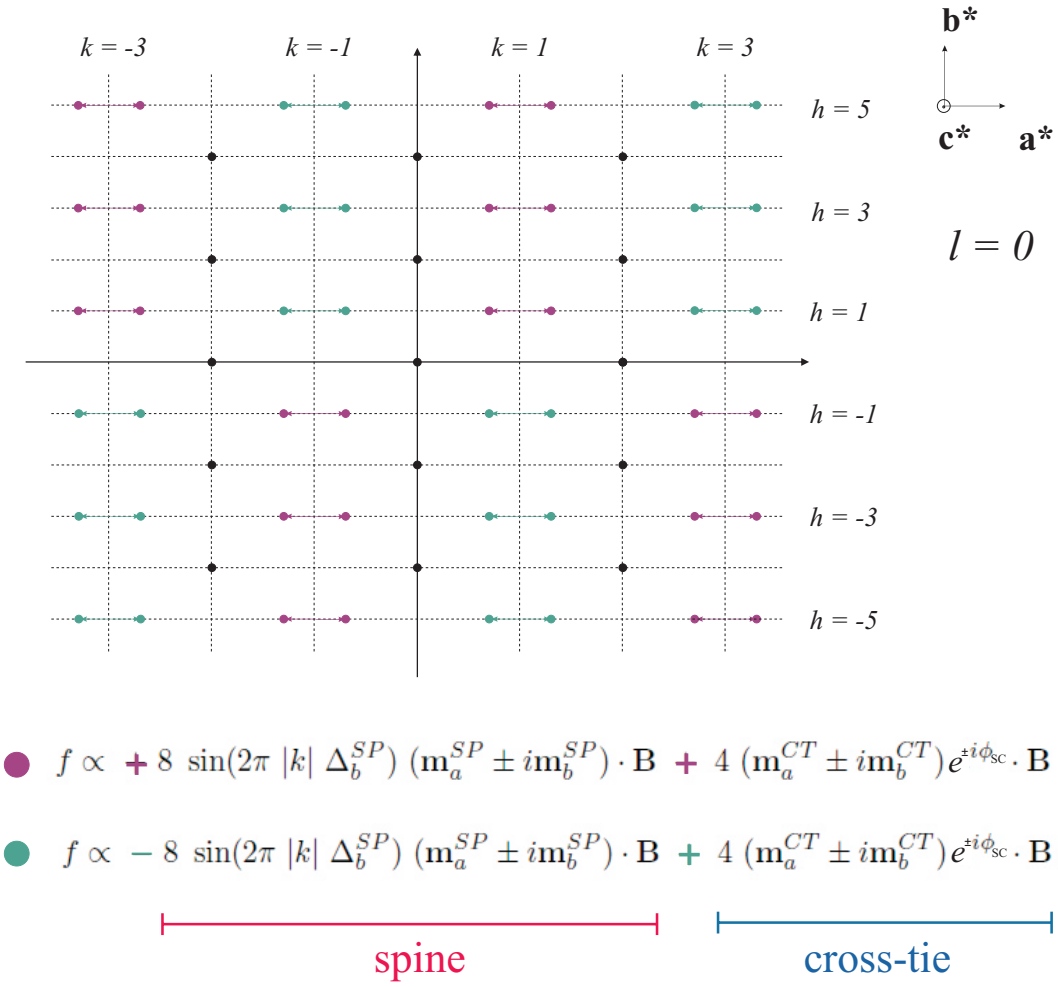

Figure 4.10: Position of the magnetic satellite reflections in the $(\mathbf{a}^*, \mathbf{b}^*)$ projection of the reciprocal lattice, with $l = 0$ (black circles indicate Bragg reflections).

amplitudes in the different types of peaks are

$$f_1 \propto 8\ \cos(2\pi k \Delta_b^{SP})\ (m_a^{SP}\hat{\mathbf{a}} - \gamma\ \alpha\ i\ m_b^{SP}\hat{\mathbf{b}}) \cdot \mathbf{B}$$

$$f_2 \propto 4\ (m_a^{CT}\hat{\mathbf{a}} - \gamma\ \alpha\ i\ m_b^{CT}\hat{\mathbf{b}}) \cdot \mathbf{B}$$

$$f_3 \propto [\ \beta\ 8\ \sin(2\pi k \Delta_b^{SP})\ (m_a^{SP}\hat{\mathbf{a}} - \gamma\ \alpha\ i\ m_b^{SP}\hat{\mathbf{b}}) + 4(m_a^{CT}\hat{\mathbf{a}} - \gamma\ \alpha\ i\ m_b^{CT}\hat{\mathbf{b}})\ e^{i\alpha\gamma\phi_{SC}}\ ] \cdot \mathbf{B}$$

where $\beta = (-1)^{p+n}$, with $h = 2n + 1$ and $l = 2p$, determines the sign of the sum between spine and cross-tie contributions, together with the factor $\sin(2\pi k \Delta_b^{SP})$. The phase relationship between the spine and cross-tie magnetic modulation (ϕ_{SC}), that was not determined from neutron diffraction, is kept as a free variable to be determined from the data, together with the refinement of the amplitudes m_i^{SP} and m_i^{CT}, $i = a, b$ (see the following sections). The diagrams in Fig. 4.10 and 4.11 depict the distribution of the different types of reflection in the reciprocal space.

4.1.4 Overview of the data

The investigation of the magnetic structure consisted in electric field cooling to create a magnetic monodomain via the magneto-electric coupling, and performing a full Stokes analysis of the scattered

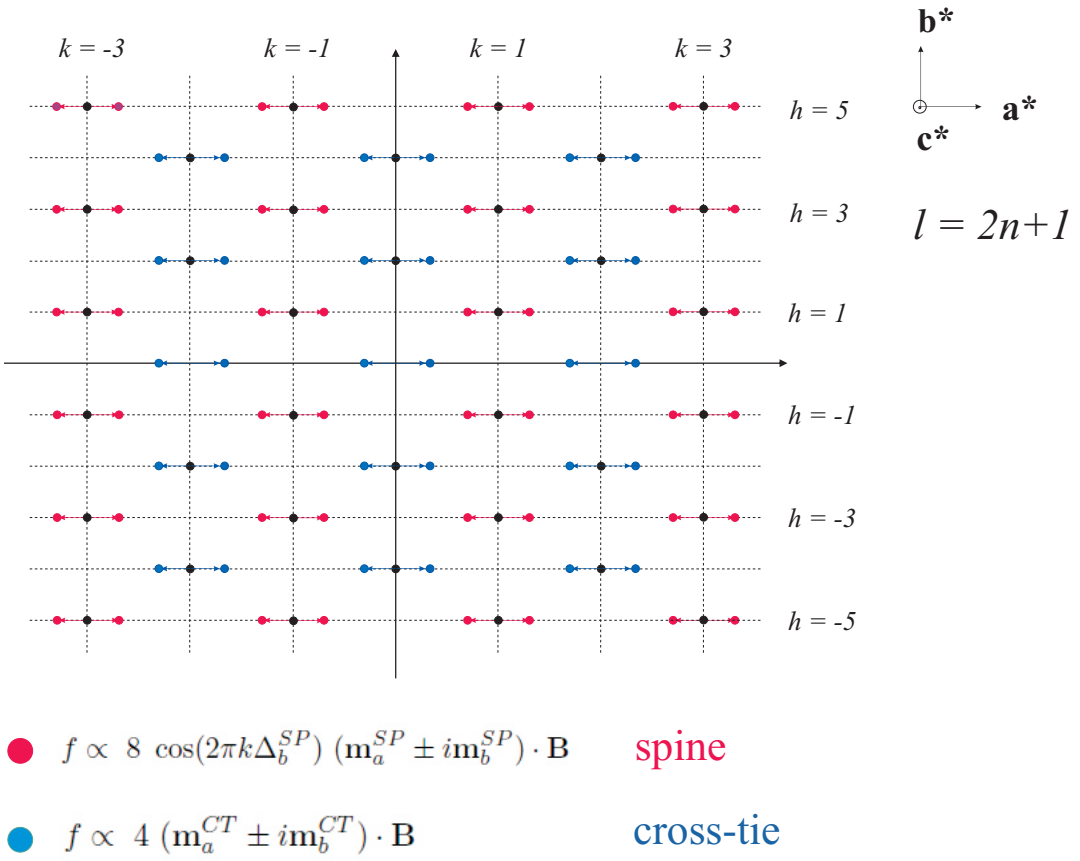

Figure 4.11: Position of the magnetic satellite reflections in the $(\mathbf{a}^*, \mathbf{b}^*)$ projection of the reciprocal lattice, with $l = odd$.

intensity, as established in Chapter 2. The field cooling procedure for performing the measurements was to apply -1.4 kV/mm across the sample as it was cooled from 20 K, in the paramagnetic phase, to 4.2 K, in the LTI phase. The electric field was then removed before illuminating the sample with X-rays.

It was decided to measure a spine-type reflection, $\mathbf{k}' - \mathbf{k} = (5 + \delta, 1, 1)$, and two reflections of the third type, $(5 + \delta, 1, 0)$ and $(5 + \delta, -1, 0)$, specularly chosen so that the sign of $\beta \sin(2\pi k\Delta_b^{SP})$ is opposite between them. No signal could be detected in the expected position of a cross-tie reflection. This led to consider the possibility of cross-tie moments being weaker than the values initially proposed.

In preparation to the measurement of the Stokes scans on the reflections, the phase plate was aligned as to optimise the positions for left and right circular polarisation (hereafter LCP and RCP). The results show a degree of residual linear polarisation less than 1 % (see Fig. 4.12). These alignment scans were regularly repeated before and after each Stokes scan collected on magnetic diffraction, in order to have complete control of the purity of the incident polarisation during the whole experiment. The Stokes scans were collected with both circular polarisations for each magnetic peak. The rocking curve of the analyser for every value of η was then treated by subtraction of the background. Said background was collected by shifting the motor θ of the sample (which is coupled

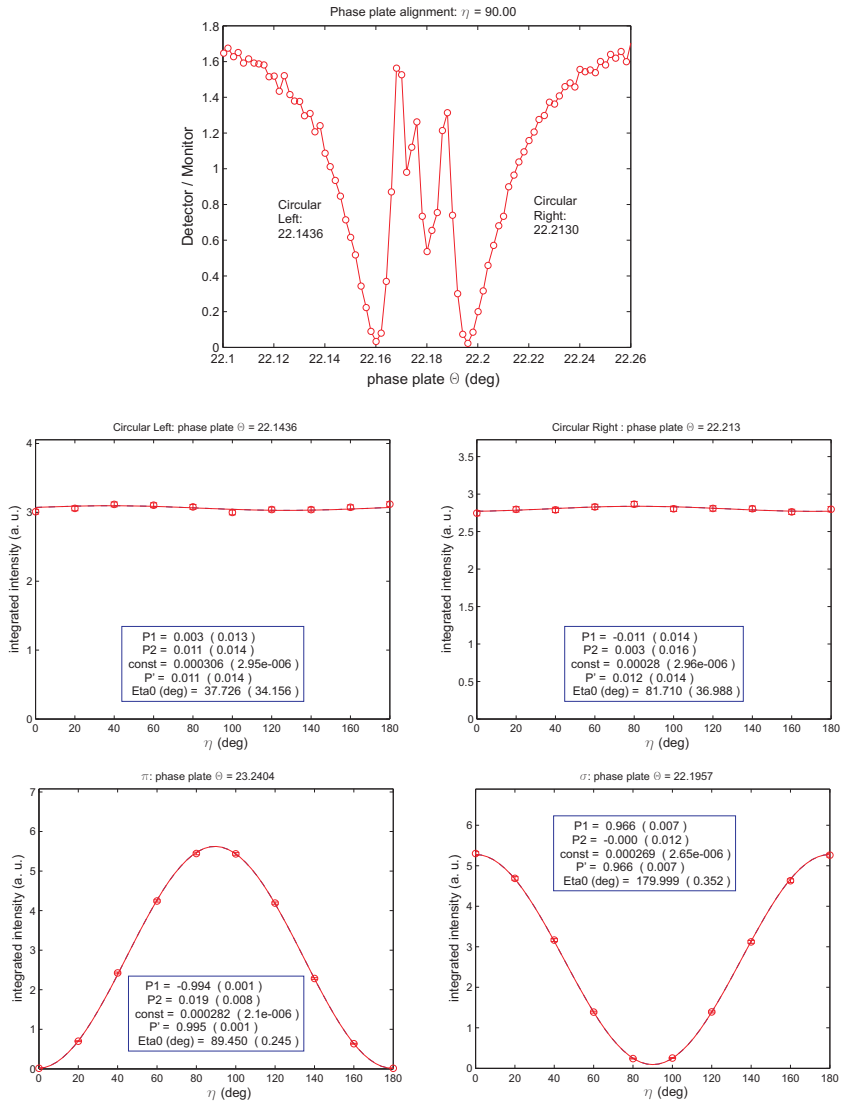

Figure 4.12: Alignment scans of the phase plate: the positions of the two circular polarisations are identified from the rocking curve θ of the plate (upper figure). The quality of the rotated polarisations is then checked by means of a full Stokes scan on the direct beam. As a comparison, and to refine the alignment of the plate in the angle χ (cf. Chapter 3), the Stokes scans are performed also in the positions corresponding to vertical rotated polarisation (σ) and unrotated polarisation (π), i.e. away from any Bragg reflection of the plate.

to the Bragg angle) away from the diffraction position by 0.2°, and measuring a different set of rocking curves of the analyser at various values of η; the resulting integrated intensities are then fitted to a Stokes dependence that can be subtracted from the signal. The procedure is illustrated for the $(5+\delta, 1, 0)$ reflection with circular right incident polarisation in Fig. 4.13.

An overview of the data is presented in Fig. 4.14. At a qualitative level, it is seen that the circular polarisation of the incident light is profoundly altered by the diffraction, being converted after interaction with the sample into a linear oblique state, in which the Stokes parameter P_2 is dominant while P_1 is close to zero (the maxima and minima in the integrated intensities lie close to 45° and 135°, cf. Eq. 3.2 - 3.5 and Fig. 3.4). The sign of P_2 is dependent on the handedness of the circular polarisation of the incident beam (the positions of maxima and minima are reversed for LCP vs RCP incidence), and the average intensity arising from the two incident polarisation states

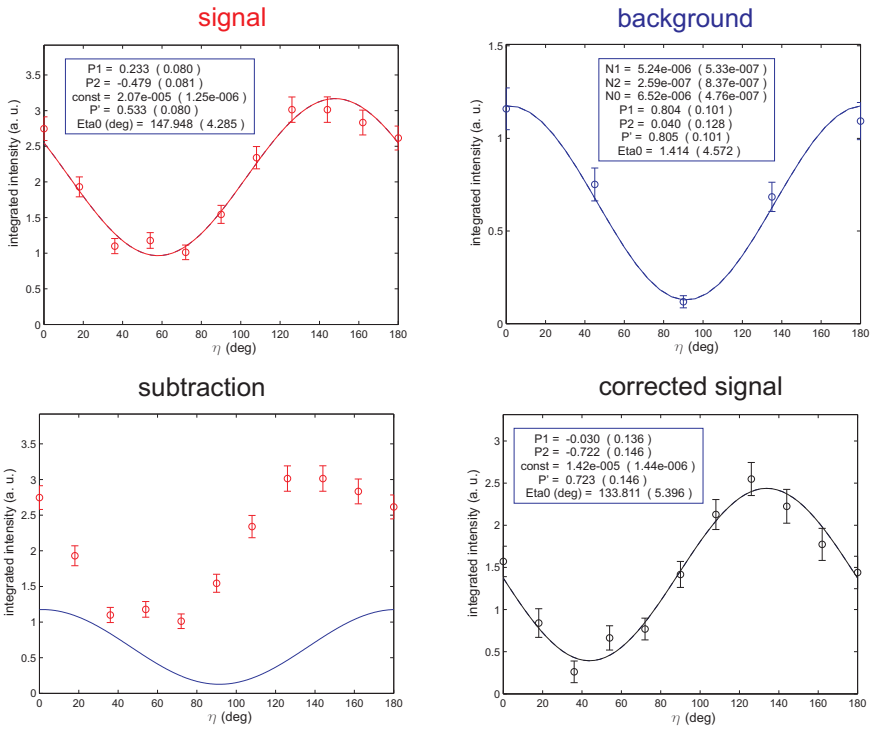

Figure 4.13: Procedure for the measurement of a Stokes scan on the magnetic reflection $(5+\delta, 1, 0)$. The first scan is collected on the magnetic peak (red) while the second one is the background found at 0.2° away from the peak in θ (blue). Each point is obtained from a rocking scan of the analyser, normalised by the incident intensity and numerically integrated. The fitted background is then subtracted from the signal to give the final result (black).

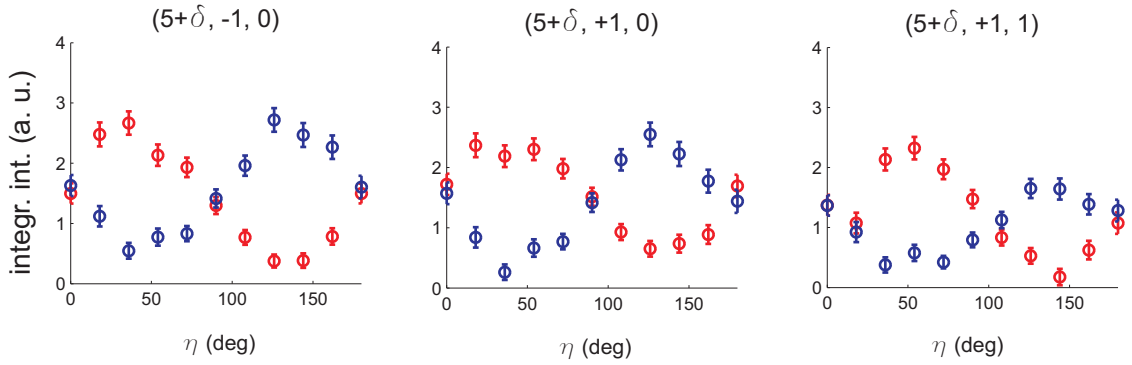

Figure 4.14: Overview of the data collected on the three magnetic peaks $(5+\delta, -1, 0)$, $(5+\delta, 1, 0)$ and $(5+\delta, 1, 1)$ with polarisation of the incident light tuned into circular right (blue) or circular left (red) state.

is approximately the same. These results hold true for every reflection.

By comparing the results of different reflections, it is seen that the twin reflections $(5+\delta, -1, 0)$ and $(5+\delta, 1, 0)$ have the same average intensity. The degree of oblique polarisation (absolute value of P_2) is the same for each peak and for each handedness of the polarisation of the incident beam: $|P_2| \approx 0.7$. Conversely, the spine-only reflection $(5+\delta, 1, 1)$ presents slightly weaker intensity with respect to the other two, and an asymmetric value of $|P_2|$ between the two sets of results, being 0.72 when the incident beam is in a circular left polarisation state, and -0.58 in the opposite case.

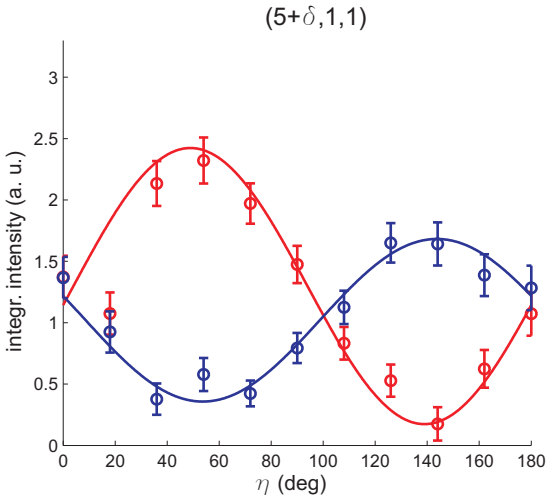

Figure 4.15: Stokes scans in spine satellite $(5+\delta,1,1)$, in LTI phase. The data are taken with circular left (red) and right (blue) incident polarisation. The curves represent the calculation (see text).

4.1.5 Fit of the data and interpretation

The data have been fitted to the model presented in 4.1.3, both by analytical calculation in an approximated scattering geometry (in the case of spine + cross-tie reflections) and by numerical calculation, using the Matlab program described in section 3.2 that takes the exact geometry into account.

Spine type satellite $(5+\delta,1,1)$

The first test of the proposed model was done on the reflection of easiest interpretation, the spine reflection $(5+\delta,1,1)$. The results of the numerical fit are shown in Fig. 4.15 and take into account the exact geometry of the experiment. The **a** and **b** components of the magnetic moments have been extracted from the neutron results (Eq. 4.1), and the only free variable in this case is the population of domains. The curve represented in the figure is the best fit, obtained for a percentage of 88(3)% of Domain 1. It can be seen that the same population of domains is able to fit the data for both circular polarisations, thus confirming that the state of the sample has not been significanlty altered in temperature between the two measurements. The calculation returns an arbitrary intensity factor that has been fixed to match the average intensity of the data.

It has been concluded that, for this reflection, the model proposed by neutron diffraction works very well, predicting a specular symmetry in the position of the max η between the two curves, a similar value of the average intensity, and the polarisation of the outcoming beam being more linear when the incidence is circular left.

Spine and Cross-tie type satellites $(5+\delta,1,0)$ **and** $(5+\delta,-1,0)$

The next step involved fitting the two twin reflections $(5+\delta,1,0)$ and $(5+\delta,-1,0)$, belonging to the third type. Here the significant parameters to be refined were the phase shift between the spine and

cross-tie modulations (ϕ_{SC}) and, possibly, the magnitudes of the cross-tie components, since it was not possible to test them on a purely cross-tie reflection. To clarify the refinement of the cross-tie contributions, two parameters can be explicitly introduced into their expressions:

$$\begin{aligned} m_a^{CT} &= \quad a\ (1.4\ r)\ \mu_B \\ m_b^{CT} &= \quad\ \ a\ 1.4\ \mu_B \end{aligned}$$

The parameter a is an overall magnitude factor for both components, while r represents the ratio between the components. In the initial model proposed by Kenzelmann, $a = 1$ and $r = 2.2/1.4 = 1.5714$.

The absolute intensities of the reflections $(5+\delta, 1, 0)$ and $(5+\delta, -1, 0)$ have been calculated by comparison with the reflection $(5+\delta, 1, 1)$ already measured, with the opportune corrections for absorption. The absorption correction to be multiplied to the intensity of every reflection is

$$\frac{1}{1+\sin(\psi_a)/\sin(\psi_b)}$$

where ψ_a and ψ_b represent the angle of the incident and the scattered beam with the surface of the sample, respectively, and are dependent on the specific scattering geometry of the peak. On the other hand, the energy-dependent absorption coefficient (μ) is the same for all peaks.

Analytical calculation

In this subsection an analytical simplified model is presented, as a tool to qualitatively understand the experimental results prior to the numerical fit. For both satellites, the following simplifying assumptions have been made:

- Let the Bragg angle be $\theta = 45°$ (exact value = 48.12°);
- The scattering plane is perfectly horizontal. This is equivalent to assuming: 1) the azimuthal angle with respect to the **b** axis = 180° (exact value for the two satellites is = 178.4°); 2) the shift from the exact polarisation σ' in the zero of the motor η being negligible (the exact value is less than 0.1°);
- Within the scattering plane, let the angle between the **b** axis and the scattering vector be = 45° (exact values for the two satellites are 40.9° and 52.2°).

A purely monodomain magnetic density is being considered. The scattering amplitudes are then, following Eq. 2.16:

$$\begin{aligned} f_{\hat{\sigma}'} &\propto \quad [\ kS_a + C_b \sin\phi_{SC} - C_a \cos\phi_{SC}\ ] + [\ kS_b - C_b \cos\phi_{SC} - C_a \sin\phi_{SC}\ ]\ i \\ f_{\hat{\pi}'} &\propto \quad \epsilon\ [\ kS_b - C_b \cos\phi_{SC} + C_a \sin\phi_{SC}\ ] + \epsilon\ [\ kS_a - C_b \sin\phi_{SC} - C_a \cos\phi_{SC}\ ]\ i \end{aligned}$$

where the following shorthand notations have been introduced

$$\begin{aligned} S_a &= \ 8\sin(2\pi\Delta_b^{SP})\ m_a^{SP} &&= 8\sin(2\pi\Delta_b^{SP})\ 1.6\ \mu_B \\ S_b &= \ 8\sin(2\pi\Delta_b^{SP})\ m_b^{SP} &&= 8\sin(2\pi\Delta_b^{SP})\ 1.3\ \mu_B \\ C_a &= \qquad 4\ m_a^{CT} &&= 4\ a\ (1.4\ r)\ \mu_B \\ C_b &= \qquad 4\ m_b^{CT} &&= 4\ a\ 1.4\ \mu_B \end{aligned}$$

and where $k = \pm 1$ identifies the reflection $(5+\delta, k, 0)$, and $\epsilon = \pm 1$ refers to the handedness of the incoming circular light.

Relative intensities between the two satellites (condition on phase parameter ϕ_{SC})

The first thing that has been considered is the relative intensities of peaks $(5+\delta, 1, 0)$ and $(5+\delta, -1, 0)$. As it is seen from the data in Fig. 4.14, the four intensities are very close to each other, both when the incident beam is in a circular left and in a circular right state of polarisation. This analysis will show that the ratios between the intensities are directly related to the phase difference ϕ_{SC}. The average intensity for the two peaks can be expressed as

$$|f_{\hat{\sigma}'}|^2 + |f_{\hat{\pi}'}|^2 =$$

$$|kS_a + C_b \sin\phi_{SC} - C_a \cos\phi_{SC}|^2 + |kS_b - C_b \cos\phi_{SC} - C_a \sin\phi_{SC}|^2 +$$

$$|kS_b - C_b \cos\phi_{SC} + C_a \sin\phi_{SC}|^2 + |kS_a - C_b \sin\phi_{SC} - C_a \cos\phi_{SC}|^2.$$

The sign of the incident polarisation does not appear, thus assuring that the intensities for left and right illumination are bound to be the same, for every choice of parameters. This is simply a consequence of no magnetic moments being directed out of the scattering plane. For the intensities between the two peaks to be the same, it is necessary to eliminate the contributions in $C_b \cos\phi_{SC}$ and $C_a \cos\phi_{SC}$. This implies

$$\boxed{\phi_{SC} = \pm\pi/2}.$$

The numerical calculations agree very well with this result, as shown in Fig. 4.16.

Stokes parameters P_1 and P_2 (condition on parameter r)

The next step is fitting the values of the Stokes parameters P_1 and P_2. From the data, it is clear that P_1 is basically absent, while P_2 is strong and has opposite values for the two incident states on the same reflection, while mantaining the same values between the two reflections. By inserting the result found for ϕ_{SC}, the amplitudes become

$$f_{\hat{\sigma}'} \propto [kS_a + C_b] + [kS_b - C_a]i$$

$$f_{\hat{\pi}'} \propto \epsilon[kS_b + C_a] + \epsilon[kS_a - C_b]i.$$

- **Value of $\mathbf{P_1}$.**

  The value of P_1 is different from zero when $|f_{\hat{\sigma}'}|$ and $|f_{\hat{\pi}'}|$ are different. Since it had been reasonably assumed that the values for the spine components are correct and very similar to each other, one can simplify the expression by considering

  $$\boxed{S_a \approx S_b},$$

  which shows that P_1 is close to zero if and only if the two cross-tie components are also similar to each other:

  $$\boxed{C_a \approx C_b}.$$

The numerical simulations confirm that a P_1 component arises when either the ratio S_a/S_b or the ratio C_a/C_b (i.e. the parameter r) becomes very different from 1: see some cases in Fig. 4.17. The values proposed by Kenzelmann and co-workers are close enough to satisfy this condition, thus leading to P_1 being reasonably close to zero.

- **Value of $\mathbf{P_2}$.**

  Turning now to P_2, this parameter is different from zero when $|f_{\hat{\sigma}'} + f_{\hat{\pi}'}|$ and $|f_{\hat{\sigma}'} - f_{\hat{\pi}'}|$ are different. In the present case:

$$|f_{\hat{\sigma}'} + f_{\hat{\pi}'}|^2 = |kS_a + C_b + \epsilon kS_b + \epsilon C_a|^2 + |kS_b - C_a + \epsilon kS_a - \epsilon C_b|^2$$

$$|f_{\hat{\sigma}'} - f_{\hat{\pi}'}|^2 = |kS_a + C_b - \epsilon kS_b - \epsilon C_a|^2 + |kS_b - C_a - \epsilon kS_a + \epsilon C_b|^2$$

  or, equivalently,

	$\lvert f_{\hat{\sigma}'} + f_{\hat{\pi}'}\rvert$ and $\lvert f_{\hat{\sigma}'} - f_{\hat{\pi}'}\rvert$
$\epsilon = +1$	$\lvert f_{\hat{\sigma}'} + f_{\hat{\pi}'}\rvert = \lvert(S_a + S_b) + (C_a + C_b)\rvert^2 + \lvert(S_a + S_b) - (C_a + C_b)\rvert^2$
$(k = \pm 1)$	$\lvert f_{\hat{\sigma}'} - f_{\hat{\pi}'}\rvert = \lvert(S_a - S_b) + (C_a - C_b)\rvert^2 + \lvert(S_a - S_b) - (C_a - C_b)\rvert^2$
$\epsilon = -1$	$\lvert f_{\hat{\sigma}'} + f_{\hat{\pi}'}\rvert = \lvert(S_a - S_b) + (C_a - C_b)\rvert^2 + \lvert(S_a - S_b) - (C_a - C_b)\rvert^2$
$(k = \pm 1)$	$\lvert f_{\hat{\sigma}'} - f_{\hat{\pi}'}\rvert = \lvert(S_a + S_b) + (C_a + C_b)\rvert^2 + \lvert(S_a + S_b) - (C_a + C_b)\rvert^2$

  It can already be noted that reversing the sign of the circular polarisation (ϵ) means switching between P_2 and $-P_2$; this is again a consequence of the moments lying within the scattering plane. Moreover, P_2 remains the same for the two satellites (it does not depend on k). As for its values, it is already established that $S_a \approx S_b$ and $C_a \approx C_b$. Therefore, $(S_a - S_b)$ and $(C_a - C_b)$ are close to zero, while $|(S_a + S_b) + (C_a + C_b)|$ is strong. The conclusion is that a high contrast between $|f_{\hat{\sigma}'} + f_{\hat{\pi}'}|$ and $|f_{\hat{\sigma}'} - f_{\hat{\pi}'}|$ is present, which leads to a high value of P_2, and is reversed when the circular polarisation is switched.

Note that the overall ratio between the magnitude of the spine moments versus cross-tie moments (the parameter a) does not affect the results found for P_1, nor the symmetry of the results found for P_2, but only the actual value of P_2.

Relative intensities between the peaks $(5 + \delta, \pm 1, 0)$ and the spine peak $(5 + \delta, 1, 1)$ (condition on parameter a)

The final fit to the data consisted in matching the intensity of these peaks with the intensity of the spine peak $(5 + \delta, 1, 1)$. By introducing all the results obtained so far, the average intensity of the

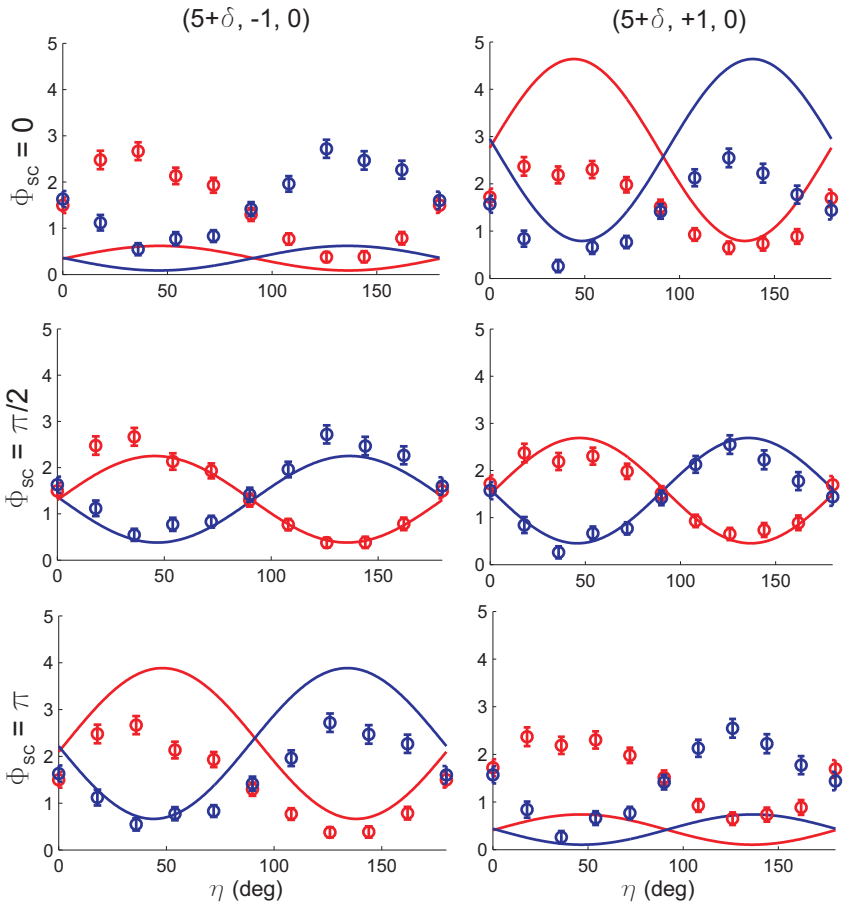

Figure 4.16: Effect of parameter ϕ_{SC} (phase between spine and cross-tie modulation) on the relative intensities of $(5+\delta, 1, 0)$ and $(5+\delta, -1, 0)$. The other parameters are fixed at $a = 1/2$; $r =$ as given in [10]

peaks $(5+\delta, 1, 0)$ and $(5+\delta, -1, 0)$ is given by

$$|S_a + C_b|^2 + |S_a - C_b|^2 + |S_b + C_a|^2 + |S_b - C_a|^2$$

and is an increasing function of a, for every r. From the numerical calculation, it will be seen that the cross-tie contributions appear to be weaker than expected (Fig. 4.18).

Numerical optimisation of the parameters ϕ_{SC}, a, r

The values extracted with this approximated analysis have constituted the starting point for a numerical optimisation, where the parameters r, a and ϕ_{SC} have been varied in proximity of those initial guesses in order to best fit the data. The calculation has considered the effective population of domains, the absorption correction and the exact scattering geometry. The fits obtained from this first optimisation procedure are shown in Fig. 4.19, with parameters $\phi_{SC} = \pi/2$, $r = 1.3$, $a = 0.55$. The most notable finding is the unexpectedly weak contribution arising from the cross-tie magnetic moments: the data seem to indicate an upper limit for the two components of about 1 μ_B. Unfortunately, this result is not only based on the polarisation measurements but also on the intensity measurements, which are less sensitive to any variations in the model and are measured with a lesser degree of precision due to the requested comparison between different peaks. On the

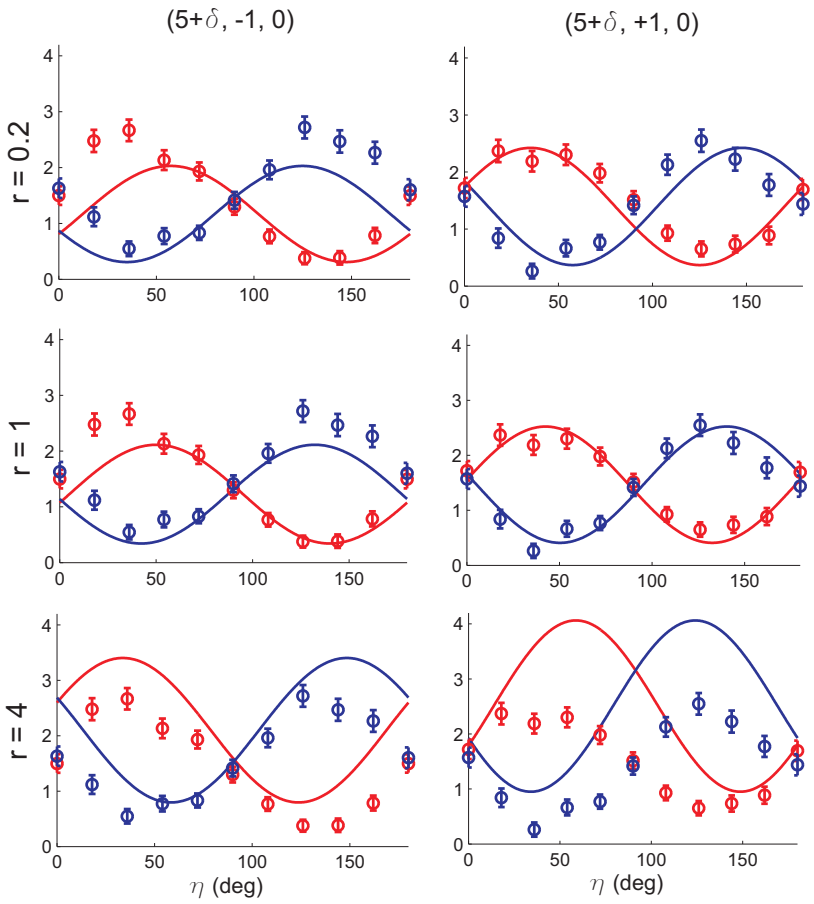

Figure 4.17: Effect of parameter r (ratio between a and b magnetic components in the cross-tie sites) on the Stokes parameters. P_1 becomes noticeable (the positions of the max in η move away from 45° and 135°) when r is different from 1. The other parameters are fixed at $\phi_{SC} = \pi/2$, $a = 1/2$.

other hand, the phase relationship ϕ_{SC} between the magnetic modulations on the spine and cross-tie sites, whose value influences the polarisation state of the diffracted beam, is determined with much more accuracy, being estimated in the range $0.50\ \pi \pm 0.02\ \pi$ even if the cross-tie moments may be very small.

To clarify this issue it was decided to repeat the measurement on the intensities, by aligning the various reflections in the σ' and π' polarisation channels and rocking the sample along orthogonal directions, so to determine the overall intensity with the highest degree of precision allowed by the setup.

4.1.6 Further refinement by intensity measurements and Conclusions

The absolute intensities of the peaks $(5+\delta, -1, 0)$, $(5+\delta, 1, 0)$ and $(5+\delta, 1, 1)$, have been checked in a separate experiment, in an attempt to refine the model proposed in the previous subsection. The beamline was tuned to E = 7.45 keV, the analyser crystal Au (2 2 2) was used, and the sample was cooled down to the LTI phase in an applied electric field along -**b**, as in the previous measurements. Since the focus of this experiment was measuring the relative intensities of different magnetic peaks, particular care has been taken in aligning the sample translations, and in fixing the detector slits to the most suitable width, to make sure that all the signal was being detected without introducing

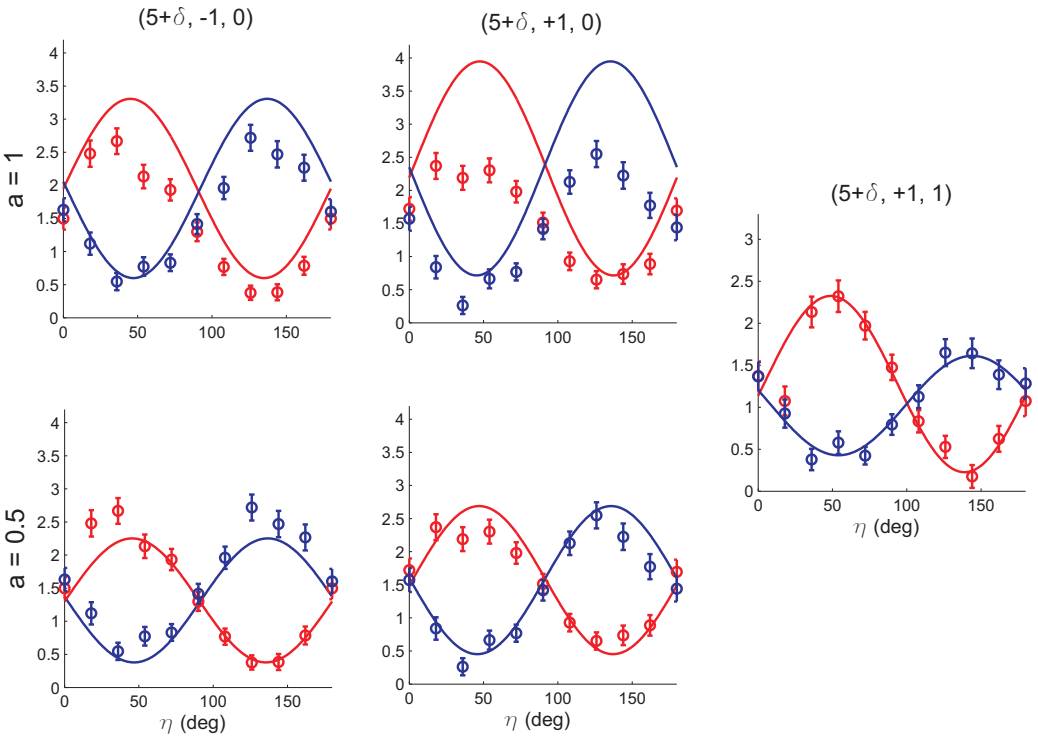

Figure 4.18: Effect of parameter a (ratio between spine and cross-tie moments) on both the intensities of $(5+\delta, 1, 0)$ and $(5+\delta, -1, 0)$. The spine reflection $(5+\delta, 1, 1)$ has been used to normalise the calculated intensities. The other parameters are fixed at $\phi_{SC} = \pi/2$; r = as given in [10]

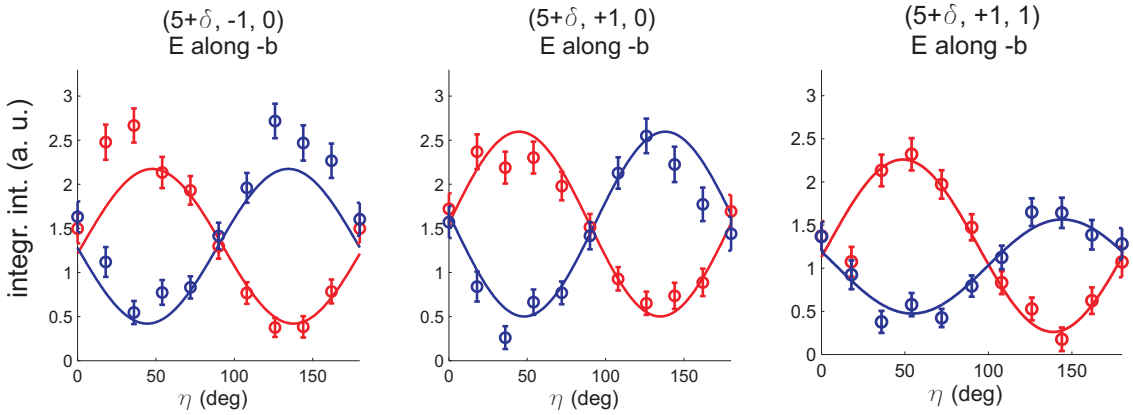

Figure 4.19: Numerical optimisation of the parameters around the initial guesses. The figure is generated from the values: $\phi_{SC} = \pi/2$, $r = 1.3$, $a = 0.55$. The population of Domain 1 is 86% in the simulations for all the peaks. The quality of the fit is given by $\chi^2 = \Sigma_i^n w_i (I_o^i - I_c^i)^2/(n-m) = 2$, where I_o^i and I_c^i are the observed and calculated intensities, $w_i = 1/\sigma_i^2$, σ_i is the error bar of the observed intensity I_o^i, and finally m is the number of parameters of the fit. Compare this result with the final fit in Fig. 4.21, in which the refinement of the intensities has been taken into account.

background unnecessarily.

For each reflection, a set of scans was collected by tuning the incident light into linear, circular left and circular right state, and the detected light into channels σ' and π'. For each condition the sample was scanned along various directions, including the rocking curve of the analyser ('θ'), the

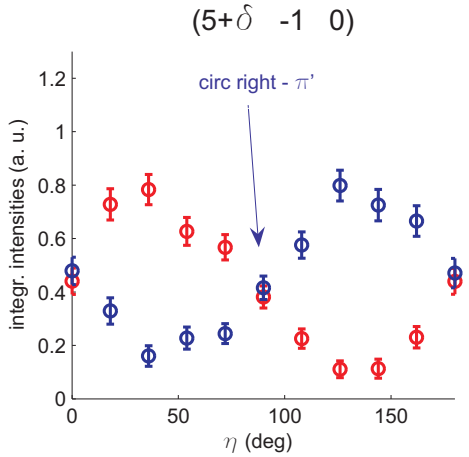

Figure 4.20: Scaling of the data collected in peak $(5+\delta, -1, 0)$: the circular right-π' intensity (blue arrow) is corrected on the basis of the newfound results. All the other intensities for this peak are corrected by the same multiplying factor.

direction of the scattering vector ('$\theta - 2\theta$'), and the orthogonal direction identified by the motor γ of the diffractometer (cf. Fig. 3.2 - (c)). The 'θ' and '$\theta - 2\theta$' scans have been numerically integrated (with subtraction of the background) and averaged together, while the 'γ' scan has been used as a confirmation that all the signal was being integrated by the surface of the analyser.

These intensities have been used to correct the Stokes scans. The procedure is illustrated in Fig. 4.20 in the case of the reflection $(5+\delta, -1, 0)$. The value of the intensity measured in the channel circular right-π' has been used to set the data point indicated by the arrow in the figure; all the other data points for both circular incidences have been scaled by the same factor. The intensities measured in the other channels have been used as a check of this scaling procedure.

The same numerical procedure to optimise the magnetic structure already used in the previous section 4.1.5 has been repeated on the corrected data. Calculations provided estimates of $m_a^{CT} = 0.55(50)$ and $m_b^{CT} = 0.35(35)$ (units of μ_B), with a 87(4) % domain type 1 population, and a phase difference of 0.50(2) π. It can be noted that the percentage of domains has remained reasonably constant through the whole experiment. It is confirmed that the cross-tie moments are indeed smaller than expected and may even not be ordered at all. However, the error bars on the magnitudes remain quite large, as opposed to the value of the phase relationship ϕ_{SC} which is accurately determined to be close to $\pi/2$, even in the case of very small magnitude of the cross-tie moments. The analysis of more recent neutron diffraction measurements seems consistent with the possibility of there being no moment on the cross-tie nickel ions (I. Cabrera et al., unpublished). Thus it may be concluded that the cross-tie moments are most likely negligible, from which it follows that spatial inversion symmetry is broken by the non-collinear magnetic structure of the spine-sites alone. This frustration of the cross-tie sites can be simply explained within a model with isotropic interactions between the spine and cross-tie sites since then there would be zero mean field on the crosstie sites. This possibility was raised by Kenzelmann et al. [10], although they concluded that this frustration had been lifted by anisotropic pseudodipolar interactions, to explain their proposed LTI structure as

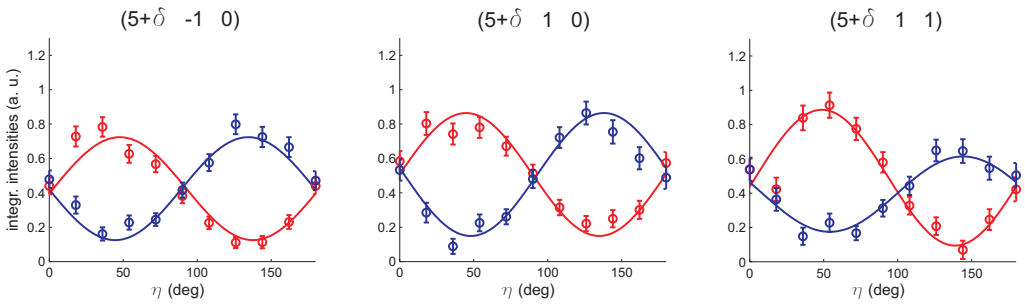

Figure 4.21: Best fit obtained with the refined model detailed in the text: $m_a^{CT} = 0.55\ \mu_B$, $m_b^{CT} = 0.35\ \mu_B$, a 87 % domain type 1 population, and a phase difference of 0.50 π. This fit gives $\chi^2 = 1.5$ (compare with the previous result in Fig. 4.19, in which the refined intensity measurements had not been incorporated).

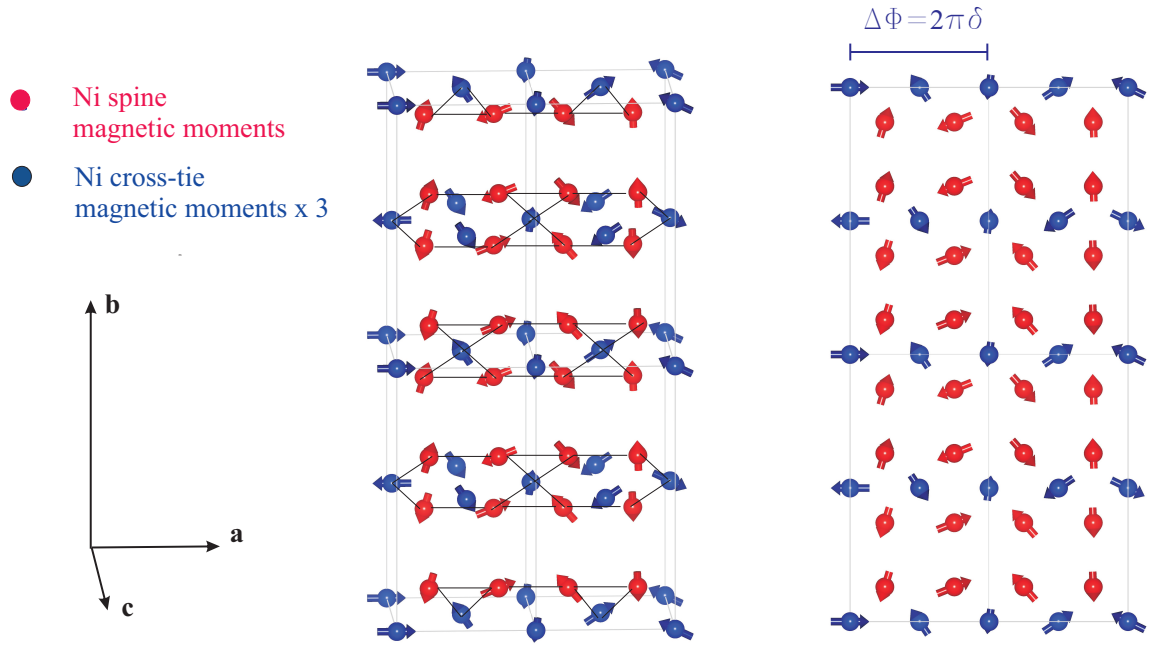

Figure 4.22: Magnetic structure of $Ni_3V_2O_8$ according to the refinement described in the present work. The unit cell is delimited by the gray lines; a projection into the $(\mathbf{a}, \mathbf{b})$ plane is shown in the right. The magnitude of the magnetic moments in the cross-tie sites is multiplied by a factor of 3 to make them more visible; the phase relationship between spine and cross-tie modulations is fixed at $\pi/2$, according to the fit.

shown in Fig. 4.9. The refined magnetic structure is depicted in Fig. 4.22.

4.2 Imaging of the magnetic domains

The data in Fig. 4.21 also suggest a novel route to imaging multiferroic domains. The reversal evident in the sign of the Stokes parameter P_2 when switching the incident X-ray polarisation, would also occur for fixed incident polarisation if the cycloidal magnetic domain switched its handedness (cf. Chapter 2). It follows that the domain population can therefore be determined at different points in the sample by determining the value of P_2.

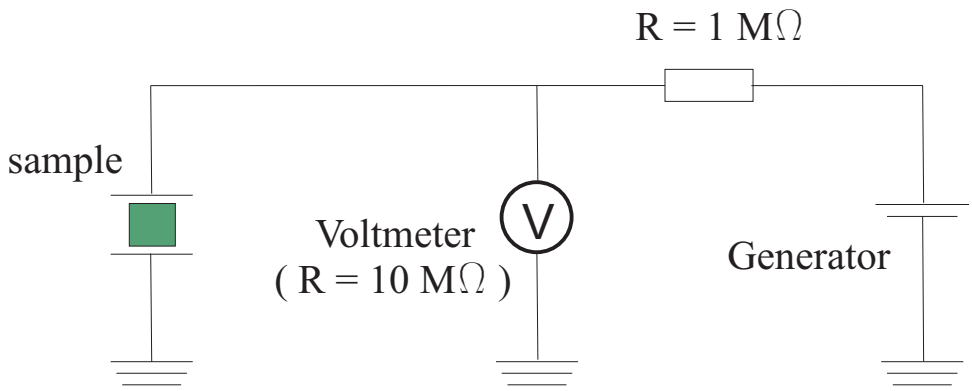

Figure 4.23: Schematic of the electric setup. A Keithley multimeter was mounted in parallel with the sample, to act as a voltmeter and offer a direct measurement of the applied voltage.

4.2.1 Experimental method

The application of electric field has been completed by the insertion of a multimeter device, as per Fig. 4.23, to carefully control the voltage at the surfaces of the sample, and to check for any abrupt changes or discharges. The sample has been cooled down in no applied electric field into the LTI phase, and the magnetic peak $\mathbf{k}'-\mathbf{k} = (5+\delta, 1, 0)$ has been aligned. The size of the incident beam has been narrowed down to 0.25 x 0.25 mm, to maximise the resolution whilst still giving a reasonable count rate in the detector; given the tilt of the sample with respect to the beam (motor $\theta = 40.91°$), the spot size on the surface of the sample turns out to be 0.25 mm (vertical) x 0.257 $\sin(\theta)$ mm (horizontal) = 0.25 x 0.382 mm. The polarisation of the incident light was turned into circular left, then circular right. For each incidence, the intensity of the diffracted beam has been collected in the linear polarisation states oriented along $\eta = 45°$ and 135°.

The sample was then translated in order to test different zones of its surface. From a preliminary scan in the motors associated to the vertical and the horizontal translation, it was seen that the overall zone that could be tested has dimensions of at least 1.3 (v) x 0.66 (h) mm. It was decided to measure a grid of 10 points (v) x 5 points (h), spaced by each other (centre to centre) by 0.1 (v) and 0.125 (h) mm. The overlap between different spots is enough to allow a good accuracy of the data. The situation is shown in Fig. 4.24 (all dimensions are in scale).

All the measured intensities have been corrected by background subtraction. The background has been measured by driving the sample off diffraction (motor θ shifted as usually by 0.2°), and by performing a mesh with a more limited number of spots: 3 points (v) x 3 points (h), spaced by each other (centre to centre) by 0.35 (v) and 0.2 (h) mm. These intensities have been averaged together, and subtracted to each of the spots measured in diffraction condition (see Fig. 4.25). This procedure has been repeated for every channel of the diffracted light ($\eta = 45°$ and 135°) and every polarisation state of the incident light (circular left and right). The data have then been processed by the Matlab

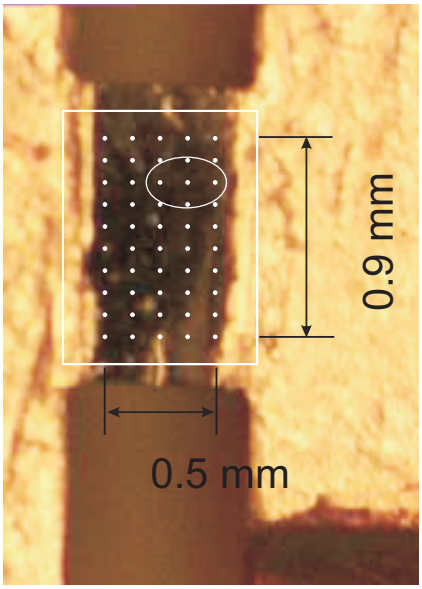

Figure 4.24: Image of the sample sandwiched between the Cu electrodes used to form a capacitor. The dotted mesh superimposed on the image indicates points at which the domain population was determined. The ellipse indicates the size of the X-ray beam.

function *countourf*, that interpolates them to give the graphical result displayed in Fig. 4.26.

This allows to extract for each spot the P_2 parameter of the diffracted beam, as per Eq. 3.4

$$P_2 = \frac{I(\eta = 45°) - I(\eta = 135°)}{I(\eta = 45°) + I(\eta = 135°)}.$$

From the analysis done in the previous experiment, it was known that the parameter P_2 is extremely sensitive to the percentage of cycloidal domains, while the sensitivity of P_1 is negligible. Therefore the measurements focused on the former, allowing a strong contrast to be detected between the two magnetic domains. For every spot, the corresponding value of P_2 has been extracted, and the interpolation gives the picture of Fig. 4.27.

To connect the value of P_2 to the actual percentage of domains, the model of the magnetic structure proposed in 4.1.6 has been adopted. Given an incident polarisation (say circular left), the expected Stokes parameters in the satellite $(5 + \delta, 1, 0)$ are calculated as a function of the percentage of domains. This is shown in Fig. 4.28 and 4.29. Then, the actual value of P_2 found in each spot is related to the corresponding percentage value. The interpolation of all these values gives the pattern shown in Fig. 4.30.

Two important checks have been done at this point. First, the two circular incidences are expected to give similar results in terms of the percentage of domains. This is in fact confirmed by the data. Secondly, they should also give similar results in terms of the average intensity between $\eta = 45°$ and $\eta = 135°$. This has been calculated and confirmed (Fig. 4.31).

4.2.2 Results

The same procedure now outlined has been repeated after applying electric field on the sample, and mantaining the temperature fixed so to not exceed the boundaries of the the LTI phase. The

application of the electric voltage was only limited by the problem of discharges in the exchange gas surrounding the sample space; despite this constraint, it was possible to complete a hysteresis loop that shows very clearly how the electric field controls the percentage of domains. The results are summarized in Fig. 4.32. They demonstrate that the technique was able to resolve inhomogeneities in the domain populations with good resolution. Inspection of the individual images reveals that for zero applied electric field the distribution of the two domains is not equal, but instead shows a preference towards Domain 2, i.e. moments rotating anticlockwise. This may either be a surface strain effect or some memory effect of an earlier domain state induced by field cooling in previous experiments, as has been observed in $MnWO_4$ [66]. Applying an increasing electric field along $-\mathbf{b}$ leads to a reversal of the domain populations, with the production of almost a mono-Domain 1 state for E = +270 V/mm. The evolution of the domain populations is gradual, with the boundary between the two shifting as a function of applied electric field, as opposed to the nucleation of Domain 1 within Domain 2 leading to a more randomised distribution. When the electric field direction is then reversed the domain distributions are little changed until between -250 V/mm and -370 V/mm the distribution is again reversed with a preference towards Domain 2. Whilst the domain populations are preserved on returning to E = 0 V/mm, due to time constraints no additional data were collected for applied positive electric fields.

One way to quantitatively render the domain homogeneities is to average the images over different areas of interest to produce position dependent magnetic domain population hysteresis loops. Figure 4.33 - (a) shows the domain population averaged over the entire sample. On average the excess population of Domain 2 in zero field is quickly reversed in a positive applied field, with Domain 1 prevailing such that even large negative fields are incapable of restoring an excess of Domain 2. In Fig. 4.33 - (b), the response from the bottom left-hand corner is plotted, where it is clear that close to the edge of the sample there is strong pinning of Domain 1 with it dominating at all fields. Imaging allows these edge effects to be excluded from the data (Fig. 4.33 - (c)), and restores more of a symmetrical character to the electric field dependence of the magnetic domain population. This allows to compare our data with the electric polarisation measurements of Cabrera et al [13], as shown in Fig. 4.33 - (c), where an excellent agreement is found. The result establishes the link between the magnetic domains and the electric polarisation in multiferroic $Ni_3V_2O_8$, proving that by imaging the magnetic domains we are in effect also imaging the ferroelectric domains.

4.3 Conclusions and future outlook

In conclusion, the present work has refined the magnetic structure of $Ni_3V_2O_8$, confirming the cycloidal ordering of the Ni spins on the spine sites whilst finding that there is no ordered moment on the cross-tie sites, thus indicating that it is the magnetic order on the spine sites alone that breaks inversion symmetry. Further, it has successfully demonstrated how polarisation enhanced X-ray imaging (PEXI), through the contrast provided by the magnetic structure, enables the imaging of the magnetic domains in $Ni_3V_2O_8$ which endow this material with its multiferroic properties.

Comparison of the magnetic domain population hysteresis loops with bulk electric polarisation measurements reveals the coupling between the magnetic and ferroelectric domains. This opens the

prospect of using this technique to image multiferroic domains in related materials, and even in operational devices. With the improved focussing offered by beamlines currently under development the spatial resolution for this technique will be reduced to 100 nm and below, at which point it will be possible not only to image the domains themselves, but also the structure of the domain walls, the engineering of which ultimately determines the usefulness of a given material.

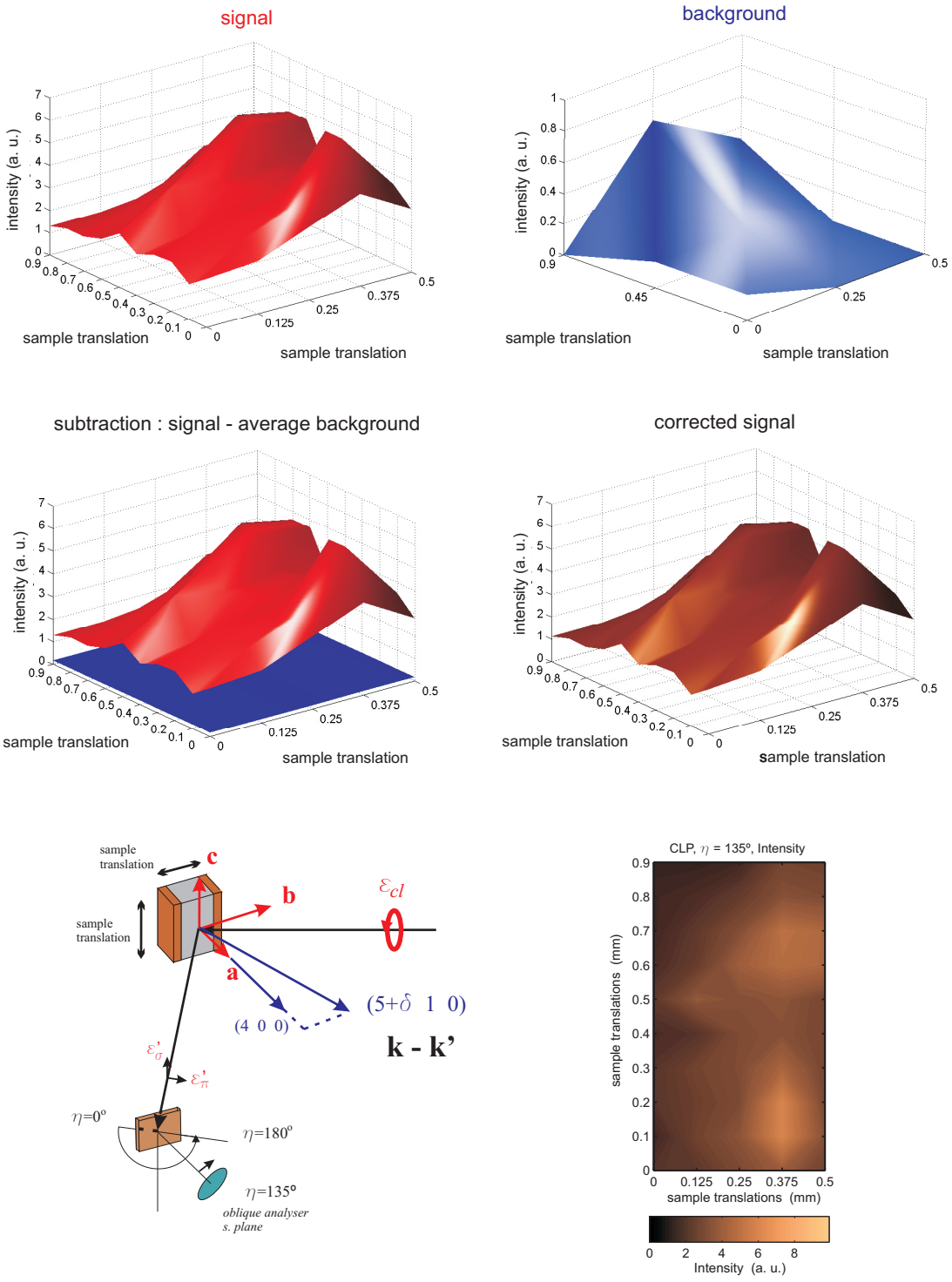

Figure 4.25: Procedure for the measurement of a mesh on the magnetic reflection (5+δ, 1, 0). In this case the incident beam is CLP and the detector is positioned at $\eta = 135°$, as depicted in the setup scheme. The measured intensity represents the photon counts normalised by the incident beam (counting time was 120 seconds per point). The first translation mesh is collected on the magnetic peak (red) while the second one is the background found at 0.2° away from the peak in θ (blue). The averaged background is subtracted from the signal to give the final result. The scale of the translations here and in all subsequent meshes is to be compared to the dimensions of the sample surface reported in Fig. 4.24.

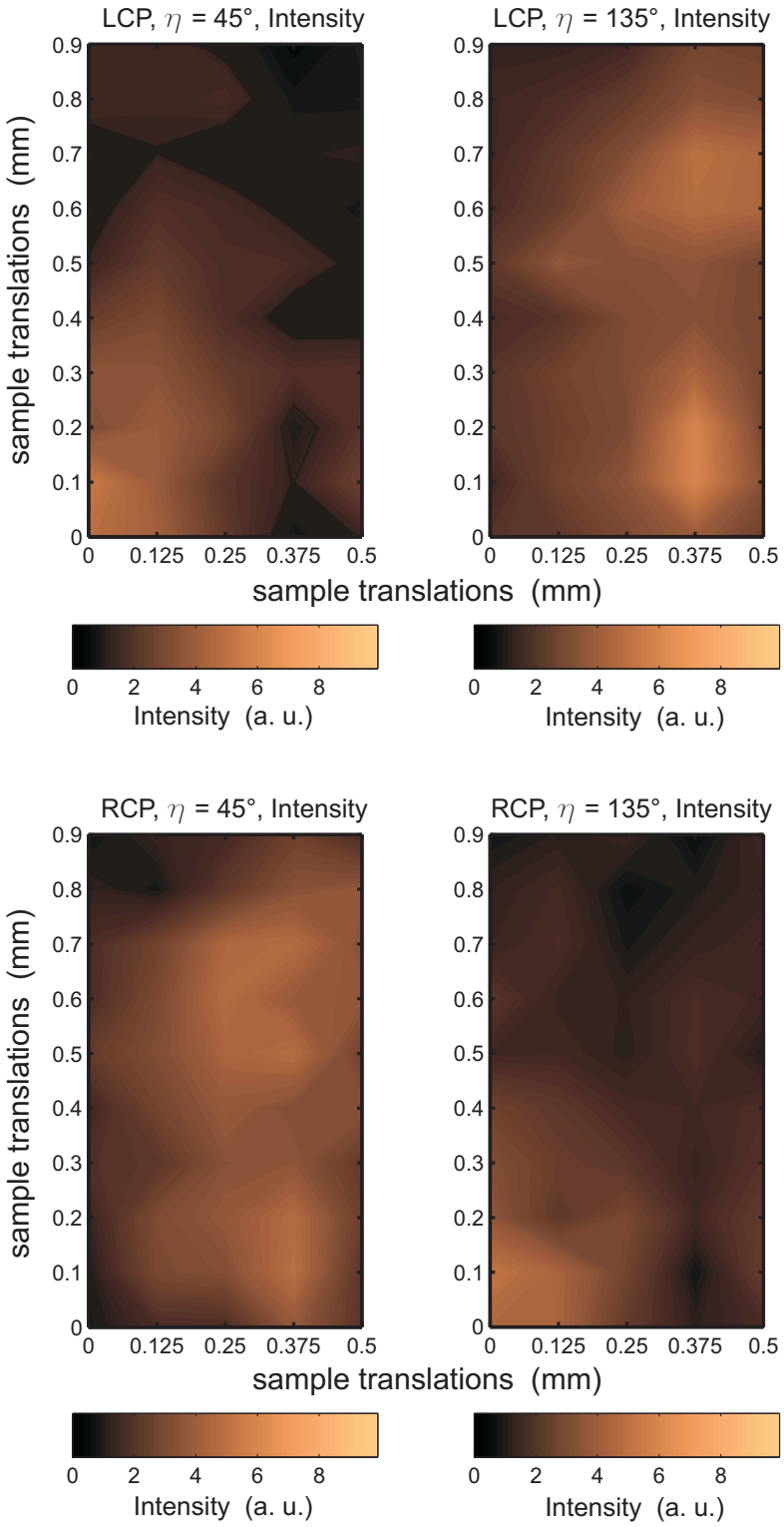

Figure 4.26: Maps of the intensities measured by the mesh, corrected by background and interpolated on the surface of the sample. The results are obtained with incident light polarisation tuned to be circular left (upper panel) and circular right (lower panel), while the polarisation channels of the diffracted light are oriented along $\eta = 45°$ (maps on the left) and 135° (maps on the right).

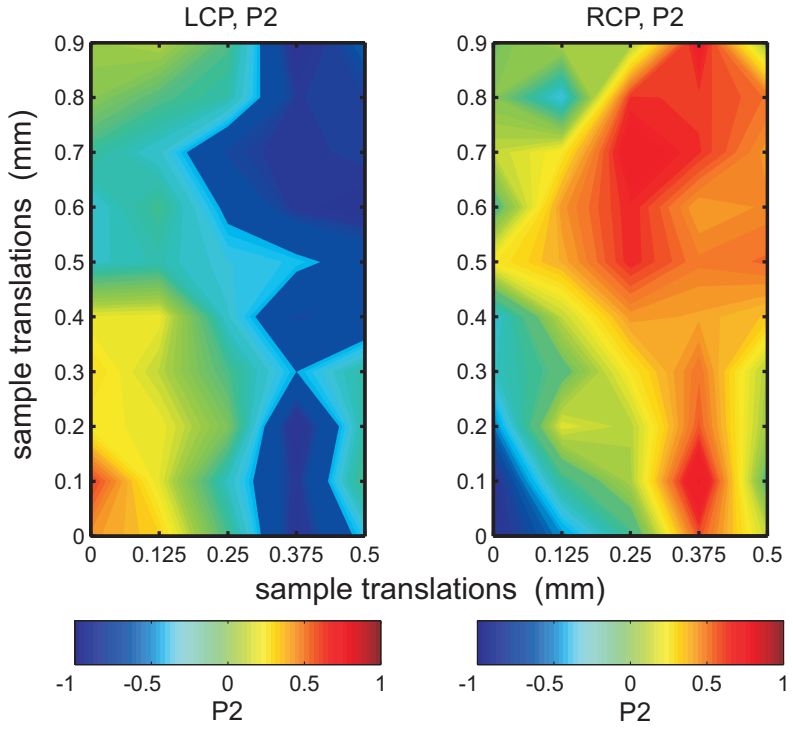

Figure 4.27: Maps of the values for the parameter P_2 extracted from the mesh, and interpolated on the surface of the sample. The results are obtained with incident light polarisation tuned to be circular left (map on the left) and circular right (map on the right).

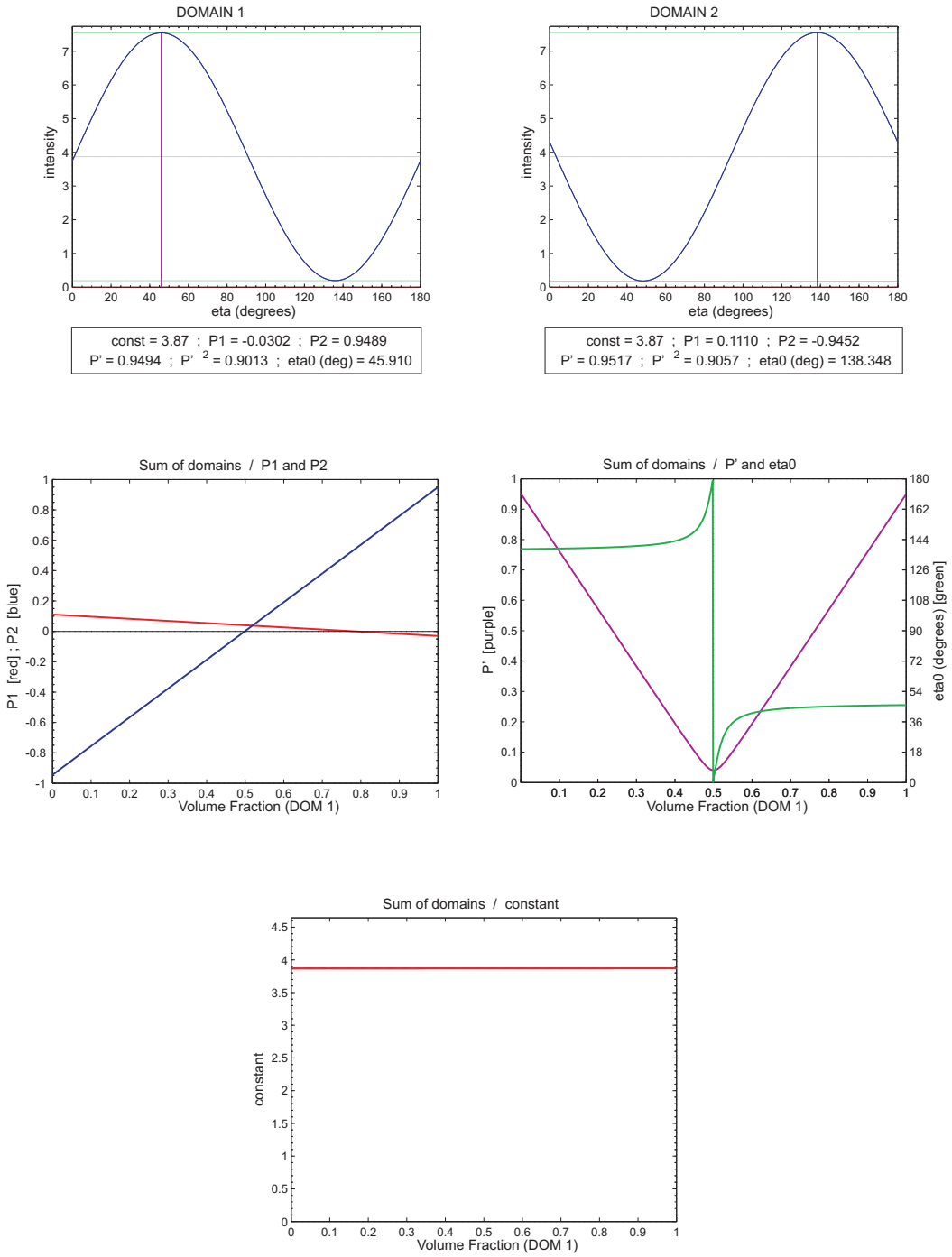

Figure 4.28: Calculation of the expected polarisation for the diffracted beam when the incident light is circular left. In the first two sketches (first row), the Stokes scans that would emerge from a purely Domain 1 and a purely Domain 2 magnetic structure are shown. In the third and fourth sketches (second row), it is shown the dependence of the parameters P_1 (red) and P_2 (blue), and the parameters η_0 (green) and P' (purple), on the volume fraction of Domain 1 with respect to the total volume of the sample. In the fifth sketch, the variation of the constant representing the average intensity is shown. It should be noted that P_2 is very sensitive to the percentage of domains, while P_1 and the average intensity are almost insensitive to it.

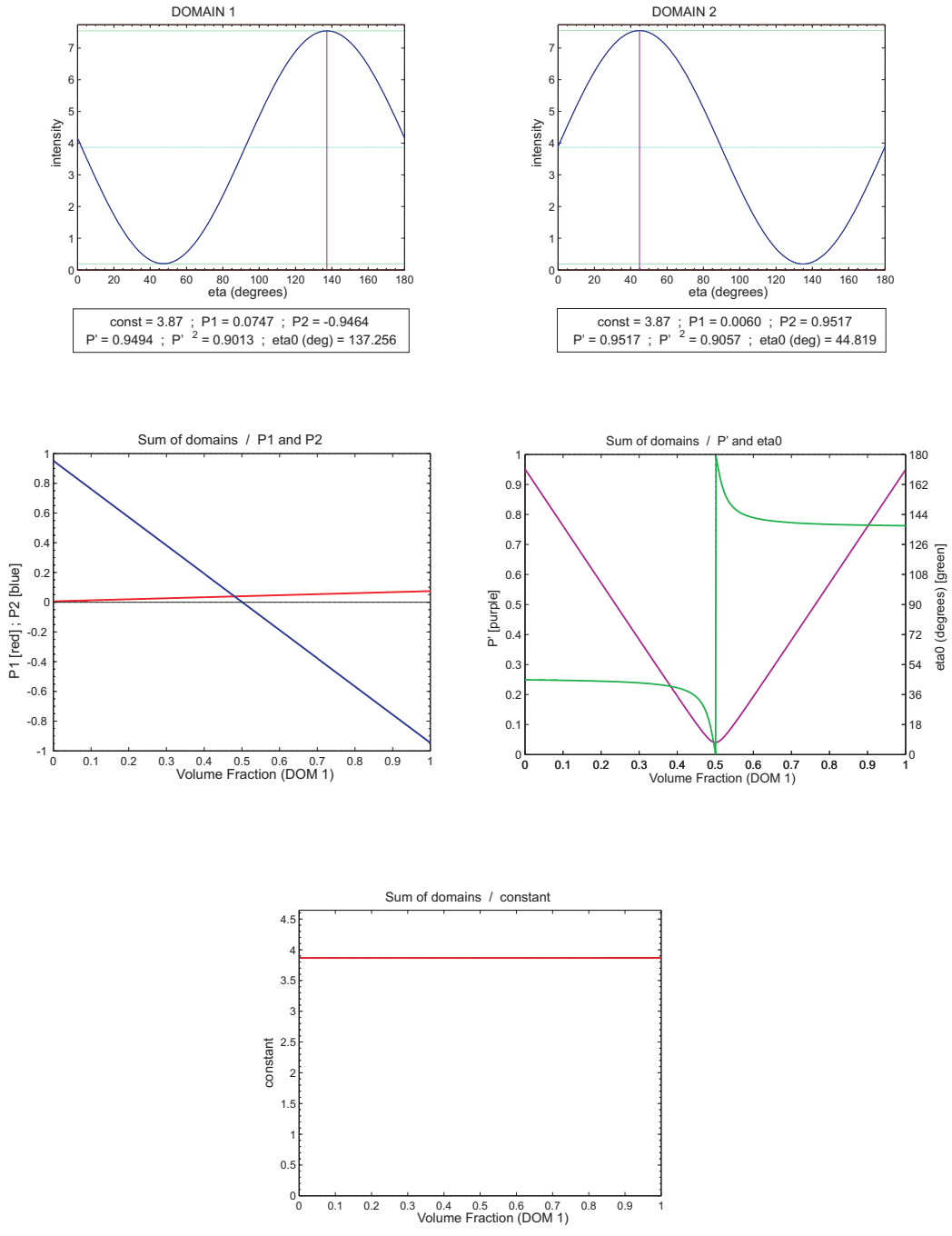

Figure 4.29: Calculation analogous to the one in Fig. 4.28, but for circular right polarisation of the incident light, shown as a comparison. Note the radically different dependence of the parameter P_2 on the volume fraction of the magnetic Domain 1.

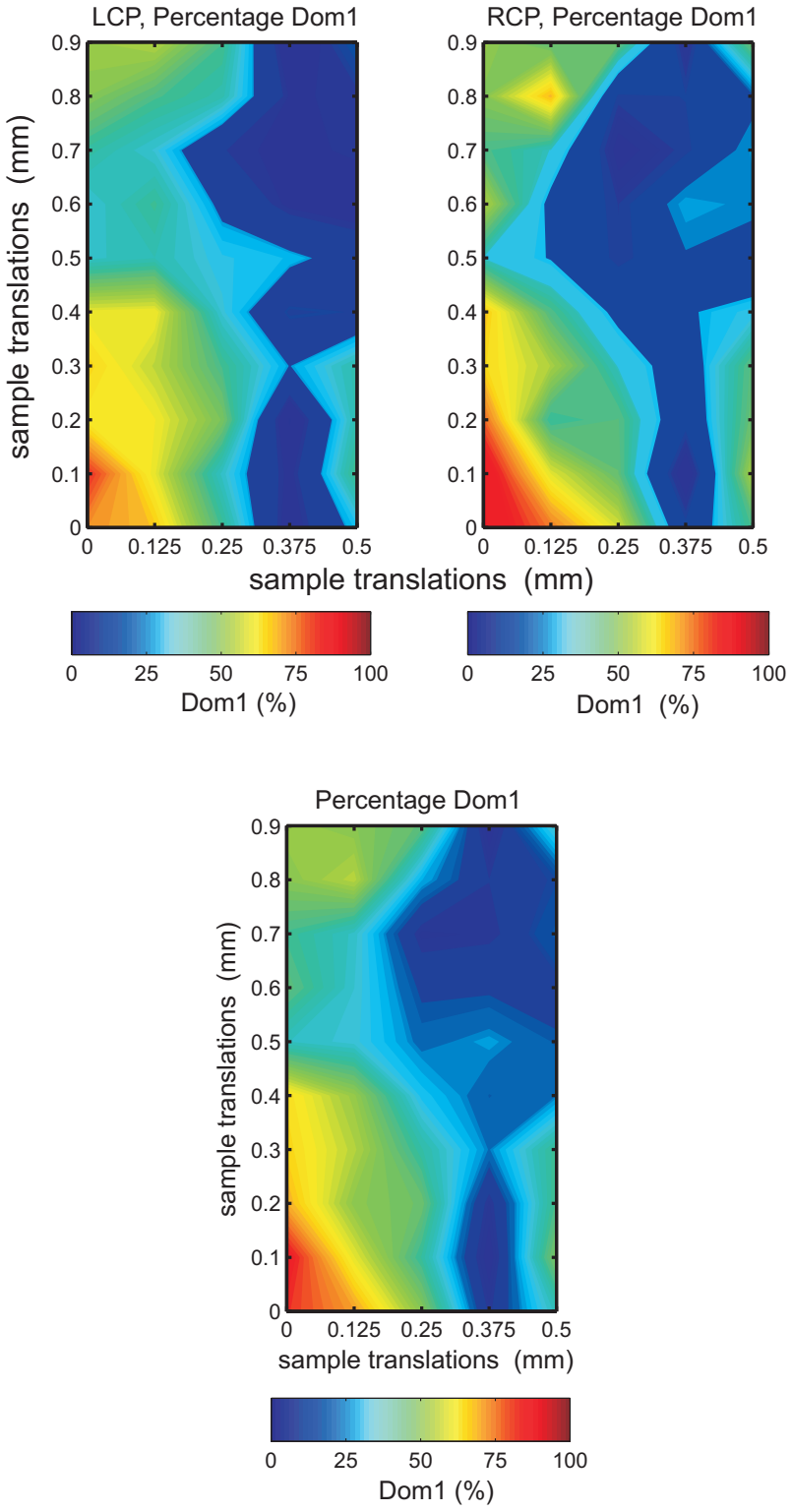

Figure 4.30: In the upper part of the figure: maps of the volume percentage of Domain 1 extracted from the mesh, and interpolated on the surface of the sample. The results are obtained with incident light polarisation tuned to be circular left (map on the left) and circular right (map on the right). The two are very similar, as it should be expected. The final values for the percentage have been taken as an average between the two (in the lower part of the figure).

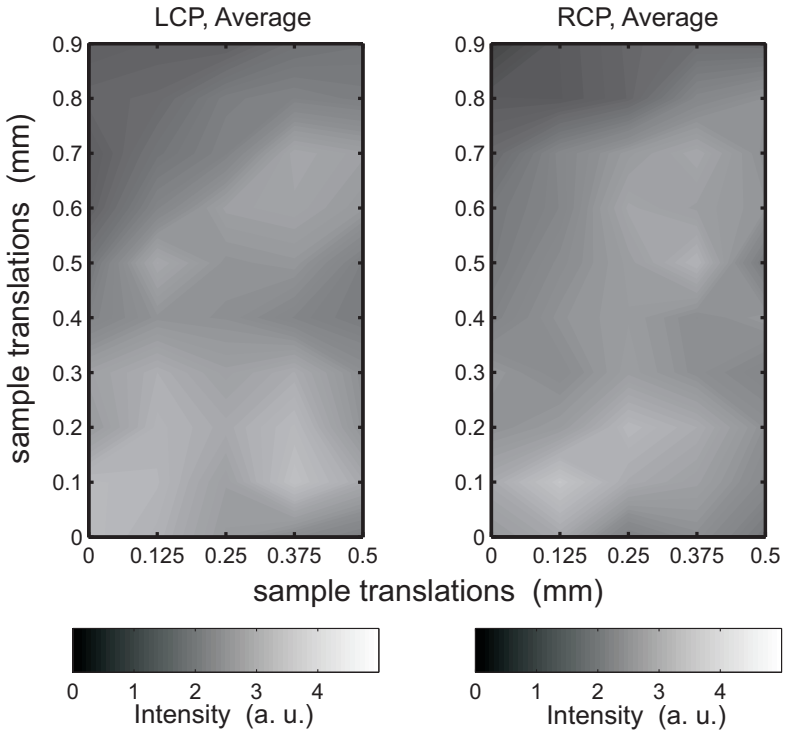

Figure 4.31: Maps of the average intensities measured by the mesh, and interpolated on the surface of the sample. The results are obtained with incident light polarisation tuned to be circular left and circular right. The two are very similar, as it should be expected, since the average intensity should not depend on the percentage of domains.

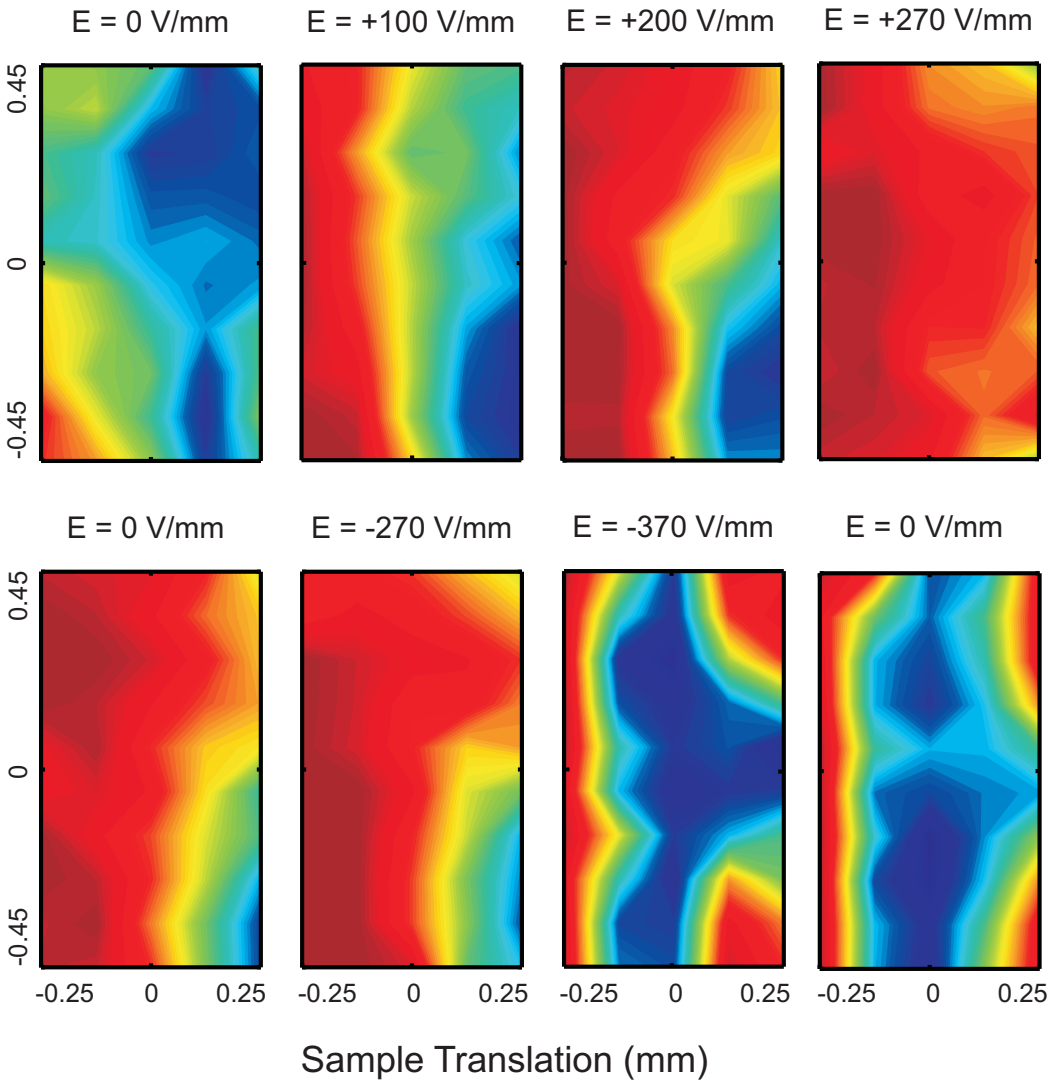

Figure 4.32: Images of the domain populations as a function of applied electric field for the magnetic reflection $(5 + \delta,\ 1,\ 0)$, where the colour represents the percentage of the clockwise and anti-clockwise magnetic cycloidal domains.

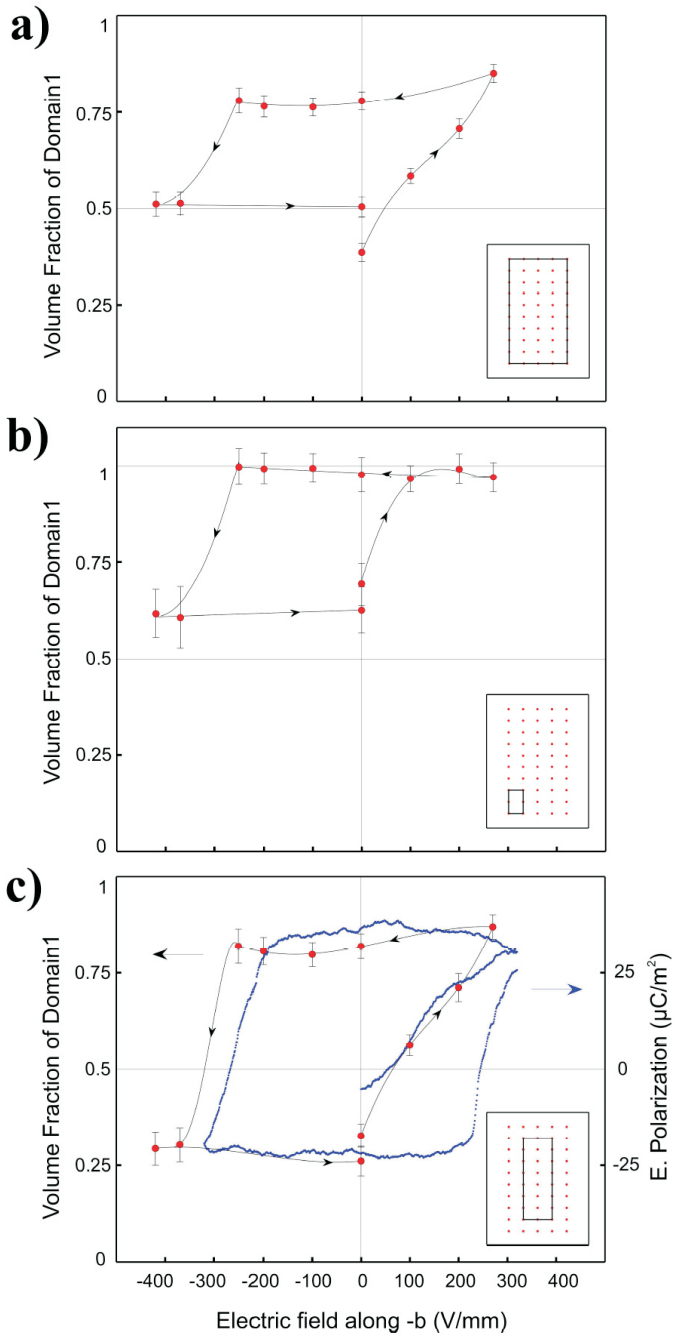

Figure 4.33: Position dependent magnetic domain population hysteresis loops obtained from the domain images shown in Fig. 4.32 averaged over different areas of interest: (a) entire sample area; (b) edge; (c) central region. In (c) the data are compared with bulk measurements of the electric polarisation published in [13], where an appropriate scaling has been applied.

Chapter 5

Magnetic Structure Refinement in $TbMnO_3$

Non-resonant X-ray magnetic scattering has been used to study the magnetic structure of multiferroic $TbMnO_3$ in its ferroelectric phase. Circularly polarised X-rays were combined with full polarisation analysis of the scattered beam to reveal important new information on the magnetic structure of this canonical multiferroic. An applied electric field is shown to create essentially a single magnetic domain state in which the cycloidal order on the Mn sublattice rotates either clockwise or anticlockwise depending on the sign of the field. It is demonstrated how this technique provides sensitivity to the absolute sense of rotation of the Mn moments and to components of the ordering on the Tb sublattice and phase shifts that earlier neutron diffraction experiments could not resolve, including discrimination between spin and orbital component of the Tb magnetic moments.

5.1 Phase diagram and previous diffraction studies

The phase diagram of $TbMnO_3$ (Fig. 5.1) is characterised by a cycloidal magnetic phase in which the magnetic moments rotate within the plane $(\mathbf{b}, \mathbf{c})$ while propagating along $\mathbf{b}$, and a spontaneous electric polarisation occurs in the direction $\pm\mathbf{b} \times (\mathbf{b} \times \mathbf{c}) = \pm\mathbf{c}$, thus meeting the features described in Chapter 1 for spin-driven magneto-electric multiferroics. The ferroelectricity and the cycloidal magnetic structure are coupled to a relevant extent, as demonstrated by two separate effects: the flop of the direction of the spontaneous electric polarisation, by application of a magnetic field, and the selection of one cycloidal magnetic domain, by means of an applied electric field. In this chapter the structural, magnetic and ferroelectric properties of $TbMnO_3$ in absence of external fields will be reviewed. The compound is an orthorhombically distorted perovskite whose cell parameters, at room temperature, are $a_0 = 5.3019$ Å, $b_0 = 5.8557$ Å, and $c_0 = 7.4009$ Å. The crystallographic symmetry belongs to the space group *Pbnm* (No. 62 in International Tables for Crystallography [62]). $TbMnO_3$ is both paramagnetic and paraelectric for temperatures above $T_N = 41$ K. Early measurements of the magnetic susceptibility on powder samples, conducted by Quezel et al. [67], have shown that the Mn^{3+} moments order at T_N; an anomaly is detected at $T_C = 28$ K, thus identifying a second magnetic transition; finally, a third transition is found at $T_N^{Tb} = 9$ K. These

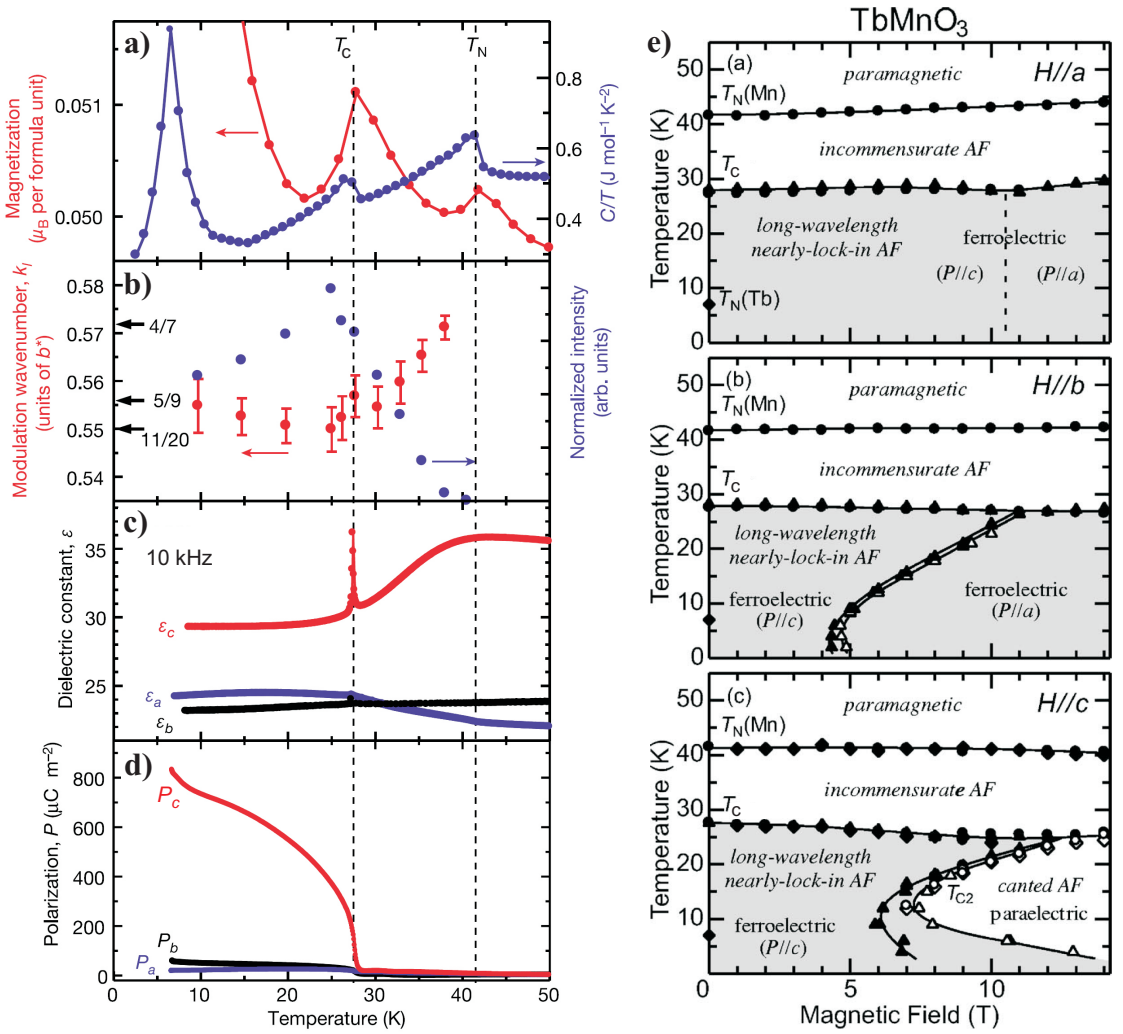

Figure 5.1: Study of the phase diagram of $TbMnO_3$, adapted from [1, 69]. In the left panel, measurements at zero field: (a) temperature profiles of magnetisation and specific heat divided by temperature; (b) wavenumber of lattice modulation τ_L (see text); (c) dielectric constant ϵ at 10 kHz; (d) and electric polarisation **P** along the principal axes in single crystals of $TbMnO_3$. In the right panel (e), the temperature versus magnetic field phase diagram for $TbMnO_3$ for magnetic field applied along the three axes. The measurements under applied field are shown in detail in Chapter 6. Circles, triangles, and diamonds represent the data obtained by measurements of dielectric constant, pyroelectric (or magneto-electric) current, and magnetisation, respectively. Open and closed symbols denote the data obtained with decreasing temperature (or increasing magnetic field) and increasing temperature (or decreasing magnetic field), respectively. Gray regions indicate ferroelectric phases.

three magnetic phases will be referred to as phase I (41-28 K), phase II (28-9 K), phase III (below 9 K). Experiments at zero field ([1], [68], [69]), summarised in Fig. 5.1, have measured a spontaneous ferroelectric polarisation along the **c** axis, emerging below $T_C = 28$ K; its magnitude, measured at T = 4 K, is 8×10^{-4} C m^{-2}.

Several neutron and X-ray diffraction studies have been performed to reveal the magnetic structure in phases I, II and III. Fundamental experiments were carried out by Quezel et al. in 1977 [67], Blasco et al. in 2000 [70], Kimura et al. in 2003 [1], Kajimoto et al. in 2004 [29], and Kenzelmann et al. in 2005 [2], which led to a classification of the superlattice diffraction peaks and to the

characterisation of their temperature dependence.

- *Magnetic reflections at propagation vector τ, and higher harmonics.* Upon cooling the sample below the first transition, it is found that incommensurate magnetic reflections appear at $(h, k \pm \tau, l)$. All studies confirm that A-type reflections ($h + k = even, l = odd$, as named within Bertaut's representational theory [71]) are dominant. The propagation wave vector τ slowly decreases from 0.286 at T_N to 0.276 at T_C.

  After the second transition, the reflections increase in intensity while the propagation vector is more or less constant at 0.276. These reflections were initially attributed to a pure Mn contribution [67]; only in more recent studies [72] - [74] it has been understood that the moments on the Tb atoms are an important contribution to those magnetic peaks.

  There is no complete agreement about the presence of weaker G-type ($h + k = odd, l = odd$), C-type ($h + k = odd, l = even$), F-type ($h + k = even, l = even$) peaks. In the first study by Quezel et al., only weak G-type peaks are reported below 20 K, but no F and C-type peaks were found. This was confirmed by Blasco and co-workers [70]. Kajimoto et al. [29] measure all the four types of reflections, finding G, C, F to be extremely weak in phase I, and slightly more intense in phase II and II. The study conducted by Kenzelmann et al. [2] only detects the strong A-type reflections. More recent measurements concentrate on other types of peaks [75, 76]. It is agreed that the A-type peaks strongly dominate the others in intensity, and must be the starting point to determine the magnetic structure.

  Kajimoto el al. [29] also report about third-harmonic peaks for A, G and C-type reflections below T_C. While this result shows that the incommensurate modulation of the magnetic moments is not purely sinusoidal, the relative weakness of these higher-harmonic peaks leads to the conclusion that the deviation from an ideal sinusoidal modulation is small.

- *Lattice reflections at propagation vector* 2τ. Kimura et al. [1] find lattice reflections at a propagation vector τ_L corresponding to the double of the magnetic vector τ. The temperature dependence of τ_L is strictly related to that of τ, slowly decreasing from T_N to T_C, and then becoming more or less constant in phase II and III . Hence the relation $\tau_L \sim 2\tau$ holds for the different magnetic phases. It is known that the crystallographic deformations upon magnetic ordering are caused by the magnetic atoms increasing their exchange interaction energy by shifting their positions (exchange striction). The super-lattice reflections due to atomic displacement can be regarded as a second-harmonic that is magnetoelastically induced by the sinusoidal magnetic order [1].

- *Magnetic reflections at propagation vector τ_T.* Finally, in phase III additional peaks appear at $(h, k \pm \tau_T, l)$, $\tau_T = 0.424$. They were first found by Quezel and co-workers [67] and are attributed to the Tb^{+3} moments. The study by Blasco et al. [70] confirms this result, but the broad shape of the reflections leads the authors to conclude that the Tb order is short-ranged. In the study by Kajimoto et al. [29], these reflections are instead quite sharp and intense, and coupled with corresponding super-lattice reflections at $2\tau_T$, that show the same temperature dependence by also disappearing above 9 K.

The magnetic structure has been extracted from a fit of the observed peaks. In phase I, the A-type magnetic reflections are found to arise from a collinear sinusoidally modulated spin arrangment of the Mn moments, lying along the **b** axis. This was already reported by Quezel [67], and confirmed by all subsequent studies. In phase II, it was initially thought [67] that the structure would remain collinear with spins directed along **b**. A major improvement in the understanding of the magnetic structure was achieved by Kenzelmann et al. in 2005 [2]. A large number of $(h, k \pm \tau, l)$ A-type, first-harmonic magnetic peaks were measured in phases I and II. The range of possible magnetic structures was narrowed down by representational analysis, in order to identify the irreducible representations allowed by the symmetry. The relative intensities of the measured peaks were used to establish the irreducible representations and the magnitude of the magnetic moments which would best fit the data. While confirming the results previously given for phase I, this approach led to a radically different conclusion about the magnetic structure in phase II. It was found that the Mn moments are modulated in a cycloid lying in the $(\mathbf{b}, \mathbf{c})$ plane, and the Tb moments, essentially oriented along the **a** axis and with possible undetermined components along the **b** and **c** directions, also contribute to a significant extent to the overall magnetization. The presence of a cycloidal structure in the $(\mathbf{b}, \mathbf{c})$ plane is compatible with the appearance of a ferroelectric polarisation along the direction **c**, following the phenomenological description of magneto-electric multiferroics given in Chapter 1.

While the magnetic and magneto-electric response of the system under the application of a magnetic field has been accurately investigated, the phase diagram of $TbMnO_3$ upon the application of electric field is only the subject of more recent research. The most notable study is the one conducted by Yamasaki et al. [77], showing a reverse magneto-electric effect (manipulation of the magnetic structure by an applied electric field). As the direction of the spontaneous polarisation is related to the handedness of the rotation of the spins in the cycloid, when the system is brought into its cycloidal phase (phase II), it can be expected that a melange of magnetic domains is present, thus averaging the overall polarisation to zero. A small poling electric field (160 kV/m), applied along the direction of the spontaneous polarisation while cooling down the system, is able to select the sign of the cycloidal handedness, thus driving the magnetic structure towards a monodomain state. This result has been tested by polarised neutron diffraction and indeed confirmed by comparing the relative intensities of satellite reflections (h k+τ l) and (h k-τ l). This magneto-electric coupling was used in the present work to drive the sample into a monodomain state, and allow the refinement of the magnetic structure.

5.2 Experimental setup

The experimental setup followed the standard configuration described in section 2.1.5 with the Orange cryostat. The beam has been aligned at E=7.45 keV, below the Tb-edge, so as to excite non resonant processes. The choice of the same photon energy employed in the experiment with $Ni_3V_2O_8$ allowed the use of the good quality crystal analyser Au (2 2 2) (cf. section 4.1.2). After mounting the analyser on the detector arm and moving the arm in the path of the incident beam, the two alignment scans over the rocking angle θ of the analyser were performed. The cross-talk is confirmed to be less than 0.3 %.

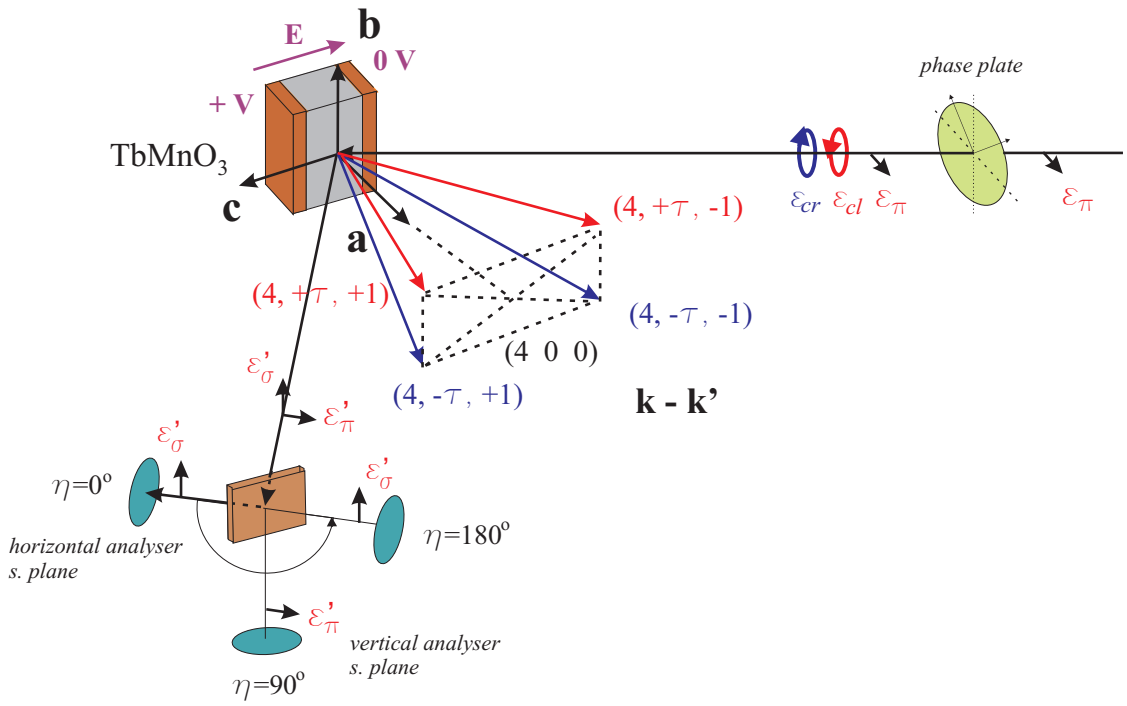

Figure 5.2: Schematic of the experimental setup, including the orientation of the $TbMnO_3$ sample with respect to the scattering plane and the direction of the applied electric field.

The single crystal of $TbMnO_3$ used for the experiments has been grown by the floating zone method at the University of Oxford, by D. Prabhakaran. It has been cut along the main crystallographic axes with dimensions $2 \times 2 \times 0.8$ mm^3, with the shorter axis (0.8 mm) corresponding to the **c** direction. The two **c** faces have been glued by conductive silver paint to the electrodes of the stick, while the **b** axis has been placed vertically, in view of successive advancements in the experimental project involving the application of magnetic field (see Chapter 6). This geometry allows accessibility to a star of four A-type magnetic peaks around the Bragg reflection (4 0 0), characterized by positions $\mathbf{k}' - \mathbf{k} = (4 \pm\tau \pm 1)$. The situation is shown in Fig. 5.2.

The charge reflections close to (4 0 0) and attainable with our setup are typically characterised by an angular width in the Bragg angle θ of $\approx 0.012°$. The reflection (4 0 0) aligned at room temperature is presented in Fig. 5.3. Upon cooling down the sample to T = 15 K, the magnetic reflections are aligned, revealing a typical angular width of $\approx 0.016°$ in θ (see Fig. 5.7). The phase plate alignment optimised the positions for circular left and right polarisation of the incident light, as per Fig. 5.4. These were consistently checked before and after each of the measurements of the Stokes scans on the magnetic peaks.

5.3 Results and interpretation

The overall aim of the experiments can be deconstructed in three separate goals: to demonstrate that the electric field annealing could succeed in creating a magnetic monodomain; to support the previous result by switching the population of magnetic domains when reversing the direction of the poling field; once a monodomain state had been obtained, to extract the fine details of the

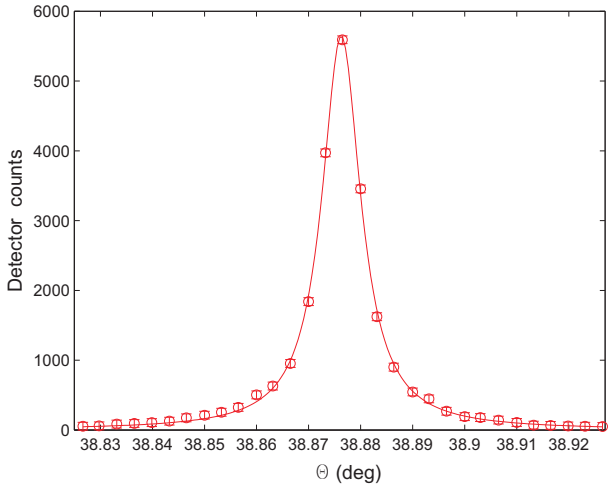

Figure 5.3: Profile of the charge reflection (4 0 0) measured in the polarisation channel π - π'.

magnetic structure. In order to understand the magnetic state of the sample from the features of the diffraction peaks, a preliminary analysis has been carried out on the basis of the magnetic structure proposed in [2] (subsection 5.3.1). The comparison with the data (5.3.2) has subsequently revealed that, while the creation of a quasi-monodomain state and the switching of domain by electric field had been achieved, the details of the magnetic structure were not compatible with the polarisation characterisation of the diffracted beam. A refined model (5.3.4) could then be elaborated on the basis of the newly found results.

5.3.1 Previously proposed magnetic structure

The model proposed by Kenzelmann et al. in [2] suggests that in the incommensurate phase with $k = (0, \tau, 0)$ at T = 15 K two irreducible representations of the little group G_k are required to describe the magnetic structure. The best agreement with the intensity of first-order magnetic Bragg peaks is found with $\chi^2 = 2.19$ for magnetic ordering involving Γ_2 and Γ_3. The character table for the two irreducible representations is

	1	2_y	m_{xy}	m_{yz}
Γ_1	1	1	1	1
Γ_2	1	1	-1	-1
Γ_3	1	-1	1	-1
Γ_4	1	-1	-1	1

.

An explicit description of the magnetic moments on the Mn and Tb sites belonging to the two representations can be given by labeling the atomic positions within the unit cell as

Mn	$(1/2, 0, 0)$	$M1$	Tb	$(1-\Delta_a^{Tb}, \Delta_a^{Tb}, 1/4)$	$T1$
	$(0, 1/2, 0)$	$M2$		$(1/2+\Delta_a^{Tb}, 1/2+\Delta_b^{Tb}, 1/4)$	$T2$
	$(1/2, 0, 1/2)$	$M3$		$(\Delta_a^{Tb}, 1-\Delta_b^{Tb}, 3/4)$	$T3$
	$(0, 1/2, 1/2)$	$M4$		$(1/2-\Delta_a^{Tb}, 1/2-\Delta_b^{Tb}, 3/4)$	$T4$

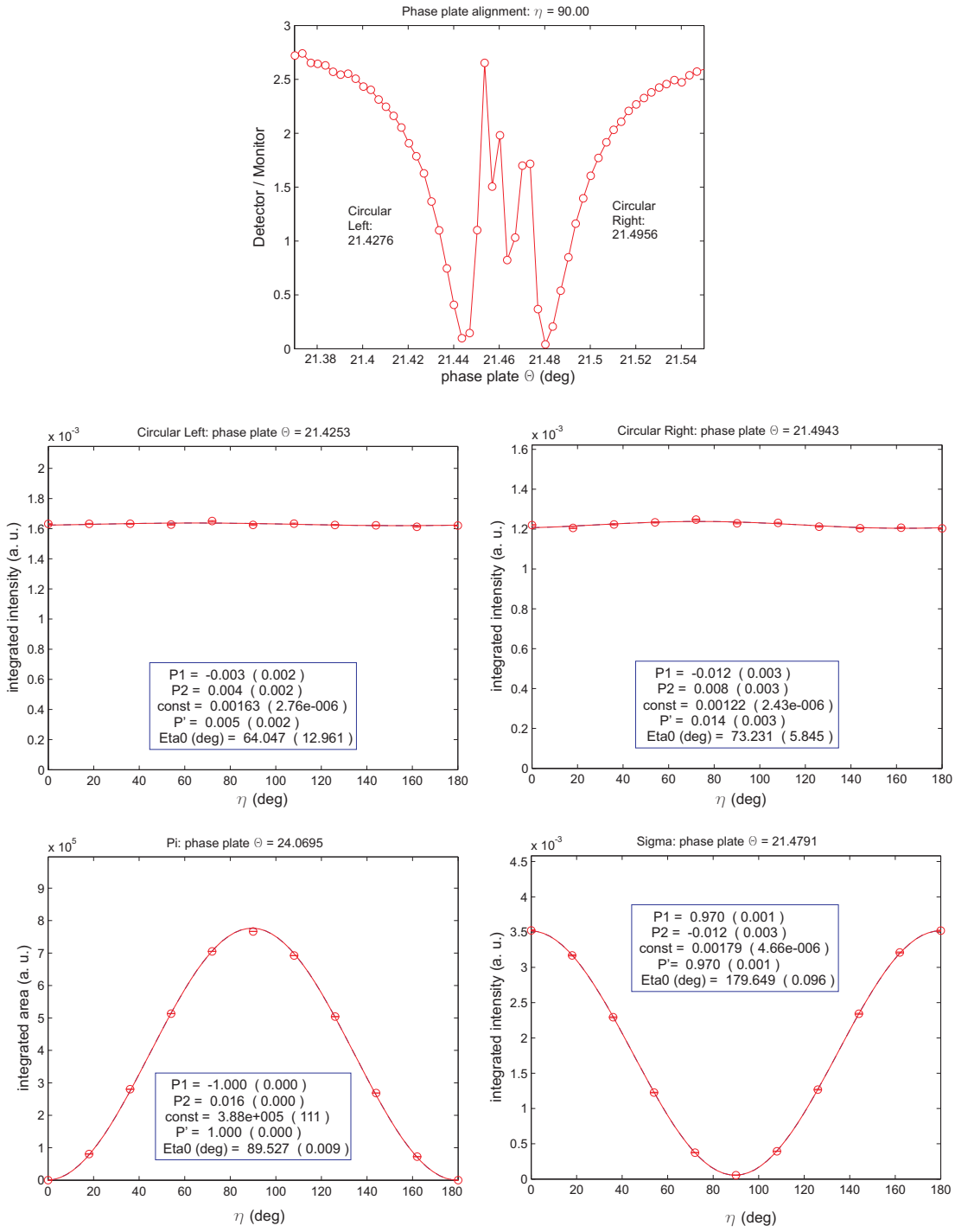

Figure 5.4: Alignment scans of the phase plate, showing the quality of the circular polarisation of the incident beam attained during the experiment. First, the positions of the two circular polarisations are identified from the rocking curve θ of the plate (upper figure). The rotated polarisation is then checked and finely adjusted by means of a full Stokes scan on the direct beam. As a comparison, and to refine the alignment of the plate in the angle χ (cf. subsection 3.1.6), the Stokes scans are performed also in the positions corresponding to vertical rotated polarisation (σ) and unrotated polarisation (π), i.e. away from any Bragg reflection of the plate.

and by applying the symmetry operations of the cell on the magnetic moments within each representation:

magnetic moment			Γ_2	Γ_3
$\mathbf{m}^{Mn}$		$M1$	m_a	m_a
			m_b	m_b
			m_c	m_c
		$M2$	$-m_a$	$-m_a$
			m_b	m_b
			m_c	m_c
		$M3$	m_a	$-m_a$
			m_b	$-m_b$
			$-m_c$	m_c
		$M4$	$-m_a$	m_a
			m_b	$-m_b$
			$-m_c$	m_c
$\mathbf{m}^{Tb}$	*orbit* 1	$T1$	m_a	m_a
	[*orbit* 2]	[$T3$]	m_b	m_b
			0	m_c
		$T2$	$-m_a$	0
		[$T4$]	m_b	0
			0	m_c

Note that the symmetry splits the Tb moments into two orbits ($T1$, $T2$) and ($T3$, $T4$), which representation theory normally treats as independent. However, as suggested by Landau theory [2], the two Tb amplitudes were taken to be identical. The magnetic structure was found to be:

$$\begin{aligned}
\mathbf{m}_{\Gamma 3}^{Mn} &= [0.0(5), 3.9(1), 0.0(7)]\mu_B \\
\mathbf{m}_{\Gamma 3}^{Tb} &= [0, 0, 0(1)]\mu_B \\
\mathbf{m}_{\Gamma 2}^{Mn} &= [0.0(1), 0.0(8), 2.8(1)]\mu_B \\
\mathbf{m}_{\Gamma 2}^{Tb} &= [1.2(1), 0(1), 0]\mu_B
\end{aligned}$$

where the absence of the error bar indicates that the component is forbidden by the internal symmetry of the cell. The experiment was not sensitive to the phase between the **b** and **c** component of the Mn moments, but the similar size of the components along the two directions suggested that the Mn moments form an elliptical cycloid in order to conserve an almost fixed spin length while propagating, for reasons analogous to those outlined in 4.1.1. The Tb moments clearly possess an **a** component, and are linearly arranged in a transverse sinusoidal modulation. The phase difference between the Tb and Mn moments remained undetermined, while the phase between the two orbits of the Tb sites was found to be 1.3(3) π. The work from Kenzelmann and co-workers provided evidence that

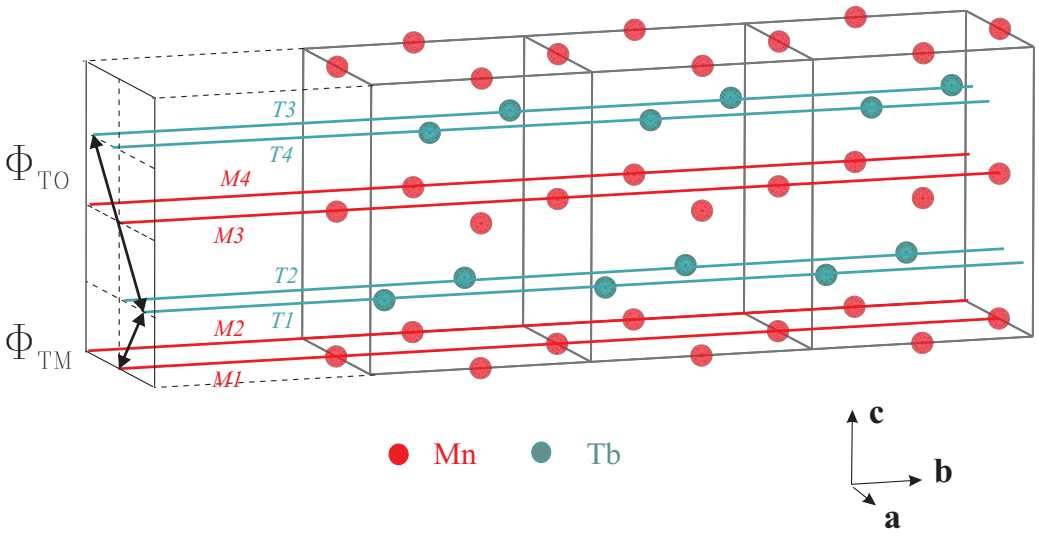

Figure 5.5: Positions in the unit cell of the Mn and Tb ions; the atomic sites are labeled according to the coordinates given in section 5.3.1. The adjacent *Pbnm* unit cells (indicated by black lines) show the direction of the magnetic modulation (red and green lines connecting atoms characterised by the same magnetisation function). The phase shifts between the magnetisation functions associated to different sites that are not univocally determined by symmetry are indicated following the definitions provided in the same section.

the Tb sublattice carries significant magnetisation in the incommensurate phase, presumably as a consequence of the exchange field from the ordered Mn sublattice.

The construction of the non resonant magnetic X-ray scattering amplitude from this model allows us to evaluate the effect of the cycloidal domain population on the intensity and polarisation of the diffraction peaks $(4, \pm\tau, \pm 1)$. The magnitudes of the magnetic moments are assumed as indicated above. The phase shift between different atomic sites and between different components in the same site is defined following Chapter 2 as the shift between the sinusoidal modulations at the same coordinate in space. The phase of the Mn component m_b on site M1 has been taken to be zero as a reference. The phase of the m_c component on the same atom is then $= +\pi/2$ $(-\pi/2)$ if the magnetic moments rotate clockwise (anticlockwise) when moving along $+\mathbf{b}$ and looking at the $(\mathbf{b}, \mathbf{c})$ plane from $+\mathbf{a}$. The phases of the Tb moments lying in the first orbit (positions $T1$, $T2$) are defined via the phase difference ϕ_{TM} between the m_A component in $T1$ and m_b in $M1$. The phases of the Tb moments in the second orbit ($T3$, $T4$) are defined via the phase difference ϕ_{TO} between m_a in $T3$ and the same component in $T1$; this phase difference was found to be $\phi_{TO} = 1.3(3)\ \pi$ in [2], and it is left here as a free parameter for refinement.

Scattering amplitude

The general expression for the X-ray non-resonant magnetic amplitude is analogous to the one introduced in Chapter 2. In the present case, the magnetic structure factor is calculated for a reflection $\mathbf{k}' - \mathbf{k} = (4, \alpha\tau, \beta)$, where $\alpha = \pm 1$ selects the sign of the index k, $\beta = \pm 1$ the sign of l, and $\gamma = \pm 1$ the domain state (anticlockwise rotation, defined as Domain 1, being represented by $\gamma = +1$). Considering for the moment a purely spin contribution, as in the examples in section 2.3

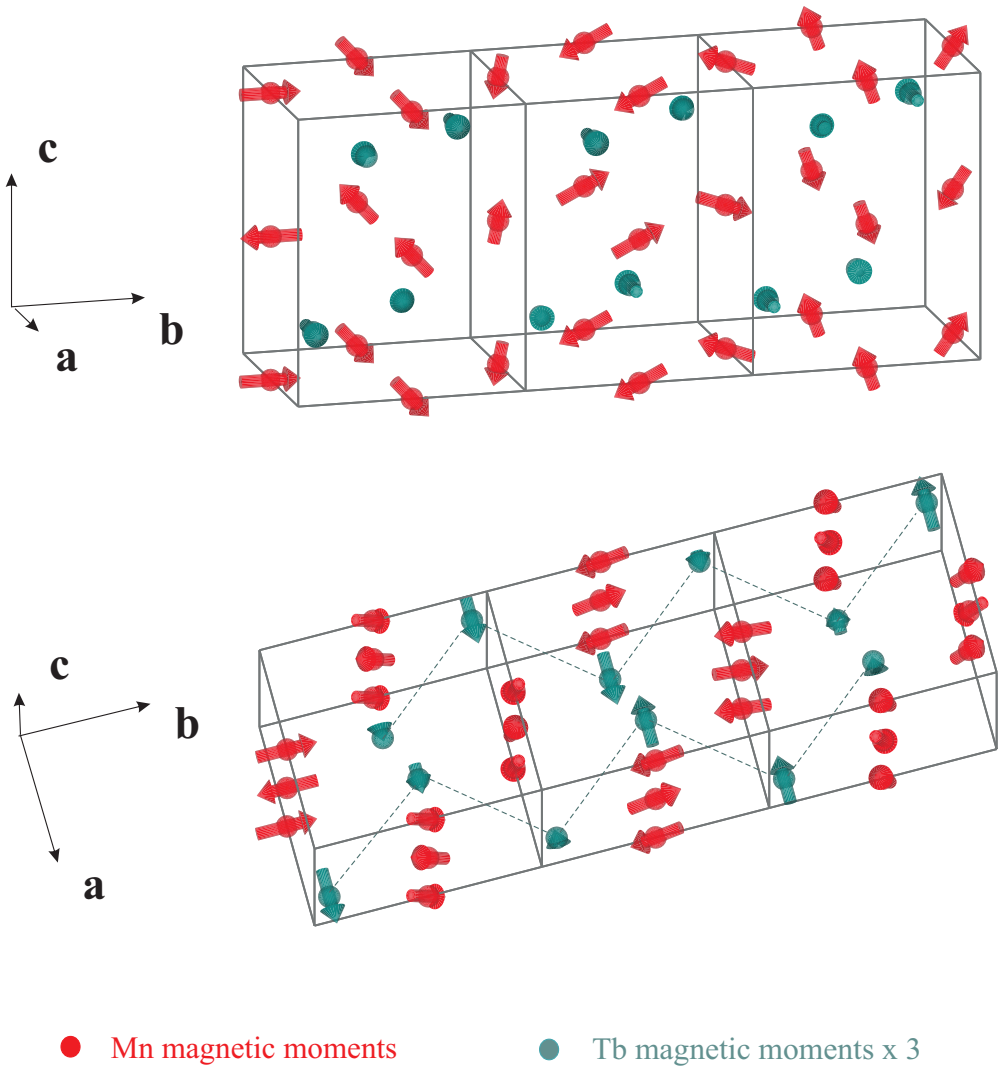

Figure 5.6: Sketch of the magnetic structure proposed in [2] (unit cell delimited by black lines), shown from two different points of view to emphasize the ordering on the Mn and the Tb sublattice respectively. While the Mn magnetic moments rotate in a cycloid within the $(\mathbf{b}, \mathbf{c})$ plane, the Tb moments are sinusoidally modulated with the same wavevector along the direction $\mathbf{a}$, transverse to the plane. Since the phase relation ϕ_{TM} between the modulations in the Mn and Tb sites (cf. Fig. 5.5) is not defined within this model, it has been arbitrarily established to be 0 in the present figure. The phase relation ϕ_{TO} between the two crystallographic orbits of the Tb sites is 1.3π according to this model.

and in Chapter 4, the scattering amplitude is

$$f_{nr} = \left(\frac{1}{2}\, i \frac{\hbar\omega}{mc^2} \right) \cdot \sum_s e^{i2\pi(hx_s + ky_s + lz_s)} \left(\mathbf{M}_s \cdot \mathbf{B}\right) \tag{5.1}$$

where $(x_s,\ y_s,\ z_s)$ are the fractional coordinates of the magnetic atoms within the unit cell. The structure factor is found to be

$$\sum_s e^{i2\pi(hx_s+ky_s+lz_s)}\,\mathbf{M}_s = \begin{array}{lcll} e^{i2\pi[-4(1/2)]} & \cdot & \frac{1}{2}[m_b^M\hat{\mathbf{b}} + m_c^M e^{-i\alpha\gamma\pi/2}\hat{\mathbf{c}}]+ & M1 \\ e^{i2\pi[0]} & \cdot & \frac{1}{2}[m_b^M\hat{\mathbf{b}} + m_c^M e^{-i\alpha\gamma\pi/2}\hat{\mathbf{c}}]+ & M2 \\ e^{i2\pi[-4(1/2)-\beta(1/2)]} & \cdot & \frac{1}{2}[-m_b^M\hat{\mathbf{b}} - m_c^M e^{-i\alpha\gamma\pi/2}\hat{\mathbf{c}}]+ & M3 \\ e^{i2\pi[-\beta(1/2)]} & \cdot & \frac{1}{2}[-m_b^M\hat{\mathbf{b}} - m_c^M e^{-i\alpha\gamma\pi/2}\hat{\mathbf{c}}]+ & M4 \\ e^{i2\pi[-4(1-\Delta_a^T)-\beta(1/4)]} & \cdot & \frac{1}{2}[m_a^T e^{i\alpha\phi_{TM}}\hat{\mathbf{a}}]+ & T1 \\ e^{i2\pi[-4(1/2+\Delta_a^T)-\beta(1/4)]} & \cdot & \frac{1}{2}[-m_a^T e^{i\alpha\phi_{TM}}\hat{\mathbf{a}}]+ & T2 \\ e^{i2\pi[-4(\Delta_a^T)-\beta(3/4)]} & \cdot & \frac{1}{2}[m_a^T e^{i\alpha(\phi_{TM}+\phi_{TO})}\hat{\mathbf{a}}]+ & T3 \\ e^{i2\pi[-4(1/2-\Delta_a^T)-\beta(3/4)]} & \cdot & \frac{1}{2}[-m_a^T e^{i\alpha(\phi_{TM}+\phi_{TO})}\hat{\mathbf{a}}] = & T4 \end{array}$$

$$= 2[m_b^M\hat{\mathbf{b}} - i\alpha\gamma m_c^M\hat{\mathbf{c}}] + \beta e^{i\alpha\phi_{TM}}\sin(8\pi\Delta_a^T)[m_a^T(1+e^{i\alpha\phi_{TO}})\hat{\mathbf{a}}] \tag{5.2}$$

where $\mathbf{B}$ contains the polarisation dependence and the values assumed by the phase shifts ϕ_{TM} and ϕ_{TO} in the two domains are related by inversion symmetry.

Analytical calculation

To perform the scalar product with the polarisation vector $\mathbf{B}$, we introduce a simplified scattering geometry. This approximation is done for illustrative purposes, while the actual simulation used to fit the data will be done taking into account the exact geometry of the experiment (see 5.3.4). It is supposed that:

- The scattering angle is $2\theta = 90°$ (exact value $\approx 79°$) .
- The $\mathbf{b}$ axis is perpendicular to the scattering plane (the exact orientation is off by $\approx \pm 5°$, for the four reflections).
- The $\hat{\mathbf{u}}_1$ and $\hat{\mathbf{u}}_3$ axes of the reference system defined in 2.15 correspond to the crystallographic axes $\mathbf{c}$ and $-\mathbf{a}$ (in the exact orientation they are off by $\approx \pm 9°$, for the four reflections).

Within these assumptions, the Jones matrix defined in 2.16 becomes

$$\begin{bmatrix} f_{\sigma'} \\ f_{\pi'} \end{bmatrix} = \begin{bmatrix} S_b & -\frac{1}{\sqrt{2}}(S_c+L_c) - \frac{1}{\sqrt{2}}S_a \\ \frac{1}{\sqrt{2}}(S_c+L_c) - \frac{1}{\sqrt{2}}S_a & S_b + L_b \end{bmatrix} \begin{bmatrix} 1 \\ i\epsilon \end{bmatrix}.$$

In this first calculation all magnetic moments are assumed to be of purely spin origin, therefore the terms in the Jones matrix then can be identified with

$$\begin{aligned} S_a &= +\beta e^{i\alpha\phi_{TM}}\sin(8\pi\Delta_a^T)[s_a^T(1+e^{i\alpha\phi_{TO}})] \\ S_b &= +2s_b^M \\ S_c &= -2is_c^M \end{aligned} \tag{5.3}$$

or, in short notation,

$$\begin{aligned} S_a &= +\beta e^{i\alpha\phi_{TM}}[S_a^T(1+e^{i\alpha\phi_{TO}})] \\ S_b &= +S_b^M \\ S_c &= -i\alpha S_c^M \end{aligned}$$

where the following definitions have been employed

$$S_a^T = \sin(8\pi\Delta_a^T)s_a^T$$
$$S_b^M = 2s_b^M$$
$$S_c^M = 2s_c^M.$$

The two components of the diffracted beam in the Jones basis are then

$$\begin{aligned} f_{\sigma'} &= S_b^M - \tfrac{1}{\sqrt{2}}\epsilon\alpha\gamma S_c^M - i\tfrac{1}{\sqrt{2}}\epsilon\beta e^{i\alpha\phi_{TM}}(1+e^{i\alpha\phi_{TO}})S_a^T \\ f_{\pi'} &= -i\tfrac{1}{\sqrt{2}}\alpha\gamma S_c^M - \tfrac{1}{\sqrt{2}}\alpha e^{i\alpha\phi_{TM}}(1+e^{i\alpha\phi_{TO}})S_a^T + i\epsilon S_b^M. \end{aligned} \tag{5.4}$$

To qualitatively assess the features of the diffracted light, it can be recognised that the Mn contribution is dominant over the Tb one, since ϕ_{TO} is close to π, and the factor $\sin(8\pi\Delta_a^T) \approx 0.36$ further reduces the Tb contribution. By only considering the magnetic diffraction from Mn moments, it can be noted that

$$|f_{\sigma'}| = |f_{\pi'}|$$

thus implying $P_1 = 0$ (cf. Eq. 3.3) and, since $f_{\sigma'}$ is real and $f_{\pi'}$ imaginary,

$$|f_{\sigma'} + f_{\pi'}| = |f_{\sigma'} - f_{\pi'}|$$

thus implying $P_2 = 0$ as well (cf. Eq. 3.4). The Mn contribution produces a scattered beam that is mainly circularly polarised, in contrast with the results obtained in the case of $Ni_3V_2O_8$, where the incident polarisation was converted into linear, due to the different scattering geometry (cf. Chapter 4). The intensity of the beam is large (small) if $\epsilon\alpha\gamma = -1$ $(+1)$. An imbalanced distribution of domains can be immediately recognised by a difference in the scattering intensity between $(4, +\tau, \beta)$ and $(4, -\tau, \beta)$, when the two peaks are illuminated with the same incident polarisation, or by a difference in the intensity of one peak when illuminated with the two circular polarisations. Any departure from a circularly polarised diffracted beam is to be interpreted as arising from the Tb contribution, which will be analysed in in detail in 5.3.2 and 5.3.4.

5.3.2 Overview of the data

The initial objective of the study was to establish whether or not the experimental setup provided sufficient sensitivity to any imbalance in the population of magnetic domains produced by the applied E field. A poling field of about 1kV/mm was applied during the cooling procedure. The field was removed during the X-ray measurements. Figure 5.7 shows the polarisation dependence of the magnetic scattering for the four satellite reflections $(4\ \pm\tau\ \pm1)$, measured at 15 K in the ferroelectric phase, after cooling the sample with an electric field $E < 0$ (i.e., negative voltage V as per the scheme in Fig. 5.2). The polarisation of the scattered light is analyzed in the $\hat{\pi}'$ channel ($\eta = 90°$). The incident light polarisation has been left unrotated (black diamonds), changed to circular right $\hat{\epsilon}_c^+$ (green dots), and changed to circular left $\hat{\epsilon}_c^-$ (red dots). When the incident linear polarisation $\hat{\pi}$ is selected, the magnetic satellite reflections have similar intensities, whereas for the incident circular polariaations they have different and complementary behaviour with respect to the sign of the magnetic satellite wavevector arms. This stands as a proof of a heavily unbalanced population of magnetic chiral domains. Subsequently, a detailed analysis of the polarisation of the scattered beam

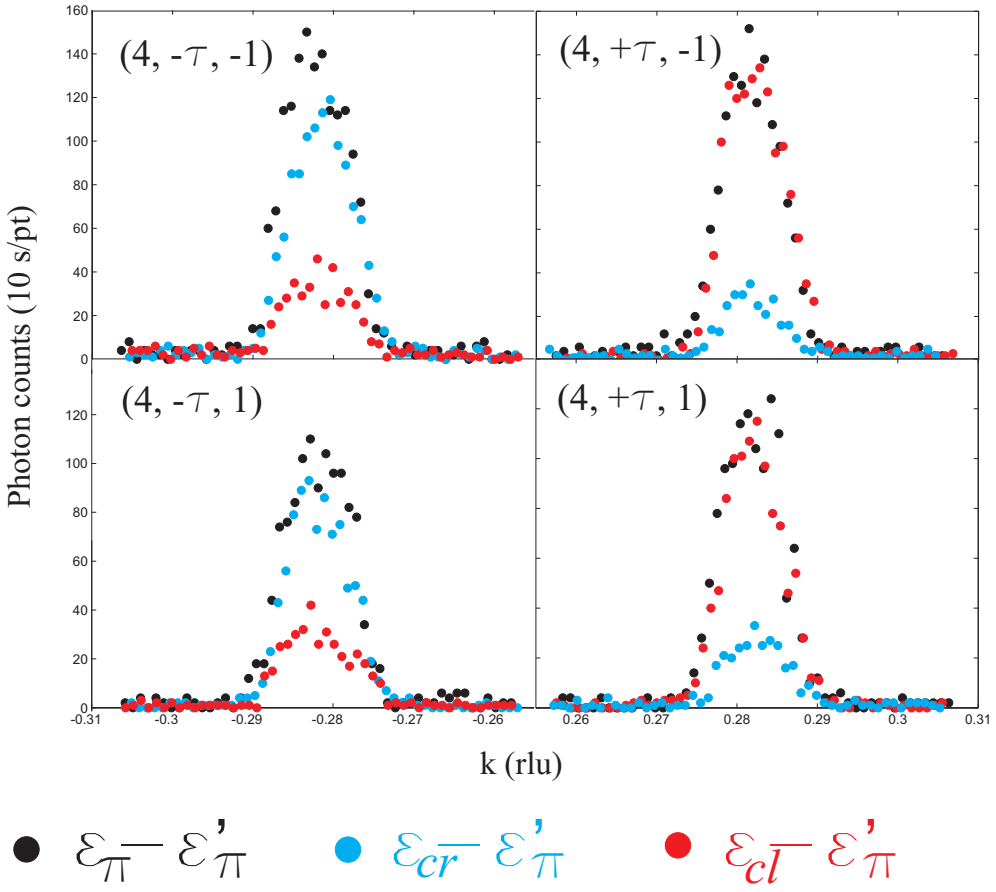

Figure 5.7: Alignment scans along the reciprocal lattice direction $\mathbf{b}^*$ of the magnetic reflections $(4, \pm\tau, \pm 1)$, and their dependence on the incident polarisation of the beam: linear and oriented within the scattering plane (π, black); circular left (red); circular right (blue). Data are taken in the FE cycloidal phase at 15 K, and obtained after annealing the sample in a poling electric field E < 0. The polarisation of the scattered photons is analysed in the π' channel ($\eta = 90^\circ$). Note that while the four peaks display similar intensities when illuminated with linear polarisation π, in the case of circular polarisation their intensity is strongly dependent on the sign of τ and the handedness of the polarisation.

has been undertaken, by carefully measuring the Stokes dependence I(η) for each of the satellites shown in Fig. 5.7. Figure 5.10 summarizes the data for field coolings performed with either E > 0 or E < 0.

Turning first to consider the case of incident linear ($\hat{\pi}$) polarisation shown in the figure, it is clear that, for a particular choice of the direction of E, only small differences in I(η) are observed for the various satellites and that reversing the direction of E does not appear to have any effect. Clear differences in I(η) of the various satellites are observed for incident circular polarisation. In this case, reversing the direction of E has a profound effect on the observed intensities. For a given field direction, changing the sign of τ at fixed l leads to a switching of the handedness of incident X-rays that produces the maximum intensity, whereas the handedness associated with the maximum satellite intensity is invariant with respect to changes in the sign of l. Of considerable significance is the fact that reversing the sign of E leads to a switching of the dominant handedness. Also apparent

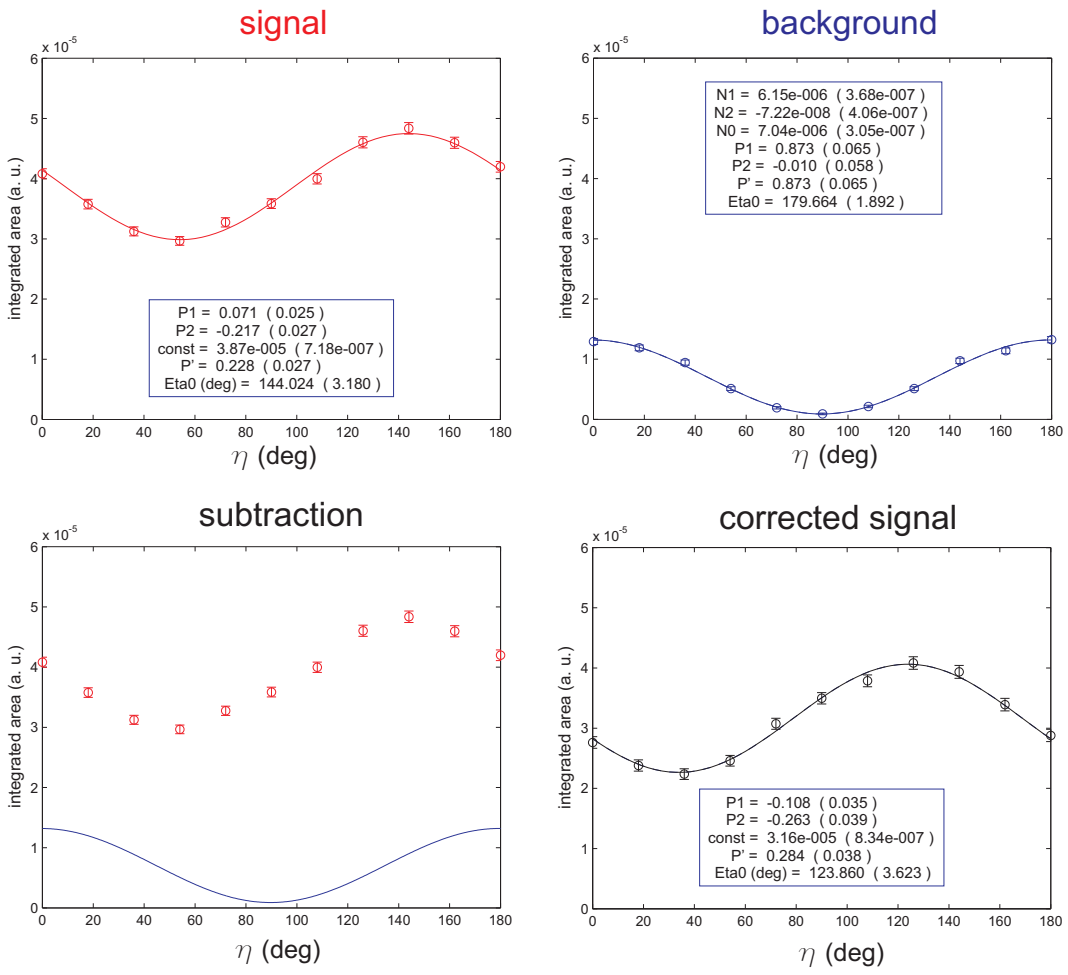

Figure 5.8: Procedure for the measurement of a Stokes scan on the magnetic reflection $(4, +\tau, -1)$ with circular left incident polarisation. As in the case of $Ni_3V_2O_8$ (cf. Fig. 4.13), the first scan is collected on the magnetic peak (red) and the second one on the background (blue); the fitted background is subtracted from the signal to give the final result (black). Note that this reflection and circular polarisation, combined together, give rise to a 'strong' diffraction intensity (cf. Fig. 5.7), thus making the background subtraction less crucial than in the opposite case, shown in Fig. 5.9.

are clear mirror symmetries between LCP and RCP X-rays for the same reflection and between satellites for the same incident polarisation state. Thus at a qualitative level the data displayed in Fig. 5.10 reveal an imbalance in the population of the two possible magnetic domains created by the applied electric field, an imbalance that can be reversed by switching the direction of the field. The polarisations of the diffracted beam differ from a circular state by a considerable amount, revealed by the appearance of the Stokes parameter $P_2 \approx 0.2$ (linear oblique polarisation). To explore the potential richness of information encoded in the data, it is necessary to perform extensive modeling of the magnetic scattering and specifically of the contribution arising from the Tb moments.

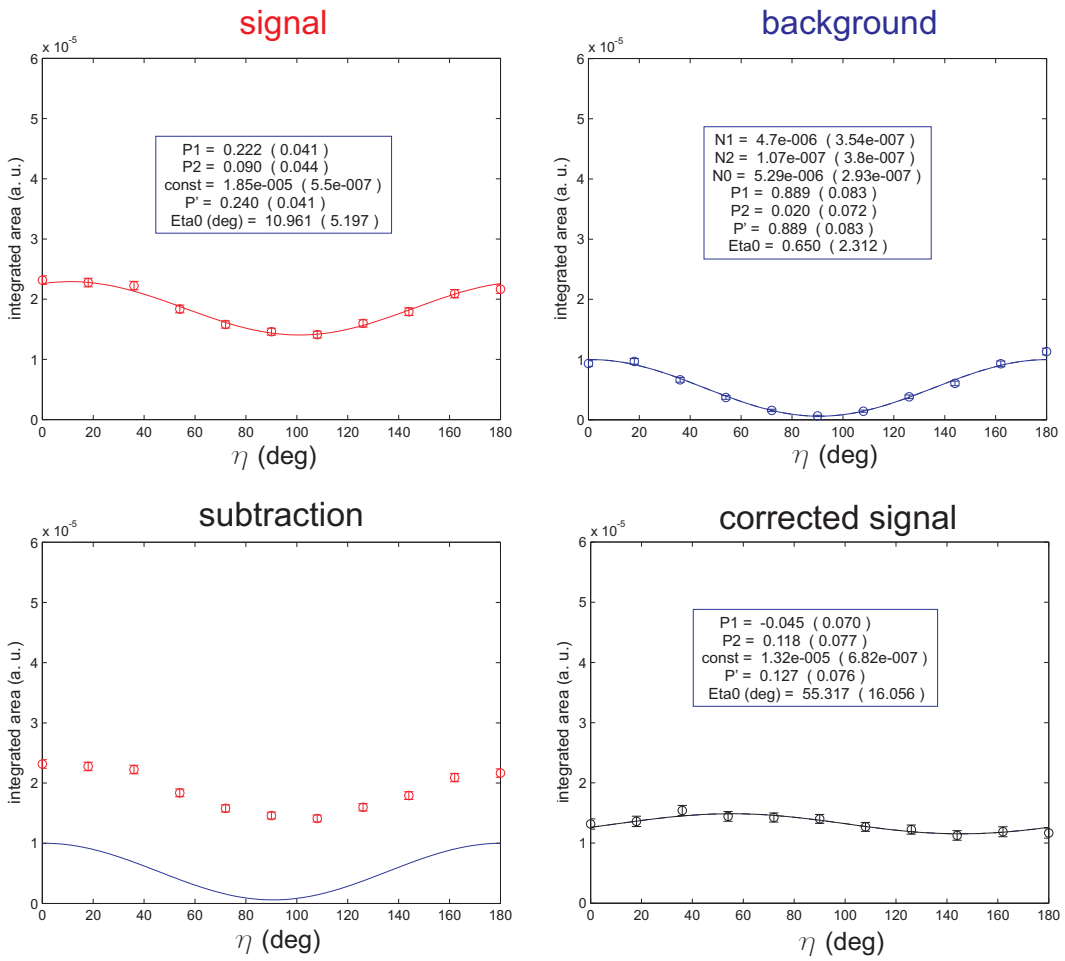

Figure 5.9: Procedure for the measurement of a Stokes scan on the same magnetic reflection $(4, +\tau, -1)$ as in Fig. 5.8, but with circular right incident polarisation. This is an example of a 'weak' diffraction intensity, due to the combination of the sign of τ and the handedness of the polarisation, as visible in Fig. 5.7. In all of these cases the background subtraction has been carried out with particular accuracy by repeating the measurement multiple times, since the symmetry properties displayed by the data rely on the small value of the parameter P_2 (i.e., the polarisation of the diffracted beam is very close to being circular).

5.3.3 Interpretation

For the initial model, the contribution of the Tb moments as detailed in 5.3.1 has been introduced. In the simplified geometry, let's consider for the sake of simplicity a monodomain state. Equation 5.4 can be rewritten in shorthand notation by defining the dominant Mn contribution as

$$A = S_b^M - \frac{1}{\sqrt{2}}\epsilon\alpha\gamma S_c^M \tag{5.5}$$

and the phase factors multiplying the Tb contribution as

$$\frac{1}{\sqrt{2}}e^{i\alpha\phi_{TM}}(1 + e^{i\alpha\phi_{TO}}) = w' + i\alpha w'' \tag{5.6}$$

thus becoming

$$\begin{aligned} f_{\sigma'} &= A - i\epsilon\beta(w' + i\alpha w'')S_a^T \\ f_{\pi'} &= i\epsilon A - \beta(w' + i\alpha w'')S_a^T. \end{aligned} \tag{5.7}$$

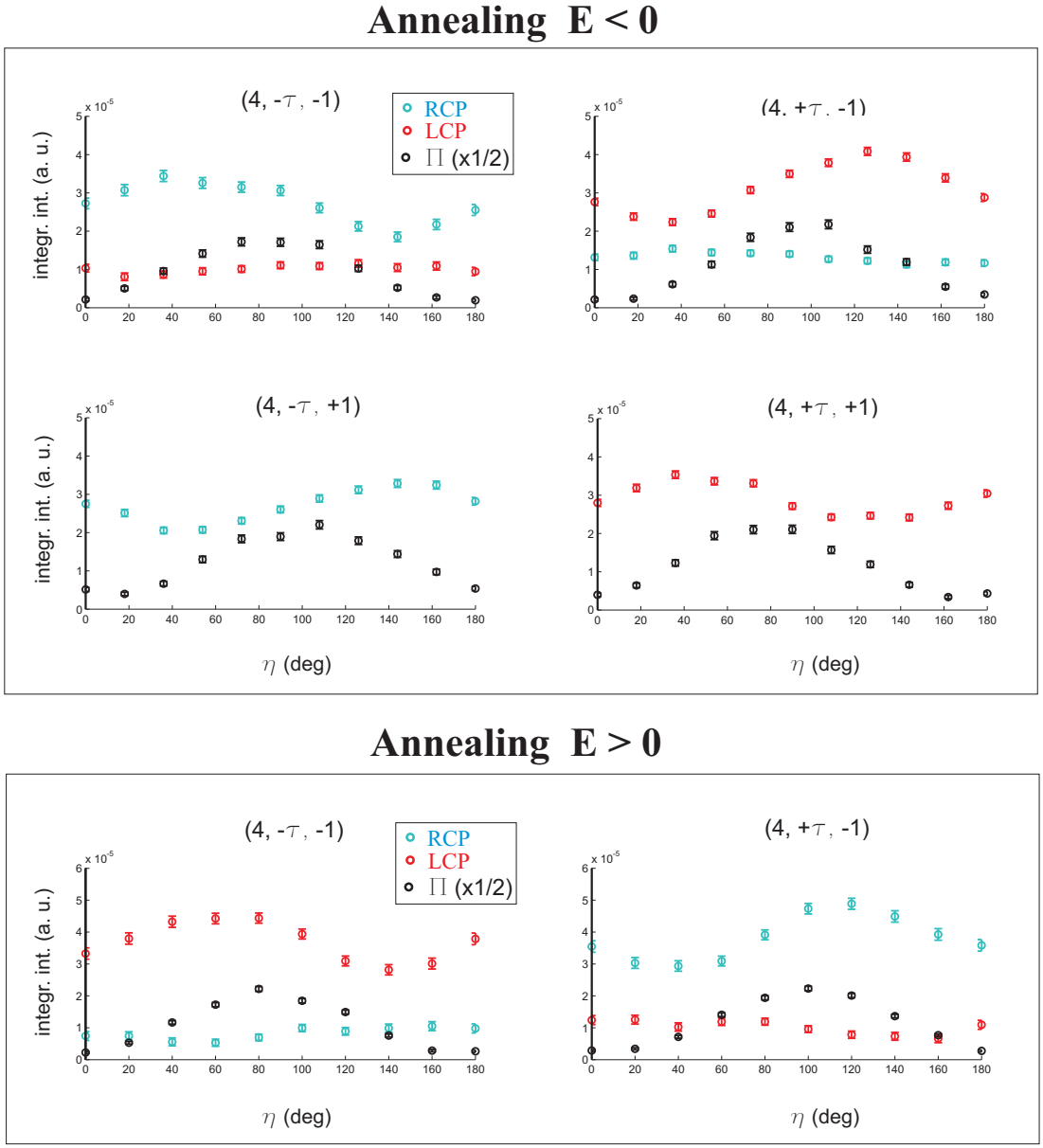

Figure 5.10: Variation with analyser rotation angle η of the X-ray magnetic intensity from A-type satellites $(4, \pm\tau, \pm 1)$ in $TbMnO_3$ at 15 K, for linear $\hat{\pi}$ (black), circular left $\hat{\epsilon}_c^-$ (red) and circular right $\hat{\epsilon}_c^+$ (blue) incident photon polarisations, and field cooling with either E< 0 (upper panel) or E> 0 (lower panel)

.

The creation of a net P_1 can be verified by comparing the absolute intensities in the two diffracted polarisation channels σ' and π':

$$|f_{\sigma'}|^2 = |A - i\beta\epsilon w' S_a^T + \alpha\beta\epsilon w'' S_a^T|^2$$
$$|f_{\pi'}|^2 = |A + i\beta\epsilon w' S_a^T - \alpha\beta\epsilon w'' S_a^T|^2.$$

An emerging P_1 is indeed possible as both the real and imaginary contributions arising from the Tb moments are added with opposite signs in $f_{\sigma'}$ and $f_{\pi'}$. The sign of P_1 is reversed when changing the handedness of the incident polarisation (ϵ), the sign of the index l (β) and of the index k (α, provided that the factor $w' + iw''$ has a dominant imaginary component). These results are indeed confirmed by numerical simulations.

The creation of a net P_2 is evaluated by comparing the difference in the moduli of $f_{\sigma'} + f_{\pi'}$ and $f_{\sigma'} - f_{\pi'}$:

$$|f_{\sigma'} + f_{\pi'}|^2 = |A - \beta w' S_a^T + \alpha\beta\epsilon w'' S_a^T|^2 + |A - \beta w' S_a^T - \alpha\beta\epsilon w'' S_a^T|^2$$
$$|f_{\sigma'} - f_{\pi'}|^2 = |A + \beta w' S_a^T + \alpha\beta\epsilon w'' S_a^T|^2 + |A + \beta w' S_a^T - \alpha\beta\epsilon w'' S_a^T|^2.$$

In this case it is seen that P_2 can be different from zero only due to the term in w', while the term in w'' is contributimg with the same sign to both expressions. Moreover, the sign of P_2 is left unchanged by reversing the incident polarisation and the sign of τ, while it is reversed by a change in l. By comparison of these results with the data, it is apparent that a transverse spin contribution along **a** of the Tb moments can not account for the amount of P_2 found in the data, in which the reversing of the first two parameters produces a change in the sign of P_2, while the reversing of the third parameter does not. In Fig. 5.12 and 5.12, the results of the numerical fit based on this model are represented. For the calculations, the exact scattering geometry of the six-circle setup was taken into account.

5.3.4 Refined model

The comprehensive set of Stokes scans that has been collected has provided very specific symmetry constraints. Although corrections to the model presented in the previous section have been tried in several ways (modification of the phases between the different components of the magnetic moments, displacement of magnetic ions, introduction of a Thomson contribution), the only solution that meets the characteristics of the diffraction peaks involves the mgnetic moments of the Tb atoms possessing a component along **b**, that comprises both spin and orbital contribution. Note that in the work carried out by Kenzelmann and co-workers, undetermined magnetic moments of the Tb ions are allowed up to 1 μ_B along **b** and **c**. The atomic spin $s_i(\mathbf{K})$ and the orbital $l_i(\mathbf{K})$ magnetic components employed for numerical calculation in this section contain the form factors for Mn^{3+} and Tb^{3+} at a given scattering vector **K**. It is supposed also that the orbital contribution of Mn is quenched, and that of Tb equal to its spin moment ($l^{Tb}/s^{Tb} = 1$) as follows from the first and second Hund's rule for a $^7F_6$ electronic configuration.

Scattering amplitude

This situation can be described as follows (cf. Eq. 2.13)

$$f_{nr} \;=\; \left(\frac{1}{2}\, i\frac{\hbar\omega}{mc^2}\right) \cdot \sum_s e^{i2\pi(hx_s+ky_s+lz_s)} \left[\frac{1}{2}\mathbf{l}_s \cdot \mathbf{A}'' \;+\; \mathbf{s}_s \cdot \mathbf{B}\right] \tag{5.8}$$

where $\mathbf{A}''$ represents the coupling of the orbital moment with the polarisation of the beam, while **B** represents the coupling of the spin (see Eq. 2.12). The structure factors are found to be

$$\begin{aligned}
\sum_s e^{i2\pi(hx_s+ky_s+lz_s)}\ \mathbf{s}_s = \;& 2[s_b^M\hat{\mathbf{b}} - i\alpha\gamma s_c^M\hat{\mathbf{c}}] + && M1-4\\
& \beta e^{i\alpha\phi_{TM}}\sin(8\pi\Delta_a^T)[s_a^T(1+e^{i\alpha\phi_{TO}})\hat{\mathbf{a}}] + && T1-4\\
& e^{i2\pi[-4(1-\Delta_a^T)-\beta(1/4)]} \;.\; \tfrac{1}{2}[s_b^T e^{i\alpha\phi_{TM}}\hat{\mathbf{b}}] + && T1\\
& e^{i2\pi[-4(1/2+\Delta_a^T)-\beta(1/4)]} \;.\; \tfrac{1}{2}[s_b^T e^{i\alpha\phi_{TM}}\hat{\mathbf{b}}] + && T2\\
& e^{i2\pi[-4(\Delta_a^T)-\beta(3/4)]} \;.\; \tfrac{1}{2}[s_b^T e^{i\alpha(\phi_{TM}+\phi_{TO})}\hat{\mathbf{b}}] + && T3\\
& e^{i2\pi[-4(1/2-\Delta_a^T)-\beta(3/4)]} \;.\; \tfrac{1}{2}[s_b^T e^{i\alpha(\phi_{TM}+\phi_{TO})}\hat{\mathbf{b}}] && T4
\end{aligned}$$

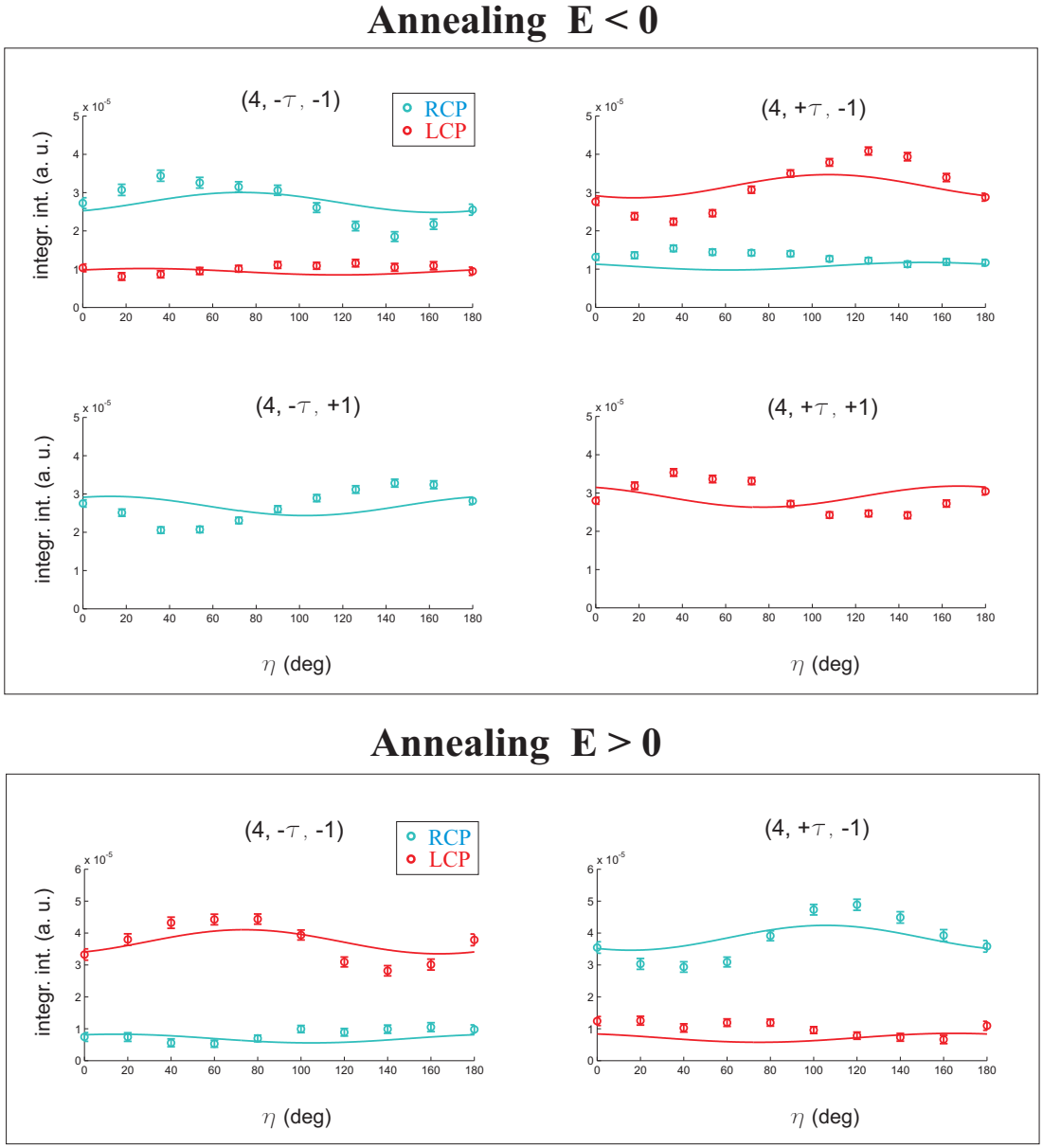

Figure 5.11: Fit of the data presented in Fig. 5.10 with the model reported in [2], for circular left $\hat{\epsilon}_c^-$ (red) and circular right $\hat{\epsilon}_c^+$ (blue) incident photon polarisations, and field cooling with either E< 0 (upper panel) or E> 0 (lower panel)

.

and

$$\sum_s e^{i2\pi(hx_s+ky_s+lz_s)}\,\mathbf{l}_s = \beta e^{i\alpha\phi_{TM}}\sin(8\pi\Delta_a^T)[l_a^T(1+e^{i\alpha\phi_{TO}})\hat{\mathbf{a}}]+ \qquad T1-4$$

$$e^{i2\pi[-4(1-\Delta_a^T)-\beta(1/4)]} \cdot \tfrac{1}{2}[l_b^T e^{i\alpha\phi_{TM}}\hat{\mathbf{b}}]+ \qquad T1$$

$$e^{i2\pi[-4(1/2+\Delta_a^T)-\beta(1/4)]} \cdot \tfrac{1}{2}[l_b^T e^{i\alpha\phi_{TM}}\hat{\mathbf{b}}]+ \qquad T2$$

$$e^{i2\pi[-4(\Delta_a^T)-\beta(3/4)]} \cdot \tfrac{1}{2}[l_b^T e^{i\alpha(\phi_{TM}+\phi_{TO})}\hat{\mathbf{b}}]+ \qquad T3$$

$$e^{i2\pi[-4(1/2-\Delta_a^T)-\beta(3/4)]} \cdot \tfrac{1}{2}[l_b^T e^{i\alpha(\phi_{TM}+\phi_{TO})}\hat{\mathbf{b}}] \qquad T4$$

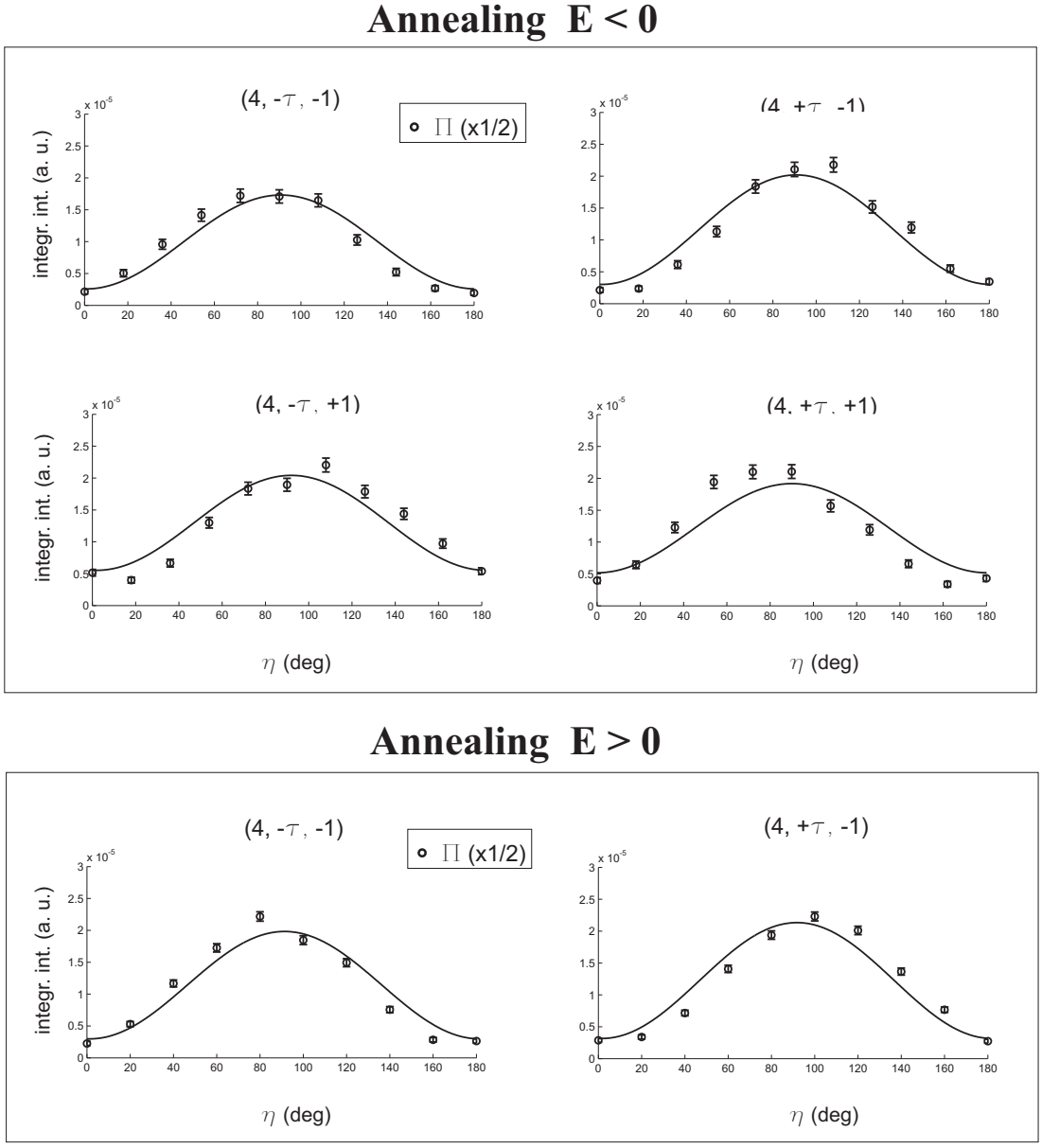

Figure 5.12: Fit of the data presented in Fig. 5.10 with the model reported in [2], for linear $\hat{\pi}$ incident photon polarisation, and field cooling with either E< 0 (upper panel) or E> 0 (lower panel)

.

thus leading to

$$f_{nr} = \left(\tfrac{1}{2}\, i \tfrac{\hbar\omega}{mc^2} \right) \cdot \Big\{ \Big[2[s_b^M \hat{\mathbf{b}} - i\alpha\gamma s_c^M \hat{\mathbf{c}}] + \beta e^{i\alpha\phi_{TM}} \sin(8\pi\Delta_a^T)[s_a^T(1+e^{i\alpha\phi_{TO}})\hat{\mathbf{a}}] + i\beta e^{i\alpha\phi_{TM}} \cos(8\pi\Delta_a^T)[s_b^T(e^{i\alpha\phi_{TO}}-1)\hat{\mathbf{b}}] \Big] \cdot \mathbf{B} + \beta e^{i\alpha\phi_{TM}} \sin(8\pi\Delta_a^T)[\tfrac{1}{2} l_a^T(1+e^{i\alpha\phi_{TO}})\hat{\mathbf{a}}] + i\beta e^{i\alpha\phi_{TM}} \cos(8\pi\Delta_a^T)[\tfrac{1}{2} l_b^T(e^{i\alpha\phi_{TO}}-1)\hat{\mathbf{b}}] \cdot \mathbf{A}'' \Big\} \quad (5.9)$$

where the contribution of the Mn spins and the contribution of the Tb spins along **a** have been retained from the previous model.

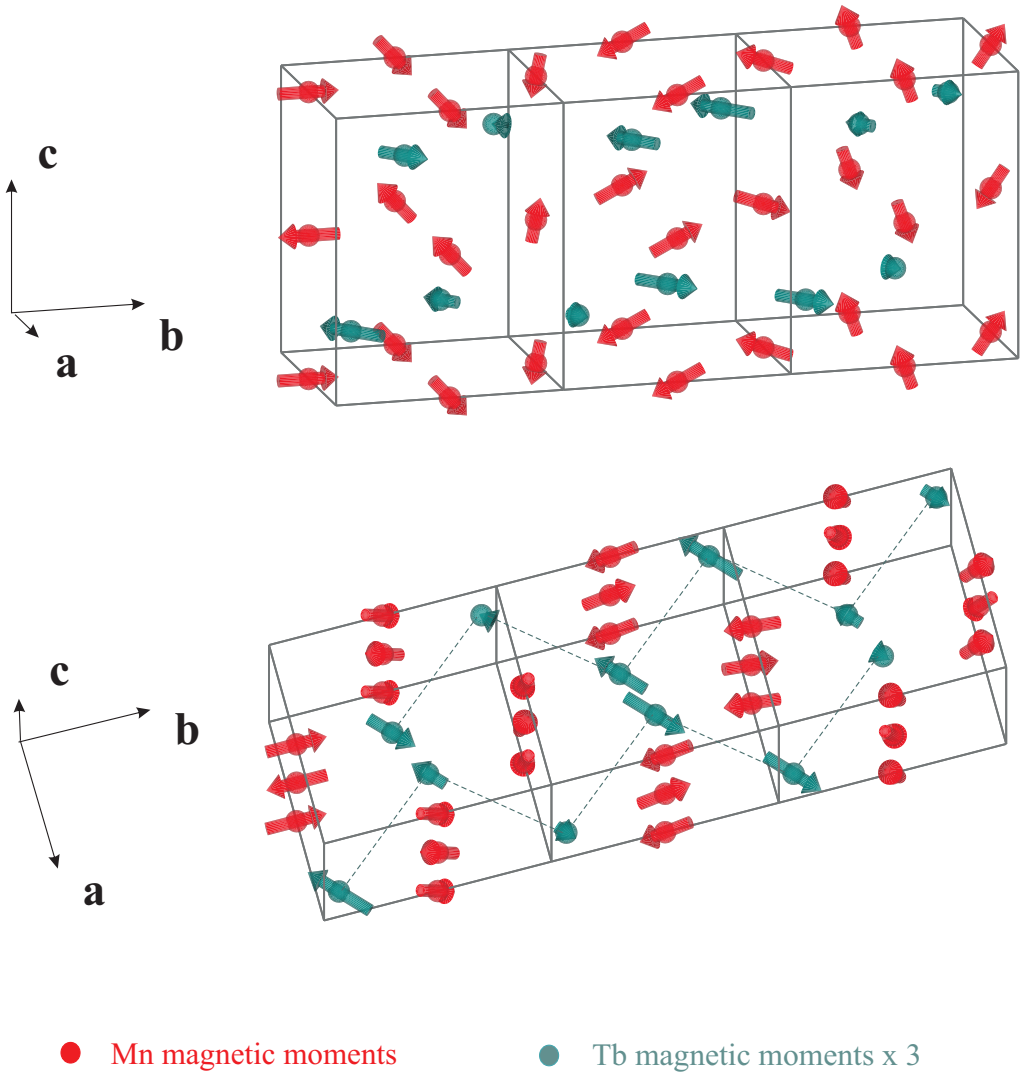

Figure 5.13: Sketch of the newly refined magnetic structure, to be compared with Fig. 5.6, including the previously undetermined longitudinal component along **a** of the Tb moment, the phase relation between the modulations in the Mn and Tb sites $\phi_{TM} = 0$, and the phase relation between the two crystallographic orbits of the Tb sites $\phi_{TO} = \pi$.

Analytical calculation

In the approximated analytical calculation, initially only the newfound **b** component will be taken into account for the Tb moments, in order to highlight its effects. The **a** component is going to be neglected at first, since it has already been proved that it can not provide a suitable correction to the dominant Mn contribution in order to account for the oblique degree of polarisation displayed by the data. Its role will be discussed at the end of the analysis.

According to the refined model, the components to be introduced in the Jones matrix 2.16 become

(cf. with previous model in Eq. 5.3):

$$\begin{aligned} S_b &= +2s_b^M + i\beta e^{i\alpha\phi_{TM}}\cos(8\pi\Delta_a^T)[s_b^T(e^{i\alpha\phi_{TO}}-1)] \\ L_b &= i\beta e^{i\alpha\phi_{TM}}\cos(8\pi\Delta_a^T)[l_b^T(e^{i\alpha\phi_{TO}}-1)] \\ S_c &= -2is_c^M \end{aligned} \tag{5.10}$$

or, in short notation,

$$\begin{aligned} S_b &= +S_b^M + i\beta e^{i\alpha\phi_{TM}}(e^{i\alpha\phi_{TO}}-1)S_b^T \\ L_b &= i\beta e^{i\alpha\phi_{TM}}(e^{i\alpha\phi_{TO}}-1)L_b^T \\ S_c &= -i\alpha S_c^M \end{aligned}$$

where the following definitions have been employed:

$$\begin{aligned} S_b^M &= 2s_b^M \\ S_b^T &= \cos(8\pi\Delta_a^T)s_b^T \\ L_b^T &= \cos(8\pi\Delta_a^T)l_b^T \\ S_c^M &= 2s_c^M. \end{aligned} \tag{5.11}$$

The scattering amplitudes in the two polarisation channels become

$$\begin{aligned} f_{\sigma'} &= S_b^M - \tfrac{1}{\sqrt{2}}\epsilon\alpha\gamma S_c^M + i\beta e^{i\alpha\phi_{TM}}(e^{i\alpha\phi_{TO}}-1)S_b^T \\ f_{\pi'} &= -i\tfrac{1}{\sqrt{2}}\alpha\gamma S_c^M + i\epsilon S_b^M - \epsilon\beta e^{i\alpha\phi_{TM}}(e^{i\alpha\phi_{TO}}-1)(S_b^T + L_b^T) \end{aligned} \tag{5.12}$$

and can be rewritten by regrouping the Mn contribution within the term A (as done in Eq. 5.5), and the new phase factors that multiply the Tb contribution within the term

$$e^{i\alpha\phi_{TM}}(e^{i\alpha\phi_{TO}}-1) = u' + i\alpha u'', \tag{5.13}$$

thus leading to

$$\begin{aligned} f_{\sigma'} &= A + i\beta(u' + i\alpha u'')S_b^T \\ f_{\pi'} &= i\epsilon A - \epsilon\beta(u' + i\alpha u'')(S_b^T + L_b^T). \end{aligned} \tag{5.14}$$

Turning now to consider how this new model can account for the presence of a net value of P_2 in the data, one must compare $|f_{\sigma'} + f_{\pi'}|$ and $|f_{\sigma'} - f_{\pi'}|$:

$$\begin{aligned} |f_{\sigma'} + f_{\pi'}|^2 &= |A - \epsilon\beta u'(S_b^T + L_b^T) - \alpha\beta u'' S_b^T|^2 + |A + \epsilon\beta u' S_b^T - \alpha\beta u''(S_b^T + L_b^T)|^2 \\ |f_{\sigma'} - f_{\pi'}|^2 &= |A + \epsilon\beta u'(S_b^T + L_b^T) - \alpha\beta u'' S_b^T|^2 + |A - \epsilon\beta u' S_b^T - \alpha\beta u''(S_b^T + L_b^T)|^2 \end{aligned}$$

or, separating the orbital and spin contrinution,

$$\begin{aligned} |f_{\sigma'} + f_{\pi'}|^2 = \;& |[A - \epsilon\beta u' S_b^T - \alpha\beta u'' S_b^T] - \epsilon\beta u' L_b^T|^2 + \\ & |[A + \epsilon\beta u' S_b^T - \alpha\beta u'' S_b^T] - \alpha\beta u'' L_b^T|^2 \\ |f_{\sigma'} - f_{\pi'}|^2 = \;& |[A + \epsilon\beta u' S_b^T - \alpha\beta u'' S_b^T] + \epsilon\beta u' L_b^T|^2 + \\ & |[A - \epsilon\beta u' S_b^T - \alpha\beta u'' S_b^T] - \alpha\beta u'' L_b^T|^2 \end{aligned}$$

where it is highlighted that the spin contribution alone does not produce a net P_2 (it gives $|f_{\sigma'} + f_{\pi'}|$ = $|f_{\sigma'} - f_{\pi'}|$), while it is the small orbital contribution that creates an imbalance between the two moduli, resulting in a non-zero value of P_2, provided that u' (real part of the phase factors of the Tb contribution) is significant. Note that $|u'|$ is maximized when $\phi_{TO} = \pi$ and $\phi_{TM} = \pi$ or 0 (Eq. 5.13). In such a case, the sign of the emerging P_2 is reversed in accordance with the sign of β and ϵ, but does not depend on the sign of α. From inspection of the data (Fig. 5.10), it is seen that indeed P_2 is reversed when the handedness of the polarisation or the sign of l are reversed, but not when the sign of τ is. These phase values are then good candidates as initial guesses for the numerical optimisation.

Numerical optimisation of m_b^T, ϕ_{TM} and ϕ_{TO}

Numerical simulations taking into account the exact geometry of the diffraction have been carried out as in the case of $Ni_3V_2O_8$ in Chapter 4. The best fit gives a **b** component of $1.0 \pm 0.3\ \mu_B$ for the total magnetic moment m_b^T, which is compatible with the large error bar set by Kenzelmann and co-workers in [2]. The phase shift between the two orbits of Tb atoms is determined to be $1.0 \pm 0.2\ \pi$. Moreover, the model fixes the phase angle between the magnetic modulations of the Tb and the Mn atoms. Consider one Mn atom, and the subsequent Tb atom moving along $\pm\mathbf{c}$ (sign determined accordingly to the direction of the electric polarisation), then the phase angle between their magnetic modulations, evaluated at the same coordinate in space, is found to be $0.0 \pm 0.1\ \pi$ (with reference to the **b** components). These values are in agreement with the analytical calculation carried out in the previous section. Given those phases, it is found that the resultant magnetic amplitude is not sensitive to the **a** components of the Tb atoms, which cancel each other out in the sum over the unit cell: the factor $1 + e^{i\alpha\phi_{TO}}$ implies that the contributions from the two crystallographic orbits add up to zero. The complete expression for the scattering amplitude, in the star of magnetic peaks observed, is found to be:

$$f(\mathbf{K}) \propto (s_b^M(\mathbf{K})\hat{\mathbf{b}} - \gamma\ \alpha\ i\ s_c^M(\mathbf{K})\hat{\mathbf{c}}) \cdot \mathbf{B}$$
$$- \gamma\ \beta\ i\ (s_b^T(\mathbf{K})\hat{\mathbf{b}} \cdot \mathbf{B} + \frac{1}{2} l_b^T(\mathbf{K})\hat{\mathbf{b}} \cdot \mathbf{A}'') \cos(8\pi\Delta_a^T).$$

The final fit is shown in Fig. 5.14 and 5.15 by continuous lines, and the improvement upon the previous model is stressed by the comparison with the dotted lines. Besides the parameters already reported, an accurate description of the domain state as a function of applied electric field has been extracted. It can be concluded that cooling in a positive electric field led to a population of 96(3)% of the cycloidal domain in which the transverse spiral of the Mn atoms is anticlockwise, when moving along $+\mathbf{b}$ and looking from $+\mathbf{a}$ (Domain 1), while field cooling in a negative electric field produced a population of 83(2)% for the domain of opposite sense of rotation (Domain 2). Differences in the domain populations found with E may result from a number of effects such as domain pinning, slight variations in the volume probed by the x-ray beam, etc.

5.4 Conclusions and future outlook

The results presented in this chapter establish the benefits of performing NRXMS experiments with circularly polarised X-rays combined with full polarimetry of the scattered beam, to the refinement of complex magnetic structures. For the specific case of multiferroic $TbMnO_3$, with two different types of magnetic ion, making it by any standards a challenging test case, it has been shown surprisingly that this approach allows us to make important refinements to the magnetic structure obtained from neutron diffraction. Unlike traditional structure refinements by intensity measurements, which involve the characterisation of a large number of superlattice reflections, in this case the analysis of polarised diffraction from a star of four reflections has been sufficient to resolve fundamental details of the magnetic ordering, including phase shifts between magnetic modulations on different crystallographic sites, separation of spin and orbital contributions to the atomic magnetic moment, and determination of the absolute sense of rotation of the magnetic cycloids.

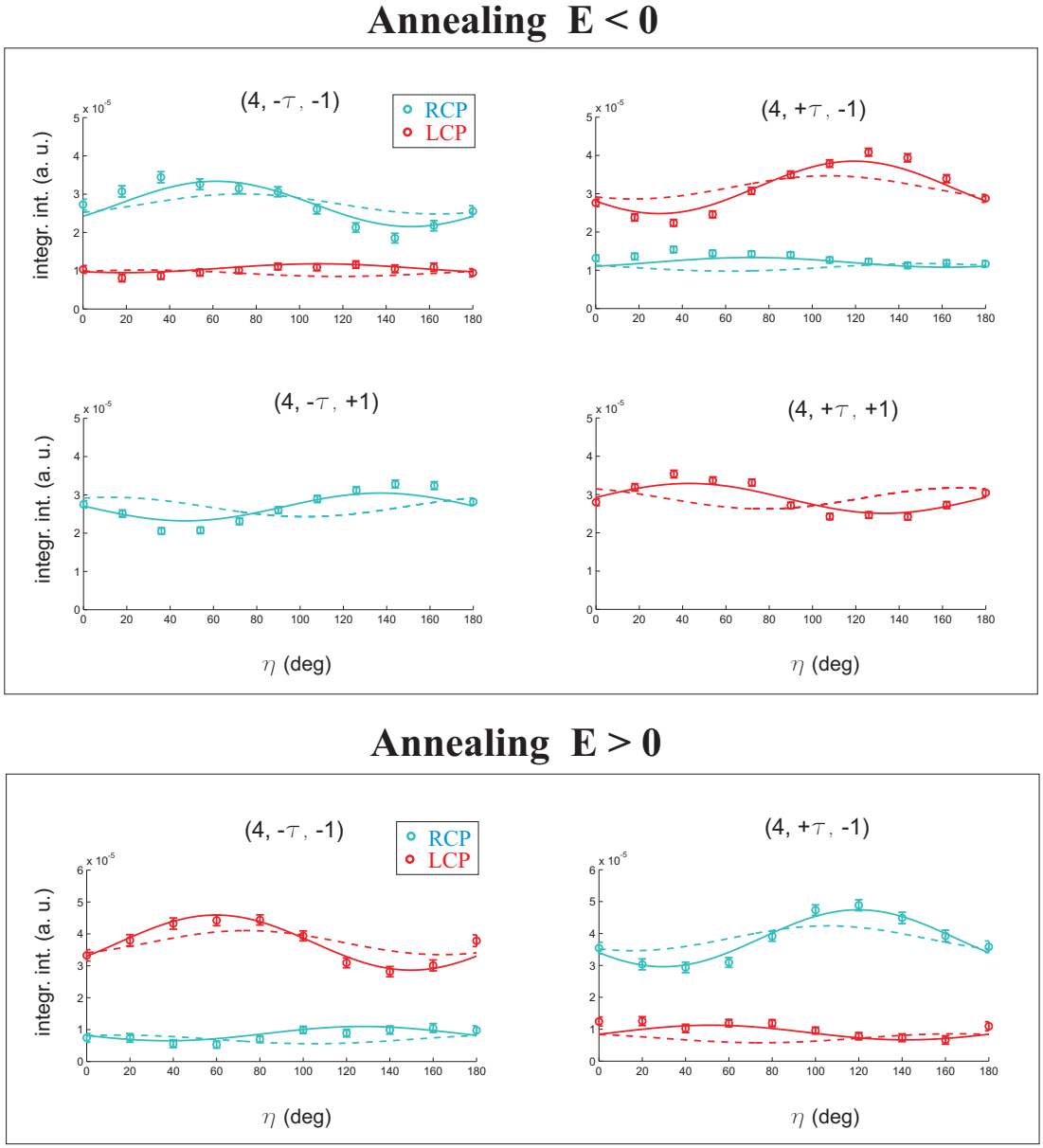

Figure 5.14: Fit of the data presented in Fig. 5.10 with the refined model found in 5.3.4 (continuous lines), for circular left $\hat{\epsilon}_c^-$ (red) and circular right $\hat{\epsilon}_c^+$ (blue) incident photon polarisations. Dotted lines report the fit with the initial model as a comparison (cf. Fig. 5.11). The overall fit, comprising both the measurements with circular light shown in this figure and those with linear light shown in Fig. 5.15, gives $\chi^2 = \Sigma_i^n w_i (I_o^i - I_c^i)^2/(n-m) = 3.6$, where I_o^i and I_c^i are the observed and calculated intensities, $w_i = 1/\sigma_i^2$, σ_i is the error bar of the observed intensity I_o^i, and m is the number of parameters of the fit.

This technique could readily be applied to other multiferroics, particularly those such as $BiFeO_3$ [78, 79] for which open questions remain concerning the magnetic structure of bulk samples and its modification in thin films [80] - [83].

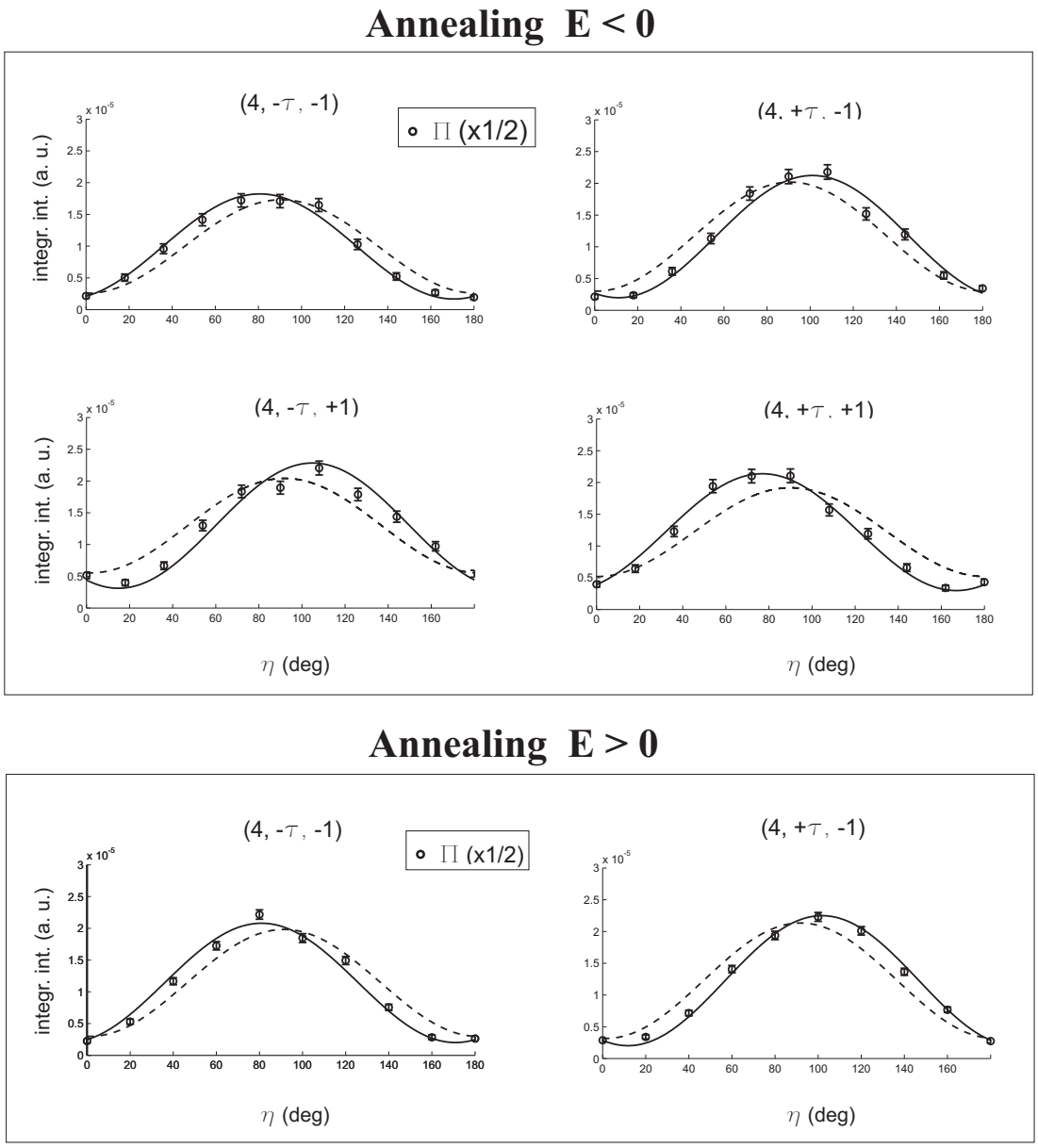

Figure 5.15: This figure completes Fig. 5.14, by presenting the fit with the refined model found in 5.3.4 for the data collected with linear $\hat{\pi}$ incident photon polarisation. Dotted lines report the fit with the initial model as a comparison (cf. Fig. 5.12).

Chapter 6

Magnetoelastic Distortions induced by a Magnetic Field in $TbMnO_3$

In this Chapter the investigation of the magnetic structure of $TbMnO_3$ under applied magnetic field is reported. The technical equipment described in Chapter 3 has been used to apply a magnetic field along the **b** crystallographic axis as well as a poling electric field along **c** in order to achieve a monodomain in the magnetic state. The results were collected up to the metamagnetic transition at $H_C \approx 8$ T. Non-resonant scattering has been performed on two magnetic reflections; the Stokes scans, compared with the results found in Chapter 5, reveal a profound difference in the polarisation of the diffracted beam. The results are interpreted in terms of magnetostrictive displacements of the Mn, Tb and O ions, giving rise to a Thomson contribution which interferes with the magnetic diffraction at the same incommensurate position τ of the reciprocal space. This analysis leads to a quantitative estimation of the atomic displacements both under applied field and in zero field; this task is currently ongoing and being developed by H. Walker and co-workers at the European Synchrotron Radiation Facility.

6.1 H-T phase diagram of $TbMnO_3$

The effect of an applied magnetic field on the phase diagram of $TbMnO_3$ has been systematically studied first by Kimura and co-workers. The results are published in a series of papers [1, 68, 69]. The measurements undertaken consisted in the temperature dependence of the electric polarisation and dielectric constant in applied magnetic fields of various magnitudes, and in the field dependence (from 0 T up to 15 T) of the magnetisation and electric polarisation at various temperatures. The overall conclusions obtained by this work lead to the temperature-magnetic field phase diagram shown in Fig. 6.1.

When a magnetic field is applied along the **a** or **b** crystallographic axis, it eventually leads to a metamagnetic phase transition, at which point a flop of the ferroelectric polarisation takes place, switching its direction from the **c** to the **a** axis. The critical value of the magnetic field (H_C) is a function of the temperature, and the boundaries in the phase diagram have been determined with some precision in the case of a field applied along **b** (see Fig. 6.1 - (c)). The fact that the magnetic

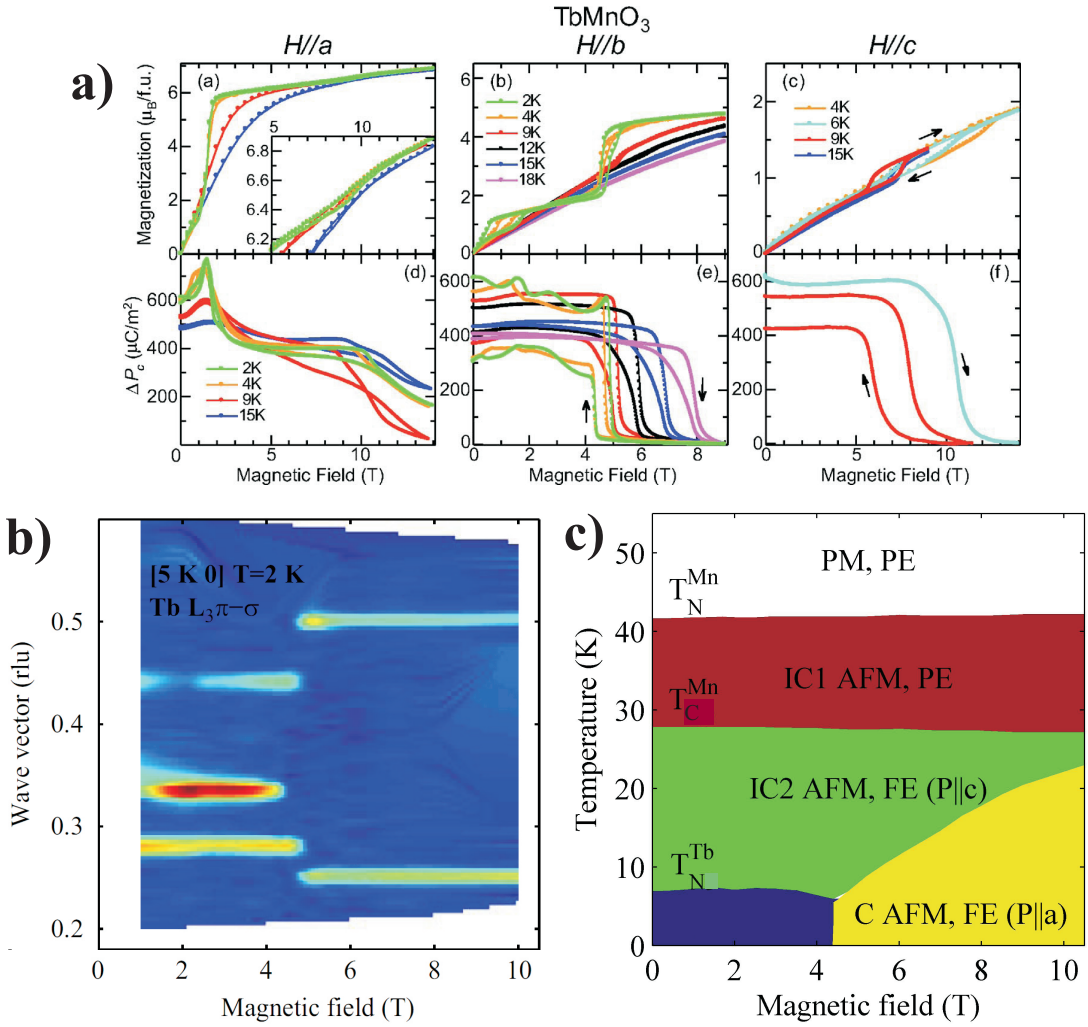

Figure 6.1: Magneto-electric phase diagram of $TbMnO_3$, as determined from bulk and diffraction measurements. (a) Magnetisation and magnetic-field-induced change in electric polarisation along **c** as a function of external magnetic fields parallel to the three axes, at fixed temperatures. These measurements by Kimura et al. [69] complete the results at zero field previously discussed (cf. Fig. 5.1). (b) Intensity colour map from [87] of X-ray resonant scattering at the Tb L_{III} edge. The scans were performed along (5 k 0) as a function of magnetic field applied parallel to **b** at T = 2 K (phase III, see section 5.1). Below 4.5 T the propagation wavevectors of the incommensurate Tb and Mn ordering are visible: magnetic C-type reflection (5 τ 0) $\approx$ (5 0.28 0); lattice reflection (5 1 $-\ \tau_L$ 0) $\approx$ (5 0.44 0), $\tau_L \approx 2\tau$; magnetic reflection at (5 1/3 0), attributed to a phase transition on the Tb sublattice at around 1 T, from an incommensurate ($\tau_T \approx 0.425$) to a commensurate structure. Above 4.5 T only the propagation wavevectors of the commensurate magnetic ordering are visible, at (5 1/4 0) and (5 1/2 0). This transition is coincident with the flop in the electric polarisation from **c** to **a**. (c) Resulting phase diagram of $TbMnO_3$, for a magnetic field applied along the **b** axis (the complete phase diagram for fields along the three axes has been shown in Fig. 5.1 - (c)). The metamagnetic transitions correspond to the flop in **P**.

transition and the polarisation flop occur at the same value of the field for every temperature is a clear confirmation of the link between ferroelectricity and the magnetic order. When the field is applied along the **c** axis, a magnetic transition occurs and brings the sample into a parelectric state.

From X-ray diffraction studies of superlattice peaks in strong magnetic fields **H** $\parallel$ **b** [84], it has been deduced that the phase transition is accompanied by the onset of a commensurate AF spin

alignment, with a modulation vector of 1/4 $\mathbf{b}^*$. Neutron and X-ray diffraction studies on magnetic peaks confirmed this result for both $\mathbf{H} \parallel \mathbf{a}$ and $\mathbf{H} \parallel \mathbf{b}$ [85]. Some recent and detailed measurements by Strempfer et al. [86] and Walker et al. [87] report on the simultaneous flop of the polarisation and the jump of the magnetic wavevector to the commensurate value, for both field configurations $\mathbf{H} \parallel \mathbf{a}$ and $\mathbf{H} \parallel \mathbf{b}$. It is suggested that these results reflect the flop of the magnetic cycloidal plane from the $(\mathbf{b}, \mathbf{c})$ to the $(\mathbf{a}, \mathbf{b})$ plane. This would be consistent with the flop of the polarisation; however, it is shown that the magnetic interactions between Mn and Tb moments remain significant in applied field, and may be considered as a perturbation upon the simple model of the flop of the cycloidal plane. Neutron studies with $\mathbf{H}$ aligned along $\mathbf{c}$ completed the investigation by measuring F and C-type reflections [75]. X-ray diffraction showed that a discontinuous jump in the wavevector occurs during the transition, with both IC and C peaks co-existing for a narrow range of values of the magnetic field near H_C.

As for the effects of a magnetic field below H_C, the evolution of both resonant and non-resonant X-ray scattering at the superlattice reflections as a function of applied magnetic field has been studied by several groups. Both Aliouane et al. [85] and Strempfer et al. [86] report the observation of charge reflections not only at the double harmonic positions $\tau_L = 2\tau$ (also present at zero field, cf. Chapter 5), which can be attributed to quadratic magnetoelastic coupling between the spin density wave and the lattice, but also at the single harmonics. They present this as evidence of a linear magnetoelastic coupling, but there has been no quantitative analysis until now of the magnetic structure under applied field before the metamagnetic transition.

6.2 Experimental method

In this study, X-ray non-resonant scattering has been used in an attempt to identify the atomic displacements induced by a magnetic field $\mathbf{H} \parallel \mathbf{b}$, which so far have eluded experimental detection. Using the interference between the magnetic and Thomson displacive amplitudes at the same reflection for different incident energies, it is possible to obtain detailed information regarding the nature of the displacements as a function of the applied field, which in turn has consequences for the magnitude of the off-centre atonic displacements responsible for the spontaneous ferroelectric polarisation in zero magnetic field. At the present time, this work is still ongoing. I was involved in the planning and the execution of the first experiments described in this section, while the data analysis and interpretation is currently being developed by Walker and co-workers at the European Synchrotron Radiation Facility (to be published). I will present here a qualitative interpretation of the data.

Experiments were performed using the same single crystal of $TbMnO_3$ and the same setup configuration described in Chapter 5; however, this time the sample stick was inserted into the Oxford Instruments 10 T cryomagnet (Fig. 3.2), allowing the application of a verical field (along the $\mathbf{b}$ axis of the sample). A specific feature of this series of experiments is that they were performed at different non-resonant energies, so as to take advantage of the changing ratio of the dispersion corrections for the atomic scattering factors for Mn and Tb as a function of energy, a technique somewhat similar to that used in macromolecular crystallographic structure determination. Unless the radiation energy

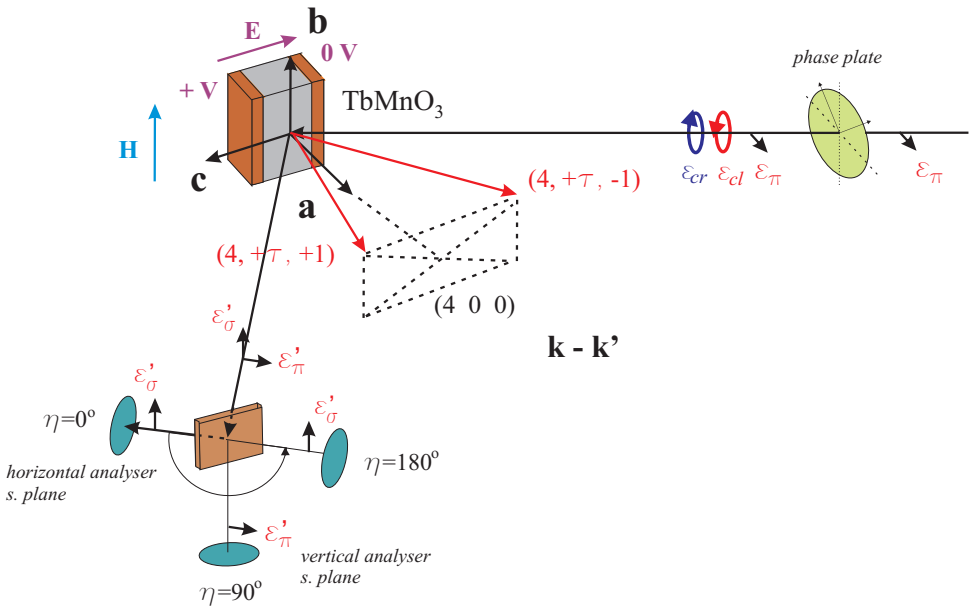

Figure 6.2: Scheme of the experimental setup. The sample, glued to the E-field stick as in previous measurements (Chapter 5), was placed inside the Oxford Instruments 10 T magnet described in 3.1.3, allowing the application of a field along the vertical direction as per the scheme. The reflections investigated were (4 τ 1) and (4 τ -1).

is much smaller than any of the absorption edge wavelengths in the atom, the Thomson scattering is expressed by the atomic form factor f_0 (Fourier transform of the charge density, cf. Eq. 2.11) corrected by a complex dispersion factor

$$f_{TH}(K,\omega) = f_0(K) + f'(\omega) + if''(\omega)$$

where $K = |\mathbf{K}| = |\mathbf{k} - \mathbf{k}'|$, and f', f'' represent respectively the real and imaginary part of the correction (involving a small shift in phase of the scattered radiation). The measurements were collected at three energies with the corresponding dispersion corrections for the atomic scattering factors (Fig. 6.3):

$E(keV)$	$f_0 + f'(Mn)$	$f"(Mn)$	$f_0 + f'(Tb)$	$f"(Tb)$	$f_0 + f'(O)$	$f"(O)$
6.160	22.5	0.5	59.0	4.9	8.08	0.06
6.850	22.6	3.6	57.4	4.2	8.06	0.04
7.770	24.2	3.0	55.2	9.8	8.05	0.03

i.e. below the Mn K-edge, between the Mn K-edge and the Tb L_{III}-edge, and above the Tb L_{III}-edge. As in previous measurements, incident horizontally linearly polarised beam was converted into a circular polarisation state using an in-vacuum quarter-wave diamond phase plate. Despite the different energies, the 720 mm thickness of the diamond allowed us to produce a beam which was 99 % circularly polarised. The polarisation state of the scattered beam was obtained using single crystal analysers as appropriate for the different incident energies (LiF(220) at E = 6.16 keV, Cu(220) at E = 6.85 keV and Pt(222) at E = 7.77 keV). A voltage of $\approx$ 500 V was applied across the sample as it was cooled from T = 60 K to 15 K, in order to drive the magnetic structure into a monodomain cycloidal state, as documented in Chapter 5. Stokes scans were performed for various magnetic

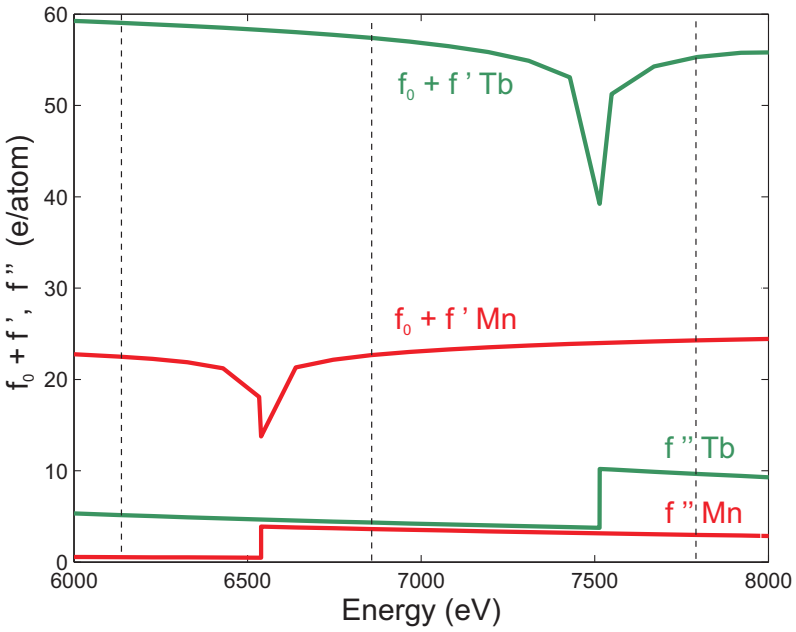

Figure 6.3: Atomic scattering factors for Tb and Mn at $K = 0$ (real and imaginary part) including dispersion correction in the energy range of interest. The energies at which the experiments were performed are marked by dashed lines; it can be noted that the imaginary contribution f'' is strongly affected by the energy change.

fields at the two magnetic satellites $\mathbf{k} - \mathbf{k}' = (4\ \tau\ 1)$ and $(4\ \tau$ -1). The background signal was also measured after deplacing the sample by $\Delta\Theta = 0.2°$, enabling it to be subtracted from the total signal, as shown for previous measurements (Chapters 4 and 5). In addition to the Stokes scans, the intensity of the peaks as a function of the applied magnetic field has been recorded through scans along the reciprocal space direction $\mathbf{b}^*$, in various polarisation channels.

6.3 Overview of the experimental results

Several scans along the reciprocal space direction $\mathbf{b}^*$ were measured through the magnetic reflection $(4\ \tau$ -1) as a function of magnetic field applied along the $\mathbf{b}$ axis, for both left (LCP) and right (RCP) circularly polarised X-rays incident on the sample, and with the polarisation analyser oriented at $\eta = 45°$; $90°$; $135°$. The incommensurate reflection was observed up to H = 9 T, whilst there was a coexistence of the commensurate and incommensurate phases between H = 8 and 9 T. The wavevector remained constant below 7 T before starting to reduce in magnitude, implying the onset of the transition. The results plotted in Fig. 6.4 reveal that the intensity for $\eta = 90°$, i.e. the scattering in the $\hat{\pi}'$ channel obtained by numerically integrating the area under the measured peak, is approximately independent of the applied magnetic field for both incident polarisation states. In contrast, the intensities for $\eta = 45°$ and $135°$ show a marked parabolic dependence on the applied magnetic field. Comparing the results for LCP and RCP incident beam reveals that the general trend is exchanged between $\eta = 45°$ and $135°$, whilst the minima lie closer to the zero of magnetic field for LCP than RCP incident.

To learn more about the origin of the scattering intensity, the Stokes dependence of the two reflections $(4\ \tau$ -1) and $(4\ \tau\ 1)$ was measured with LCP and RCP incident X-rays in an applied

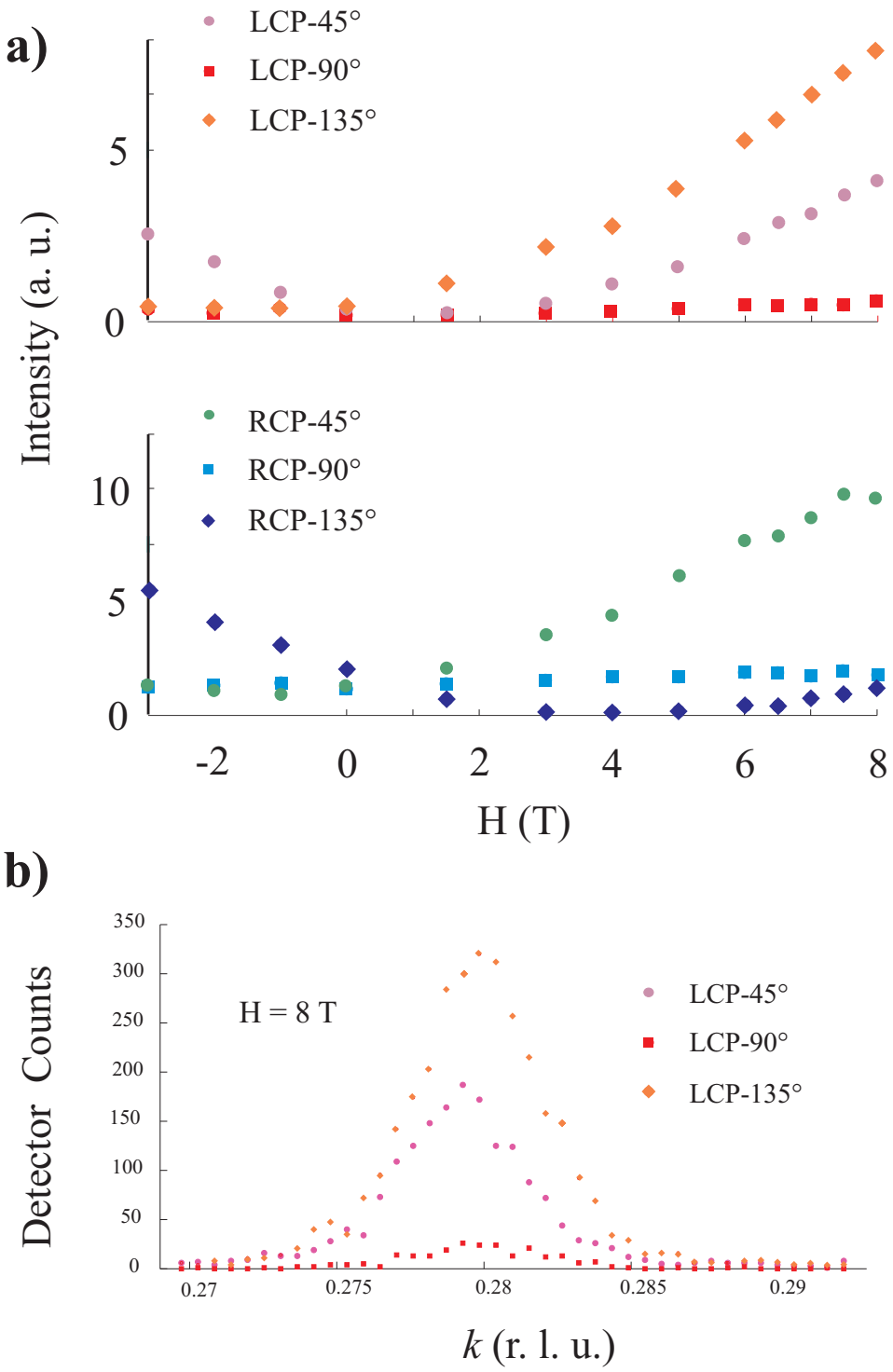

Figure 6.4: (a) Magnetic field dependence of the intensity of the reflection (4 τ -1) at 15 K, for LCP (upper) and RCP (lower panel) incident light (energy E = 6.16 keV), measured at η = 45°; 90°; 135°. Each point represents the integrated intensity obtained from a scan along the direction $\mathbf{b}^*$ in the reciprocal space. (b) Example of the raw data in the case of H = 8 T and LCP incident light. The integrated intensity of each of the three curves constitutes one point in the upper panel of (a).

magnetic field of H = 3 T (Fig. 6.5). In contrast to the measurements obtained in zero magnetic field (Chapter 5), in which there is a strong imbalance in the intensities measured for LCP and RCP as a result of the coupling between the quasi-monodomain and the handedness of the X-rays, in

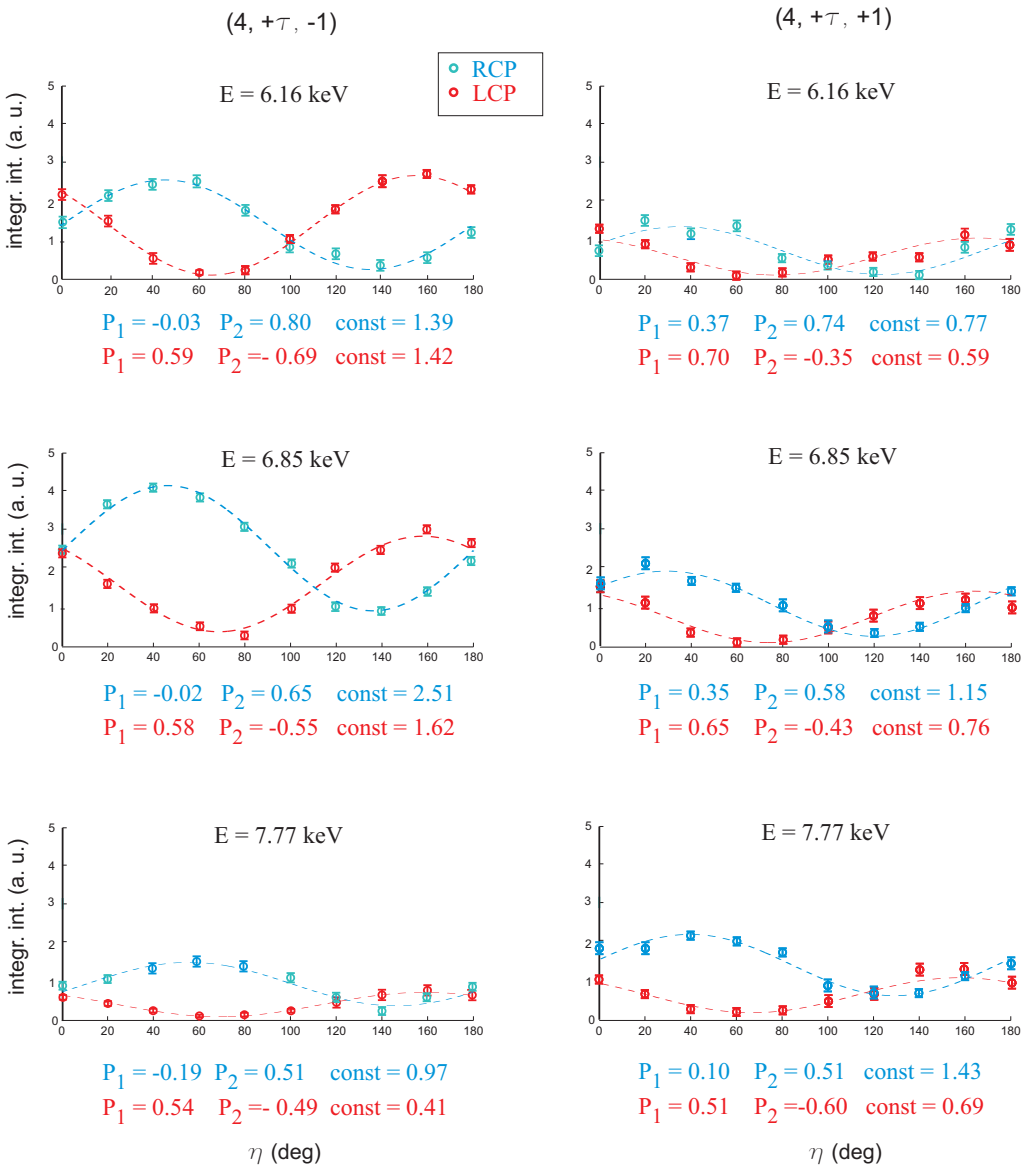

Figure 6.5: Variation with the analyser rotation angle η (Stokes scans) of the X-ray magnetic scattering from the reflections (4 τ $\pm$1) in $TbMnO_3$ at T = 15 K and **H** $\parallel$ **b** = 3 T, for different energy (E = 6.16; 6.85; 7.77 keV) and incident polarisation (LCP in red and RCP in blue) of the incident X-rays. Dashed lines represent a fit to Eq. 3.2 describing polarised light, to extract the Stokes parameters (printed below each panel).

this case the intensities for the two different polarisation states are more similar, as can be seen in the top two panels of Fig. 6.5. A further difference from the Stokes dependence of the scattering in zero magnetic field is that, with the exception of the absolute intensity, the form of the sine waves is similar for a given incident polarisation state for both reflections, as opposed to being in anti-phase. In addition the Stokes dependence shows that the minimum intensities are approaching to zero, and lie close to $\eta = 45°$ and 135°, indicating that the incident circular polarisation state on scattering has been converted into an almost linear polarisation state inclined at $\approx 45°$ from the scattering plane. The same Stokes measurements at the two reflections were repeated for two additional incident energies of E = 6.85 and 7.77 keV. As Fig. 6.5 shows, the general form of the Stokes dependence is similar for the different energies.

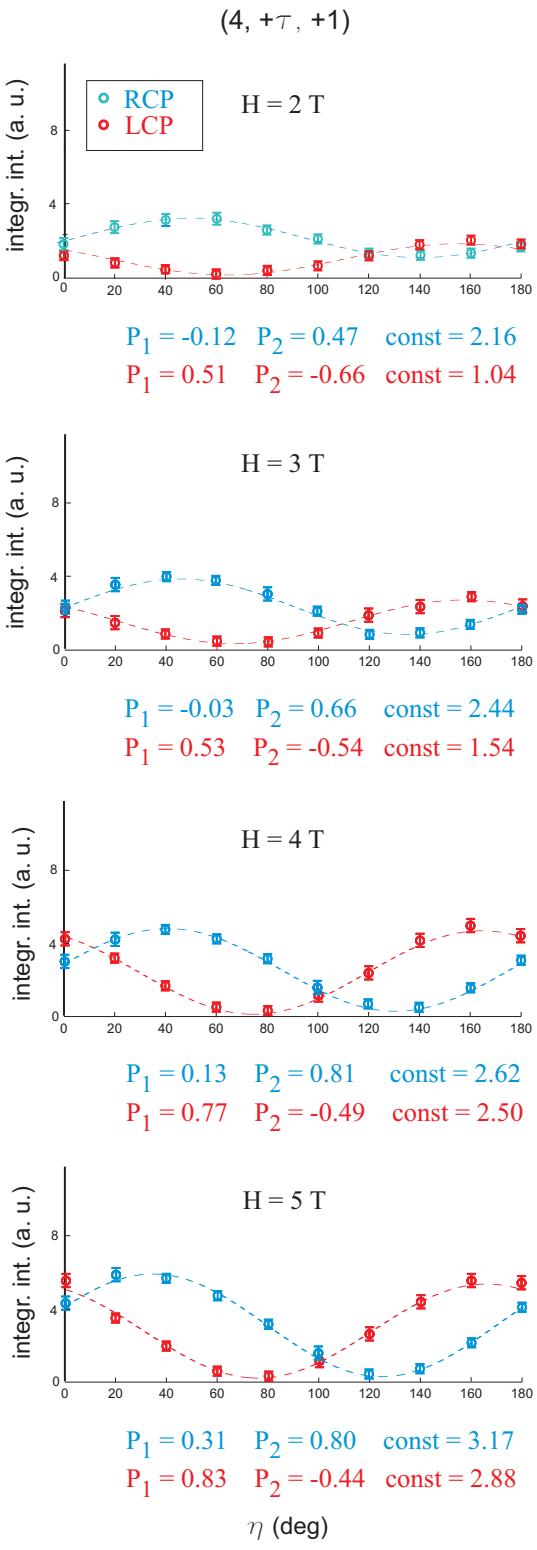

Figure 6.6: Stokes scans on the reflection (4 τ 1) in $TbMnO_3$ at T = 15 K and E = 6.85 keV, for different magnetic fields applied along the **b** axis, with LCP (red) and RCP (blue) incident X-rays. The Stokes parameters are extracted as per Fig. 6.5.

At E = 6.85 keV the Stokes dependence of the scattering reflection (4 τ -1) was investigated for different magnetic fields $\mathbf{H} \parallel \mathbf{b}$ = 2, 3, 4, and 5 T. Inspection of Fig. 6.6 shows that with increasing applied magnetic field the scattering intensity grows, with the amplitudes of the scattering for LCP and RCP incident becoming more equal.

6.4 Interpretation

There are no reports in the literature of a change in the magnetic structure of $TbMnO_3$ below the critical field, and the measured Stokes dependence could not be reproduced using calculations based on a modification of the magnetic structure. Instead, if one considers the magnetic field to have induced an additional small moment on the Tb and Mn ions polarised along the **b** axis with ordering wavevector = 0, then charge Thomson scattering associated with the induced magnetoelastic distortion will arise at (4 τ -1) and (4 τ +1). Suppose that the application of the magnetic field along the **b** axis induces a constant magnetisation $\mathbf{M}_H^{Mn(Tb)}$ of the Mn (Tb) lattice, ignoring any modulated magnetization possibly also induced. Due to exchange striction or magnetocrystalline anisotropy, $\mathbf{M}_H^{Mn(Tb)}$ in combination with the zero field magnetic moments, $\mathbf{M}(\mathbf{x}_1)$ at $\mathbf{x}_1$, produce atomic displacements, where to lowest order the displacement of an atom at $\mathbf{x}_2$ is

$$\delta(\mathbf{x}_2) = \sum_{\mathbf{x}_1} \mathbf{M}(\mathbf{x}_1)\ (\alpha_{Mn}(\mathbf{x}_2,\mathbf{x}_1)\mathbf{M}_H^{Mn} + \alpha_{Tb}(\mathbf{x}_2,\mathbf{x}_1)\mathbf{M}_H^{Tb}) \tag{6.1}$$

The tensor $\alpha(\mathbf{x}_2,\mathbf{x}_1)$ combines the coefficients of two free energy terms, a term of magnetostriction $\delta(\mathbf{x}_2)\mathbf{M}(\mathbf{x}_1)\mathbf{M}_H$, and a term of stiffness $\delta^2(\mathbf{x}_2)$. Because the atomic displacement $\delta(\mathbf{x}_2)$ is quadratically dependent on the magnetisation, a monoharmonic sinusoidal spin modulation (as the one present in zero field) and an additional ferromagnetic component allow $\delta(\mathbf{x}_2)$ to mirror the sinusoidal dependence of the spin modulation, thus contributing to a Thomson scattering at propagation vector τ along the $\mathbf{b}^*$ direction in the reciprocal space, interfering with the purely magnetic scattering reflections (see Fig. 6.7).

On this basis the qualitative features of the data shown in Fig. 6.5 and 6.6 can be reproduced using the scattering amplitude for the magnetic structure taken at zero magnetic field (developed in Chapter 5) combined with a complex Thomson scattering term (A_{TH}+iB_{TH}):

$$f_{nr+TH} \ = \ (A_{TH} + iB_{TH}) \ - \ i\frac{\hbar\omega}{mc^2} f_{nr}.$$

Note that A_{TH}+iB_{TH} is proportional to the sum of the Thomson contributions over the atomic sites $\sum_j f_{TH,j}(K,\omega)e^{i\mathbf{K}\cdot\mathbf{r}_j}$ and $f_{TH,j}(K,\omega) = f_{O,j}(K) + f'_j(\omega) + if''_j(\omega)$, and thus may contain a non trivial dependence on the Miller indexes and the sign of τ, as it has been the case for the magnetic structure factor (cf. Chapter 5).

These contributions manage to reproduce the general features of the data. In the Jones matrix basis and under the same approximation used in the analytical calculations of Chapter 5, the scattering amplitude becomes:

$$\begin{bmatrix} f_{\sigma'} \\ f_{\pi'} \end{bmatrix} = \begin{bmatrix} S_b^M - 2i\beta S_b^T + (A'_{TH} + iB'_{TH}) & i\frac{1}{\sqrt{2}}\alpha\gamma S_c^M \\ -i\frac{1}{\sqrt{2}}\alpha\gamma S_c^M & S_b^M - 2i\beta(S_b^T + L_b^T) \end{bmatrix} \begin{bmatrix} 1 \\ i\epsilon \end{bmatrix}$$

where, since $2\Theta \approx 90°$, the Thomson scattering reduces to the $\sigma - \sigma'$ channel. The magnetic components S_b^M, S_c^M, S_b^T, L_b^T are the same as defined in Eq. 5.11. The optimal values found for the two phase shifts ϕ_{TM} and ϕ_{TO} have been used. The sign factors α, β, γ, ϵ define respectively the sign of the index k of the reflection ($\pm\tau$), the sign of the index l (±1), the magnetic cycloidal domain and the handedness of the circular polarisation of the incident beam. Finally, the coefficients describing the Thomson scattering A'_{TH} and B'_{TH} are directly related to the coefficients A_{TH} and

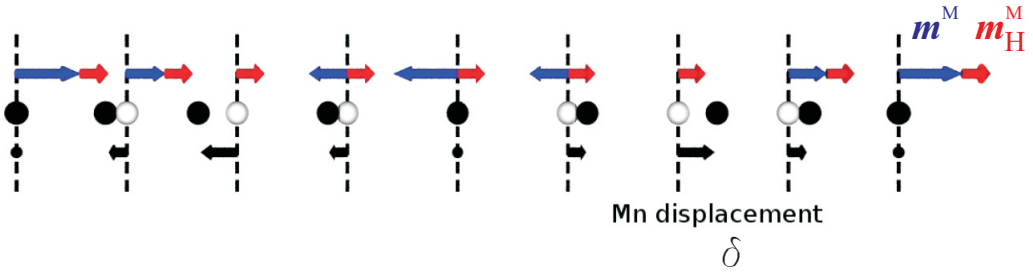

Figure 6.7: Schematic demonstrating how a magneto-electric distortion can have the same periodicity as the magnetic order, resulting in Thomson scattering at the same wavevector. The sketch depicts the projection on the **B** axis of the Mn cycloidal magnetic structure (blue arrows), the additional ferromagnetic component resulting from the application of a magnetic field along **b** (red), and the displacement of the Mn atoms arising from the coupling of the two magnetic orderings (black), following the model presented in Eq. 6.1.

B_{TH} just intrduced, taking into account the imaginary scale factor $-i\hbar\omega/\ mc^2$ between Thomson and non-resonant scattering.

The scattering amplitudes in the two polarisation channels σ' and π' become:

$$\begin{aligned} f_{\sigma'} &= S_b^M - 2i\beta S_b^T + (A'_{TH} + iB'_{TH}) - \tfrac{1}{\sqrt{2}}\epsilon\alpha\gamma S_c^M &&= A - 2i\beta S_b^T + (A'_{TH} + iB'_{TH}) \\ f_{\pi'} &= -i\tfrac{1}{\sqrt{2}}\alpha\gamma S_c^M + i\epsilon S_b^M + 2\epsilon\beta(S_b^T + L_b^T) &&= i\epsilon A + 2\epsilon\beta(S_b^T + L_b^T) \end{aligned}$$

where the parameter A includes the dominant magnetic contribution from the Mn atoms and is defined as in Eq. 5.5 as

$$A = S_b^M - \frac{1}{\sqrt{2}}\epsilon\alpha\gamma S_c^M.$$

The dominant features of the data which distinguish them from the results at zero field are a high value of P_2 for both incident polarisations, and also an increased value of P_1. Turning first to P_2, the degree of linear polarisation oriented along $\eta = \pm 45°$ can be estimated by comparing $|f_{\sigma'} + f_{\pi'}|^2$ and $|f_{\sigma'} - f_{\pi'}|^2$:

$$\begin{aligned} |f_{\sigma'} + f_{\pi'}|^2 &= |A + 2\epsilon\beta(S_b^T + L_b^T) + A'_{TH}|^2 + |A - 2\epsilon\beta S_b^T + \epsilon B'_{TH}|^2 \\ |f_{\sigma'} - f_{\pi'}|^2 &= |A - 2\epsilon\beta(S_b^T + L_b^T) + A'_{TH}|^2 + |A + 2\epsilon\beta S_b^T - \epsilon B'_{TH}|^2. \end{aligned}$$

Obviously the orbital contribution found on the Tb atoms, responsible for the nonzero value of P_2 in zero field, cannot account for such a strong P_2 as seen in the data. The Tb contribution is therefore omitted in the present analysis as negligible with respect to the Mn magnetic scattering and the Thomson scattering:

$$\begin{aligned} |f_{\sigma'} + f_{\pi'}|^2 &= |A + A'_{TH}|^2 + |A + \epsilon B'_{TH}|^2 \\ |f_{\sigma'} - f_{\pi'}|^2 &= |A + A'_{TH}|^2 + |A - \epsilon B'_{TH}|^2. \end{aligned}$$

From this expression, it can be seen that the Thomson contribution is able to create an imbalance between the two terms thanks to its imaginary part B'_{TH}, thus allowing a relevant value of P_2 to emerge. Moreover, the sign of P_2 is reversed when the handedness of the circular polarisation is switched (parameter ϵ). As for P_1, the degree of linear polarisation along $\eta = 0 - 90°$ is extracted from the difference between $|f_{\sigma'}|^2 \approx |A + A'_{TH} + iB'_{TH}|^2$ and $|f_{\pi'}|^2 \approx |A|^2$, and in this case, both real and imaginary part of the Thomson scattering can contribute to an imbalance between the two. In conclusion, the Thomson contribution possesses the symmetry requirements to reproduce

the qualitative features of the data. As a final note, it can be seen from Fig. 6.6 that the distorsion from the zero field polarisation induced by the Thomson terms increases with the magnitude of the field, such that the A'_{TH} and B'_{TH} coefficients appear to be linearly dependent on H.

6.5 Conclusions and future outlook

Since the physical origin of the Thomson scattering is magnetostrictive atomic displacements due to interactions between the zero field moments and those induced by the applied magnetic field, an exact model of the displacements can be found by a symmetry analysis imposing constraints on the atomic positions, followed by a standard crystallographic study looking at the measured structure factors as a function of the displacements. This study is currently being developed by Walker and co-workers. The preliminary results reveal that it is possible to identify the displacement modes and, through the energy dependence of the atomic scattering factors, the displacements of the diferent atomic species. The quantitative information thus obtained allows for an estimation of the displacments in zero magnetic field.

Chapter 7

Conclusion and future perspectives

It has been shown how interest in multiferroics (materials in which ferroelectricity coexists with magnetic order) and magneto-electric coupling has been revived in recent years, since the discovery of magnetically induced ferroelectricity in $TbMnO_3$. Besides the challenge that these materials represent to our fundamental understanding of ordering phenomena in solids, a fundamental driver for this research on the applied side is the hope that it will provide new materials to be used in data storage and processing devices. In this respect, of paramount importance is the quest for a material that can be written electrically and read magnetically at room temperature, since localised electric fields are much easier to generate and much less energy demanding as compared to magnetic fields. The requirement of strong magneto-electric effect has oriented the research within the range of compounds in which ferroelectricity appears as a consequence of magnetic ordering and, indeed, it has been found that spin-driven cycloid multiferroics exhibit an exceptionally strong cross-coupling between the different types of order, as demonstrated in a number of studies where non-conjugate fields have been used to control the order, i.e. the control of magnetization **M** by **E** or ferroelectric polarization **P** by **H**. However, the symmetry breaking necessary for the onset of spontaneous polarisation is only to be found in rather complex magnetic structures. The appropriate magnetic materials are usually characterised by an interplay of competing exchange interaction and/or geometrically-driven magnetic frustration, which leads the symmetry-breaking phase to appear at very low temperatures. Recently, an intense experimental effort combined with a refined understanding of the symmetry requirements that can allow ferroelectricity to exist have expanded the range of candidate materials to exhibit spin-driven multiferroic behaviour. An interesting line of research has developed specifically on magnetochiral or proper-screw systems even at room temperature [89, 90].

In this scenario, an experimental technique capable to capture the fine details of the magnetic ordering is as an essential tool to progress in the discovery and characterisation of such increasingly complex materials. In this work, it has been demonstrated that non-resonant X-ray magnetic diffraction, enhanced by polarisation control via phase plate and polarimetry of the diffracted beam, is an effective method for magnetic structure refinement of spin-driven multiferroics $Ni_3V_2O_8$ and $TbMnO_3$. Its advantages over other traditional techniques such as neutron scattering or X-ray magnetic scattering with azimuthal scans have been explored. Firstly, one star of magnetic superlattice peaks has been sufficient to perform a refinement, as opposed to collecting a large number of mag-

netic reflections. This greatly eases the ability to apply external fields and, in future research, other experimental conditions such as, for example, mechanical pressure. Moreover, the data on a single star of peaks are collected under homogeneous geometric conditions and are less affected by variations in the experimental conditions and in the absorption by the sample. This aspect is enhanced by the use of polarisation-varying techniques, in lieu of azimuthal scans. In view of the quest for new multiferroic materials outlined above, the trend towards increasingly complex magnetic structures makes this approach particularly suitable, primarily because of its sensitivity to the finer details of the magnetic modulations, such as the phase difference between different atomic spin density waves and the distinction between spin and orbital contribution to the magnetic moments. The kind of detail provided by the phase shifts is key to the search and characterisation of new multiferroics, as it affects the symmetry properties of the magnetic structure and, in turn, of the ferroelectricity that consequently emerges. In particular, the proper-screw magnetic arrangement found in many of the novel materials lends itself to experimental probing by means of circularly polarised incident X-rays, in a way analogous to the cycloidal arrangement studied in the course of this work.

While the magnetic order in many canonical multiferroics is by now mostly understood, the nature of the ferroelectricity has remained much more elusive. In the case of $TbMnO_3$, competing models have been proposed to explain the ferroelectricity, associated respectively with charge transfer and ionic displacements. Exploiting the magneto-electric coupling, it has been shown how an electric field can be used to produce a single magnetic domain state, and a magnetic field to induce ionic displacements. Under these conditions, interference between charge and magnetic X-ray scattering arises, encoding information both in phase and amplitude. These data, when combined with a theoretical analysis, can provide information on the displacements of the constituent ions, and show how such displacements make a significant contribution to the zero-field ferroelectric moment. The technique introduced here can be extended to other multiferroics, and to the wider class of systems with complex order in the presence of magnetoelastic coupling.

Finally, one of the outstanding challenges in this field of research is the development of methods capable of imaging multiferroic domains, and most especially their evolution under applied external fields. However, the imaging of ferroelectric and magnetic domains has largely remained two separate fields, with a few exceptions [91]. Imaging of ferroelectric domains is well established, and can be achieved through a variety of probes including X-ray charge scattering [92, 93], and atomic force microscopy [94]. In contrast, the imaging of antiferromagnetic domains has emerged in more recent times, driven by the availability of highly brilliant X-ray beams from synchrotron sources. The high spatial resolution attainable with such sources has enabled new imaging methods based on either the absorption [95] or scattering [96, 97, 98] of an X-ray beam through various processes which yield sensitivity to the antiferromagnetic order. In the case of $Ni_3V_2O_8$, the technique presented in this work enabled the imaging of multiferroic domains through polarisation enhanced topography, and this approach has been used to image the spatial distribution of magnetic domains as the sample is cycled by an electric field through its hysteresis loop. This method has potential for imaging domains in multiferroic devices and other classes of correlated electron systems which are characterised by unconventional or coupled order parameters, and by revealing in this case the gradual switching of domains without nucleation, and exposing the existence of strong pinning effects close to the edge

of the sample, proves to be able to help the design of better functional materials.

Bibliography

[1] T. Kimura, T. Goto, H. Shintani, K. Ishizaka, T. Arima and Y. Tokura, Nature **426**, 55 (2003).

[2] M. Kenzelmann, A. B. Harris, S. Jonas, C. Broholm, J. Schefer, S. B. Kim, C. L. Zhang, S.-W. Cheong, O. P. Vajk and J.W. Lynn, Phys. Rev. Letters **95**, 087206 (2005).

[3] S.-W. Cheong and M. Mostovoy, Nature Materials **6**, (2007).

[4] W. Eerenstein, N. D. Mathur and J. F. Scott, Nature **442**, 759 (2006).

[5] D.I. Khomskii, J. Magn. Magn. Mater. **306**, (2006).

[6] T. Kimura, Annual Review of Materials Research **37**, 387 (2007).

[7] M. Fiebig, J. Phys. D: Appl. Phys. **38**, R123 (2005).

[8] N. A. Hill and A. Filippetti, J. Magn. Magn. Mater. **242-245**, 976 (2002).

[9] N. A. Hill, J. Phys. Chem. B **104**, 6694 (2000).

[10] M. Kenzelmann, A. B. Harris, A. Aharony, O. Entin-Wohlman, T. Yildirim, Q. Huang, S. Park, G. Lawes, C. Broholm, N. Rogado, R. J. Cava, K. H. Kim, G. Jorge and A. P. Ramirez, Phys. Rev. B **74**, 014429 (2006).

[11] F. Fabrizi, H. C. Walker, L. Paolasini, F. de Bergevin, A. T. Boothroyd, D. Prabhakaran and D. F. McMorrow, Phys. Rev. Lett. **102**, 237205 (2009).

[12] F. Fabrizi, H. C. Walker, L. Paolasini, F. de Bergevin, T. Fennell, N. Rogado, R. J. Cava, Th. Wolf, M. Kenzelmann and D. F. McMorrow, Phys. Rev. B **82**, 024434 (2010).

[13] I. Cabrera, M. Kenzelmann, G. Lawes, Y. Chen, W. C. Chen, R. Erwin, T. R. Gentile, J. B. Leo, J. W. Lynn, N. Rogado, R. J. Cava and C. Broholm, Phys. Rev. Lett. **103**, 087201 (2009).

[14] G. A. Smolenskii and I. E. Chupis, Sov. Phys. Uspekhi **25**, 475 (1982).

[15] Y. N. Venevtsev and V. V. Gagulin, Ferroelectrics **162**, 23 (1994).

[16] R. Z. Levitin, E. A. Popova, R. M. Chtsherbov, A. N. Vasiliev, M. N. Popova, E. P. Chukalina, S. A. Klimin, P. H. M. van Loosdrecht, D. Fausti and L. N. Bezmaternykh, Pis'ma Zh. Eksp. Teor. Fiz., **79**, 531 (2004); JETP Lett., **79**, 423 (2004).

[17] J. B. Goodenough and J. M. Longo, Landolt-Bornstein, Numerical Data and Functional Relationships in Science and Technology, New Series, Group III, Vol. 4, Springer-Verlag, Berlin, 1970, p. 126.

[18] T. Mitsui, M. Adachi, J. Harada, T. Ikeda, S. Nomura, E. Sawgu-chi and T. Yamada, Landolt-Brnstein, Numerical Data and Functional Relationships in Science and Technology, New Series, Group III, Vol. 16, Springer-Verlag, Berlin, 1981, Pt 1A.

[19] A. M. Kadomtseva, A. K. Zvezdin, Yu. F. Popov, A. P. Pyatakov and G. P. Vorobev, JETP Lett. **79**, 571 (2004).

[20] A. M. dos Santos, S. Parashar, A. R. Raju, Y. S. Zhao, A. K. Cheetham and C. N. R. Rao, Solid State Commun. **122** 49 (2002).

[21] N.A. Hill, J. Phys. Chem. B **104**, 6694 (2000).

[22] R. Seshadri and N.A. Hill, Chem. Mater. **13**, 1892 (2001).

[23] B. van Aken, T.T.M. Palstra, A. Filippetti and N.A. Spaldin, Nature Mater. **3**, 164 (2004).

[24] C.H. Ahn, K.M. Rabe and J.-M. Triscone, Science **303**, 488 (2004).

[25] N. Hur, S. Park, P. A. Sharma, J. S. Ahn, S. Guha and S.-W. Cheong, Nature **429**, 392 (2004).

[26] G. Lawes, A. B. Harris, T. Kimura, N. Rogado, R. J. Cava, A. Aharony, O. Entin-Wohlman, T. Yildirim, M. Kenzelmann, C. Broholm and A. P. Ramirez, Phys. Rev. Lett. **95**, 087205 (2005).

[27] T. Kimura, G. Lawes and A.P. Ramirez, Phys. Rev. Lett. **94**, 137201 (2005).

[28] S. Quezel, F. Tcheou, J. Rossat-Mignod, G. Quezel and E. Roudaut, Physica B **86-88**, 916 (1977).

[29] K. Kajimoto, H. Yoshizawa, H. Shintani, T. Kimura and Y. Tokura, Phys. Rev. B **70**, 012401 (2004).

[30] M. Mostovoy, Phys. Rev. Lett. **96**, 067601 (2006).

[31] I. E. Dzyaloshinskii, Sov. Phys. JETP **10**, 628 (1960).

[32] I. E. Dzyaloshinskii, Sov. Phys. JETP **19**, 960 (1964).

[33] T. Kimura, S. Ishihara, H. Shintani, T. Arima, K. T. Takahashi, K. Ishizaka and Y. Tokura, Phys. Rev. B **68**, 060403(R) (2003).

[34] H. Katsura, N. Nagasoa and A. V. Balatsky, Phys. Rev. Lett. **95**, 057205 (2005).

[35] I.A. Sergienko and E. Dagotto, Phys. Rev. B **73**, 094434 (2006).

[36] T. Moriya, Phys. Rev. **120**, 91 (1960).

[37] K. Taniguchi, N. Abe, T. Takenobu, Y. Iwasa and T. Arima, Phys. Rev. Lett. **97**, 097203 (2006).

[38] O. Heyer, N. Hollmann, I. Klassen, S. Jodlauk, L. Bohaty, P. Becker, J. A. Mydosh, T. Lorenz and D. Khomskii, J. Phys. Condens. Matter **18**, L471 (2006).

[39] T. Arima, J. Phys. Soc. Jpn. **76**, 073702 (2007).

[40] P. G. Radaelli and L. C. Chapon, Phys. Rev. B **76**, 054428 (2007).

[41] P. M. Platzman and N. Tzoar, Phys. Rev. B **2**, 3556 (1970).

[42] F. de Bergevin and M. Brunel, Physics Letters A **39**, 141 (1972).

[43] F. de Bergevin and M. Brunel, Acta Cryst. A **37**, 314 (1981).

[44] M. Blume, J. Appl. Phys. **57**, 3615 (1985).

[45] M. Blume and D. Gibbs, Phys. Rev. B **37**, 1779. (1988).

[46] J. p. Hill and D. F. McMorrow, Acta Cryst. **A52**, 236 (1996).

[47] C. Mazzoli, S. B. Wilkins, S. Di Matteo, B. Detlefs, C. Detlefs, V. Scagnoli, L. Paolasini and P. Ghigna, Phys. Rev. B **76**, 195118 (2007).

[48] U. Fano, Rev. Mod. Phys. **29**, 74 (1957).

[49] M. Blume, Phys. Rev. **130**, 1970 (1963).

[50] M. Blume and O. C. Kistner, Phys. Rev. **171**, 417 (1968).

[51] C. Sutter, G. Grübel, C. Vettier, F. de Bergevin, A. Stunault, D. Gibbs and C. Giles, Phys. Rev. B **55**, 954 (1997).

[52] L. Paolasini, C. Detlefs, C. Mazzoli, S. Wilkins, P. P. Deen, A. Bombardi, N. Kernavanois, F. de Bergevin, F. Yakhou, J. P. Valade, I. Breslavetz, A. Fondacaro, G. Pepellin and P. Bernard, J. Synch. Rad. **14**, 301 (2007).

[53] V. E. Dmitrienko and V.A. Belyakov, Soy. Techn. Phys. Lett. **6**, 621 (1980).

[54] V. A. Belyakov and V. E. Dmitrienko, Sov. Phys. Usp. **32**, 697 (1989).

[55] K. Hirano, K. Izumi, T. Ishikawa, S. Annaka and S. Kikuta, Jpn. J. Appl. Phys. **30**, L407 (1991).

[56] K. Hirano, K. Kanzaki, M. Mikami, M. Miura, K. Tamasaku, T. Ishikawa and S. Kikuta, J. Appl. Cryst. **25**, 531 (1992).

[57] T. Ishikawa, K. Hirano and S. Kikuta, J. Appl. Cryst. **24**, 982 (1991).

[58] C. Giles, C. Malgrange, J. Goulon, F. de Bergevin and C. Vettier, J. Appl. Cryst. **27**, 232 (1994).

[59] C. Giles, C. Malgrange, J. Goulon, F. de Bergevin, C. Vettier, A. Fontaine, E. Dartyge, S. Pizzini, F. Baudelet and A. Freund, Physica B **208-209**, 784 (1995).

[60] C. Giles, C. Vettier, F. de Bergevin, C. Malgrange, G. Grubel and F. Grossi, Rev. Sci. Instrum. **66**, 1518 (1995).

[61] V. Scagnoli, C. Mazzoli, C. Detlefs, P. Bernard, A. Fondacaro, L. Paolasini, F. Fabrizi and F. de Bergevin, J. Synch. Rad. **16**, 778 (2009).

[62] Th. Hahn (Ed.), International Tables for Crystallography, Volume A, 5th edition, Wiley (2002).

[63] E. E. Sauerbrei, F. Faggiani and C. Calvo, Acta Crystallogr., Sect. B: Struct. Crystallogr. Cryst. Chem. **29**, 2304 (1973).

[64] G. Lawes, M. Kenzelmann, N. Rogado, K. H. Kim1, G. A. Jorge, R. J. Cava, A. Aharony, O. Entin-Wohlman, A. B. Harris, T. Yildirim, Q. Z. Huang, S. Park, C. Broholm and A. P. Ramirez, Phys. Rev. Lett. **93**, 247201 (2004).

[65] V. Fernandez, C. Vettier, F. de Bergevin, C. Giles and W. Neubeck, Phys. Rev. B **57**, 7870 (1998).

[66] T. Finger, D. Senff, K. Schmalzl, W. Schmidt, L. P. Regnault, P. Becker, L. Bohaty and M. Braden, Phys. Rev. B **81**, 054430 (2010).

[67] S. Quezel, F. Tcheou, J. Rossat-Mignod, G. Quezel and E. Routaud, Physica B & C **86-88B**, 916 (1977).

[68] T. Goto, T. Kimura, G. Lawes, A. P. Ramirez and Y. Tokura, Phys. Rev. Letters **92**, 257201 (2003).

[69] T. Kimura, G. Lawes, T. Goto, Y. Tokura and A. P. Ramirez, Phys. Rev. B **71**, 224425 (2005).

[70] J. Blasco, C. Ritter, J. Garcia, J. M. de Teresa, J. Perez-Cacho and M. R. Ibarra, Phys. Rev. B **62**, 5609 (2000).

[71] E. F. Bertaut, J. Magn. Magn. Mater. **24**, 267 (1981).

[72] A. B. Harris, Phys. Rev. B, **76**, 054447 (2007).

[73] G. Prokhnenko, R. Feyerherm, M. Mostovoy, N. Aliouane, E. Dudzik, A. U. B. Wolter, A. Maljuk and D. N. Argyriou, Phys. Rev. Letters, **99**, 177206 (2007).

[74] N. Aliouane, O. Prokhnenko, R. Feyerherm, M. Mostovoy, J. Strempfer, K. Habicht, K. C. Rule, E. Dudzik, A. U. B. Wolter, A. Maljuk and D. N. Argyriou, J. Phys. Condens. matter **20**, 434215 (2008).

[75] D. N. Argyriou, N. Aliouane, J. Strempfer, B. Bohenbuck, K. Habicht and M. v. Zimmermann, Phys. Rev. B **75**, 020101 (2007).

[76] D. Mannix, D. McMorrow, R. A. Ewings, A. T. Boothroyd, D. Prabhakaran, Y. Joly, B. Janousova, C. Mazzoli, L. Paolasini and S. B. Wilkins, Phys. Rev. B **76**, 184420 (2007).

[77] Y. Yamasaki, H. Sagayama, T. Goto,M. Matsuura, K. Hirota, T. Arima and Y. Tokura, Phys. Rev. Letters **98**, 147204 (2007).

[78] J. R. Teague, R. Gerson and W. J. James, Solid State Commun. **8**, 1073 (1970).

[79] I. Sosnowska, T. P. Neumaier and E. Steichele, J. Phys. C **15**, 4835 (1982).

[80] S. Lee, T. Choi, W. Ratcliff, R. Erwin, S.-W. Cheong and V. Kiryukhin, Phys. Rev. B **78**, 100101(R) (2008).

[81] J. Wang, J. B. Neaton, H. Zheng1, V. Nagarajan, S. B. Ogale, B. Liu, D. Viehland, V. Vaithyanathan, D. G. Schlom, U. V. Waghmare, N. A. Spaldin, K. M. Rabe, M. Wuttig and R. Ramesh, Science **299**, 1719 (2003).

[82] C. Ederer and N. A. Spaldin, Phys. Rev. B **71**, 224103 (2005).

[83] T. Zhao, A. Scholl, F. Zavaliche, K. Lee, M. Barry, A. Doran, M. P. Cruz1, Y. H. Chu, C. Ederer, N. A. Spaldin, R. R. Das, D. M. Kim, S. H. Baek, C. B. Eom and R. Ramesh, Nature Mater. **5**, 823 (2006).

[84] T. Arima, T. Goto, Y. Yamasaki, S. Miyasaka, K. Ishii, M. Tsubota, T. Inami, Y. Murakami and Y. Tokura, Phys. Rev. B **72**, 100102 (2005).

[85] N. Aliouane, D. N. Argyriou, J. Strempfer, I. Zegkinoglou, G. Landsgesell and M. v. Zimmermann, Phys. Rev. B **73**, 020102 (2006).

[86] J. Strempfer, B. Bohenbuck, I. Zegkinoglou, N. Aliouane, S. Landsgesell, M. v. Zimmermann and D. N. Argyriou, Phys. Rev. B **78**, 024429 (2008).

[87] H. Walker, R. Ewings, F. Fabrizi, D. Mannix, C. Mazzoli, S. Wilkins, L. Paolasini, D. Prabhakaran, A. Boothroyd and D. McMorrow, Physica B: Condensed Matter **404**, 3264 (2009).

[88] N. Aliouane, K. Schmalzl, D. Senff, A. Maljuk, K. Prokes, M. Braden and D. N. Argyriou, Phys. Rev. Lett. **102**, 207205 (2009).

[89] T. Kimura, G. Lawes and A. P. Ramirez, Phys. Rev. Lett. **94**, 137201 (2005).

[90] K. Marty, V. Simonet, E. Ressouche, R. Ballou, P. Lejay and P. Bordet, Phys. Rev. Lett. **101**, 247201 (2008).

[91] M. Fiebig, T. Lottermoser, D. Frohlich, A. V. Goltsev and R. V. Pisarev, Nature **419**, 818 (2002).

[92] P. Rejmankova, J. Baruchel, P. Moretti, M. Arbore, M. Fejer and G. Foulon, J. Appl. Cryst. **31**, 106 (1998).

[93] M. Gonzalez-Manas, B. Vallejo and M. A. J. Caballero, Appl. Cryst. **38**, 1012 (2005).

[94] S. Hong, J. Woo, H. Shin, J. U. Jeon, Y. Eugene Pak, E. L. Colla, N. Setter, E. Kim and K. No, J. Appl. Phys. **89**, 1377 (2001).

[95] F. Nolting, A. Scholl, J. Stohr, J. W. Seo, J. Fompeyrine, H. Siegwart, J.-P. Locquet, S. Anders, J. Luning, E. E. Fullerton, M. F. Toney, M. R. Scheinfein and H. A. Padmore, Nature **405**, 767 (2000).

[96] S. Eisebitt, J. Luning, W. F. Schlotter, M. Lorgen, O. Hellwig, W. Eberhardt and J. Stohr, Nature **432**, 885 (2004).

[97] P. Evans, E. D. Isaacs, G. Aeppli, Z. Cai and B. Lai, Science **295**, 1042 (2002).

[98] O. G. Shpyrko, E. D. Isaacs, J. M. Logan, Yejun Feng, G. Aeppli, R. Jaramillo, H. C. Kim, T. F. Rosenbaum, P. Zschack, M. Sprung, S. Narayanan and A. R. Sandy, Nature **447**, 68 (2007).